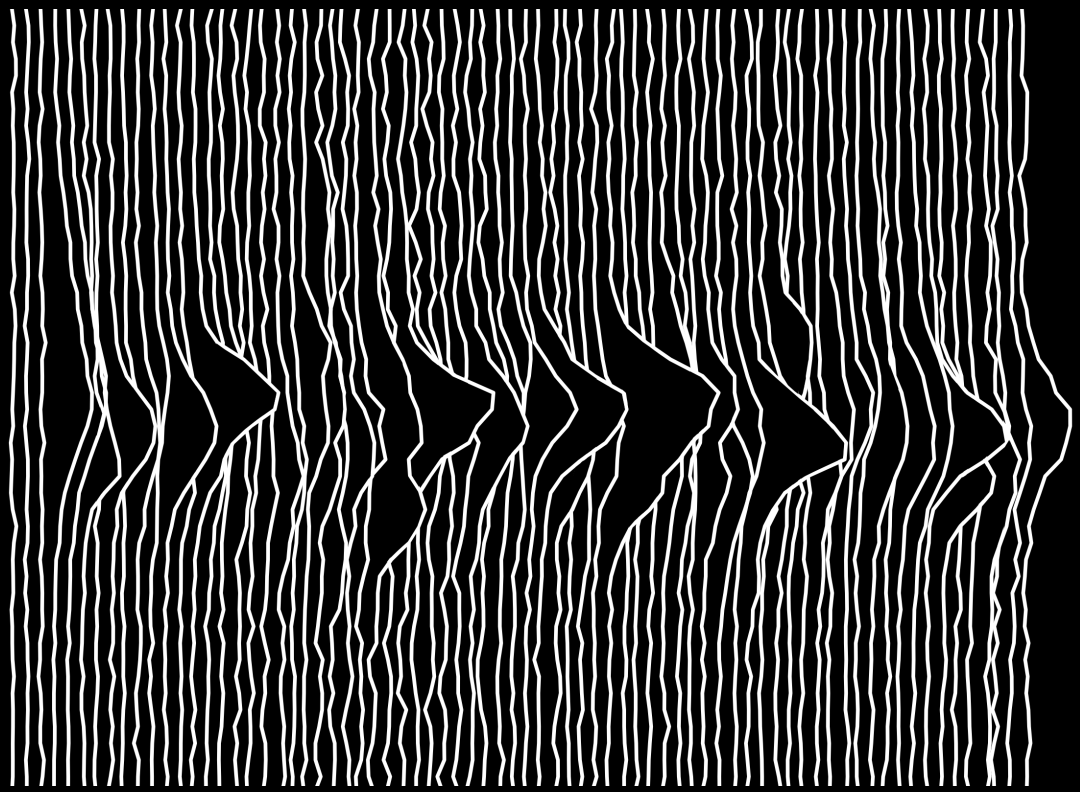

Image credit: C. Sobey for the LOFAR collaboration

Investigating astrophysical plasmas with pulsars using LOFAR and other telescopes

Dissertation
zur
Erlangung des Doktorgrades (Dr. rer. nat.)
der
Mathematisch-Naturwissenschaftlichen Fakultät
der
Rheinischen Friedrich-Wilhelms-Universität Bonn

vorgelegt von
Charlotte Anne Sobey
aus
Bristol, Großbritannien

Bonn 2014

Angefertigt mit Genehmigung der Mathematisch-Naturwissenschaftlichen Fakultät der Rheinische Friedrich-Wilhelms-Universität Bonn

Berichterstatter:

Prof. Dr. M. Kramer

Prof. Dr. U. Klein

Tag der Promotion: 26.01.2015

Erscheinungsjahr: 2015

RHEINISCHE FRIEDRICH-WILHELMS-UNIVERSITÄT BONN

Abstract

The Faculty of Mathematics and Natural Sciences

Doctor rerum naturalium

by Charlotte Anne Sobey

Pulsars are rapidly-rotating, highly-magnetised neutron stars that produce radio emission in their magnetospheres, which is detected as pulses on Earth. The focus of this thesis is observing pulsars as the means to study the properties of astrophysical plasmas that span many orders of magnitude in magnetic field strength (B) and scale. **Chapter 1** provides an introduction to pulsars, their use as as probes of astrophysical plasmas, and our current knowledge of the Galactic magnetic field. **Chapter 2** presents the numerous magnetospheric ($B \sim 10^{12}$ G) emission characteristics of a mode-changing pulsar, PSR B0823+26, the mechanism behind which is not yet well understood. Using Low Frequency Array (LOFAR) observations, I report on the discovery that PSR B0823+26 has a weak and sporadically-emitting 'quiet' mode that is over 100 times weaker than that of the more regularly-emitting 'bright' mode. The transition between emission modes is concurrent across the range of frequencies observed and occurs within one rotational period (0.531 seconds). In **Chapter 3** I review the practical methods for determining Faraday rotation measures (RMs) towards polarised sources, and collect the literature RMs measured towards pulsars and extragalactic (EG) sources, for the purpose of studying the Galactic magnetic field (GMF, $B \sim \mu$G). **Chapter 4** describes the effect of the ionosphere on radio observations of astronomical sources. Observations of pulsars using LOFAR demonstrate the high accuracy of a code used to calculate the amount of ionospheric Faraday rotation towards a specific line-of-sight using publicly available, GPS-derived total electron content maps and the geomagnetic reference field ($B \sim 0.5$ G). I show that this technique can confidently determine some of the highest-precision ionosphere-corrected RMs towards pulsars ever achieved, towards more accurately measuring and monitoring the GMF. **Chapter 5** presents new, or increased-accuracy, ionosphere-corrected RMs towards pulsars using polarisation observations with three different central radio frequencies. The RMs towards pulsars and EGs collected in Chapters 3 and 5 are used to reconstruct a map of the large-scale GMF using wavelet analysis, for which the additional RM data were beneficial. However, to more accurately reconstruct the three-dimensional GMF, more RMs and independent pulsar distances are required, especially towards the Galactic halo. **Chapter 6** summarises this thesis and provides prospects for future related work.

Acknowledgements

This thesis would not have been possible without the support of my supervisors, Michael Kramer and Aris Noutsos, and the financial support from the DFG, within the research unit FOR 1254 chaired by Uli Klein and vice-chaired by Rainer Beck. I thank them wholeheartedly for their respective contributions to this project. Thank you also to the other members of the DFG research unit for interesting magnetism-related discussions at our annual meetings.

Thank you to the members of the LOFAR Pulsar Working Group, especially to the co-PIs Jason Hessels and Ben Stappers, who helped me with everything pulsar-related and allowed me to gain experience working in the community. Thank you also to the members of the LOFAR Magnetism Key Science project, especially George Heald, who helped me with everything RM-synthesis and magnetism related.

Many thanks to the members of the MPIfR 'Research in Fundamental Physics' group for sharing their expertise and advice, usually during coffee breaks, and best wishes to those of you who shared the 'student dungeon' with me! Special thanks go to Carolina Mora who helped me to survive Russia!

Thanks to my friends in Argelander, especially to Nadychen Ben Bekthi, for sharing interesting discussions and advice, also usually over coffee.

Thank you to everyone at the MPIfR and Argelander who helped me with all things practical, including Frau Breuer, Frau Kramer, Frau Menten, Frau Mertens, Frau Tran, the IT department, the catering department, et al.

In fond memory of our supportive and helpful secretary, Gabi Breuer.

Thank you to the operators, observers, and reducers who helped me with the Effelsberg, LOFAR, Lovell, and WSRT observations. This work is partly based on observations with the 100-m telescope of the Max-Planck-Institut für Radioastronomie at Effelsberg. The WSRT is operated by ASTRON/NWO. The Low-Frequency Array (LOFAR) was designed and constructed by ASTRON, the Netherlands Institute for Radio Astronomy, and has facilities in several countries, that are owned by various parties (each with their own funding sources), and that are collectively operated by the International LOFAR Telescope (ILT) foundation under a joint scientific policy.

The experience of doing research over the past four years has been a valuable and eye-opening one. I have met so many new people, who are too numerous to name here, but have all contributed in some way to my overall experience – thank you!

Thank you to my family for supporting me for all of these years.

Thank you to George for your love and support.

Woof woof to Kirby!

Contents

List of Figures

List of Tables

Chapter 1

Introduction

1.1 Motivation

Magnetic fields are ubiquitous throughout the Universe and are important on all scales in nature: from quantum scales, e.g., the magnetic dipole moment of electrons, up to the largest virialised systems in the Universe – galaxy clusters (e.g. Feretti et al., 2012) – and beyond (e.g. Kunze, 2013); from the microgauss field strengths in the interstellar medium of galaxies (e.g. Beck and Wielebinski, 2013) up to the petagauss field strengths generated by magnetars (neutron stars characterised by their extreme magnetic field strength, Kouveliotou et al., 1998).

The effects of cosmic magnetic fields in are diverse, and they play a crucial role in numerous astrophysical processes. For example, magnetic reconnection in the Earth's magnetotail is the primary source of the magnificent polar aurora (Angelopoulos et al., 2008). Galactic magnetic fields accelerate and deflect cosmic rays (Medina Tanco et al., 1998, Troitsky, 2006), impact evolution of molecular clouds and star formation (Peters et al., 2011, Crutcher, 2012), and effect the transport of heat, angular momentum and energy (Boulares and Cox, 1990, Schekochihin and Cowley, 2007).

There is often no direct method for measuring cosmic magnetic fields, however it is possible to observe their effects in order to study them. For example, Zeeman splitting identified in Solar spectra was used to infer the magnetic field direction and strength in sunspots (Hale, 1908). Synchrotron radiation, and its polarisation, is a significant portion of the diffuse Galactic radio continuum emission and has provided constraints on

the regular large-scale Galactic magnetic field strength in the disk and halo of the Milky Way (Sun et al., 2008). Faraday rotation measurements towards polarised extragalactic sources led to the discovery that a large scale, organised magnetic field permeates the disk of our Galaxy (Davies, 1968), and are still a component of Galactic magnetic field structure studies (e.g. Van Eck et al., 2011). Despite these studies, astrophysical magnetic fields in plasmas are still poorly understood: the mechanism by which the strong magnetic fields in the pulsar magnetosphere generate radio emission is still elusive and measurements of the structure of the Milky Way's magnetic field are sparse, especially at distances greater than several kiloparsecs from the Sun.

The study of pulsars has contributed to numerous areas of research, from tests of gravity (Kramer et al., 2006a) to constraining the neutron-rich dense matter equation of state (Demorest et al., 2010), leading to their description as 'a physicist's dream come true' (Lorimer and Kramer, 2012). This work uses radio-frequency observations of pulsars to study astrophysical plasmas with various magnetic field strengths (B): the pulsar magnetosphere ($\mathrm{B} \sim 10^{12}\,\mathrm{G}$), the ionosphere ($\mathrm{B} \sim 0.5\,\mathrm{G}$), and the Galactic magnetic field (GMF, $\mathrm{B} \sim \mu\mathrm{G}$).

There are many advantages to observing pulsars at low-frequencies: pulsars often have steep spectral indices (e.g. Bates et al., 2013), resulting in larger flux densities at low-frequencies; effects of the interstellar medium (e.g. dispersion, Faraday rotation, scattering) are more pronounced, and therefore can be measured to greater accuracies, at low-frequencies (e.g. Lorimer and Kramer, 2012). Despite the discovery of pulsars at low frequencies (Hewish et al., 1968), low-frequency observations of pulsars have been somewhat infrequent in the interim.

In recent years, however, low-frequency radio astronomy has undergone a revival due to the construction of the Giant Metrewave Radio Telescope (GMRT, Swarup, 1991) and next-generation aperture array radio telescopes such as the Low Frequency Array (LOFAR, Stappers et al., 2011, van Haarlem et al., 2013), the Long-Wavelength Array (LWA, Kassim et al., 2010), and the Murchison Widefield Array (MWA, Mitchell et al., 2010). The first phase of the Square Kilometre Array (SKA, Garrett et al., 2010) is also planned to feature a large number of low-frequency antennas, operating at $\sim 70 - 450$ MHz. These telescopes open new scientific horizons in the area of low-frequency radio

astronomy, including providing high-quality polarisation data on pulsars, allowing studies of the pulsar emission mechanism, and determining high-precision Faraday rotation measures (RMs) towards improving constraints on the Galactic magnetic field structure.

LOFAR, used extensively for this work, is a next-generation radio telescope and low-frequency pathfinder to the SKA, currently consisting of 46 antenna stations – 38 located in the Netherlands, and eight located in neighbouring European countries, including five in Germany. Increasing the sensitivity and resolution of low-frequency radio observations are among the central goals of the project. LOFAR stations consist of: a low-band antenna (LBA) sub-station with 96 individual dipole antennas, semi-randomly arranged within an 87-metre-diameter circular area, optimised for detecting 30–80 MHz signals in full polarisation; and two high-band antenna (HBA) sub-stations, each 30.5 metres in diameter with 384 individual 'bow-tie' antennas optimised for detecting 110–240 MHz signals, arranged in 24 4×4-antenna tiles (for a further details see van Haarlem et al., 2013). Since the dipoles have no moving parts, LOFAR emulates the pointing and tracking of conventional dish antennas by forming a 'phased-array' using analogue and digital beam-forming techniques (tied-array mode, Stappers et al., 2011); the signals received by the dipoles are summed together after introducing predetermined differential time delays (using the same principle as N-slit diffraction). All 24 LOFAR core stations, with a maximum baseline of 3.5 km, can be incorporated into a tied-array mode for observing pulsars in the time-domain adding to the overall sensitivity and reducing the field-of-view to five arcminutes. Recording the resulting high data rates (up to several Gigabits per second) is made possible through high-speed fibre network infrastructure connections to a central processing unit.

1.2 Pulsars

Many scientific and technical advancements during the twentieth century led to the theoretical prediction of neutron stars (Baade and Zwicky, 1934) and Jocelyn Bell's observational discovery in 1967 that they emit at radio wavelengths (pulsars – a portmanteau of pulsating star) using the Interplanetary Scintillation phased-array telescope (a fixed dipole array at the Mullard Radio Astronomy Observatory that observed the sky at 81.5 MHz, Hewish et al., 1968, Pilkington et al., 1968). This includes the discovery of the neutron (Chadwick, 1932), and the calculation of the maximum mass of

a rotating white dwarf star beyond which the degenerate electron pressure is unable to sustain equilibrium with the object's self gravity (Chandrasekhar, 1931).

In the intervening years since their observational discovery, over 2300 pulsars stars have been discovered (Manchester et al., 2005a), and have contributed to many advances in various research fields, including: super-dense matter and the structure of neutron stars (e.g. Hessels et al., 2006); binary systems with companions including planets (e.g. Wolszczan and Frail, 1992), white dwarfs (e.g. Antoniadis et al., 2013), other neutron stars (e.g. Burgay et al., 2003), and their evolution (e.g. Backer et al., 1982, Tauris and van den Heuvel, 2014); emission from plasmas in extreme magnetic fields (e.g. Goldreich and Julian, 1969); theories of gravity in the strong-field regime and gravitational waves (Hulse and Taylor, 1975, Taylor and Weisberg, 1982, Lyne et al., 2004); probes of the electron density (e.g. Cordes and Lazio, 2002) and magnetic field (e.g. Noutsos et al., 2008) in the interstellar medium of the Galaxy. It is exciting to postulate what continuing research in the era of the SKA will reveal.

Below are brief summaries of the physical and observable properties of pulsars, including characteristics of pulsar emission and how their signals may be used as probes of the ISM (although further details and references can be found in Lorimer and Kramer, 2012).

1.2.1 Theoretical background

Pulsars are highly magnetised and rapidly rotating neutron stars. When an 8–20 $M_\odot$ main-sequence star has exhausted its source of energy for nuclear fusion it undergoes a supernova explosion, during which the core of the star collapses under decreased radiation pressure and self-gravity to form a neutron star. Pulsars are therefore extremely compact: approximately 1.4 times the mass of the Sun condensed into an object with atomic-nuclear density just tens of kilometres in diameter.

Pulsars have been observed to radiate throughout the range of the electromagnetic spectrum, from radio to gamma-ray wavelengths. They produce coherent radio emission that is understood to be generated by acceleration of particles to highly relativistic velocities at low altitudes in the magnetic polar caps of an approximately dipolar-structured magnetosphere (Goldreich and Julian, 1969). As they rapidly rotate, the beam of radiation is observed as a pulse in flux when the magnetic axis, offset from the rotation axis by

angle α, sweeps across the line-of-sight (LOS) of the observer, analogous to a 'cosmic lighthouse', see Fig. 1.1. Therefore, periodic pulses can be observed that correspond to the rotational period, P, of the pulsar. The rotation periods of currently discovered pulsars range from 1.3 milliseconds (Hessels et al., 2006) up to 11.8 seconds (Dib and Kaspi, 2014).

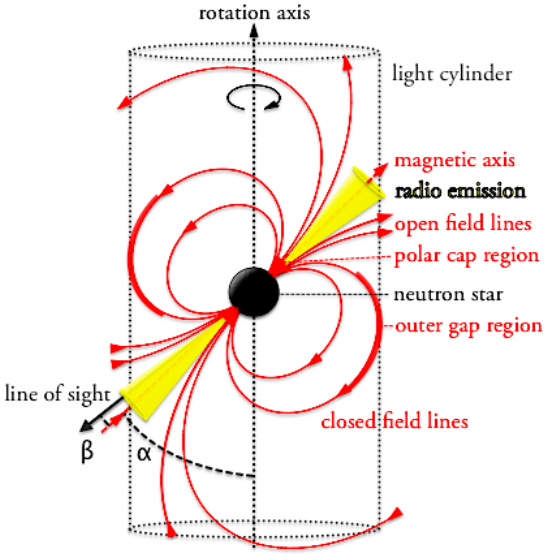

FIGURE 1.1: A schematic diagram showing the main features of the 'toy model' of a pulsar.

The rotational spin periods of isolated pulsars gradually increase with time, $\dot{\mathrm{P}} = \mathrm{d}P/\mathrm{dt}$, due to loss of rotational kinetic energy, E_{rot} of a pulsar,

$$\dot{E}_{\mathrm{rot}} = -I\dot{\Omega}\Omega = 4\pi^2 I\dot{P}P^{-3}, \tag{1.1}$$

where I is the moment of inertia and $\Omega = 2\pi/P$ is the angular frequency of the pulsar. Although the moment of inertia of pulsars is not currently known, it is often approximated as a uniform sphere, $I = 2/5MR^2$. Assuming average pulsar parameters with mass $M = 1.4\,\mathrm{M}_\odot$ and radius $R = 10\,\mathrm{km}$, the moment of inertia is approximately $10^{38}\,\mathrm{kg\,m^2}$, and the average mass density is approximately $10^{17}\,\mathrm{kg\ m^{-3}}$. The spin-down luminosity, $\dot{E}_{\mathrm{rot}}$, represents the total power output of the neutron star, which is approximately $10^{31}\,\mathrm{erg\,s^{-1}}$, assuming the previous parameters and average values of $P = 1\,\mathrm{s}$ and $\dot{P} = 10^{-15}$. Only a small fraction of this energy is converted to radio emission – the majority is converted to high-energy emission, magnetic dipole radiation and a pulsar wind. Pulsar winds observed in the radio, optical, X-ray and gamma-ray wavebands

around several pulsars are composed of relativistic charged particles (most likely leptons) and magnetic fields carrying rotational energy away from the star and depositing it in the surrounding medium (e.g. Amato, 2014).

Assuming pulsars have strong dipolar magnetic fields, as illustrated in Fig. 1.1, and their spin-down is dominated by magnetic dipole braking, the magnetic field strength at the surface of the neutron star, $B_{\rm S}$, can be estimated:

$$B_{\rm S} = \sqrt{\frac{3c^3}{8\pi^2}\frac{I}{R^6 \sin^2\alpha} P\dot{P}} \approx 10^{12}\ {\rm G} \left[\frac{P}{\rm s}\right]^{1/2} \left[\frac{\dot{P}}{10^{-15}}\right]^{1/2}. \tag{1.2}$$

The order of magnitude calculation on the right hand side of Equation 1.2, referred to as the 'characteristic magnetic field', assumes the same parameters as those used previously and $\alpha = 90°$. This infers a large magnetic field strength at the surface of such a neutron star, which is in agreement with scarce measurements from X-ray observations (e.g. Bignami et al., 2003).

The pulse period, and its rate of change, can also be used to infer the 'characteristic age' of a pulsar, assuming that the spin period at initial formation is much smaller than at present and the spin-down is due to magnetic dipole radiation:

$$\tau_{\rm c} = \frac{P}{2\dot{P}} \approx 15.8\ {\rm Myr} \left[\frac{P}{\rm s}\right] \left[\frac{\dot{P}}{10^{-15}}\right]^{-1}. \tag{1.3}$$

This does not necessarily provide an accurate age estimate, but provides a reasonable order of magnitude age for the Crab pulsar (1240 y) which was formed from a supernova observed from Earth in 1054 CE (see Lorimer and Kramer, 2012).

1.2.2 Observable radio emission properties

Pulsars are usually observed by adding (folding) many pulses at the pulsar period using several parameters contained in a timing ephemeris, including the dispersion measure (see Section 1.2.3.1), the instantaneous spin frequency and the change in spin frequency. Averaging over many rotations results in an average pulse profile – a unique 'fingerprint' for each pulsar – that is often remarkably stable, and reflects their clock-like rotational stability (e.g. Liu et al., 2012). In the simplest cases the profile may consist of single component(s) that are Gaussian-like in shape. More complex profiles include double- or

multiple-peaked shapes, and/or emit over a large pulse phase range, for examples see Figs. 1.2, 1.3, 1.4.

The natural clock-like stability of the observed pulses provides a powerful technique called 'pulsar timing' (see e.g. Lorimer and Kramer, 2012). The observed pulse profile can be correlated with a model template of the profile to create times-of-arrival of the observed pulses (TOAs). The TOA uncertainty is proportional to the width of the pulse profile, and inversely proportional to the signal-to-noise (S/N). Therefore millisecond pulsars with narrow pulse profiles and high flux densities provide arrival times with the smallest uncertainty. It is desirable to minimise the 'timing residuals', the result from comparing the TOAs to a timing model that includes several delay corrections, e.g., barycentric, clock, etc. Moreover, the period of the pulsar may notably change between observing epochs, for example, if the pulsar is in a binary system or has a high spin-down rate. Where necessary, the correct period is measured by fitting for the drift rate of the pulse against integration time, and is essential for maximising the S/N of the pulse profile, see Fig. 1.2. Figure 1.2, right panel, shows that after folding at the correct period, the true pulse profile shape is recovered and is suitable for use in timing analysis. One strength in pulsar timing is that any difference between the observational and model TOAs is required to contain an integer number of rotations. This powerful method has been used to detect pulsars in interesting systems, such as the first exoplanets orbiting PSR B1257+12 (Wolszczan and Frail, 1992), and to test theories of gravity, such as inferring emission of gravitational waves from PSRs J0737-3039 A & B (Lyne et al., 2004). It is also being applied to an array of pulsars around the sky towards a gravitational wave detector (Hobbs et al., 2010).

Early pulsar observations showed that single pulses were also frequently highly polarised, both in linear and circular polarisation at 400 MHz (Lyne and Smith, 1968, Craft et al., 1968a, Clark and Smith, 1969). The mean pulse profiles of pulsars show varying degrees of polarisation; from the Vela pulsar, PSR B0833–45, which is almost completely linearly polarised with a uniform change in position angle across the pulse window (Radhakrishnan et al., 1969); through those with high fractional polarisation such as PSRs B1929+10, Fig. 1.3, and PSR B2045–16 at 2.7 GHz (Komesaroff et al., 1970); to, for example PSR B0031–07, where the mean pulse is essentially unpolarised at 410 and 1665 MHz (Manchester, 1971). Linear polarisation arises naturally from the relativistic streaming motion of the plasma (particles or bunches) along the magnetic field lines

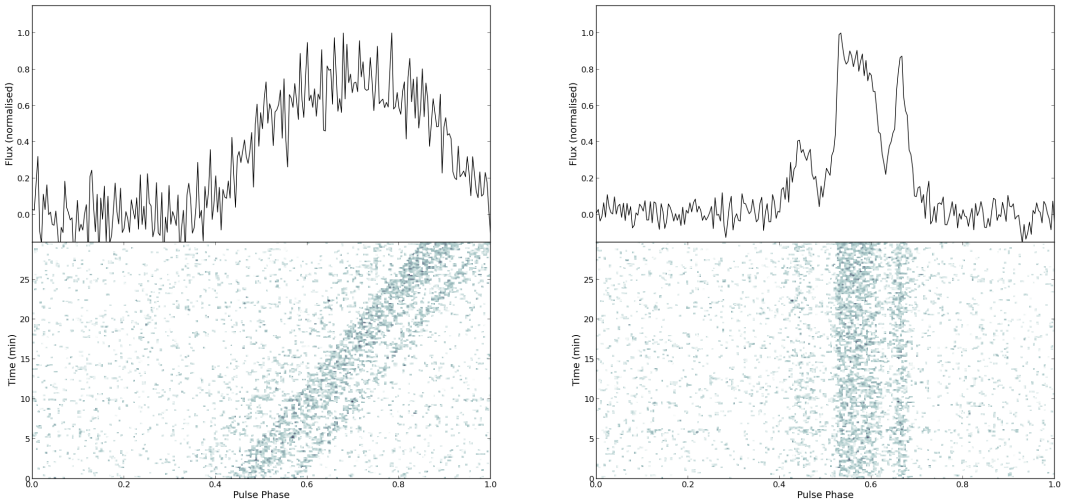

FIGURE 1.2: A time series (lower) and resulting average pulse profile (top) of PSR J0613-0200 ($P = 3.06$ ms) observed on 16 February 2012 using the Effelsberg telescope at 1347.5 MHz with 200 MHz bandwidth. *Left:* Folded at the original, slightly incorrect pulse period, the pulse drifts by ∼1.22 ms during the integration. *Right:* The same time series after folding at the corrected spin frequency using the measured drift rate. The linear trend has been removed and the rms of the timing residuals are significantly reduced.

above the pulsar polar cap (McKinnon and Stinebring, 1998). Moreover, the 'S-shaped' sweep of the polarisation position angle with pulse longitude, see Fig. 1.3, measures the pulsar's magnetic field lines upon the plane of the sky, and is observed in the polarised radio emission from many pulsars (Lyne and Manchester, 1988). The link between the particle motion and sweep of polarisation position angle (Radhakrishnan and Cooke, 1969) has become the observational cornerstone for polar cap models of pulsar radio emission (e.g. Everett and Weisberg, 2001). There are two proposed origins of circular polarisation: either intrinsic to the emission mechanism, for example, curvature radiation (e.g. Gangadhara, 2010) or relativistic effects (Melrose and Luo, 2004); or generated by propagation effects in an inhomogeneous birefringent plasma (e.g. Cheng and Ruderman, 1979). Although extensive pulsar polarimetric studies are available, the origin of pulsar emission and polarisation are still not well understood due to their diverse nature. However, further studies of the polarised emission will provide greater information about the origin of the polarised emission and its propagation through the ISM.

Since the discovery pulsars, many facets of pulsar emission have been observed. The coherent and often highly polarised emission is seen to show variability on almost all timescales which it is possible to measure (Keane, 2013): from nano-second 'shots' which

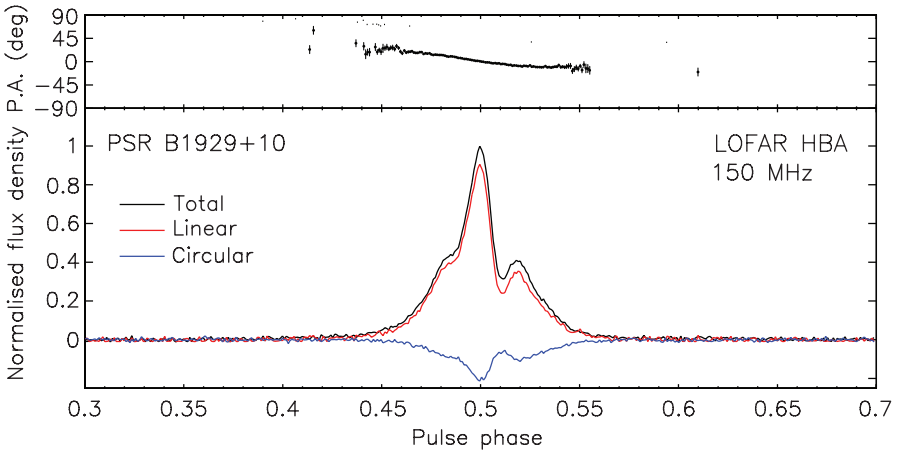

FIGURE 1.3: An example polarisation pulse profile of PSR B1929+10 observed with LOFAR at a centre frequency of 150 MHz. The normalised flux density of the total (Stokes I, black lines), linearly polarised (Stokes $\sqrt{Q^2 + U^2}$, red lines), and circularly polarised emission (Stokes V, blue lines) is shown. Above the flux density profile, the polarisation position angle (P.A.= 0.5arctan(U/Q)) of the linearly polarised emission is shown. Image credit: A. Noutsos, et al. in preparation (2014).

are expected to be the quanta of pulsar emission (Hankins et al., 2003); to multidecadal variations presumably due to evolution of the magnetic field (Lyne et al., 2013). Single pulse profiles also vary in terms of intensity or shape. Indeed, there are a number of common emission phenomena which show that pulsar magnetospheres can be both stable and dynamic, and are thought to be connected, and related to changes in the current flows in the pulsar magnetosphere (Lyne et al., 2010, van Leeuwen and Timokhin, 2012, Li et al., 2012a). Those which are most relevant in Chapter 2 are explained below.

1.2.2.1 Drifting sub-pulses

First identified by Drake and Craft (1968), the drifting subpulse phenomenon is the periodic drift of consecutive single pulses, folded at the pulsar period, through the pulse window. The time between the systematic repetition of these drift bands, P_3, can range between two to 15-times the spin period (Rankin, 1986). The sub-pulse intensity is also systematically modulated along drift bands, typically increasing toward the centre of the mean pulse envelope (Gil and Sendyk, 2003). This high degree of stability and organised behaviour on second to minute timescales has most commonly been explained by the carousel model of pulsar emission (Sturrock, 1971, Ruderman and Sutherland, 1975, Cheng and Ruderman, 1980, Ruderman, 1981, Filippenko and Radhakrishnan, 1982). At the polar cap, a 'gap' directly above the neutron star surface is formed that develops

TeV potentials. Discrete electron-positron 'sparks' precess about the magnetic axis due to an $\mathbf{E} \times \mathbf{B}$ drift, analogous to a rotating carousel. The charged particles accelerated in the gap move outwards along the field lines and produce coherent radio emission kilometres above the surface, following alleged secondary pair production. Recently, the rate of rotation was found to be proportional to the gradient of the accelerating potential across the polar cap, not the absolute value (van Leeuwen and Timokhin, 2012). However, observed properties in some pulsars are inconsistent with this model, such as steps in subpulse phase (Edwards et al., 2003). Davies et al. (1984) also noted that it is essential to introduce quadrupole or other multiple components to the assumed dipolar magnetic field together with a backwards twist of the field at large radii to fit the polar cap model to observed pulse profiles of PSR B0809+74. A proposed alternative is that beating between the pulse period and non-radial oscillations of the neutron star surface aligned with and symmetric to the magnetic axis modulates the emission (Drake and Craft, 1968, Ruderman, 1968, Clemens and Rosen, 2004). This model can reproduce the morphological features of pulsar beams such as the average pulse profile and subpulse drifting and are at least as consistent with observational data as the carousel model (Hassall et al., 2013), but cannot provide an explanation for observed curvature in subpulse drift bands. A study of 187 radio pulsars revealed that more than one in three show subpulse drifting, indicating this is a common phenomenon (Weltevrede et al., 2006a). Therefore, it is likely that this process is an intrinsic property of the pulsar emission mechanism, independent of magnetic field strength and possibly becoming more coherent as the pulsar ages.

1.2.2.2 Nulling and extreme nulling

There is evidence that subpulse drifting is related to another emission phenomenon; nulling. This is where there is an abrupt cessation in the pulsed emission amongst otherwise strong and steady pulses, first identified by Backer (1970a). The length of nulls can vary widely, from one or two spin periods to weeks or years in extreme cases (Wang et al., 2007). The null fraction, NF, quantitatively describes the fraction of pulses with no detectable emission, although this alone does not describe whether the pulsar undergoes many short nulls often or one long null in the same period of time. Nulls are also found to occur at random phases in drift bands, indicating some persisting memory in the emission mechanism for drift bands without affecting null occurrence. The drift band

rate is affected before and after a null and the single pulses after null are above average in intensity, and appear correlated with increasing null length (Lyne and Ashworth, 1983). In the model of Ruderman and Sutherland (1975), nulling might be caused by an extinction or quenching of the outward flow of charged particles in the open field lines. In pulsars which show both subpulse drifting and nulling, continuation of drifting at a reduced rate during the null implies that there is continued but reduced particle emission (Lyne and Ashworth, 1983). Also, the size of the carousel may decrease after a null, implying that the height at which radio emission is produced may also decrease (van Leeuwen et al., 2003). There is evidence that the nulling fraction is correlated with pulsar spin period, and less significantly with pulsar age (Biggs, 1992), similar to that found for subpulse drifting. Studies have revealed that there are approximately a hundred pulsars known to exhibit nulling (Gajjar et al., 2012), note that this number is strongly affected by the fraction of pulsars which are sufficiently bright to enable single pulse studies. There is also more recent evidence that shows emission during a null may not completely cease; Esamdin et al. (2005) showed that for PSR B0826–34, for which the NF is at least 70%, the integrated null data actually shows a weak pulse of about 2% of the mean flux density of the bright pulses, also with a change in the average pulse profile. Burke-Spolaor et al. (2012) also found evidence for weak emission in a previously identified null state for J1900–2600, implying that nulls are likely an extreme form of the mode-changing phenomena.

On longer time scales of weeks to years, a small number of pulsars described as 'intermittent' display extreme nulling events, in which a seemingly normal pulsar becomes undetectable for days to years at a time and then abruptly switches 'on' again. PSR B1931+24 was the first such object discovered to show this behaviour when Kramer et al. (2006b) discovered that the emission is detectable for periods of five to ten days and undetectable for longer periods of 25 to 35 days – the transition between the two modes also occurred in less than 10 seconds (the upper limit as defined by the trade-off between time resolution and S/N). The spin-down rate is also correlated with this behaviour; the pulsar spins down twice as fast in the bright mode than in the quiet mode. The second of these pulsars to be discovered is PSR B1832+0029, which was detected as a normal pulsar for approximately one year and was subsequently undetected for two years (Kramer, 2008). The third member of this class to be discovered, PSR J1841-0500, was timed at 2 GHz for a year, after which it was undetected in 28 observations spanning

580 days (Camilo et al., 2012a). After this period, the pulsar emission reappeared in the observations with approximately the same flux. Consequently, the spin-down rate in the bright mode was found to be over 2.5-times that of the mode where the pulsar is not detected. There are now approximately ten pulsars known to display similar behaviour, the majority of which were discovered within the past two years (O'Brien et al., 2006, Lorimer et al., 2012, Surnis et al., 2012, Eatough et al., 2013a). For those which have timing solutions, when the pulsar is observed in the bright mode the spin-down is almost double that when it is undetected. The mechanism behind this is also likely to be related to that of less extreme mode-changing; a rapid, global change in the pulsar magnetosphere, either in the geometry (state) of the magnetosphere and/or a change in the distribution of current (Timokhin, 2010).

1.2.2.3 Mode-changing

Mode-changing is a similarly abrupt switch in the pulsed emission between two (or more) discrete and defined profiles (Lyne et al., 2010). First identified in PSR B1237+25 by Backer (1970b), there are now tens of pulsars known which display this behaviour. Mode changes manifest as a change in the pulse shape in total intensity (Lyne, 1971, Rankin et al., 1988) and in some cases, linear polarisation (Backer et al., 1976, Morris et al., 1980) and circular polarisation (Lyne, 1971, Cordes et al., 1978). A substantial number of pulsars with large changes in spin-down rates (0.3–13%) also have detectable correlated pulse profile changes (Lyne et al., 2010). For PSR B0031-07, a change in the integrated pulse profile is also coincident with a change in subpulse drift rate (Huguenin et al., 1970). This has been observed in other pulsars including B1918+19, B1944+17, and B2319+60 (Hankins and Wolszczan, 1987, Deich et al., 1986, Wright and Fowler, 1981). Burke-Spolaor et al. (2012) note that PSRs J0941–39 and B0826–34 weak emission mode in fact consists of sporadic single pulses, indicating that nulling may be another manifestation of mode-changing. Therefore, drifting subpulses, nulling and mode-changing observed in pulsars appear to be related phenomena, where observed pulse profile variations insinuate magnetospheric changes. It is evident that mode-changes occur on a global scale; observed mode-changes in PSR B0943+10 using radio (LOFAR and GMRT) and X-ray (XMM-Newton) observatories simultaneously show that while in the radio bright, highly organised mode the X-ray emission shows an unpulsed non-thermal component, whilst in the quieter chaotic mode, the X-ray emission more than doubles and in addition shows

a pulsed thermal component (Hermsen et al., 2013). Moreover, the transition between mode changes occurs rapidly – in less than ten times the spin periods (Nowakowski, 1991). Unlike the periodicity of subpulse drifting, transitions between modes occur more randomly (Wang et al., 2013).

The wide-ranging emission phenomena introduced in Chapter 1 are thought to be connected, and related to changes in the current flows in the pulsar magnetosphere (Lyne et al., 2010, van Leeuwen and Timokhin, 2012, Li et al., 2012a). For example, nulls can be regarded as a mode during which emission ceases or is not detected. Most pulsars may exhibit these emission phenomena, but the effects of pulse-to-pulse variability are hard to identify in sources with low flux densities, because summing over many pulses is required to reach sufficient signal-to-noise ratio (S/N). Also, it is possible that fewer pulsars are identified with longer characteristic timescale phenomena, such as mode-changing and extreme nulling, because frequent observations over a longer timespan are necessary to enable this. The hope is that better understanding these emission characteristics may lead to a better understanding of the magnetospheric emission mechanism itself.

The preceding description of pulsar emission phenomena is not exhaustive; for example, giant pulses with over ten times the average energy are also observed in a handful of pulsars (Hankins et al., 2003). There is also much to be learned from higher energy observations at X-ray and gamma-ray wavelengths, which are more dominant in terms of energy loss from the pulsar, for example, the Fermi Large Area Telescope has detected over 100 pulsars above 0.1 GeV (Abdo et al., 2013). The diversity in the behaviour of pulsar emission increases the difficulty in modelling the emission mechanism. However, observing these processes in detail in numerous sources may provide clues to conditions at the neutron star surface where production of high energy charged particles flow along open field lines.

1.2.3 Observable properties as probes of the interstellar medium

The radio waves emitted by pulsars are affected as they propagate through the ionised and magnetised interstellar medium (ISM). The signals are subject to effects such as dispersion, scattering, scintillation, and Faraday rotation. As such, these effects provide

additional insight into the nature of the ISM, for example, the electron density and magnetic field in the intervening medium between the pulsar and the Earth.

1.2.3.1 Dispersion

As electromagnetic radiation propagates through the ionised ISM, the signal is dispersed such that the arrival time of a radio pulse becomes increasingly delayed towards lower frequencies. The ionised component of the ISM affects the wave group velocity, causing it to be frequency-dependent. This effect was noted soon after the discovery of pulsars (Hewish et al., 1968). The delay in arrival time, $\Delta t_{\rm DM} = t_1 - t_2$, for a single pulse observed at two frequencies, ν_1 and ν_2, is given by the cold dispersion law,

$$\Delta t_{\rm DM} = 4148.808(3)\ {\rm s} \left[\frac{\rm DM}{\rm pc\ cm^{-3}}\right] \left[\left(\frac{\nu_2}{\rm MHz}\right)^{-2} - \left(\frac{\nu_1}{\rm MHz}\right)^{-2}\right], \tag{1.4}$$

(e.g. Lorimer and Kramer, 2012). The DM is a direct probe of the electron density, $n_{\rm e}$, in the column between the location of the pulsar and the observer on Earth,

$$\rm DM = \int_{observer}^{source} n_e dl, \tag{1.5}$$

where $n_{\rm e}$ is measured in $\rm cm^{-3}$, the distance of the pulsar is measured in pc, and hence the unit of DM is $\rm pc\,cm^{-3}$.

Since the time delay is inversely proportional to the square of the observing frequency, dispersion becomes increasingly severe at lower radio frequencies. For example, the expected time delay of the 5-ms extragalactic radio burst discovered at 1.4 GHz with a DM of $375\,\rm pc\,cm^{-3}$ (Lorimer et al., 2007) observed between 30 MHz and 80 MHz (the optimised frequency range of the LOFAR Low Band Antennas) would be 25 minutes! Measurements of dispersion therefore become more accurate when observing at lower frequencies, given that there is sufficient fractional bandwidth, such as that of LOFAR observations. Figure 1.4 shows the effect of dispersion on the pulses observed from an example pulsar, PSR B1133+16 with DM = 4.825(1) pc $\rm cm^{-3}$, using LOFAR at a centre frequency of 150 MHz. Even with this modest DM, the higher frequency emission arrives almost one pulse period (1.188 s) before the low frequency emission from equivalent pulses. Correction for this effect is essential for recovering the pulse profile, Fig. 1.4. PSR B1133+16 is located at approximately 0.35 kpc from the Sun (Manchester et al.,

2005b), and therefore the electron density in the ISM is approximately $0.014\,\mathrm{cm}^{-3}$ on average between the Sun and the pulsar. In early pulsar observations, Tanenbaum et al. (1968) were able to accurately predict the dispersive time delay to within 1 part in 3000 between 40 MHz and 430 MHz. More recently, this law was found to be accurate to better than 1 part in 10^5 using wide-band simultaneous observations between 40 MHz and 8 GHz (Hassall et al., 2012). It is also essential to consider dispersion when specifying observations; the frequency channels should be sufficiently narrow that the dispersive delay is correctable without introducing too much pulse broadening.

Pulsar DMs can also be used to estimate the distance to the pulsar, given some value of the electron density, $d \approx \mathrm{DM}/n_\mathrm{e}$. HI absorption (Ables and Manchester, 1976), parallax measurements from pulsar timing (e.g. Verbiest et al., 2008) or VLBI measurements (e.g. Deller et al., 2009), or associations with globular clusters (e.g. Harris, 1996) can be used to derive independent distance measurements of pulsars with DMs and scattering times, see below, in order to calibrate a model of the Galactic distribution of n_e (Cordes and Lazio, 2002). This model can be used to estimate the distances to other pulsars for which independent distances are unknown.

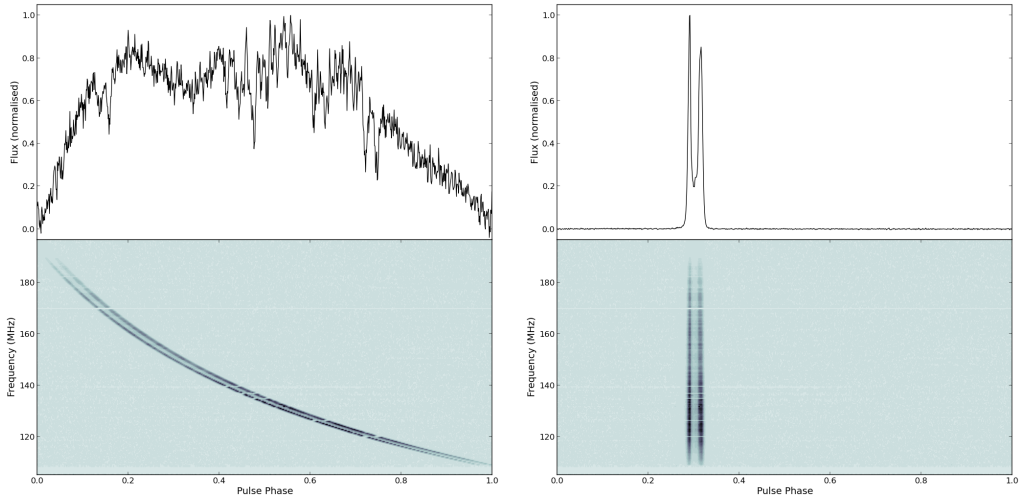

FIGURE 1.4: *Lower panels:* Flux against pulse phase and frequency for a ten-minute LOFAR HBA observation of PSR B1133+16 centred at 150 MHz with 90 MHz bandwidth. *Upper panels:* Frequency- and time-averaged pulse profiles. *Left:* dispersion of the pulse as it is observed by the telescope, showing the time delay of approximately one pulse period from the highest to lowest observing frequency. *Right:* dedispersed pulse, using the measured DM = 4.825(1) pc cm^{-3}, showing the characteristic narrow double-peaked profile.

1.2.3.2 Scattering and scintillation

Inhomogeneities in the density of the ISM also affect the propagation of pulsar signals. A scattering screen of ISM material located between the pulsar and Earth can cause refraction of the signal, where waves with larger angles of refraction arrive at later times. This scattering of rays is observed as a broadening of the pulse shape and a scattering tail – the intrinsic pulse shape convolved with an exponential decay in observed intensity, I, as a function of time,

$$I(t) \propto \exp\left(-\Delta t/\tau_{\rm s}\right), \tag{1.6}$$

where the scattering timescale, $\tau_{\rm s}$, is related to several physical constants, the electron density, scale of the structure in the scattering screen, a, pulsar distance, d, and observing frequency, ν:

$$\tau_{\rm s} = \frac{e^4}{4\pi^2 m_{\rm e}^2} \frac{\Delta n_{\rm e}^2}{a} d^2 \nu^{-4}, \tag{1.7}$$

(e.g. Lorimer and Kramer, 2012). Therefore, the observed scattering time is more strongly dependent on the observing frequency than dispersion. Similarly, high scattering times also affects the ability to detect pulsars towards low frequencies. Pulsars that have larger DMs are more likely to be affected by scattering, especially towards low observing frequencies. Figure 1.5 shows the exponential scattering tail caused by scattering of the main pulse (MP) and interpulse (IP) observed from the Crab pulsar (PSR B0531+21) at 150 MHz. This figure also shows an example of pulse profile evolution, where some pulse profile components are detected at some frequencies but not others, for example, the high-frequency components (HFC1, HFC2) following the IP, and the low-frequency component (LFC) preceding the MP. Scattering measures can also be used for studying the variation in the electron density along the LOS (e.g. Ramachandran et al., 1997).

The scattering of pulsar signals also produces interference patterns in the plane of the observer, which create patches of varying intensities that move as a function of time due to relative motions between the pulsar, observer and intervening material (e.g. Armstrong et al., 1995). This is observed as intensity variations in the signal over time and frequency, or scintillation. An example of this is shown in Chapter 2, Fig. 2.4. Scattering and scintillation can also cause depolarisation of the average polarisation pulse profiles (e.g. Komesaroff et al., 1971, Narayan, 1992).

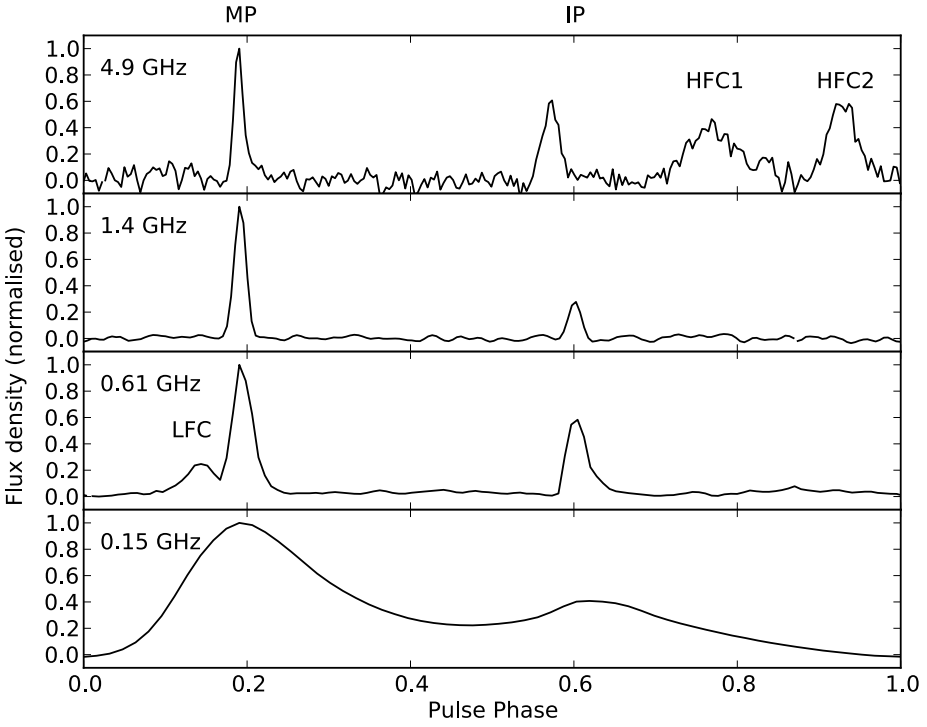

FIGURE 1.5: Multi-frequency pulse profiles of the Crab pulsar (PSR B0531+21): 150 MHz data obtained from a 15-min LOFAR observation; 606 MHz (Moffett and Hankins, 1996), 1408 MHz (Gould and Lyne, 1998), and 4885 MHz (Moffett and Hankins, 1999) obtained from the European Pulsar Network database. The pulse profile components common to all frequencies are labelled above the figure: the main pulse (MP), and interpulse (IP). Other components most identifiable at individual frequencies are labelled above the relevant profile: the high frequency components (HFC1 and HFC2) at 4885 MHz, and low frequency component (LFC) at 606 MHz.

1.2.3.3 Faraday rotation

The ISM is a magneto-ionic medium and as such is birefringent; right and left-handed circularly polarised light propagate at differing velocities. This causes the polarisation angle of linearly polarised radiation to be rotated as a function of frequency. This effect is called Faraday rotation after Michael Faraday who first demonstrated this effect in 1845. The polarised intensity, $\tilde{P}$, is obtained from the observed Q and U Stokes parameters,

$$\tilde{P} = Q + iU. \tag{1.8}$$

Similarly, the observed polarisation angle, χ, is also derived from these parameters,

$$\chi = \frac{1}{2} \arctan\left(\frac{U}{Q}\right). \tag{1.9}$$

The inverse tangent function necessary for the calculation of polarisation angles introduces the so-called $n\,\pi$ ambiguity, whereby one obtains the same polarisation angle if the angle is rotated by $n\,\pi$, where $n \in \mathbb{Z}$. The four Stokes parameters, I, Q, U, and V, are obtained from the electric field detected by the two polarisation feeds from the observing system, $\mathcal{E}_{\rm x}$ and $\mathcal{E}_{\rm y}$ if using linear feeds and $\mathcal{E}_{\rm L}$ and $\mathcal{E}_{\rm R}$ if using circular feeds:

$$\mathbf{S} = \begin{bmatrix} I \\ Q \\ U \\ V \end{bmatrix} \equiv \begin{bmatrix} \langle \mathcal{E}_{\rm x}^2 + \mathcal{E}_{\rm y}^2 \rangle \\ \langle \mathcal{E}_{\rm x}^2 - \mathcal{E}_{\rm y}^2 \rangle \\ \langle 2\mathcal{E}_{\rm x}\mathcal{E}_{\rm y} \cos\delta \rangle \\ \langle 2\mathcal{E}_{\rm x}\mathcal{E}_{\rm y} \sin\delta \rangle \end{bmatrix} \equiv \begin{bmatrix} \langle \mathcal{E}_{\rm L}^2 + \mathcal{E}_{\rm R}^2 \rangle \\ \langle -2\mathcal{E}_{\rm L}\mathcal{E}_{\rm R} \sin\delta \rangle \\ \langle 2\mathcal{E}_{\rm L}\mathcal{E}_{\rm R} \cos\delta \rangle \\ \langle \mathcal{E}_{\rm L}^2 - \mathcal{E}_{\rm R}^2 \rangle \end{bmatrix}, \tag{1.10}$$

(e.g. Lorimer and Kramer, 2012). Stokes I gives the total intensity and Stokes V gives the circular polarisation of the observed source. The angled brackets indicate time averages. For a single polarised source along the LOS, the RM of the ISM toward the source is conventionally expressed as a rotation of the linearly polarisation position angle as a function of wavelength squared

$$\chi\left(\lambda^2\right) - \chi_0 = \mathrm{RM}\lambda^2. \tag{1.11}$$

where χ_0 is the intrinsic polarisation angle emitted by the source, and λ is the observing wavelength. The measured RM can be used to investigate the electron density, $n_{\rm e}$, and the magnetic field, $\mathbf{B}$, along the various LOSs, since

$$\mathrm{RM} = \kappa \int_{\rm source}^{\rm observer} n_{\rm e}\mathbf{B} \cdot \mathrm{d}\mathbf{r}\ \mathrm{rad\,m^{-2}}, \tag{1.12}$$

where $n_{\rm e}$ is measured in $\mathrm{cm^{-3}}$, B in μG, d in pc, and the constant:

$$\kappa = 0.81\,\mathrm{rad\,m^{-2}\,cm^3\,\mu G\,pc^{-1}s}. \tag{1.13}$$

The conventional positive direction for $\mathbf{r}$ is towards the observer. Therefore a magnetic field with a net direction toward the observer produces a positive RM whereas a magnetic field with a net direction away from the observer produces a negative RM.

Equation 1.11 indicates that the rotation of the polarisation angle due to Faraday rotation becomes larger with increasing observing wavelength squared. Therefore, akin to DM, this effect is also more prominent at lower frequencies or longer wavelengths. For

example, given the large fractional bandwidth of the LOFAR LBA observations with frequencies between 30 MHz and 80 MHz, the expected change in polarisation angle due to Faraday rotation is 86×RM rad. Therefore, even if a source has a relatively small absolute RM of $1\,\mathrm{rad\,m^{-2}}$, the rotation of the polarisation angle between the two frequencies will be at least 27×180°. One should also take care when specifying observations that the frequency resolution is sufficient so that when observing polarised sources such as pulsars that Faraday rotation does not cause significant depolarisation within each frequency channel. The RM is also useful for producing pulsar polarisation profiles because the Stokes Q and U parameters for each frequency channel can be de-rotated before collapsing in frequency to maximise the linear polarisation in the pulsar profile (e.g. Weltevrede and Johnston, 2008). The practical methods for determining RMs from observations are presented in Chapter 3.

Using both RM and DM, Equations 1.12 and 1.5, respectively, the average magnetic field parallel to the LOS from a pulsar toward the observer, $\langle B_\parallel \rangle$, weighted by the electron density along the LOS, can be determined:

$$\langle B_\parallel \rangle = 1.232 \frac{\mathrm{RM}}{\mathrm{DM}}\ \mu\mathrm{G}. \tag{1.14}$$

However, this method of estimating the magnetic field assumes that n_e and $B_\parallel$ vary independently along the LOS, which may not be the case (e.g. Beck et al., 2003).

1.3 Galactic magnetism

The Galactic magnetic field (GMF) permeates the diffuse ISM and plays an important role in numerous astrophysical processes. The GMF was discovered 65 years ago (Hall, 1949, Hiltner, 1949), and is now thought of as comprising a large-scale, ordered, regular component, coherent over kiloparsec scales, and a small scale, random, turbulent component. For example, the large scale component causes the deflection of high-energy cosmic rays (e.g. Farrar, 2014), and the small scale components play a role in formation of molecular clouds and star formation (e.g. Hennebelle and Iffrig, 2014). Our Galaxy provides a unique opportunity for higher resolution observations of the GMF in comparison to nearby galaxies (Nota and Katgert, 2010). Despite this, the structure of the Milky Way's GMF remains largely unexplored (Han, 2004). The following sections

describe possible observables to probe the GMF (Section 1.3.1), a brief overview of our current knowledge of the GMF (Section 1.3.2), and theoretical models for the origin of galactic magnetic fields (Section 1.3.3).

1.3.1 Observables

Observationally, there are essentially six different tracers of the strength and/or direction of magnetic fields in a diffuse astrophysical medium:

- Zeeman splitting of spectral lines: directly measures the strength and orientation of magnetic fields (e.g. Crutcher et al., 2010). Only the most dense regions of the ISM are currently probed due to tiny frequency splitting.
- Optical linear polarisation of starlight: caused by selective extinction due to prolate dust particles preferentially aligned along local magnetic field lines, linear polarisation observed is parallel to the magnetic field (e.g. Fosalba et al., 2002).
- Linear polarisation of thermal (mm, sub-mm, IR) dust emission: preferentially aligned along local magnetic field lines, net linear polarisation observed is perpendicular to the magnetic field (e.g. Chuss et al., 2003).
- Polarisation of diffuse radio synchrotron radiation: yields the total strength of the magnetic field assuming energy equipartition between relativistic particles and the magnetic field (e.g. Sun et al., 2007).
- Faraday rotation of polarised sources: the observed Faraday rotation of polarised pulsars and extragalactic sources has been used to derive the magnitude and direction of the GMF parallel to the LOS, i.e. (Noutsos et al., 2008, Han et al., 2006, Brown et al., 2007, Oppermann et al., 2012).
- Ultra-high energy cosmic rays (UHECRs): the ultra-relativistic nuclei of extragalactic origin are deflected as they propagate the GMF. When sources of UHECRs are better characterised, they will also serve as a direct tool for studying the GMF as their deflection is dependent only on the UHECR charge (e.g. Farrar et al., 2013).

There are several advantages for using polarised pulsar emission to measure the GMF, including:

- High degrees of linear polarisation allow RMs to be easily measured, e.g. Fig. 1.3.
- RM values are associated with the ISM, with negligible contribution from the pair plasma created in the pulsar magnetosphere (Wang et al., 2011).
- The distribution of pulsars throughout the Galactic volume allows three-dimensional GMF sampling. Dense concentrations in the plane and pulsars at higher latitudes provide a good sample of the planar and halo (combined with extragalactic RM values) GMF, respectively.
- Pulsar DMs provide additional information about the column electron density along the LOS, and distance estimates (using a Galactic free-electron density model, e.g., NE2001 Cordes and Lazio, 2002).

1.3.2 The Galactic magnetic field: current knowledge

The Milky Way is known to be a barred-spiral galaxy (in terms of stars and gas). A schematic diagram showing an artists' impression of the appearance of the Milky Way to an outside observer is shown in Fig. 1.6, and includes the names of the spiral arms which are discussed further below. Since the Galaxy has a spiral structure and radio telescopes have a fixed and limited area of the Galaxy which they can observe, many studies have focussed on specific regions of the Milky way, e.g., the 'local', spiral arm and inter-arm region magnetic fields.

1.3.2.1 Ordered regular field

GMF is most likely organised along the logarithmic spiral arms (Nota and Katgert, 2010), and increasing in strength towards the Galactic centre (Rand and Lyne, 1994). One of the latest analyses of pulsar and extragalactic source RMs in the fourth Galactic quadrant suggest the GMF has large-scale structure of a few μG with field reversals (from the Norma arm to the Norma-Crux interarm region and from the Norma-Crux interarm region to the Crux arm), most closely resembling the theoretical quadrisymmetric spiral (QSS) of Stepanov et al. (2008) (Nota and Katgert, 2010). A bisymmetric spiral model

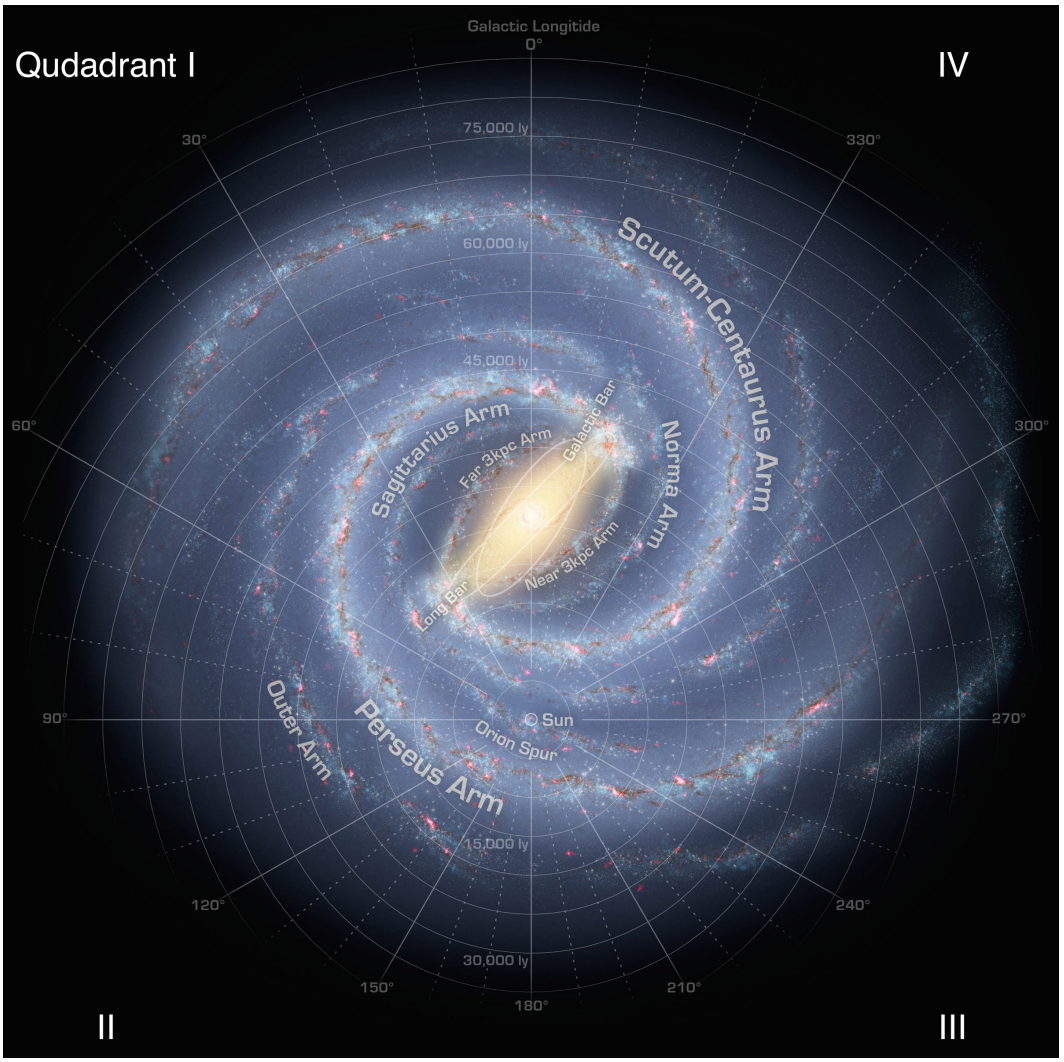

FIGURE 1.6: Artists concept schematic of the Milky Way viewed face-on. The spiral arms, the position of the Sun, and the Galactic quadrants are noted. Image credit: Robert Hurt

for the GMF, with reversals at arm-interarm boundaries, has been proposed by many authors (Van Eck et al., 2011, Han et al., 2006). The small-scale magnetic field strength is approximately at least that of the large-scale field. The process which forms such a GMF configuration remains a largely unanswered question (Nota and Katgert, 2010, and references therein).

One of the first studies of the GMF using the RMs of 19 pulsars (Manchester, 1972) showed that the largest magnetic fields are located near the galactic plane, and that there was no apparent sign of differing directions above or below the plane. The spiral arms, with increasing distance from the Galactic centre, are discussed below.

Norma Arm:

Noutsos et al. (2008) found the field of the Norma arm to be counter-clockwise in direction and an order of magnitude larger than the average GMF value; this abnormally high value was attributed to local fluctuations of the ISM fields caused by small-scale turbulence, most likely not representative of the large-scale component. Han et al. (2006) also find the field in the Norma arm to be counter-clockwise in both quadrants I and IV, the direction of which may be maintained beyond 10 kpc from the Sun in the direction $\ell = 330°$. However, Van Eck et al. (2011) suggest that the magnetic field in this arm is clockwise, although it is noted that the data in these regions is relatively sparse.

Sagittarius–Scutum-Centaurus (or Scutum-Crux) Arm:

There are a large number of RMs in the direction of these spiral arms. Noutsos et al. (2008) measured 150 pulsar RMs using Parkes. This study found the Scutum field tangential to 30°–35°, and the Crux arm field tangential to 305°–310°. They found a field reversal from clockwise to counter-clockwise between Carina and Crux arms near 8 kpc and that there is an increase in field strength in the Crux arm at larger distances (5–10 kpc). Noutsos et al. (2008) also found a field reversal between 1–2 kpc inside the Sagittarius arm, from clockwise to counter-clockwise directions. Rand and Lyne (1994) determined the RMs of 27 pulsars mostly in quadrant I of the Galaxy. This study found further evidence that the large-scale GMF along the Sagittarius arm is opposite in direction to the local field; the field changes in direction at a Galactic radius of 8.1 kpc (0.4 kpc towards the centre of the Galaxy from the Sun), points to Galactic longitude 88° and has a strength of 1.4 μG. They also found evidence of a second reversal at a radius of 5.5 kpc from the Galactic centre, with a much stronger field beyond the reversal, possibly reaching 6–7 μG. The data also infer small-scale irregularities in the magnetic field and possibly a more complex large-scale structure in the inner Galaxy. Han et al. (2006) measured the RMs of 223 pulsars, many of which are located in these regions. They found a counter-clockwise field along the entire Scutum-Crux arm, similarly to the study by Van Eck et al. (2011).

Carina Arm:

The field in the Carina arm – just outside the Scutum-Centaurus arm tangential to 280°–285° – becomes counter-clockwise at 2–4 kpc where elsewhere it is clockwise (Noutsos et al., 2008). Han et al. (2006) also note that the Carina arm appears to be more complicated, where in general the RMs are increasingly negative, also consistent with

a counter-clockwise field. However, at distances greater than 4 kpc the RMs become unexpectedly positive, which Han et al. (2006) interpret as a field reversal between 3 and 5 kpc from the Sun – the 'Carina anomaly' – which could be attributed to many large HII regions influencing the observed RMs. However, Van Eck et al. (2011) determine a clockwise direction of the GMF in this spiral arm.

Perseus Arm:

The Perseus arm has been studied in the least detail as there are a small number of known pulsars in this region of the Galaxy and hence a small number of pulsar RMs. There are however still a large number of RMs measured towards extragalactic (EG) sources which can provide constraints on the magnetic fields within the LOS through the entire Galaxy. Mitra et al. (2003a) measured RMs of 11 pulsars in the Perseus arm. Using this sample, together with 34 published sources, they found the large-scale magnetic field amplitude of 1.7(10) μG, and no evidence for field reversals. These data also indicated the region towards $l \sim 149°$ has a random field component of up to 5.7 μG. Also, the magnetic arm pitch angle of 12(8)° is not the same as that of the optical spiral arm with pitch angle of –10(8)°. Mitra et al. (2003a) study also found evidence that HII regions affect pulsar RMs, which is further discussed in Chapter 5. Rotation measures for EG sources were used in combination with pulsar data to also argue that there are no field reversals towards the outer part of the Galaxy (Van Eck et al., 2011, Brown et al., 2003). However, due to the sparsity of pulsar data, the uncertainty in the distances and the fact that the LOS is close to perpendicular to the spiral arm, the direction of the field in the Perseus arm is not entirely clear; Han et al. (2006) notes evidence of both a clockwise field within the solar neighbourhood and counter-clockwise fields at larger distances from the Sun.

Inter-arm regions:

Some studies have suggested that there is evidence for field reversals between arm and inter-arm regions. In quadrant I between the Scutum and Sagittarius arms, although the RMs for interarm regions is particularly sparse, there may be some evidence of a field reversal (Han et al., 2006). This Furthermore, in quadrant IV, where there is more RM data and angular distances between the spiral arms is larger, Nota and Katgert (2010) find a significant reversal from the Norma arm to the Norma-Crux interarm region and also from the Norma-Crux interarm region to the Crux arm. This was also echoed in Han et al. (2006), where the data were found to suggest field reversals between the Norma

and Norma-Crux inter-arm, the Norma-Crux interarm and the Crux arm, as well as from the Crux arm to the Crux-Carina interarm, and from the Crux-Carina interarm to the Carina arm. However, this is many more field reversals than those found in other studies (e.g. Van Eck et al., 2011). It has also been suggested that the field strengths within the inter-arm regions are less than those within the spiral arms (Han et al., 2006).

Halo field:
The extent of the electron density and GMF towards the halo of the Galaxy is difficult to constrain. Assuming approximate equipartition between non-thermal pressure from magnetic fields, cosmic rays, and dynamics, varying with height from the disk, Boulares and Cox (1990) found the vertical scale height to be greater than 1 kpc. In an all-sky map of Faraday rotation towards EG sources, Oppermann et al. (2012) found a quadrupole-like structure on large scales that has been claimed to be caused by a toroidal component of the large-scale GMF that changes sign over the Galactic plane (see e.g. Han et al., 1997). However, this pattern may also be caused by local features in the solar neighbourhood (e.g. Mao et al., 2010). Therefore, obtaining more pulsar RMs will provide a more accurate three-dimensional reconstruction of the GMF.

1.3.2.2 Random small-scale fields

The ISM is turbulent over a range of scales, described by a power-law with a spectral index consistent with a Kolmogorov spectrum (e.g. Armstrong et al., 1995). Energy injection on the largest, approximately parsec, scales in the spiral arms are dominated by stellar winds or protostellar outflows, while interarm regions are dominated by supernovae and super bubble expansions (Haverkorn et al., 2008).

The local region refers to the solar neighbourhood, i.e., regions in the Galaxy which are approximately within 2–3 kpc of the Sun, located between the Carina-Sagittarius and Perseus arms. In this region, the field direction has long been known to have a clockwise direction (Manchester, 1974).

1.3.2.3 Comparison to magnetic fields in external galaxies

The total magnetic field strength observed in face-on galaxies is 9(3) μG. These fields tend to follow optical spiral arms with typical pitch angles between 10 and 40 degrees.

Observations of synchrotron emission from edge-on galaxies have shown that the magnetic fields in the halo are "X"-shaped. This field is probably transported from the disk into the halo by an out-flow emerging from the disk (e.g. Beck, 2009).

1.3.3 Theoretical origins of Galactic magnetic fields

When a sufficient seed field is present in a galaxy, a dynamo mechanism can act to increase the coherence length and field strength (e.g. Pariev et al., 2007, Widrow, 2002). For example, the $\alpha - \Omega$-dynamo model acts by a supernova bubble stretching a magnetic field line into a loop, which is twisted by coriolis forces and stretched by differential rotation. Part of the field line is expelled from the disk and magnetic flux in the disk increases. Therefore, the large-scale galactic magnetic field in the disk is expected to show signatures of at least one dynamo mode.

1.4 Thesis outline

The introduction has introduced several instances in which observing pulsars has provided the means to study the properties of astrophysical plasmas that span many orders of magnitude in magnetic field strength and scale. Chapters 2 to 5 continue by presenting results from observations of pulsars to study magnetic fields in astrophysical plasmas from the pulsar magnetosphere to the GMF.

In **Chapter 2**, *emission characteristics of PSR B0823+26: discovery of a quiet emission mode*, the emission processes of pulsars with gargantuan magnetic fields ($\sim 10^{12}$ G) are explored by studying the numerous emission characteristics of a mode-changing pulsar, PSR B0823+26, using LOFAR and multi-frequency observations. The process by which the various pulsar magnetospheric emission phenomena occur is not yet well understood, but may affect results from using their emission as probes, for example, as gravitational wave detectors within a pulsar timing array. We report on the LOFAR discovery that PSR B0823+26 has a weak and sporadically emitting 'quiet' emission mode that is over 100 times weaker (on average) than that of the more regularly-emitting 'bright' mode. The transition between emission modes is concurrent across the range of frequencies observed and occurs within one rotational period (0.531 seconds).

In **Chapter 3**, *published rotation measures and techniques*, the current state of practical methods and published results of Faraday rotation measures (RMs) towards pulsars, and also extragalactic sources (EGs), are collected and reviewed, for the purpose of studying the Galactic magnetic field (GMF, $\sim \mu$G).

Chapter 4, *correcting for ionospheric Faraday rotation*, describes the effect of the ionosphere (also a magnetised plasma) on RM measurements towards astronomical sources. Observations of pulsars using the Low Frequency Array (LOFAR) demonstrate the high accuracy of a code used to calculates the amount of ionospheric Faraday rotation towards a specific line-of-sight using publicly available, GPS-derived total electron content maps and the geomagnetic reference field (~ 0.5 G). This shows that we can accurately determine some of the highest-precision RMs towards pulsars ever achieved, towards more accurately measuring and monitoring the GMF.

Chapter 5, *new pulsar rotation measures towards constructing the Galactic magnetic field*, presents the results from polarisation observations used to measure ionosphere-corrected RMs towards 77 pulsars which either do not have published RM data (45) or which increase the accuracy in values in the catalogue RM. The RMs towards pulsars and EGs collected in Chapters 3 and 5 were used to reconstruct a map of the large-scale GMF using wavelet analysis. We find that the reconstruction is improved by the additional data points in the Galactic plane. However, to more accurately construct the GMF, more RM data and more independent pulsar distance measurements are required, especially towards the Galactic halo, so that a fully three-dimensional reconstruction of the GMF may be possible.

Chapter 6 summarises the work and provides prospects for future work related to this thesis.

Note that throughout this thesis numbers in parentheses are the uncertainties corresponding to the least significant figure in the value quoted.

Chapter 2

Emission characteristics of PSR B0823+26: discovery of a quiet emission mode

2.1 Abstract

PSR B0823+26, a 0.53-s radio pulsar, displays a host of emission phenomena over timescales of seconds to (at least) hours, including nulling, subpulse drifting and mode-changing. Studying pulsars like PSR B0823+26 provides further insight into the relationship between these various emission phenomena and what they might teach us about pulsar magnetospheres. Here we report on the LOFAR discovery that PSR B0823+26 has a weak and sporadically emitting 'quiet' (Q) emission mode that is over 100 times weaker (on average) and has a nulling fraction forty-times greater than that of the more regularly-emitting 'bright' (B) mode. Previously, the pulsar has been undetected in the Q-mode, and was assumed to be nulling. PSR B0823+26 shows a further decrease in average flux just before the transition into the B-mode, and perhaps truly turns off completely at these times. Furthermore, simultaneous observations taken with the LOFAR, Westerbork, Lovell, and Effelsberg telescopes between 105 MHz and 2.7 GHz demonstrate that the transition between the Q-mode and B-mode occurs within one single rotation of the neutron star, and that it is concurrent across the range of frequencies observed. It is also important to understand the emission characteristics of pulsars so

that we may better understand limitations in terms of using them as probes of the ISM and of gravitational waves.

The contents of this chapter have been submitted to a scientific journal: Sobey, C., et al., "Discovery of a quiet emission mode in PSR B0823+26", MNRAS submitted (2014).

2.2 Introduction

PSR B0823+26 is the focus of this work because it has been shown to exhibit a host of emission phenomena, including most of the emission phenomena introduced in Section 1.2.2. This includes bursts of subpulses that drift slowly in longitude, towards both the leading and, more commonly, trailing edge of the main pulse (Weltevrede et al., 2007). The nulling fraction is estimated to be 7(2)%[1], and nulls occur clustered in groups more often than at random (Herfindal and Rankin, 2009, Redman and Rankin, 2009). Recently, Young et al. (2012) showed that PSR B0823+26 nulls over a broader range of timescales (from minutes to at least five hours), and that the pulsar is detected only 70–90% of the time when observed. They also found no detectable change in spin-down rate between emitting and long null states to a limit of less than 6% fractional change. Long-term timing of the pulsar shows relatively high timing noise residuals of 89 ms (Hobbs et al., 2004), including changes in the sign of the spin frequency second derivative (Shabanova et al., 2013). Thus, PSR B0823+26 is a good candidate for studying many facets of the pulsar emission mechanism.

PSR B0823+26 was one of the first pulsars to be discovered (Craft et al., 1968b), and is one of the brightest radio pulsars in the Northern sky, with 73(13) mJy flux density at 400 MHz (Lorimer et al., 1995) and a distance of $0.32^{+(8)}_{-(5)}$ kpc (Verbiest et al., 2012). It has been detected from 40 MHz (Kuz'min et al., 2007) up to 32 GHz (Löhmer et al., 2008), with little profile evolution (Bartel et al., 1978), see Fig. 2.1. It is also one of ten slowly-spinning, rotation-powered pulsars with pulsations detected in X-rays (Becker et al., 2004). The interpulse in the pulse profile indicates that it is nearly an orthogonal rotator, which is confirmed by polarisation observations (Everett and Weisberg, 2001).

[1]Note: Throughout the paper, numbers in parentheses are the uncertainties corresponding to the least significant figure in the value quoted.

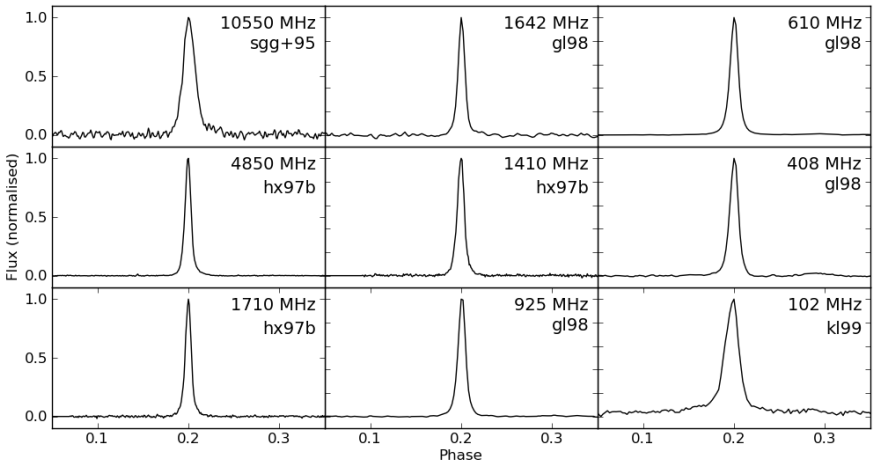

FIGURE 2.1: Pulse profiles for PSR B0823+26 at multiple frequencies from 102 MHz to 10.55 GHz obtained from the European Pulsar Network database . References; kl99 (Kassim and Lazio, 1999), gl98 (Gould and Lyne, 1998), hx97b (von Hoensbroech and Xilouris, 1997), sgg+95 (Seiradakis et al., 1995).

To further investigate the emission phenomena displayed by PSR B0823+26, we conducted radio observations at low frequencies (<200 MHz) using the Low-Frequency Array (LOFAR), where brightness modulation due to scintillation is averaged out across the band. We also conducted simultaneous observations using the LOFAR, Westerbork, Lovell, and Effelsberg telescopes to record data from 105 MHz to 2.7 GHz.

The observations and data reduction are described in Section 2.3. In Section 2.4 we report on the data analysis and results of the observations. We show that the long-term nulls previously reported are in fact a very weak and sporadically emitting mode, similar to that identified in PSR B0826−34 (Esamdin et al., 2005). Hereafter we refer to this mode as the 'quiet' (Q) emission mode, and therefore the regular strong emission as 'bright' (B), analogous to other mode-changing pulsars[2]. In Section 2.5 we discuss these and further results and present our conclusions.

[2]PSR B0823+26 has a dispersion measure (DM) of 19.454(4) pc cm^{-3} (Hobbs et al., 2004), and both diffractive and refractive scintillation is observed – the decorrelation bandwidth at 1.7 GHz is 81(3) MHz (Daszuta et al., 2013). We note, however, that the 2–10 hour 'disappearances' of PSR B0823+26 interpreted as due to scintillation by Daszuta et al. (2013) are more likely to be instances of the weakly-emitting Q-mode observed in this work.

2.3 Observations

LOFAR observations of PSR B0823+26 were obtained on 13–14 November 2011, 9 February 2012, and 7 April 2013 (see van Haarlem et al., 2013, for a description of LOFAR). Between 5 and 21 High-Band-Antenna (HBA) core stations were coherently combined using the LOFAR Blue Gene/P correlator/beam-former to form a tied-array beam (see Stappers et al., 2011, for a description of LOFAR's pulsar observing modes).

Starting at 23:18 UT on 13 November 2011, and ending at 08:12 UT on 14 November 2011, 26 three-minute commissioning observations were taken with a gap of 19 minutes between successive observations. Data were taken using the central six Core stations (the 'Superterp'), and were written as 32-bit complex values for the two orthogonal linear polarisations at a centre frequency of 143 MHz and bandwidth of 9.6 MHz. PSR B0823+26 switched from the Q- to B-mode emission mode during the thirteenth observation, see Table 2.1 for a summary of the specifications. The pulsar was not detected during the other 25 similar observations in this campaign, even after all observations were summed together in time.

To further evaluate the moding behaviour at LOFAR frequencies, a longer, three-hour observation was taken on 9 February 2012 using five of the central HBA Core stations, where the linear polarisations were summed in quadrature and the signal intensities (Stokes I) were written out as 32-bit, 245.76-μs samples, at a centre frequency of 143 MHz with 47.6 MHz bandwidth, see Table 2.1.

To investigate the broadband behaviour of PSR B0823+26, a further eight-hour observation on 7 April 2013 was conducted simultaneously using LOFAR and three telescopes observing at higher frequencies: the Westerbork Synthesis Radio Telescope (WSRT), the Lovell Telescope and the Effelsberg 100-m Telescope, see Table 2.1 for a summary. The LOFAR observation used 21 HBA Core stations, where the linear polarisations were summed in quadrature, and the signal intensities (Stokes I) were written out as 32-bit 245.76-μs samples, at a centre frequency of 149 MHz with 78 MHz bandwidth. The WSRT observation was taken in tied-array mode using the PuMaII pulsar backend (Karuppusamy et al., 2008). Baseband data was recorded for 8 slightly overlapping 10-MHz bands, resulting in a total bandwidth of 71 MHz centred at 346 MHz. The Lovell telescope observed the pulsar using the digital Reconfigurable Open Architecture

TABLE 2.1: Summary of observations. Columns 1–8 indicate the observing telescope, date, start time, integration time, centre frequency, bandwidth, individual channel width, and sampling time. Column 9 shows the duration of the B-mode relative to the start time, where '+' indicates that the pulsar remained in the B-mode until at least the end of the observation. For the LOFAR observations on 14 November 2011, 9 February 2012, and 7 April 2013: the observation IDs are L34789, L45754, L119505, respectively; HBA[0,1] stations included in tied-array mode were CS00[2–7], CS00[2,3,4,6,7] and CS0[01-07,11,17,21,24,26,28,30,32,101,103,201,301,302,401], respectively.

Telescope	Date (dd.mm.yyyy)	Start Time (UT)	$\tau_{\rm int}$	Frequency (MHz)	Bandwidth (MHz)	Channel-width (kHz)	$\tau_{\rm samp}$ (μs)	Time in B mode
LOFAR	14.11.2011	03:42	3.0 (min)	143	10	12	81.9	1.69+ (min)
LOFAR	09.02.2012	20:30	3.0 (h)	143	48	12	245.8	2.71+ (h)
LOFAR	07.04.2013	14:00	8.0 (h)	149	78	12	245.8	3.07–3.11,5.09+ (h)
WSRT	07.04.2013	14:00	8.0 (h)	346	71	24	64.7	3.07–3.11,5.09+ (h)
Lovell	07.04.2013	14:00	8.0 (h)	1532	400	4000	518.2	3.07–3.11,5.09+ (h)
Effelsberg	07.04.2013	14:43	7.3 (h)	2635	80	195	259.1	(3.07–3.11),5.09+ (h)

Hardware (ROACH) backend. Dual polarisations were Nyquist sampled over a 400-MHz band centred at 1532 MHz and digitised at 8 bits. The Effelsberg 100-m Telescope observation was conducted using the PSRIX backend (ROACH-board system for online coherent dedispersion), which recorded the data at a centre frequency of 2635 MHz with 80 MHz bandwidth.

The data from the LOFAR observations were converted to 8-bit samples offline. The data from all observations were coherently dedispersed, except the LOFAR observations on 9 February 2012 and 7 April 2013 that were incoherently dedispersed, and folded using the pulsar's rotational ephemeris (Hobbs et al., 2004) and the `dspsr` program (van Straten and Bailes, 2011) to produce single-pulse integrations. Radio frequency interference (RFI) in the pulsar archive files was removed in affected frequency subbands and time subintegrations using both automated (`paz`) and interactive (`pazi`) programs from the PSRCHIVE[3] library (Hotan et al., 2004). The LOFAR polarisation data was calibrated for parallactic angle and beam effects by applying a Jones matrix, see Noutsos et al. (in prep.) for further details. The linear polarisation parameters in the LOFAR data from the 14 November 2011 observation were also corrected for Faraday rotation, see Section 2.4.1 for further details.

[3]see http://psrchive.sourceforge.net for more information.

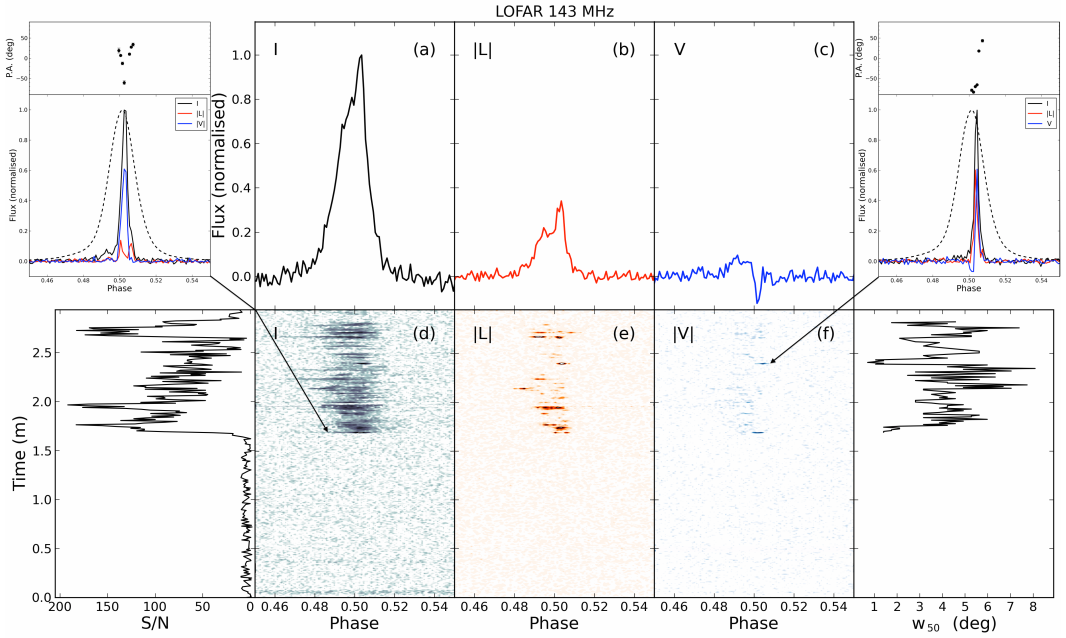

FIGURE 2.2: Overview plot of the LOFAR observation on 14 November 2011. *Panels a,b,c:* Time- and frequency-averaged pulse profiles for the B-mode in total (Stokes I), linearly polarised ($|L|$ = Stokes $\sqrt{Q^2+U^2}$) and circularly polarised (Stokes V) intensities, respectively. The average Q-mode profile is not shown as it is indistinguishable from the noise in this short observation. *Panels d,e,f:* The flux density of single pulses against pulse phase and integration time in total (increasing from white to black), linearly polarised (increasing white to red) and absolute circularly polarised (increasing from white to blue) intensities, respectively. *Lower left:* S/N of total intensity single pulses against time. *Lower right:* Full-width-half-maximum, w_{50}, against time for total intensity single pulses with S/N>7. *Inset plots:* Normalised polarisation profiles for two narrow and highly polarised single pulses indicated with arrows: initial B-mode pulse (*left*), and second pulse with similar characteristics at 2.4 min (*right*). *Lower panels* show the total (black), linearly polarised (red) and circularly polarised (blue) intensities. The stable average pulse profile in total intensity from the 9 February 2012 LOFAR observation is also shown (dotted line) for the same frequency and using the same timing ephemeris (from Pilia et al. in prep.). *Upper panels* show the position angle of the linear polarisation (P.A. = 0.5 $\tan^{-1}(U/Q)$).

2.4 Analysis and results

Here we describe the analysis and results of the observations summarised in Table 2.1. PSR B0823+26 switched between emission modes at least once during each observing campaign. Initially we focus on the time- and frequency-averaged properties at LOFAR frequencies, Section 2.4.1, and at a range of frequencies, Section 2.4.2. In Section 2.4.3, we focus on the single-pulse analysis of the data from the simultaneous observations.

2.4.1 Emission modes description

Figure 2.2 shows an overview of the emission characteristics of PSR B0823+26 over the course of the three-minute LOFAR observation taken on 14 November 2011, during which the pulsar switched from Q- to B-mode emission. This is the only observation with recorded polarimetric information. Figure 2.2, panel *d*, clearly shows the sudden increase in total flux density 1.69 minutes after the start of the observation. Panels *e* and *f* show that this is also the case for polarised flux density. The B-mode continues for at least 160 single pulses until the end of the observation. This is an inadequate number of pulses to obtain a stable average pulse profile, which is shown for comparison in Fig. 2.2, *inset plots*. The total duration of the B-mode in this case is not known exactly. During all 12 preceding and 13 following three-minute observations no emission was detected, and we infer that PSR B0823+26 was emitting in the Q-mode. Assuming this was also the case during the 19-minute gaps between the observations, the duration of the Q-mode can be constrained to at least 4.4 h before and 4.75 h after the observation summarised in Fig. 2.2. This multi-hour duration in the Q-mode is similar to the length of prolonged nulls also observed by Young et al. (2012). It is also possible that 'flickers' of emission on the order of minutes in duration, such as that shown in Fig. 2.2, could have occurred in between observations.

Inspection of the single pulses from Fig. 2.2 shows that the transition between the Q and B-modes is very rapid, occurring within one single rotational period. This is notable in the profiles of the single pulses and in the dramatic increase, at least 60-times, in median S/N.

We also note significant changes in the pulse width and morphology. Figure 2.2, *lower right*, shows that the full-width-half-maximum, w_{50}, of the initial single pulses in the B-mode are very narrow (1.4°), compared to the average pulse profile at the same frequency (7°, see Fig. 2.2 *inset plots* and below). Subsequent B-mode pulses increase in width and drift towards earlier and later pulse phases until an equally narrow pulse (1.1°) occurs 80 pulses later at 2.40 min. This may be expected due to intrinsic variability, e.g., subpulse drifting. Moreover, the narrow pulses are located towards the trailing edge of the average pulse profile, similar to what is observed from PSR B1133+16 (Kramer et al., 2003).

Further investigation of the polarisation properties was carried out. The RM of the integrated pulse profile and the two narrow highly-polarised pulses was determined using

RM-synthesis (Brentjens and de Bruyn, 2005). The observed RM of the integrated B-mode pulse profile was determined to be 6.28(4) rad m^{-2}. We find the RMs of the narrow single pulses to be consistent with this value. This RM value was used to correct the linear polarisation Stokes parameters for Faraday rotation in order to maximise the linear polarisation in the average pulse profile. The RM due to the ISM alone was determined to be 5.25(8) rad m^{-2}, after correcting for ionospheric Faraday rotation (Sotomayor-Beltran et al., 2013). This is in good agreement with (within less than 2σ) and more precise than the current ATNF pulsar catalogue value of 5.9(3) rad m^{-2} (Manchester, 1974). The DM and corrected RM values can be used to determine the Galactic magnetic field direction and magnitude parallel to the line-of-sight towards PSR B0823+26 (e.g. Noutsos et al., 2008), which was calculated to be 0.332(6) μG. These results are discussed further in Section 2.5.5.

Variable pulse-to-pulse fractional polarisation was also identified. The two narrow pulses identified show relatively high polarisation (especially circular) fractions, see Fig. 2.2 *inset plots*. The initial B-mode pulse is 55(5)% right-hand circularly polarised and the narrow pulse at 2.4 min is 56(5)%, left-hand circularly polarised. The initial B-mode pulse and subsequent narrow pulse are 10(5)% and 38(5)% linearly polarised, respectively. The fractional circular polarisation for these single-pulses is therefore considerably larger than for the average pulse profile, which is 6(5)% circularly polarised and 15(5)% linearly polarised.

In order to further examine the moding behaviour, we observed PSR B0823+26 again for a continuous three hours using LOFAR on 9 February 2012. As shown in Fig. 2.3, *lower panels*, the pulsar began emitting in the Q-mode and switched to B-mode emission after 2.71 h. The *lower panels* of Fig. 2.3 clearly demonstrate that weak emission is detected from the start to 2.5 h into the observation, at approximately the same location in pulse phase as that of the main pulse during the B-mode. This weak, but significant, Q-mode emission has not previously been detected; this mode was previously thought to be a long-term null. Between the weak Q-mode at 2.55 h and the beginning of the B-mode at 2.71 h, the flux density of the pulsar decreases even further and no emission is detected. PSR B0823+26 rapidly transitions to B-mode at 2.71 h, again within one single rotational period, and continues in this mode until the end of the observation. This is clear from the abrupt increase in S/N, Fig. 2.3 *lower right*, and also in the pulse

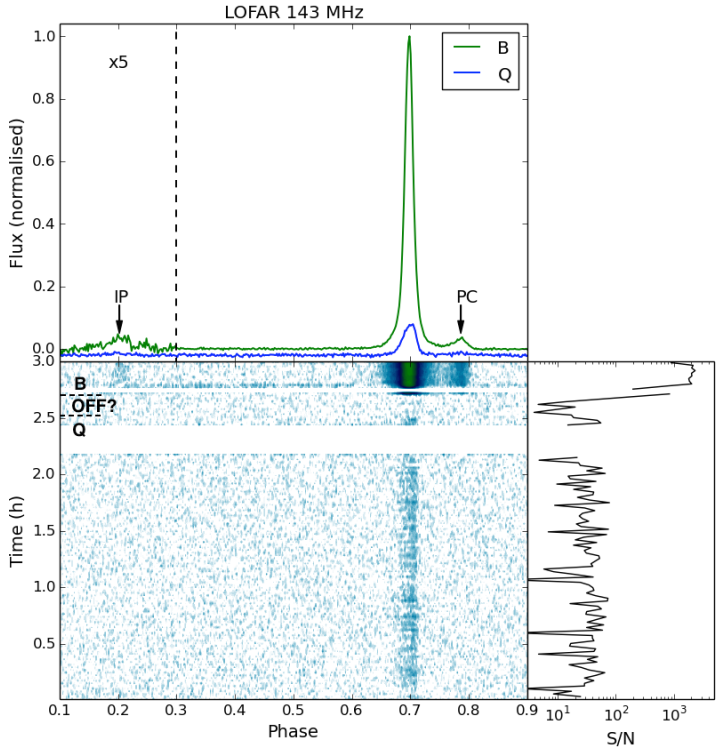

FIGURE 2.3: Overview plot of the LOFAR observation taken on 9 February 2012. *Upper panel:* Time- and frequency-averaged total intensity pulse profiles separated by emission mode into Q (0–2.71 h) and B-mode (2.71+ h), normalised to the peak flux of the B-mode profile. There appears to be a period of approximately 10 minutes in which the pulsar is not detected ('OFF?', 2.55–2.71 h). The postcursor (PC) and interpulse (IP, 5× magnified) are also indicated. *Lower left panel:* Flux density of the pulsar against pulse phase and integration time (increasing from white through blue to green). Subintegrations removed due to RFI are left blank. The modes of emission identified (Q-, B-, and, tentatively, 'OFF?') are also labelled, and the boundaries between these are marked with the dotted line. *Lower right panel:* S/N of 42-second total intensity sub-integrations against integration time.

profile, Fig. 2.3, *upper panel*. The ratio between the median S/N of single pulses in the B and Q-modes is approximately 170.

The upper panel of Fig. 2.3 illustrates the average pulse profiles of the Q and B-modes. The B-mode pulse profile shows the known components from the literature, i.e., a narrow main pulse (MP), postcursor (PC), and interpulse (IP, separated by almost exactly half a rotation period from the MP) (see Backer et al., 1973). The newly discovered Q-mode pulse profile is notably weaker. The location of the peak in flux density is also skewed towards slightly later pulse phases compared to the B-mode MP (+2(1)°, 2.9 ms). Table 2.2 includes a summary of the relative intensity, width and locations of the B and Q-mode pulse profile components. Details of how these were calculated are included in Section 2.4.2.

2.4.2 Multi-frequency analysis

In light of previous studies of other pulsars (e.g. Hermsen et al., 2013), mode-switching is expected to occur over a broad-range of wavelengths, even up to X-rays. To investigate whether this is the case for PSR B0823+26, we observed the pulsar using four telescopes (LOFAR, WSRT, Lovell, Effelsberg) at a range of centre frequencies (149, 345, 1532, 2635 MHz) simultaneously. The overview of the eight-hour observations, Fig. 2.4, shows that both Q and B-modes were detected again and that the behaviour of PSR B0823+26 is very similar across the range of frequencies.

The lower panels in Fig. 2.4 show that from the beginning of the observations until approximately 2 h, the weak Q-mode emission is visible at all four frequencies. Between $\sim$2 and 3.07 h the Q-mode becomes even more weak and is practically undetectable. After this, the pulsar abruptly 'flickers' into B mode emission for approximately 160 pulses. The pulsar transitions back into the weakly-emitting Q-mode between 3.11 and 4.8 h, which is most clearly detected at the two lower frequencies, but also towards the end of this period at the two higher frequencies. The flux in the Q-mode once again decreases even further and becomes practically undetectable between 4.8 and 5.09 h, just before the pulsar transitions again into B-mode for the remainder of the observation. This is also demonstrated in terms of S/N against observing time in Fig. 2.5.

Figure 2.4, *upper panels*, illustrate the B-mode profiles and the previously unknown and much weaker Q-mode pulse profiles between 110 MHz and 2.7 GHz. The B-mode MP, PC, and IP are visible at all frequencies and, as expected from the literature, there is little profile evolution across the frequencies observed. Again, the Q-mode is much weaker compared to the MP of the B mode, and the average peak flux occurs towards slightly later pulse phases ($> +1^\circ$, depending on frequency).

On all occasions where the emission switches from the Q to B-mode, the transition occurs within one single rotational period at all frequencies, identified by the notable increase (70$\times$) in S/N of single pulses and change in pulse profile. Figure 2.4, lower panels, also show that the mode switch from Q to B at 5.1 h occurs simultaneously for all pulse profile components, i.e., the MP, PC and IP, at all frequencies.

To determine whether the mode-switch occurs coincidently across all frequencies observed, the MJD of the initial B-mode single-pulse after the mode change was determined

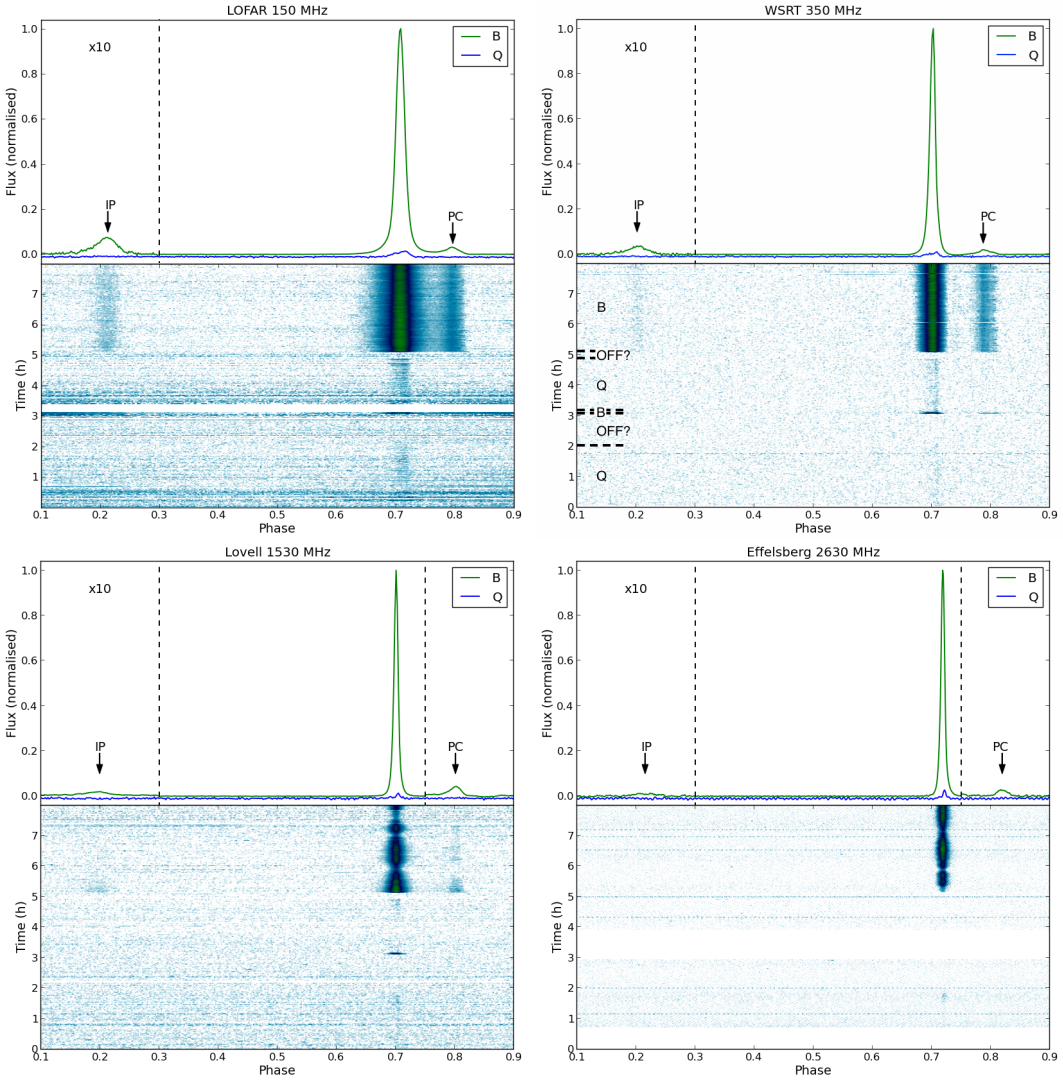

FIGURE 2.4: Overview of the multi-frequency simultaneous observations taken on 7 April 2013, using: LOFAR (*upper left*), WSRT (*upper right*), Lovell (*lower left*), and Effelsberg 100-m (*lower right*). *Upper panels:* Time- and frequency-averaged total intensity pulse profiles separated into Q-mode (0–3.07 h, 3.11–5.09 h; 4× magnified) and B-mode (3.07–3.11 h, 5.09+ h), normalised to the peak flux of the B-mode profile. There also appear to be periods in which the pulsar is not detected ('OFF?'; ∼2–3.07 h, 4.8–5.09 h). The PC (10× magnified in the lower plots) and IP (10× magnified) are also indicated. *Lower panels:* Flux density of the pulsar against pulse phase and integration time (increasing from white through blue to green). Subintegrations removed due to RFI are shown as white. The modes of emission identified (Q-, B-, and, tentatively, 'OFF?') are also labelled, and the boundaries between these are marked with the dotted line for the WSRT observation (although applicable to all observations). In the higher frequency Lovell and Effelsberg data, modulation of the B-mode brightness due to scintillation is also visible.

for each frequency. The expected time delays of equivalent pulses due to dispersion in the cold plasma of the ISM between the centre frequencies used at Effelsberg, Lovell, and WSRT and that used at LOFAR are 3.63, 3.61, and 2.97 s, respectively. Taking this into account, we find that the mode-switch is coincident at the frequencies observed to within 0.01 s.

On the single occasion where we observe the pulsar switch from the B to Q-mode, it is slightly more difficult to pinpoint the transition because the flux density of single pulses decreases over a few rotational periods, rather than showing an abrupt change in S/N, as in the 14 November 2011 observation shown in Fig. 2.2, *panel d*. For the three lower frequencies, B-mode emission was detected over a 160 single-pulse timescale during the B 'flicker' at 3.1 h. Since the transition from the Q to B-mode was determined to be simultaneous across the observed band, it is probable that this is also the case for the B-to-Q-mode change.

Figure 2.5 shows the S/N against time for the simultaneous observations. This clearly demonstrates the simultaneous wide-band transitions between emission modes, especially the decrease in flux density in the Q-mode just before the rapid transition to the B-mode at 5.1 h. Here we again see that the B- and Q-mode differ in flux density by over two orders-of-magnitude.

Fig. 2.5 illustrates fluctuations in pulse total intensity due to scintillation, which are much more evident in the prolonged B-mode emission at the two higher observing frequencies. This is because the scintillation bandwidth becomes comparable to the observing bandwidth at the higher frequencies. The DM of PSR B0823+26, measured using the LOFAR observation on 7 April 2013 using the PSRCHIVE `pdmp` program (Hotan et al., 2004), was found to be 19.475(3) pc cm^{-3}. This amount of dispersion contributes to PSR B0823+26 falling into the strong diffractive scintillation regime when observed below approximately 5 GHz (Daszuta et al., 2013). At lower frequencies the scintillation bandwidth is much smaller, causing its effects to be averaged out more effectively across the band.

The B and Q-mode multi-frequency average pulse profiles obtained from the 2012 November 9 and 7 April 2013 observations, see Figs. 2.3 and 2.4, were used to compare the behaviour of the pulse profile components with frequency. The profile components were fitted with Gaussian functions using the Levenberg-Marquardt algorithm

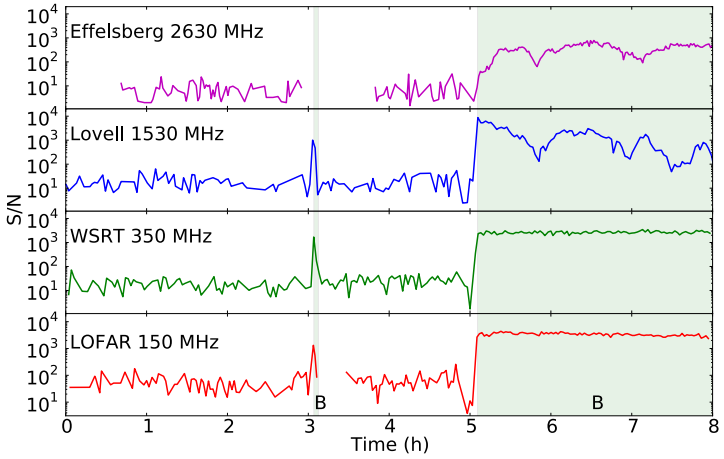

FIGURE 2.5: S/N of total intensity pulses versus integration time from the multi-frequency simultaneous observations of PSR B0823+26. *Upper to lower panels:* Effelsberg 100-m at 2635 MHz using 80-s subintegrations; Lovell at 1532 MHz using 140-s subintegrations; WSRT at 345 MHz using 140-s subintegrations; LOFAR at 149 MHz using 110-s integrations. Discontinuation of lines indicates flagged subintegrations due to RFI. The B-mode is indicated by the shaded green backgrounds labelled 'B'.

(Levenberg, 1944) to provide the normalised peak amplitude, peak location, w_{50}, and full-width-10%-maximum, w_{10}, values. Table 2.2 provides the summary of characteristics for the pulse profile components at multiple frequencies for B and Q-modes. Peak amplitude is measured in percentage relative to the B-mode MP.

After quantifying characteristics of the profile features at each frequency listed in Table 2.2, the trend with respect to frequency was explored. Assuming that each feature, x, follows a power law with respect to frequency, $x \propto \nu^{\eta}$, a weighted best fit was performed to determine the appropriate value for the exponent, η. Each feature shows reasonably good linear correlation with frequency on a log-log scale, with absolute Pearson product-moment correlation coefficients greater than 0.85. The resulting values and errors for the exponents are shown in the bottom row of Table 2.2.

We find that the width of all pulse profile components decrease with increasing frequency in both emission modes, although this trend is most notable for the Q-mode pulse. This is consistent with previous results for the B-mode pulse profile (e.g. Kramer, 1994), and also with radius-to-frequency mapping (RFM; e.g. Gil et al., 2002). The largest intra-channel DM smearing at the lowest LOFAR frequency accounts for 0.3° in pulse longitude, which does not affect the conclusions obtained from the low-frequency pulse profile. The B-mode PC and IP move further from the MP and decrease in amplitude relative to the MP with increasing frequency. The positions of the PC and IP and

TABLE 2.2: Summary of the pulse profile components from the LOFAR observation on 2012 November 9 ($LOFAR_1$) and the simultaneous multi-frequency observations on 7 April 2013. Columns 1 and 2 indicate the telescope and central frequency used. w_{50} of the B-mode MP, PC, and IP, and the Q-mode pulse are shown in columns 3, 7, 11, and 14, respectively. w_{10} of the B-mode MP, and PC are summarised in columns 4, and 8, respectively. The peak flux location of the B-mode PC, and IP, and the Q-mode pulse, with respect to that of the B-mode MP, where '+' indicates later pulse phases, are shown in columns 5, 9, and 12, respectively. The relative amplitude of the peak flux of the B-mode PC, and IP, and Q-mode pulse, with respect to the MP (corrected for different integration times using Table 2.1) are summarised in columns 6, 10, and 13, respectively. The bottom row shows the frequency dependence of each of the profile features as the exponent of a power law, η.

		B-mode MP		B-mode PC				B-mode IP			Q-mode		
Telescope (Name)	Frequency (MHz)	w_{50} (°)	w_{10} (°)	location (°)	amplitude (%)	w_{50} (°)	w_{10} (°)	location (°)	amplitude (%)	w_{50} (°)	location (°)	amplitude (%)	w_{50} (°)
$LOFAR_1$	143	6.68(5)	14.06(8)	+31.5(1)	3.76(5)	9.8(3)	17.9(5)	−178.5(7)	0.90(5)	20.5(6)	+2(1)	0.89(5)	9.4(2)
LOFAR	149	6.73(3)	13.36(8)	+31.5(1)	3.19(5)	9.6(2)	17.4(2)	−179.3(2)	0.75(5)	16.2(5)	+1.9(2)	0.62(5)	9.6(4)
WSRT	346	4.29(3)	9.14(8)	+31.7(1)	2.09(5)	9.4(2)	17.2(3)	−180.0(3)	0.30(5)	15.2(2)	+1.8(2)	0.47(3)	8.7(5)
Lovell	1532	3.12(3)	6.33(8)	+36.0(2)	0.69(4)	8.3(2)	15.2(2)	−181(1)	0.23(6)	12.3(8)	+1.3(5)	0.39(9)	3.7(3)
Effelsberg	2635	2.89(7)	5.97(9)	+36.1(1)	0.51(3)	7.2(3)	13.2(3)	−182(1)	0.12(3)	11(1)	+0.9(6)	0.7(3)	1.8(4)
All	η	−0.33(4)	−0.30(4)	+0.050(9)	−0.66(6)	−0.08(2)	−0.08(2)	+0.005(1)	−0.63(2)	−0.19(6)	−0.16(4)	−0.3(2)	−0.37(9)

their frequency dependence are in agreement with previous results (Hankins and Fowler, 1986). This is further discussed below in Section 2.5. Table 2.2 shows that the amplitude of the PC has the strongest frequency dependence and the location of the IP is the least dependent on frequency.

The relative pulse amplitude of the Q-mode profile is approximately equal to the amplitude of the B-mode IP, and also decreases with increasing frequency. The The peak amplitude of the Q-mode is located towards later pulse phases compared to the B-mode MP at the same frequencies, and seems to arrive progressively earlier in pulse phase towards higher frequencies. Furthermore, Table 2.2 shows that both B- and Q-mode pulse profiles show no significant change over one year between the LOFAR observations from 2012 February 9 and 7 April 2013.

To further investigate the relative properties of the B and Q-modes at low-frequency, the spectrum in each mode was calculated using the eight-hour LOFAR observation. The flux density, S, as a function of frequency was obtained using the radiometer equation, including an empirically-derived and tested formula for the effective area of the LOFAR stations, and correction for the primary beam using the theoretically-derived and tested beam model, described in Hassall, et al. (in prep.). The B-mode and Q-mode data were divided into 5 and 3 subbands, respectively, deemed to be appropriate based on the respective S/N. A line of best fit was also calculated assuming a single power law across the bandwidth of the observation, $S \propto \nu^{\alpha}$, and the error was determined considering

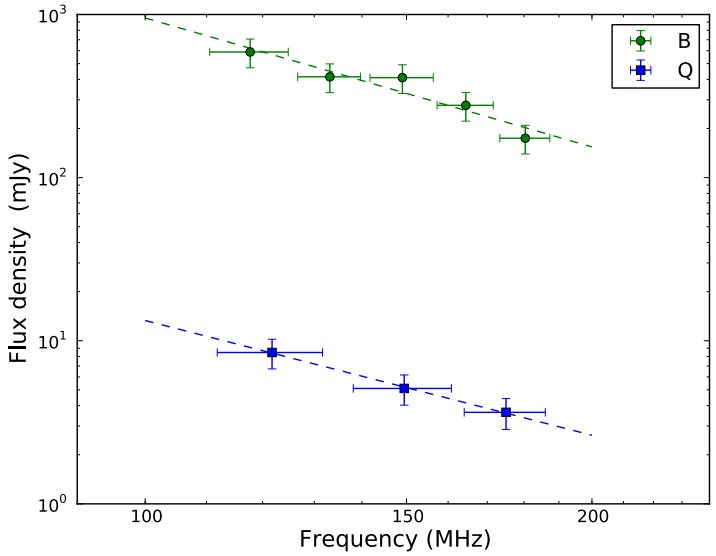

FIGURE 2.6: Low-frequency spectra of PSR B0823+26, separated into B (green circles) and Q-mode (blue squares) and obtained from the LOFAR observation taken on 7 April 2013. Frequency-axis error bars show the bandwidth used to calculate each point. The dashed lines show the best power-law fit to the data.

the flux density errors only. Figure 2.6 shows the resulting spectra in the two emission modes.

The difference in flux density between the B and Q-modes is striking, Fig. 2.6. In fact, the average flux density in the B-mode, 370 mJy at 149 MHz, is almost two orders-of-magnitude greater than that of the Q-mode, 5 mJy. This is a possible factor in the previous non-detection of this weak Q-mode.

The exponent, α, obtained from the continuous power-law best fits, weighted by the uncertainties, for the B and Q-modes are –2.6(5) and –2.3(1), respectively. Therefore, there is no significant difference in the power-law index of the spectra between emission modes. This is further discussed in Section 2.5. The relatively steep spectral index and strong scintillation are also possible factors in the previous non-detection of the weak Q-mode emission at higher frequencies. The increased bandwidth used for the observation using the Lovell telescope on 7 April 2013 in this work (400 MHz) also provided almost a factor of two better sensitivity in comparison to the observations in Young et al. (2012).

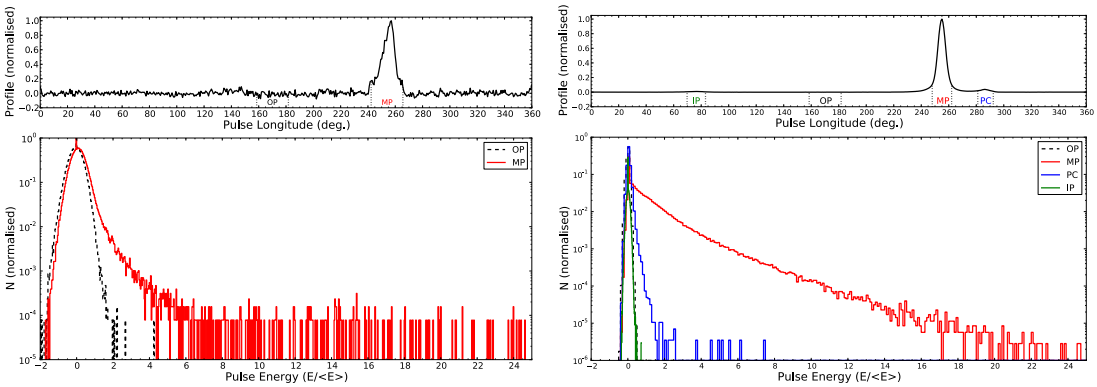

FIGURE 2.7: *Upper panels:* Normalised average pulse profiles (black line) for the Q-mode (*left*) and B-mode (*right*), showing longitude ranges included in the pulse-energy analysis (delimited by the black dotted lines). *Lower panels:* Normalised longitude-resolved PEDs for the Q- (*left*) and B-mode (*right*), using the LOFAR observation taken on 7 April 2013. The MP, PC, IP, and off-pulse (OP) distributions are shown (red, blue, green, and black dotted lines, respectively).

2.4.3 Single-pulse analysis

Potentially interesting emission features were investigated and compared for the B and Q-modes by analysing single pulses from the eight-hour simultaneous observations. This was conducted using a software package provided by P. Weltevrede (private communication) to construct centred, gated, de-baselined, and further RFI-excised single-pulse archives (e.g. Weltevrede et al., 2006b). This enabled us to extract information regarding nulling, subpulse drifting, and pulse energy distributions (PEDs).

2.4.3.1 Pulse energy distributions

Longitude-resolved PEDs were calculated for each pulse profile component of the B and Q-modes by integrating over the pulse longitude bin range selected, see Fig. 2.7. Pulse longitude ranges corresponding to w_{10} were selected for this because this is a compromise between including many pulses versus noise. They are indicated underneath the average pulse profiles in the upper panels of Fig. 2.7. The longitude range of the off-pulse (OP) region shown in Fig. 2.7 was selected to correspond to the range selected for the Q-mode pulse, and to be located mid-way between the B-mode MP and IP.

Figure 2.7, *upper panels*, shows the normalised flux-density profiles of the B and Q-mode. Note the difference in the off-pulse noise level. The lower panels in Fig. 2.7 illustrate the normalised PED with respect to the average pulse energy, $< E >$, shown

separately for the B (*left*) and Q-modes (*right*). The B-mode MP and PC PEDs are clearly distinct from that of the off-pulse region and resemble lognormal probability density distributions. For the MP, the best lognormal fit to the PED for pulse energies 1.5–20 times greater than the average yields a standard deviation of 0.77(15). The IP PED is comparable to that found for the off-pulse region because of its relatively weak single-pulse flux.

Q-mode emission shows a distinctly different PED, which falls off much more rapidly at low energies and resembles a power-law distribution. The Q-mode PED is less distinguishable from that of the off-pulse region at lower pulse energies due to the much weaker emission, but shows a tail of less frequent higher-energy pulses. The best power-law fit to the PED for pulse energies 1–8-times greater than the average gives an exponent of –3.2(2).

To investigate how the energy of the pulses affects the average pulse profile, we constructed integrated PEDs from the longitude-resolved PEDs, shown in Fig.2.7, to obtain the average pulse profile for a number of pulse energy ranges. We find that the most energetic B-mode single pulse profiles show PCs located towards lagging pulse phases. Moreover, these pulses are approximately eight-times brighter compared to the average pulse profile. Despite this, the average pulse profile shows remarkably little pulse profile evolution with increasing pulse energy, similar to that observed in PSR B1133+16 (Kramer et al., 2003). In addition, single pulses with the highest flux in the Q-mode have smaller w_{50} values than the average pulse profile. There is also a more notable contrast in pulse profile evolution with energy in the Q-mode. That is, pulses with energies greater than twice the average possess profiles akin to a skewed Gaussian, similar to that in Fig. 2.7, *top right*. Pulses with energies less than twice the average have profiles that are weak (discernible from the baseline at approximately 3-σ), irregular, and somewhat top-hat-like in shape, for examples see Fig. 2.8 *left*. Hence, the pulse profiles in the Q-mode seem to show much greater variability with energy compared to those in the B-mode.

2.4.3.2 Nulling

The integrated PEDs were used for complimentary analysis of the nulling fraction (NF). We estimated the NFs by subtracting the off-pulse pulse-energy samples from the on-pulse PEDs, as described in Wang et al. (2007). The analysis was undertaken separately for the Q-mode, the 160-pulse B-mode 'flicker', and the prolonged B-mode from the 7 April 2013 LOFAR observation, summarised in Fig. 2.4.

PSR B0823+26 displays nulling in both emission modes. More specifically, the NF for the prolonged B-mode was determined to be 1.8(5)%. This is lower than, but still within 2.2-σ of, previous estimates (Herfindal and Rankin, 2009). The NF for the B-mode 'flicker' was found to be 15(1)% – almost ten times larger than that during the prolonged B-mode emission.

Further inspection of the single pulses during this short-lived period of B-mode emission also indicates that the NF increases towards the transition back to the Q-mode. Inspection of simultaneous pulses from the 346 MHz and 1.5 GHz data also indicate that the nulls occur simultaneously at all frequencies, which is consistent with mode-switching, as observed in several other cases (e.g. Biggs, 1992, Hermsen et al., 2013). The NF throughout both occurrences of the Q-mode during the observation was determined to be 80(9)%. Therefore there are over forty-times more nulls during the Q-mode than during B-mode emission.

Figure 2.8, *left*, demonstrates the nature of the Q-mode emission through a 250-single-pulse extract from 4.6 h into the observation. A pulse extract from the B-mode emission is also shown in Fig. 2.8 *right*, for comparative purposes. The weak Q-mode emission consists of sporadic, mainly low-intensity bursts which occur in groups of approximately one to five pulses with no immediately identifiable periodicity. Therefore PSR B0823+26 seems to display similar behaviour to the weak-mode emission identified in PSR B0826–34 (Esamdin et al., 2005), also somewhat resembling emission from rotating radio transients (RRATs) (McLaughlin et al., 2006). This is also further discussed in Section 2.5.

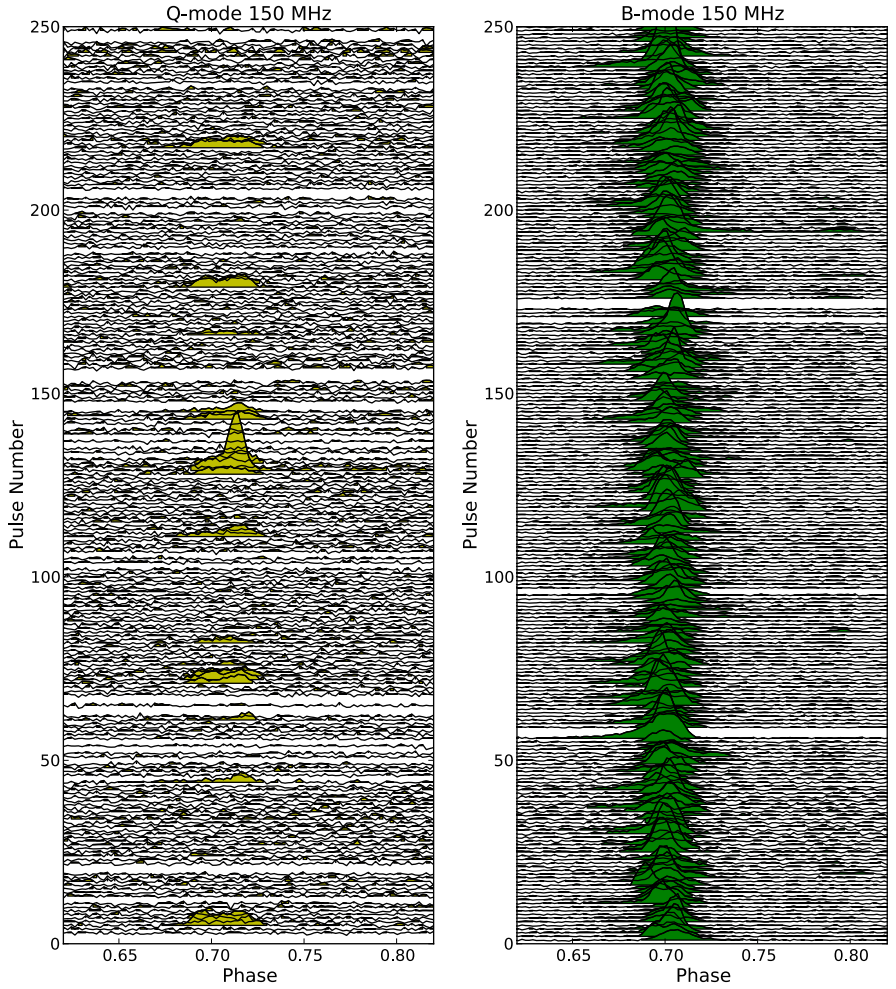

FIGURE 2.8: Representative examples of single-pulse profiles from the LOFAR observation on 7 April 2013, arbitrarily normalised. *Left:* sporadic and weak emission during the Q-mode, *right:* B-mode regular emission for comparison. Single pulses rejected due to RFI are not shown.

2.4.3.3 Subpulse modulation features

The subpulse modulation properties of the prolonged B-mode at low frequency were investigated using the LOFAR observation on 7 April 2013, and the method described in (Weltevrede et al., 2006a). The aim was to compare the modulation patterns exhibited by the different modes (e.g. van Leeuwen and Timokhin, 2012). Pulse stacks, for example see Fig. 2.8, were used to obtain the Longitude Resolved Fluctuation Spectrum (LRFS; Backer, 1970c) and hence the vertical separation between drift bands, P_3, measured in pulse periods, P_0. The LRFS obtained from the B-mode emission, Fig. 2.9 *right*, shows two drift features that are broader than 0.05 cycles per period (CPP). One feature is located at the alias border $P_0/P_3 = 0$, indicating that subpulses drift towards both

earlier and later pulse phase directions. The second feature relates to $P_3 = 5.26(5)P_0$. Since P_3 is generally independent of observing frequency, this is in excellent agreement with the value of $5.3(1)P_0$ previously determined at 92-cm (Weltevrede et al., 2007).

We also constructed Two-Dimensional Fluctuation Spectra (2DFS; Edwards and Stappers, 2002) to determine the horizontal separation between the drift bands, P_2, measured in pulse longitude. For the B-mode emission we find that although the feature in the 2DFS peaks at zero CPP, the wings are asymmetric, indicating that drifting subpulses travel towards later pulse phases more often. Calculating the centroid of the asymmetric wings at 20% of the maximum allowed us to extract the value of $P_2 = +90(20)^\circ$. This is in good agreement with the value obtained at 92-cm, $+70^{\circ}{}^{+10}_{-12}$ Weltevrede et al. (2007). Unlike P_3, P_2 is found to vary with observing frequency (Edwards and Stappers, 2003). Since $P_2 = +55^{\circ}{}^{+40}_{-7}$ at 21-cm (Weltevrede et al., 2006a), the value determined here also seems to be in agreement with the general trend that P_2 decreases with increasing observing frequency for PSR B0823+26.

The same subpulse modulation analysis was also conducted for the prolonged Q-mode emission from the 7 April 2013 LOFAR observation. No significant feature was detected in either the LRFS, Fig. 2.9 *right* or 2DFS. This may be due to the greater nulling fraction and very weak single pulses. However, PSR B0943+10, which shares many emission characteristics with PSR B0823+26, also shows subpulse drifting only during the B-mode and not in Q-mode, which is comparatively 'disordered' (Backus et al., 2011).

The longitude-resolved modulation index, a measure of the factor by which the intensity varies from pulse to pulse, was derived from the LRFS (Weltevrede et al., 2006a), Fig 2.9 *upper panels*. The median modulation index of the B-mode MP was found to be 1.4(5). The median modulation index of the PC component was found to be slightly larger, 1.6(9). The B-mode MP and PC components show similar longitude-resolved modulation characteristics, although the PC shows slightly more variability than the MP, with median modulation indices of 1.4 and 1.6, respectively. The median modulation index of the Q-mode pulse was found to be over ten-times larger than the B-mode MP, 17(5), and shows somewhat different longitude-resolved modulation compared to the B-mode, Fig 2.9 *upper panels*.

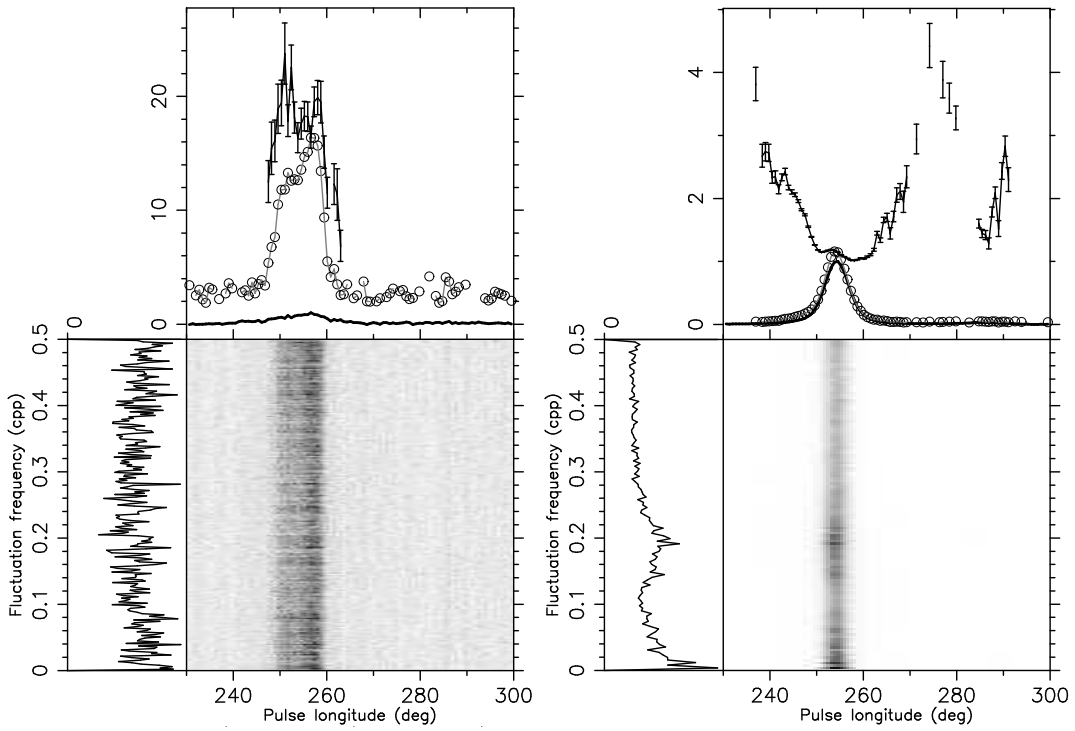

FIGURE 2.9: Pulse variability analysis products from the LOFAR observation on 7 April 2013, for the Q-mode (*left*) and the B-mode (*right*). *Upper panels:* the integrated pulse profile (solid line), longitude-resolved modulation index (solid line with error bars) and the longitude-resolved standard deviation (open circles). *Lower panels:* the LRFS is shown, with its horizontal integration to the left.

The pulse profile stability during B-mode was investigated using the 7 April 2013 simultaneous LOFAR and WSRT data. The Pearson product-moment correlation coefficient, ρ, was calculated between an analytic profile of PSR B0823+26 and the pulse profile integrated from an increasing number of effective single pulse numbers, $N_{\rm efc}$, as described in Liu et al. (2012). We find that towards higher effective pulse numbers (>200–500) the LOFAR and WSRT data follow the expected trend, i.e., $1-\rho \propto N_{\rm efc}^{-1}$ (Liu et al., 2011). However, there are some notable deviations from this trend, which tend to coincide with narrow, bright pulses. This suggests that over many pulse periods the pulse profile is stable, but over short periods the emission shows intrinsic pulse-to-pulse shape variations. This is not unexpected due to previous results that show the array of emission phenomena exhibited by PSR B0823+26.

2.5 Discussion and conclusions

In this work we have confirmed that PSR B0823+26 shows a host of emission characteristics over a wide range of timescales. The most surprising finding from the work presented here is that the long-term nulls, recently found by Young et al. (2012), are in fact a very weak and sporadically emitting mode, which we refer to as Q-mode. We find that this mode is over 100 times weaker than the B-mode. We also find evidence for a further decrease in flux just before the switch to B-mode. It is possible that this could be a third emission mode, whereby the flux density of emission decreases even further or emission completely ceases. It would also be quite interesting if this weakest (possibly completely off) mode is found to always occur before the start of B-mode – as it has in the three instances we have observed.

Considering the many studies which have been conducted on PSR B0823+26, it is surprising that the long-term nulling was only recently discovered (Young et al., 2012). It may be that the emission from PSR B0823+26 has changed over a multi-year timescale, such that mode changing is more frequent or longer in duration than in previous years, though that remains to be shown. If so, this may be due to a multidecadal change in emission, perhaps related to that observed in the Crab pulsar due to magnetic field evolution (Lyne et al., 2013).

2.5.1 Magnetospheric switches

Upon investigation of the newly-discovered Q-mode pulse profile at frequencies between 110 MHz and 2.7 GHz we find the pulse profile comprises a single component located within the regular B-mode MP envelope, but with a peak located towards slightly later pulse longitude, and a lower flux density by approximately two orders of magnitude. The PC and IP that are present during the B-mode are not detected during the Q-mode. A converse example of a pulsar that exhibits mode-changing, PSR B0943+10, has a pre-cursor in the Q-mode and not in the B-mode at 320 MHz (Hermsen et al., 2013).

During the Q-mode, the emission is weak and sporadic, with a very high NF and modulation index. This behaviour seems similar to the Q-mode identified in PSR B0834–26 (Esamdin et al., 2005). It also seems reminiscent of RRAT-like emission that may imply a common, or at least related, emission mechanism. This has previously been proposed

from both theoretical (e.g. Jones, 2013) and observational perspectives (e.g. Burke-Spolaor and Bailes, 2010, Keane et al., 2011). The detection of the weakly-emitting Q-mode from PSR B0823+26 could mean that other pulsars currently identified as extreme-nullers may also show similar weak emission if higher-sensitivity observations can be done (Wang et al., 2007, Esamdin et al., 2005, Young et al., 2014).

During the simultaneous observation on 7 April 2013 the initial undetected Q-mode, lasting approximately 0.87 h, leads to the short-duration 160 single-pulse B-mode 'flicker'. However, later in the same observation, and also in the observation on 9 February 2012, the non-detection of the Q-mode was much shorter in duration and the subsequent B-mode emission was longer in duration. This further decrease in radio emission, which tentatively may be considered as a further separate emission mode, could be caused by a change in the particle density within the magnetosphere that soon after causes the switch to B-mode. We also speculate that the duration of the undetected emission towards the end of the Q-mode, just before the mode-switch to the B-mode, may be inversely correlated with the length of time the pulsar emits in the subsequent B-mode. We stress that this is speculative due to the limited sample, and more work will be done in future to investigate this by using longer and more frequent low-frequency observations.

Single-pulse analysis allowed us to determine that the transition between modes occurs within one rotational period, and that it is broadband over the radio frequencies observed, similar to other mode changing pulsars (e.g. PSR B0943+10, Hermsen et al., 2013, Bilous, et al., in prep.), and nulling pulsars (e.g. PSR B0809+74, Bartel et al., 1981). Within the theoretical framework of force-free magnetospheres, it has been shown that multiple stable solutions with different structures are possible, e.g., with different sizes of closed field line region (Timokhin, 2010, Contopoulos, 2005). Therefore, the B and Q-modes could be caused by two stable magnetospheric states with different magnetospheric structures, affecting the current of relativistic particles, and therefore the broadband radio emission mechanism. However, the mechanism that generates the wide range of observed timescales (e.g. each emission state lasting many hours and mode-switches occurring within one rotational period) is still elusive.

2.5.2 Considering spin-down

PSR B0823+26 shows no detectable change in spin-down rate between modes (Young

et al., 2012), similar to other pulsars which exhibit mode-changing on similar timescales, e.g., PSRs B0834–26 and B0943+10, whilst other extreme-nulling pulsars identified as 'intermittent' often do (Kramer et al., 2006b, Camilo et al., 2012a, Lorimer et al., 2012). In part, this is because it is difficult to detect small changes in spin-down if the duration of the different emission modes is significantly shorter than for the extreme nulling pulsars (Young et al., 2012). This may also be due to the electromagnetic spin-down torque exerted on the neutron star, proportional to $\sin^2\theta + (1-\kappa)\cos^2\theta$ (Contopoulos and Spitkovsky, 2006), where θ is the alignment angle between the spin axis and magnetic moment, and κ the ratio between the angular velocity of the pulsar and the angular velocity at the death line. Namely, if there is some small change in θ between emission modes, then the change in spin-down torque is less severe in cases of nearly orthogonal rotators (e.g. PSR B0823+26, Everett and Weisberg, 2001). This is less certain in cases of nearly aligned rotators (e.g. PSR B0943+10, Deshpande and Rankin, 2001) (Li et al., 2012b).

2.5.3 Emission characteristics

Although we find that the spectral indices of the B and Q-modes are consistent, within errors, the broad-band spectrum of PSR B0823+26 shown in Hassall et al. (in prep.) indicates a spectral turn-over at 127(25) MHz. Future observations using the LOFAR Low Band Antennas (30–90 MHz) would be ideal for further investigating the spectral properties of PSR B0823+26 in both emission modes (if the Q-mode is detectable), including providing constraints on the presence of a spectral turn-over, and hence supplying more clues about the origin of the difference between emission modes.

PSR B0823+26 also shows certain emission characteristics which are reminiscent of several other pulsars. The PCs associated with the highest energy single pulses that were 8-times brighter than average are reminiscent of the Vela pulsar's (PSR B0833−45) 'bump' component after the main pulse, where 'giant micro-pulses' with flux densities exceeding 10-times that of the mean were observed (Kramer et al., 2002). For comparison to the highly polarised single pulses detected in the 14 November 2011 LOFAR observation, PSR B0656+14, which may be a nearby RRAT, also shows strong highly-polarised single pulses limited to the leading and central regions of the average pulse profile (Weltevrede et al., 2006b). Moreover, narrow pulses observed after the transition

to the B-mode occur towards the trailing edge of the average pulse profile, similar to that observed in PSR B1133+16 (Kramer et al., 2003). The presence of an IP and a highly linearly polarised PC (Weisberg et al., 1999, , Noutsos et al., in prep.) in the pulse profile is reminiscent of PSR B1822−09 (Gould and Lyne, 1998).

Polarisation observations allowed the MP to be classified as a core component and the IP to be classified as a possible core component of the opposite magnetic pole (Weisberg et al., 1999, and references therein). The PC's high linear polarisation fraction could originate from induced scattering of the main pulse emission into the background by the particles of the ultra-relativistic highly magnetised plasma (Petrova, 2008). This could also explain the trend in the PC location growing more distant with increasing frequency, which is contradictory to the behaviour expected from RFM (e.g. Mitra and Rankin, 2002) and has lead to reluctance in its classification as a conal component (Weisberg et al., 1999). We note that the decrease in the pulse profile component widths with increasing frequency is consistent with the RFM model (e.g. Gil et al., 2002), although this may also be caused by other mechanisms (e.g. birefringence, McKinnon, 1997). Therefore, it seems that the emission behaviour observed from PSR B0823+26 is very diverse, and may prove one of the most difficult pulsars to model in terms of accounting for the host of emission characteristics that arise over many different timescales. However, observations of PSR B0823+26 may also help in efforts to unify the diverse phenomenology of pulsar emission and provide vital data in terms of studies of the elusive pulsar emission mechanism.

2.5.4 Pulsar population implication

In the period–period-derivative (P–$\dot{P}$) diagram for normal pulsars (excluding millisecond pulsars) from the ATNF pulsar catalogue (Manchester et al., 2005a), Fig. 2.10, PSR B0823+26 is located near the centre of the distribution, and therefore appears to be a very regular pulsar in this parameter space. Other pulsars which have been identified to display at least one of the numerous emission characteristics investigated here are located throughout most of the parameter space, apart from the area occupied by very young pulsars. Therefore, there is no obvious correlation with surface magnetic field strength or characteristic age (e.g. Weltevrede et al., 2007). Most pulsars may exhibit these emission phenomena, but the effects of pulse-to-pulse variability are diminished

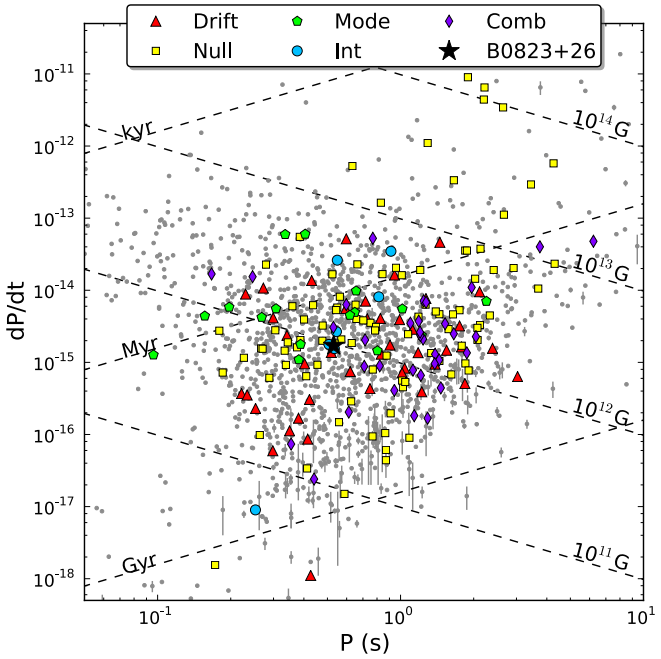

FIGURE 2.10: Period–period-derivative diagram for normal pulsars (excluding millisecond pulsars) from the ATNF pulsar catalogue (grey points Manchester et al., 2005a). Pulsars established to show emission phenomena are emphasised: subpulse drifting (red triangles), nulling (yellow squares), mode-changing (green pentagons), intermittency (blue circles), or a combination of at least two of these (purple diamonds). PSR B0823+26 is also highlighted (black star) and lines of equal characteristic ages and surface magnetic field strengths are shown (dashed lines).

due to summing over many pulses that is required to detect signals with sufficient S/N for sources with lower flus densities.

To date, only a handful out of the $\sim$ 2300 known pulsars are identified as intermittent or extreme nullers. This is because this requires frequent observations over several months/years to identify this long-term behaviour. This is also because they may also be difficult to identify in a pulsar survey due to the nature of the weak/undetectable emission during quiet modes. There may also be pulsars which emit in a Q-mode-like state over longer timescales or continuously, for which more sensitive radio-telescopes will be needed, such as the Square Kilometre Array (SKA, Garrett et al., 2010). Studying pulsars that display many of these emission characteristics, such as PSR B0823+26, will provide further insights into the possible radio emission characteristics, the relationship between phenomena, and understanding of the magnetospheric emission mechanism from pulsars and RRATs.

2.5.5 Using pulsars as probes of the ISM

Using the LOFAR observation on the 14 November 2011, we found that there is no significant variation in the observed RM over small timescales due to changes in the pulsar magnetosphere. This is reassuring in terms of using pulsar RMs as probes of the Galactic magnetic field (e.g. Van Eck et al., 2011). Although the pulsar magnetosphere is assumed to have a minor contribution to the observed RM (Noutsos et al., 2009), an interesting area of future investigation may be whether the RM, or polarisation angle, as a function of pulse phase is in any way dependent on the emission mode. LOFAR's low frequency and large fractional bandwidth facilitates such studies, where high RM precision is important. Studies of the emission characteristics from pulsars, including in polarisation, will also continue to aid in better understanding the pulsar emission mechanism itself, so that pulsars can be used increasingly effectively as probes of the ISM.

Chapter 3

Evaluation of published rotation measures and techniques, and implications for the Galactic magnetic field

3.1 Abstract

This chapter is focussed towards describing the state-of-the-art in terms of the practical methods used to obtain Faraday rotation measurements (RMs), and results collected from the literature towards polarised sources (pulsars and extragalactic sources). The powerful method of RM-synthesis is discussed, which is the most recent method used to determine RMs, including that in this work. There are currently 680 pulsars for which RMs have been published, although 215 have at least one independent measurement. These pulsars are located mainly in the galactic plane in the near side of the Galaxy, and can provide information about the three dimensional structure of the Galactic magnetic field (GMF). The current catalogue of extragalactic sources consists of over 30,000 data points, which are somewhat evenly distributed around the celestial sphere in the Northern sky, and can provide information about the entire line-of-sight through the Galaxy. These catalogues are discussed for the purpose of reconstructing the Galactic

magnetic field in Chapter 5, which is approximately eighteen orders of magnitude lower in field strength than that at the surface of pulsars.

3.2 Introduction

The aim of this chapter is to present RMs towards pulsars from a combination of the ATNF pulsar catalogue[1] (Manchester et al., 2005a) and other literature sources, as well as literature values of RMs towards extragalactic sources (EGS). The literature sources used for published RMs towards pulsars and EGS are summarised, and the pulsar data collected are presented in Appendix A. The previously published pulsar data are explored to investigate, for example, the accuracy of the data and whether there is evidence of RMs changing between observing epochs. These published RM data, as well as RMs measured from the observations, are used to reconstruct the Galactic magnetic field (GMF) in Section 5. In order to present the data more fully, the methods which have been used to measure RMs from observational data previously are also presented and discussed.

There are 2328 pulsars in version 1.5 of the ATNF pulsar catalogue, 30% (680) of which have a published RM. Figure 3.1 shows the positions of these pulsars in the Galaxy, as predicted by the NE2001 electron density model (Cordes and Lazio, 2002), projected onto the Galactic plane.

It is evident that the majority of known pulsars, especially those with RMs, are located in the near-side of the Galaxy. Galactic quadrants I and IV each contain 43% of the known pulsars, and consequently a large number of pulsars with RM data, compared to quadrants II and III which each contain 7%. This is somewhat expected because the stellar density and Galactic volume differs between the quadrants – pulsars are most commonly located in the Galactic plane in spiral arms as this is often the location of their massive progenitor stars. Furthermore, these numbers are also somewhat biased because the majority of telescope time spent on pulsar surveys and polarisation observations was using southern telescopes, namely the Parkes observatory. However, each Galactic quadrant has a comparable fraction of pulsars with RMs, 21%, 38%, 48% and 36% for quadrants I to IV, respectively. There is also a higher density of known pulsars within

[1]Maintained by the Australia Telescope National Facility (ATNF), available at http://www.atnf.csiro.au/people/pulsar/psrcat/

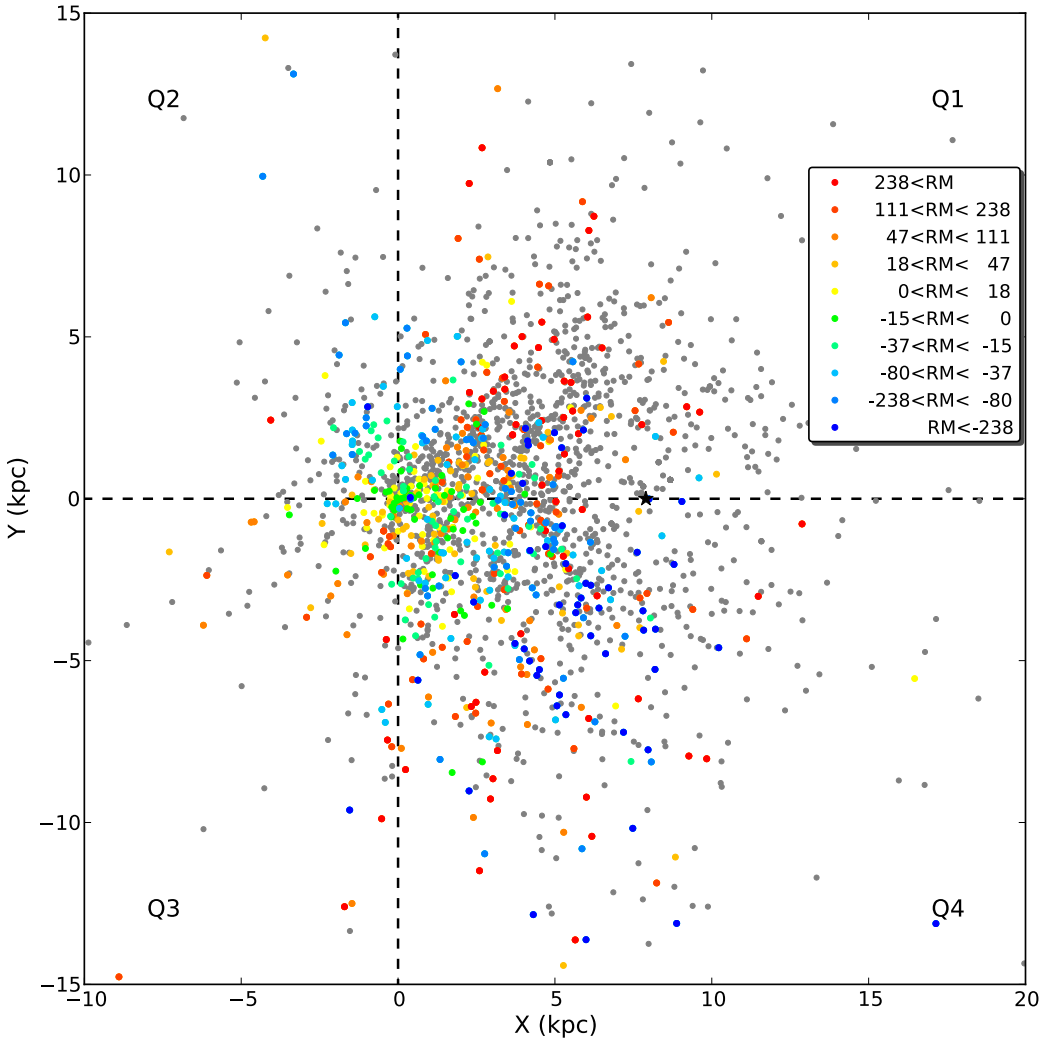

FIGURE 3.1: The approximate locations of catalogued pulsars in the Milky Way based on their known direction and DM-distance, as observed from above the Galactic plane. The pulsars without RM data (grey points) and with RM data (coloured points) are shown. Yellow through orange to red colours represent increasingly positive RMs whilst green through cyan to blue colours represent increasingly negative RMs, as shown by the legend. Each colour represents an RM range equal to a tenth percentile. The Sun is located at the origin and the Galactic Centre is indicated by the black star. The four quadrants of the Galaxy are also labelled.

3 kpc of the Sun – a selection effect because nearby pulsars have higher luminosities and are therefore easier to detect in pulsar surveys and follow-up observations. Within a cylinder of radius 3 kpc from the Sun, and height equal to that of known pulsars with the greatest approximate absolute distance from the Galactic plane (2.7 kpc), there are approximately 7 pulsars kpc^{-3} and 45% (249/551) of these have published RMs. In a hollow cylinder with radius between 3 kpc and 10 kpc from the Sun, and an equal height to that used previously, there are less than 2 pulsars kpc^{-3}, only a quarter of which have RM measurements (353/1368).

Increasing the number of known pulsars with RM data will provide more data points with which to construct the structure of the GMF. The fraction of pulsars with RMs in all Galactic quadrants can be increased by observing known pulsars without RMs, and recording data with full polarisation. Using observations from the radio telescopes specified in Chapter 5 located in the Northern hemisphere, it is possible to observe much of quadrants I to III. It is desirable to increase the number of RMs towards pulsars located in less densely populated regions of the Galaxy, particularly at larger distances from the Sun, to provide more information for reconstructing the large-scale GMF in the plane of the Galaxy. Due to the higher density of known pulsars within 3 kpc distance from the Sun, it is also favourable to increase the number of RMs within this region to better reconstruct the GMF in the Solar 'neighbourhood'. This allows higher resolution reconstruction towards smaller-scale structure, which is not possible in further regions.

Using the RM and DM towards a pulsar, the average magnetic field parallel to the LOS, weighted by the electron density, can be determined, see Eq. 1.14. The uncertainty in this value, $\sigma_{\langle B_\parallel \rangle}$, is:

$$\sigma_{\langle B_\parallel \rangle} \approx 1.232 \frac{\mathrm{RM}}{\mathrm{DM}} \sqrt{\left(\frac{\sigma_{\mathrm{RM}}}{\mathrm{RM}}\right)^2 + \left(\frac{\sigma_{\mathrm{DM}}}{\mathrm{DM}}\right)^2} \ \mu G, \tag{3.1}$$

where σ_{RM} and σ_{DM} are the errors on RM and DM, respectively. It is therefore important to minimise fractional errors on both RM and DM to determine an accurate average magnetic field. The median fractional uncertainties in RM and DM are 8% and 0.1%, respectively, and the mean fractional uncertainty in RM and DM are 28% and 0.5%, respectively. The fractional uncertainty in RM measurements towards pulsars are therefore over 55× those for DMs, on average. As such, the fractional uncertainty on the

RM measurement commonly dominates the error on the LOS magnetic field. Therefore, increasing the accuracy of RM data by observing at lower frequencies, for example using LOFAR, is also essential for more accurately determining the magnetic field parallel to each LOS. This is especially important for nearby pulsars or those towards the Galactic halo which have relatively small RMs. The average absolute magnitude of the Galactic magnetic field, calculated using all current published pulsar RM and DM data from the ATNF pulsar catalogue (Manchester et al., 2005a), is 1.1(2) μG, hence the average fractional uncertainty is 20%. Low-frequency observations will facilitate a decrease in the fractional RM error and hence decrease the error on the magnetic field by up to an order of magnitude, see Chapter 5.

3.3 Rotation measure methods

The methods that have been used to measure the RM from observational linear polarisation data are presented and discussed below.

3.3.1 Stokes QU-fitting

In observations with a linearly polarised feed at low frequencies, rotation of the polarisation angle results in a sinusoidal variation in the linearly polarised flux density as a function of frequency for highly polarised pulsars. The magnitude of the RM can be derived from the spacing between the amplitude maxima. This method was employed by early observations, for example, Staelin and Reifenstein (1969) using observations at 110–115 MHz and by Vitkevich and Shitov (1970a) at 86 and 105 MHz.

Figure 3.2 shows an example of the expected the sinusoidal variation of the Stokes Q and U parameters as a function of wavelength squared due to Faraday rotation. The data were fit with a sinusoidal function of the form $Q/U = \mathrm{A}\sin(2\,\mathrm{RM}\,\lambda^2+\delta)+\mathrm{C}$, where A is the amplitude, δ is the phase shift and C the y-direction shift. An initial ansatz for the RM value was obtained using the RM-synthesis method, explained below in Section 3.3.3. The fit output from the Stokes Q and U data gave observed RMs of 4.98(1) and 4.99(1) $\mathrm{rad\,m^{-2}}$, respectively.

This method used in a stand-alone fashion is only able to derive the magnitude of the RM (not the sign, and hence direction of the magnetic field parallel to the LOS) for highly polarised pulsars. The Stokes Q- and U-fitting method is now increasingly being investigated for applications such as distinguishing between at least two very similar RMs along a singular line of sight (e.g. O'Sullivan et al., 2012).

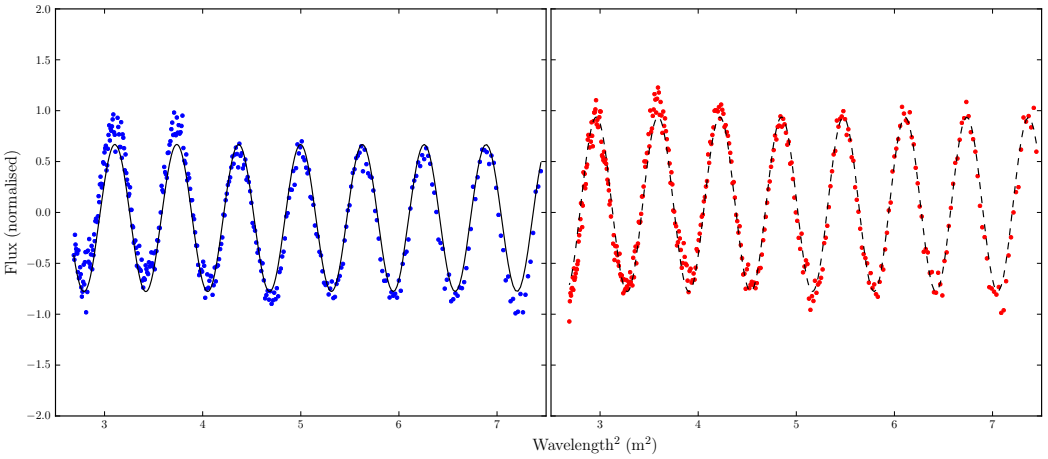

FIGURE 3.2: The normalised intensity of the Stokes Q (*left*, blue points) and U (*right*, red points) parameters as a function of wavelength squared. The sinusoidal variation is due to the effect of Faraday rotation. The data were obtained from a LOFAR observation of PSR B1133+16 at 110–183 MHz.

3.3.2 Polarisation angle

The RM towards pulsars and extragalactic sources has most commonly been measured by determining the gradient of the polarisation angle χ against wavelength squared, λ^2, (Cooper and Price, 1962, Burgay et al., 2013, e.g.) since

$$\mathrm{RM} = \frac{\mathrm{d}\chi\left(\lambda^2\right)}{\lambda^2}. \tag{3.2}$$

The RM is therefore obtained by determining the best fit to the constant linear gradient, see Fig. fig:lambda2fit for a simulation of this effect. The advantages to using this method, compared with the sinusoidal fit, are that the sign of the gradient also provides the direction of the magnetic field, and a linear fit to the polarisation angle from observations at multiple frequencies can be used, in cases of limited bandwidth at single frequencies (e.g. Rand and Lyne, 1994).

There are however some limitations to using this method. The polarisation angle is a pseudovector, and is therefore known to modulo π radians. A rotation of $n\pi$ between different observing wavelengths is hence undetectable without sufficient observing bandwidth or frequency resolution, making a linear fit of the gradient arbitrary in such cases (Rand and Lyne, 1994). This is often referred to as the $n\pi$ ambiguity, (Brentjens and de Bruyn, 2005). Moreover, sufficient polarised intensity is necessary in order to significantly detect polarisation angles at multiple frequencies, which limits the ability to detect high rotation measures in faint sources. This method also assumes a constant linear relationship between polarisation angle and wavelength squared. This is not the case for LOSs where at least two emitting regions result in detecting at least two different RMs, and also extended structures of magnetised plasma which emit polarised radiation over a range in Faraday depth (Faraday thick structures, for example, Burn slabs, where uniform field distributions and particle densities result in a top-hat function in Faraday depth Heald et al., 2009a).

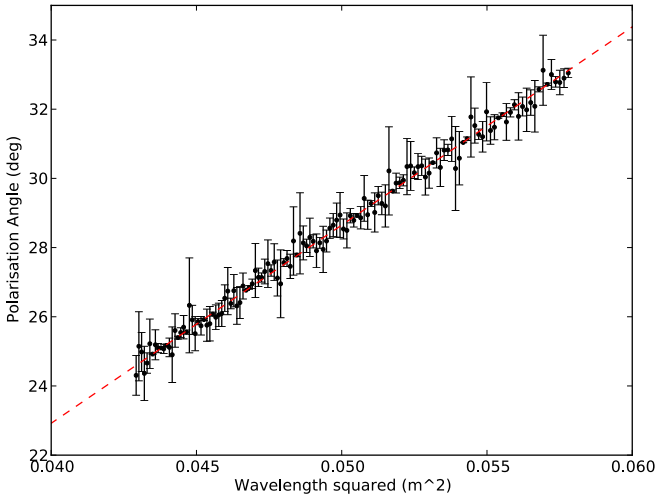

FIGURE 3.3: Simulation of the affect of Faraday rotation on the change in polarisation angle with wavelength squared. Data were simulated for an observation centred at 1.35 GHz with 200 MHz bandwidth (the same set-up as the Effelsberg observations described in Chapter 5). The unwrapped polarisation angles were compute using Equation 1.11, with zero intrinsic polarisation angle, an arbitrary RM of 10 rad m^{-2}, and added Gaussian noise (μ=0, σ=0.5). The red dashed line shows the weighted least squares fit to the data that would be performed on observational data.

3.3.3 RM-synthesis

An alternative method to measure Faraday rotation called RM-synthesis (Brentjens and de Bruyn, 2005), was first proposed by Burn (1966) and is now increasingly used for

such measurements (Heald et al., 2009b, Pizzo et al., 2011).

Following Brentjens and de Bruyn (2005) we define the observed complex polarisation pseudovector $\tilde{P}$ as:

$$\tilde{P}(\lambda^2) = \int_{-\infty}^{\infty} F(\phi) \exp\left(2i\phi\lambda^2\right) \mathrm{d}\phi, \tag{3.3}$$

where $F(\phi)$ is the intrinsic complex polarised surface brightness per unit Faraday depth, known as the Faraday dispersion function (FDF, or Faraday spectrum). Hence, the Fourier-transform like Eq. 3.3 can be inverted to obtain the Faraday spectrum from the observed complex polarisation vector:

$$F(\phi) = \int_{-\infty}^{\infty} \tilde{P}(\lambda^2) \exp\left(-2i\phi\lambda^2\right) \mathrm{d}\lambda^2. \tag{3.4}$$

Polarisation observations have a limited range in wavelength and measurements at $\lambda^2 \leq 0$ are not possible. Therefore, Brentjens and de Bruyn (2005) introduce a window function that is non-zero for all observed wavelengths and zero otherwise. In practice, the integral in Equation 3.4 is performed as a discrete sum, such that for each discrete channel i at λ_i^2:

$$F(\phi) \approx \left(\sum_{i=1}^{N} \omega_i\right)^{-1} \sum_{i=1}^{N} \omega_i \tilde{P}(\lambda_i^2) \exp\left(-2i\phi(\lambda_i^2 - \lambda_0^2)\right), \tag{3.5}$$

where ω_i is the weight of channel i and λ_0 is the weighted average of the observed λ^2. This inversion can be considered as the 'coherent' addition of the observed polarisation vectors in each channel for a range of Faraday depths. The vectors will constructively interfere within the bandwidth at the Faraday depth of the observed source, resulting in a peak at this value in the Faraday spectrum. This method can also be thought of as de-rotating the Stokes Q and U values at each frequency by values calculated using multiple trial RMs. The absolute value of linear polarised intensity, |P|, is summed across the entire bandwidth and the RM is obtained by identifying the value which maximises the peak S/N for |P|. This method has been used in the past for pulsar data, although it was not explicitly called RM-synthesis at that time (Mitra et al., 2003a, Weisberg et al., 2004). In these cases, a coarse search over a large range in RM was used to identify the most likely range of the RM to reduce computing time and then a finer search across these values leads to a more precise RM determination.

The relationship between the input observed complex polarisation vector and the output Faraday spectrum is given by the rotation measure spread function (RMSF), analogous to the point spread function of an optical telescope:

$$R(\phi) \approx \left(\sum_{i=1}^{N} \omega_i \right)^{-1} \sum_{i=1}^{N} \omega_i \exp\left(-2i\phi(\lambda_i^2 - \lambda_0^2)\right). \tag{3.6}$$

Equation 3.6 is useful in order to predict the response of particular observing setups, including side-lobe characteristics. There are further equations which are useful for planning observational specifications to measure RMs in order to determine, for example, the maximum observable Faraday depth, the precision of the measurement and the sensitivity to Faraday thick structures. The channel width, $\delta\lambda$, determines the maximum observable absolute Faraday depth, $|\phi_{\rm max}|$,

$$|\phi_{\rm max}| \approx \frac{\sqrt{3}}{\delta\lambda^2} \text{ rad m}^{-2}. \tag{3.7}$$

The range of the square of the observed wavelengths, $\Delta\lambda^2{=}\lambda^2_{max} - \lambda^2_{min}$, dictates the precision in Faraday space, i.e., the approximate FWHM of the peaks in the Faraday spectra, $\Delta\phi$,

$$\Delta\phi \approx \frac{3.8}{\Delta\lambda^2} \text{ rad m}^{-2}, \tag{3.8}$$

where the constant 3.8 is substituted for $2\sqrt{3}$ used in Brentjens and de Bruyn (2005) as it is closer to the FWHM of the sinc-function-like RMSF response (Schnitzeler et al., 2009). The shortest wavelength, $\lambda_{\rm min}$, determines the maximum detectable scale in ϕ-space, $\delta\phi$,

$$\delta\phi \approx \frac{\pi}{\lambda^2_{\rm min}} \text{ rad m}^{-2}. \tag{3.9}$$

RM-synthesis is analogous to performing aperture synthesis imaging with an interferometer in the sense that both methods make use of Fourier transforms using discrete sampling in λ^2 and spatial frequency coordinates ($(u,v,w){=}\vec{b}/\lambda$, where $\vec{b}_{ij}$ is the vector separating two antennas ij), respectively (Heald et al., 2009b). Hence, the RMSF in Faraday space is analogous to the dirty beam in angular coordinates on the sky (l,m) (Bell and Enßlin, 2012). As such, fewer gaps in the sampling of λ^2 reduce the side lobes in the RMSF and using larger bandwidths in λ^2 space increases the resolution in Faraday space, Eq. 3.8. Moreover, the uncertainty associated with locating the peak Faraday depth in the FDF, σ_ϕ, can be determined in the same way as the uncertainty

associated with locating the peak flux in an aperture synthesis image (Fomalont, 1999):

$$\sigma_\phi = \frac{\Delta\phi}{2 \times \mathrm{S/N}}, \tag{3.10}$$

where S/N is the total linearly polarised signal-to-noise ratio.

The RM-synthesis method uses the polarisation information across the entire observing bandwidth simultaneously. As such, it is not necessary to detect polarisation angles in individual frequency channels, and the full advantage of the excellent spectral coverage offered by modern radio telescopes can be used. This method also minimises the effect of the $n\pi$ ambiguity of the polarisation angles. Additionally, it relaxes the assumption that there is a single RM towards the LOS.

Figures 3.4 and 3.5 show the reconstructed Faraday spectra of simulated signals. The simulation tool used was developed by Andrew Fletcher (private communication). The RM-synthesis method is used, along with initial inputs based on the observational setups for the Effelsberg and LOFAR telescopes, which are further described in Chapter 5. Two theoretical LOSs are shown; one single Faraday-thin source and one with both a Faraday-thin and Faraday-thick source with differing intrinsic RMs. This shows that with no added noise in the data, the RM-synthesis method produces peaks at the expected Faraday depth in the Faraday spectra, convolved with the RMSF which is dependent only on the observed frequencies. The lower plot in Fig. 3.4 also shows that given a Faraday thick structure that is less extended in Faraday depth than the FWHM of the RMSF, the resulting Faraday spectra shows very little difference between this and the Faraday-thin source. Figure 3.5, lower plot, shows the contrast towards lower frequency observations, where the FWHM of the RMSF is much narrower than the extent in Faraday depth of the Faraday-thick source. As such, from the reconstruction of the signal using RM-synthesis, the Faraday-thin and Faraday-thick sources are easily differentiated and the flux ratios are also better preserved than in the higher-frequency example.

3.4 Catalogue of rotation measures towards pulsars

The complete catalogue of 680 pulsars which have at least one RM measurement, along with references, are shown in Table A.1. In total, 215 pulsars from the catalogue have

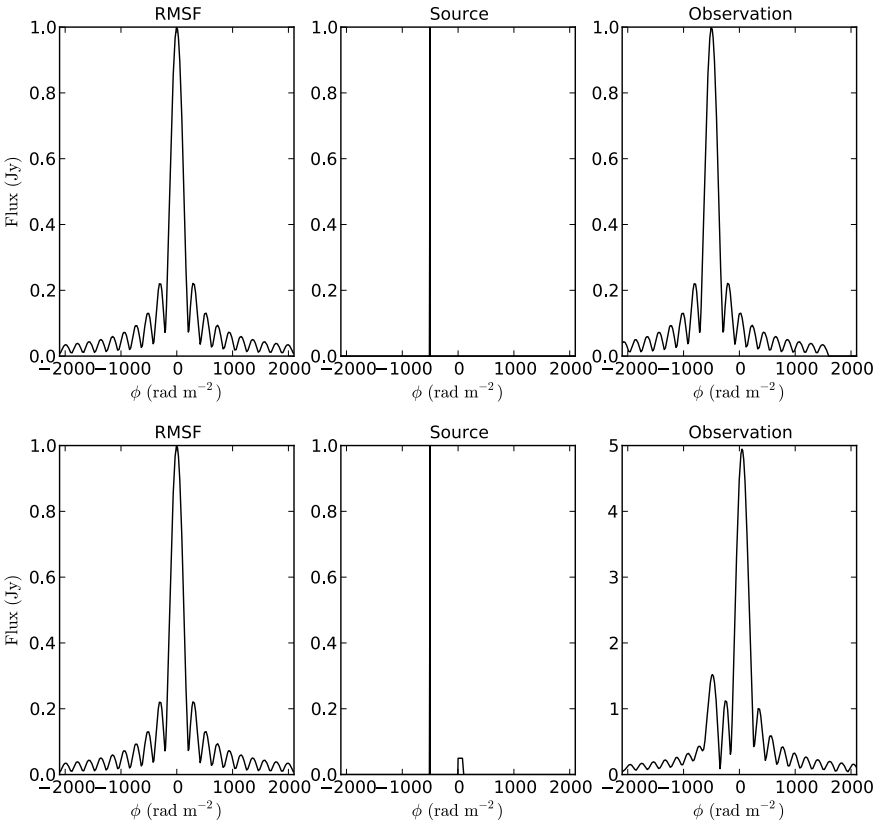

FIGURE 3.4: RM-synthesis simulation for observations centred at 1350 MHz with 200 MHz bandwidth – the same set-up as for the Effelsberg observations in Chapter 5. *Left:* The absolute value of the response function (RMSF) from the specified observational set-up. *Centre:* The simulated Faraday spectrum signal of the polarised source. *Right:* The absolute value of the Faraday spectrum recovered from a noise-free observation. The x-axis shows the Faraday depth (ϕ) and the y-axis shows the polarised flux density (Jy). The simulation considers a polarised background source with 1 Jy flux density and no intrinsic Faraday rotation. The *upper panel* shows the situation where a Faraday-thin screen with –500 rad m^{-2} is introduced to an intervening region of ionised gas with an ordered magnetic field and no cosmic ray electrons. The *lower panel* shows the situation considered in the upper panel, with an additional intervening region with cosmic ray electrons emitting synchrotron radiation, introducing a Burn-slab with 0.05 Jy flux density for Faraday depths $0< \phi <100$ rad m^{-2}.

one or more RM measurement in addition to the catalogue value. The sources of the RMs in the literature (59 in total) are listed in Table 3.1, which also includes a summary of the relevant observational parameters and analysis methods.

Pulsar observations from which RM measurements were derived were carried out at many facilities around the world, as shown in Table 3.1. These radio telescopes are listed below in alphabetical order, including the abbreviation used in Table 3.1:

- Arecibo: Arecibo Observatory, 305-m diameter single dish, semi-transit design,

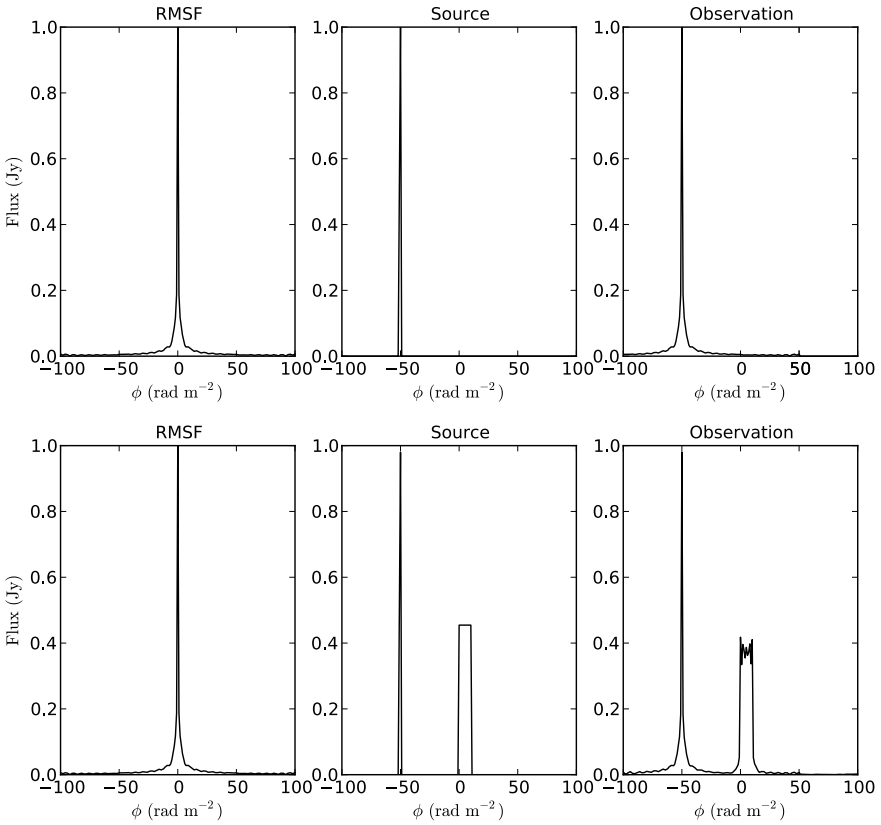

FIGURE 3.5: RM-synthesis simulation for observations centred at 150 MHz with 90 MHz bandwidth – the same set-up as for the LOFAR HBA observations in Chapter 5. The panels *left–right* are as shown in Fig. 3.4 for the Effelsberg 1350 MHz observational set-up, note however the smaller scaling for the Faraday-depth shown on the x-axis. The simulation also considers a polarised background source with 1 Jy flux density and no intrinsic Faraday rotation. The *upper panel* shows the situation where a Faraday-thin screen with –50 rad m^{-2} is introduced to an intervening region of ionised gas with an ordered magnetic field and no cosmic ray electrons. The *lower panel* shows the situation considered in the upper panel, with an additional intervening region with cosmic ray electrons emitting synchrotron radiation, introducing a Burn-slab with 0.5 Jy flux density for Faraday depths $0< \phi <10$ rad m^{-2}.

located at the National Astronomy and Ionosphere Centre in Arecibo, Puerto Rico, USA.

- ATCA: Australia Telescope Compact Array, six 22-m diameter steerable antennas, located at the Paul Wild Observatory near Narrabri, Australia.

- Effel: Effelsberg 100-m Radio Telescope, steerable 100-m diameter single dish, located near Effelsberg, Germany.

- GBT: Robert C. Byrd Green Bank Telescope, steerable 100×110-m single dish, located in Green Bank, West Virginia, USA.

- Lovell: Lovell (Mark I) Telescope, 76-m steerable single dish, located at Jodrell Bank Observatory, near Goostrey, Great Britain.
- LPA: Large Phased Array of the Pushchino Radio Astronomy Observatory, Pushchino, Russia
- Pleas: Mount Pleasant 26-m Antenna, steerable single dish, located at Mount Pleasant Radio Observatory, near Hobart, Tasmania.
- NRT: Large Nançay Radio Telescope, 200×40-m transit instrument, located in Nançay, France.
- Parkes: Parkes Observatory, 64-m steerable single dish, located near Parkes, Australia.
- VLA: NRAO Very Large Array, 27 25-metre antennas in a Y-shaped configuration, located on the Plains of San Agustin, New Mexico, USA.
- 42-m: National Radio Astronomy Observatory (NRAO) 42-m telescope, steerable single dish, closed as a user facility in 1999, located in Green Bank, West Virginia, USA.
- 91-m: NRAO 300-foot transit telescope, non-operational since 1988, previously located in Green Bank, West Virginia, USA.

The median observation from the summary of published sources of pulsar RMs in Table 3.1 was taken in the Southern Hemisphere at the Parkes Observatory, in 2008, at 1.4 GHz using 128 MHz bandwidth. The difference between the epoch of the observation and publication date ranges between 0 and 18 years. The method most commonly used for measuring pulsar RMs has been to fit the gradient of polarisation angle as a function of wavelength squared, described in Section 3.3.2. Whilst the earliest observations used the frequency of the sinusoidal variation in linearly polarised amplitude across the bandwidth to determine the RM (noted as sin in Table 3.1), RM-synthesis continues to be favoured in more recent observations (shortened to RM-syn in Table 3.1). Despite the fact that only 16 of the 55 studies listed in Table 3.1 corrected the RM for ionospheric Faraday rotation, RMs of individual pulsars in the ATNF catalogue are in general corrected for ionospheric Faraday rotation, as there is a greater number of pulsar RMs published from these particular papers. Examples of typical ionospheric Faraday rotation values

TABLE 3.1: Summary of pulsar RM measurements and references. Column 1 gives the abbreviation of the reference used in the RM catalogue presented in Table A.1 and also the ATNF pulsar catalogue (Manchester et al., 2005a). Columns 2–5 indicate the telescope(s), year(s), centre frequency(ies) and bandwidth(s) of the observations. Column 6 identifies the method used for obtaining the RM measurement(s): sinusoid (see Section 3.3.1), PA (see Section 3.3.2), or RM-synthesis (RM-syn, see Section 3.3.3). Columns 7–9 show whether the ionospheric RM was subtracted, the number of pulsar RMs measured and the full reference. Any information which was not stated is indicated as such by 'NS'. In the case of multi-frequency observations, multiple centre frequencies separated by a comma or a solidus indicates that the RM was measured using all frequencies, or the individual frequencies, respectively. Notes: $^{(a)}$ RMs measured for two pulsars in binary system J0737–3039. $^{(b)}$ average RM for pulsars A and B in globular cluster NGC6544. $^{(c)}$ three to nine data points taken within stated frequency range. $^{(d)}$ 4×7 MHz bandwidth recorded over a range of 100 MHz. $^{(e)}$ compilation of various parameters for 558 known pulsars up to 1993 from various (v) sources.

ID	Telescope	Year (YY)	ν (MHz)	$\Delta\nu$ (MHz)	Method	Ion	N_{PSR}	ref.
aaa+09d	GBT	08	2000	800	NS	N	1	(Abdo et al., 2009)
agr+11	GBT	09	1950	600	NS	N	1	(Arzoumanian et al., 2011)
ban14	GBT	11	820	200	PA	N	1	(Bangale, 2011)
bbb+13	Parkes	NS	732,1369,3100	256	PA	N	4	(Burgay et al., 2013)
blr+13	GBT	09	820	200	RM-syn	N	10	(Boyles et al., 2013)
ck03	ATCA	98	2496	128	PA	N	1	(Crawford and Keim, 2003)
ckr+12	GBT	NS	820,1500,2000	NS,NS,800	NS	N	1	(Camilo et al., 2012b)
cmh91	Parkes	87,88	600	30	PA	Y	16	(Costa et al., 1991)
cmk01	Parkes	97	660,/1350,/2264	32,128,128	NS	N	8	(Crawford et al., 2001)
cng+09	Parkes	08	1374	288	NS	N	1	(Camilo et al., 2009a)
crc+12	GBT	09,11	2000,5000,9000	800	NS	N	1	(Camilo et al., 2012a)
crj+07	Parkes	06	1400	256	PA	N	1	(Camilo et al., 2007)
crj+08	Parkes	07	2300,3200,6400	256	PA	N	1	(Camilo et al., 2008)
crr+09	GBT	09	800,2000	NS,700	NS	N	1	(Camilo et al., 2009b)
ct07	ATCA	99	1384	128	PA	N	2	(Crawford and Tiffany, 2007)
drb+04	GBT	03,04	820	28	PA	N	$2^{(a)}$	(Demorest et al., 2004)
efk+13	NRT,Effel,VLA	13	2540,4850&8350,8670	512,500,800	RM-syn	N	1	(Eatough et al., 2013b)
hmm+77	Parkes	76	283,656.5	10,17	NS	Y	1	(Hamilton et al., 1977)
hbo05	Parkes	04	685	64	RM-syn	N	1	(Hotan et al., 2005)
hl87	Lovell	NS	408,610	2	PA	Y	163	(Hamilton and Lyne, 1987)
hml+06	Parkes	99,00,03	1318.5/1375	90/256	RM-syn	Y	223	(Han et al., 2006)
hmq99	Parkes	96	436/660/1500	32/32/128	PA/RM-syn	Y	63	(Han et al., 1999)
hr09	Arecibo	90,92	50/111.5/130	0.625/2.5/2.5	PA	N	6	(Hankins and Rankin, 2010)
jhv+05	Parkes	04	1369,/3100	256,512	PA	Y	25	(Johnston et al., 2005)
jkk+07	Parkes	05	690,1369,3100	35,256,512	PA	N	22	(Johnston et al., 2007)
jw06	Parkes	05	1368,3100	256,1024	PA	Y	14	(Johnston and Weisberg, 2006)
kjb+12	Parkes	NS	1369	256	PA	N	12	(Keith et al., 2012)
kjk+08	ATCA	08	1400	128	NS	N	1	(Keith et al., 2008)
kjr+11	Parkes	NS	1352	340	NS	N	2	(Keith et al., 2011)
klm+00	Parkes	00	1374	64	PA	Y	1	(Kaspi et al., 2000)
lbb+10	Parkes	NS	1400	NS	NS	N	1	(Levin et al., 2010)
lbr+13	GBT	NS	350/820	50/NS	NS	N	5	(Lynch et al., 2013)
lfrj12	GBT	NS	2000	600	RM-syn	N	$1^{(b)}$	(Lynch et al., 2012)
lsf+06	Parkes	05	1400	256	PA	N	1	(Lorimer et al., 2006)
mac+02	Arecibo	NS	1475	100	NS	N	1	(McLaughlin et al., 2002)
man72	91-m	70,71	250–500$^{(c)}$	0.03/0.1/1	PA	Y	19	(Manchester, 1972)
man74	91-m/42-m	71,73	250–500$^{(c)}$	0.03/0.1/1	PA	Y	18	(Manchester, 1974)
mh04	Parkes	96,99,00	660,/1331	24,96	RM-syn	Y	9	(Manchester and Han, 2004)
mh11	Parkes	09–11	3100	1024	RM-syn	N	1	(Manchester and Hobbs, 2011)
mj95	Parkes	93,94	1400,4600,8300	NS	PA	N	2	(Manchester and Johnston, 1995)
mwkj03	Effel	01	1400	$100^{(d)}$	RM-syn	N	11	(Mitra et al., 2003b)
nbb+14	Parkes	01	1369	256	PA	N	4	(Ng et al., 2014)
njkk08	Parkes	06	1400	256	PA	N	150	(Noutsos et al., 2008)
nms+97	Parkes	96	438,660,1512	4,16,128	PA	Y	1	(Navarro et al., 1997)
ojk+08	Parkes	07	3100	1000	PA	N	1	(O'Brien et al., 2008)
qmlg95	Parkes	90	660,/1440	NS	NS	NS	26	(Qiao et al., 1995)
rl94	Lovell	87,88	3× ∼1400,1594,1652,1660	32	PA	N	27	(Rand and Lyne, 1994)
rrj01	Parkes	01	1517.5	256	NS	N	1	(Roberts et al., 2001)
s68	Jodrell	68	151.5,408	0.75	sinusoid	N	2	(Smith, 1968)
sj13	ATCA	13	17000	2000	PA	N	1	(Shannon and Johnston, 2013a)
skdl09	LPA	04,07	111	2.56	sinusoid	N	1	(Shitov et al., 2009)
sr69	91-m	68,69	112,234	5	sinusoid	N	2	(Staelin and Reifenstein, 1969)
tml93$^{(e)}$	v	v	v	v	v	v	237	(Taylor et al., 1993)
tpc+11	NRT	NS	1400/2100	128	NS	N	2	(Theureau et al., 2011a)
vdhm97	Parkes/Pleas	79,89,90,91	670,800,/950	NS	PA	Y	24	(van Ommen et al., 1997)
vs(a,b)70	LPA	69	86,105	0.84	sinusoid	Y	2	(Vitkevich and Shitov, 1970a,b)
wck+04	Arecibo	NS	430	5	RM-syn	Y	36	(Weisberg et al., 2004)
wj08	Parkes	NS	1400	256	PA	N	18	(Weltevrede and Johnston, 2008)
ymv+11	Parkes	07–09	1369	256	PA	Y	20	(Yan et al., 2011)

which were found ranged from –5 to –1 rad m^{-2} above the Parkes Observatory in the southern hemisphere (Han et al., 2006), and from 0.5 to 4 rad m^{-2} above the Arecibo Observatory in the northern hemisphere. The opposite signs of the ionospheric RM in the southern/northern hemisphere are simply due to the directionality of the Earth's magnetic field, also introduced in Chapter 4. The majority of the studies in Table 3.1 that did not correct the observed RM for ionospheric Faraday rotation may have been because, for example, the observed RM was simply required to de-rotate the Stokes Q and U parameters before summing in frequency to maximise the linear polarisation in the pulsar profile (Weltevrede and Johnston, 2008, e.g.), or the expected ionospheric RM was small or negligible in comparison to the errors on the measurement Hankins and Rankin (2010) and/or to the observed RM itself.

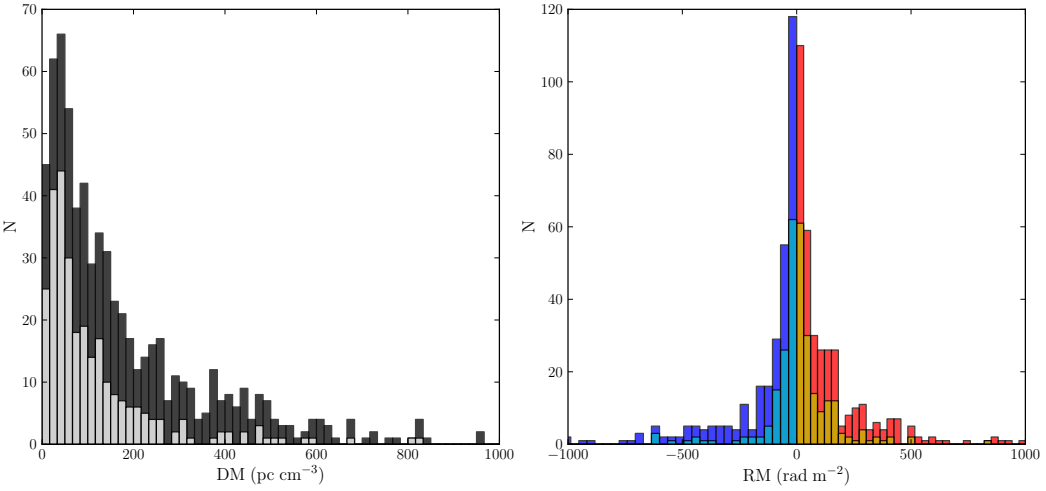

FIGURE 3.6: Histograms of DM (*left*) and RM (*right*) values for known pulsars with RMs from the ATNF pulsar catalogue. *Left:* DM values are shown for all pulsars with RM data (black), superimposed are the DM values for all pulsars with RM data which are located at least 300 pc above/below the Galactic plane (grey). *Right:* catalogue RM values for pulsars, red and blue colours represent positive and negative RM values, respectively. Superimposed are the RM values for all pulsars which are located at least 300 pc above/below the Galactic plane (yellow and cyan colours for positive and negative values respectively.

Histograms of the catalogue values of DM and RM for pulsars that have RM data are shown in Fig. 3.6. Of these 680 pulsars, 388 are located approximately within 300 pc of the Galactic plane, for which the lower quartile, median, mean, and upper quartile values of the DMs are 74, 161, 231, and 329 pc cm^{-3}, respectively. Of these 388 pulsars, 204 have a positive RM, with lower quartile, median, mean, and upper quartile values of 33, 102, 193, and 260 rad m^{-2}, respectively. The other 184 pulsars have negative RMs, with lower quartile, median, mean, and upper quartile values of –283, –83, –578,

and –29 rad m^{-2}, respectively. The pulsars that are located at least 300 pc from the Galactic plane have lower quartile, median, mean, and upper quartile DM values of 35, 67, 117, and 145 pc cm^{-3}, respectively. The majority of these values are lower, compared to those for pulsars within 300 pc of the Galactic plane, because the electron density is expected to exponentially decrease with distance from the Galactic plane. The lower quartile value is higher because the closest pulsars at least 300 pc from the Galactic plane are further away, and therefore have larger DMs, compared to those within 300 pc of the Galactic plane. Of these 292 pulsars, 162 have a positive RM, with lower quartile, median, mean, and upper quartile values of 18, 49, 91, and 139 rad m^{-2}, respectively. The other 130 pulsars have a negative RM, with lower quartile, median, mean, and upper quartile values of –79, –36, –100, and –12 rad m^{-2}, respectively. These values are also less than half those found for pulsars which are within 300 pc of the Galactic plane, which is also expected due to the decrease in electron density and magnetic field strength with distance from the Galactic plane.

The largest negative RM value in the catalogue is –66,960(50) rad m^{-2} towards PSR J1745–2900 (Eatough et al., 2013b), which is the closest known pulsar to the Galactic centre (ℓ,b=359.94°,–0.05°), and has an RM of the same order of magnitude as Sagittarius A* = –4.3(1)×10^5 (Bower et al., 2003). This pulsar also has the largest DM of any known pulsar, 1,778(3) pc cm^{-3}. The largest positive RM value in the catalogue is 2,400(30) rad m^{-2} towards J1410–6132 (O'Brien et al., 2008), which is a young, highly energetic pulsar also in the Galactic plane 47.7 degrees from PSR J1745–2900 (ℓ,b=312.20°,–0.09°, d = 8 kpc) and is located approximately in the Scutum-Centaurus spiral arm, near the tangent between the arm and our LOS in Galactic quadrant IV, see Fig. 1.6. The second largest negative RM value in the catalogue, –2,993(50) rad m^{-2} (Camilo et al., 2012a), is towards the extreme-nulling PSR J1841–0500, which is located approximately in the same Scutum-Centaurus arm, except on the opposite side of the Galaxy, near the tangent between the arm and our LOS in Galactic quadrant I (ℓ,b= 27.32°,–0.03°, $d \approx 6.77$ kpc). This already gives the impression of a large-scale counter-clockwise magnetic field in the Scutum-Centaurus Arm (also demonstrated in, e.g., Van Eck et al., 2011). This is shown in Fig. 3.7, where the catalogue RMs towards pulsars are plotted as a function of Galactic longitude, whose distances dissect the Galaxy's spiral arms at various distances. The trend in Fig. 3.7 also shows that PSRs J1745–2900 and J1841–0500 may be outliers, and therefore the direction of the GMF in the rest of

the spiral arms may be opposite to that in the Scutum-Centaurus Arm, i.e., clockwise, (also demonstrated in, e.g., Van Eck et al., 2011).

The minimum positive and negative RMs in the catalogue are 0.0(4) rad m^{-2} towards PSR J0437–4715 (Yan et al., 2011), and –0.1(12) rad m^{-2} towards PSR J1633–2009. The millisecond pulsar PSR J0437–4715 also has a very small DM value of 2.64476(7) pc cm^{-3} (Verbiest et al., 2008), which is expected due to its location towards high Galactic latitude and being relatively close to the Sun (ℓ,b= 253.39°, −41.96°, d = 0.16 kpc). Pulsars like this can probe the relatively small GMF strength and direction within the Solar neighbourhood. However, the normal pulsar PSR J1633–2009 has a relatively large DM, 48.19(6) pc cm^{-3}, and distance, ≈2.76 kpc, but it located approximately 870 pc from the Galactic plane. Pulsars like this provide a probe of the relatively small GMF strength and direction towards the Galactic halo.

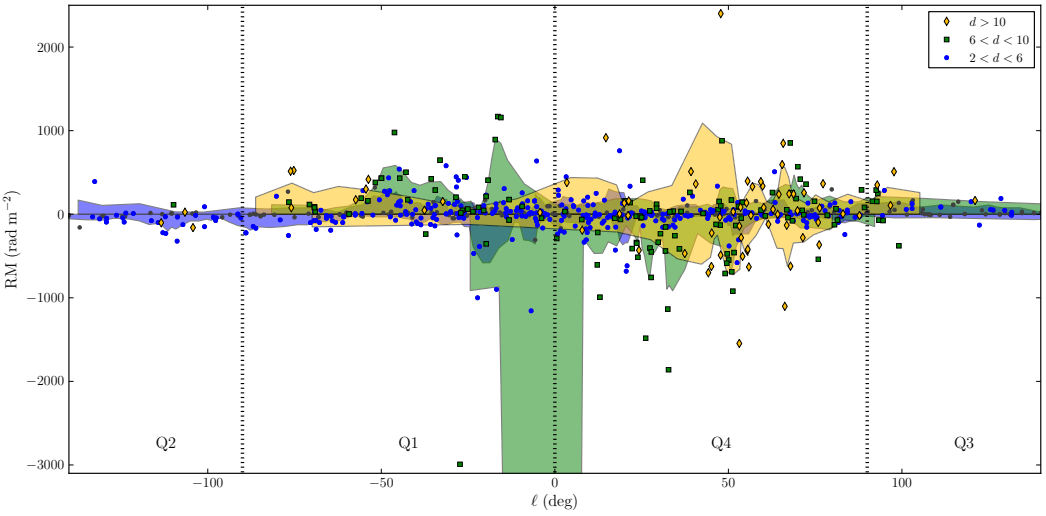

FIGURE 3.7: The catalogue RMs towards pulsars as a function of Galactic longitude. All pulsars with RMs that are located between approximately 2 and 6 kpc from the Sun are shown as blue points, pulsars that are located between approximately 6 and 10 kpc from the Sun are shown as green squares, and pulsars that are located over 10 kpc from the Sun are shown as yellow diamonds. The area between the moving averages of the positive and negative RMs are shown as the shaded regions of the same colour as the points.

To investigate the agreement between RMs for pulsars with two or more independent measurements, the catalogue RM was compared to the alternative RM measurements collected in Table A.1. Figure 3.8 shows the comparison between the absolute values of the RM to the same source from the ATNF pulsar catalogue with one or more alternative RMs collected from the literature. The data generally fit the expected trend, i.e.,

that the independent RM measurements are consistent. This indicates that many of the RMs determined are reliable because repeating the observations with different telescopes, epochs, and/or frequencies produces approximately the same RM, within uncertainties. There are however a number of notable outliers which are evident both in the left panel for all pulsars and also in the right panel for pulsars with absolute RMs in the range 0–150 $\mathrm{rad\,m^{-2}}$. The reasons for the disparity between measurements due to the observation and/or data analysis may include: underestimated uncertainties, although for some of the outlying points in Fig. 3.8 these are required to be approximately equal to the absolute RM value in order to fit the expected trend; neglecting to correct for ionospheric Faraday rotation, although this would result in a minor correction approximately less than 10 $\mathrm{rad\,m^{-2}}$, although this depends on the time of year, geographic location, etc. (Sotomayor-Beltran et al., 2013); systematic uncertainties introduced when determining the RM using the polarisation angle gradient method, Section 3.3.2, opposed to the RM-synthesis method, Section 3.3.3. The disparity between independently measured RMs may be because of variability with time, either due to properties of the source or due to the ISM. There may be intrinsic variations in the balance between quasi-orthogonal polarisation emission modes in the pulsar magnetosphere. For example, Weisberg et al. (2004) found RM variations between 0 and 39 $\mathrm{rad\,m^{-2}}$ in 19 pulsars between two epochs, see also Fig. 3.9. There may be variations in the magnetic field and/or electron density along the LOS (either intrinsic to the LOS, or due to the proper motion of the pulsar 'illuminating' a different LOS in the ISM). Frequency-dependent scattering, which introduces an exponential scattering tail to the pulsar profile, could affect the observed polarisation angle in a frequency-dependent, and perhaps time-dependent, way (e.g. Noutsos et al., 2009).

The most extreme outlying data point in the left plot of Figure 3.8 represents PSR J1413–6141 which has two RM measurements which disagree by more than 7σ: –35(10) $\mathrm{rad\,m^{-2}}$ (Han et al., 2006) and –400(40) $\mathrm{rad\,m^{-2}}$ (Johnston and Weisberg, 2006). The observations were conducted at similar frequencies and although published in the same year, the independent observation epochs are in fact separated by approximately 5 years. Both of the studies corrected for the ionospheric Faraday rotation, and even if this was not the case, the ionospheric RM could not account for such a large difference, see Chapter 4. It is noted that the pulsar profile shows a small linear polarisation fraction and is also scatter broadened at 1.4 GHz (Johnston and Weisberg, 2006). Although the pulse

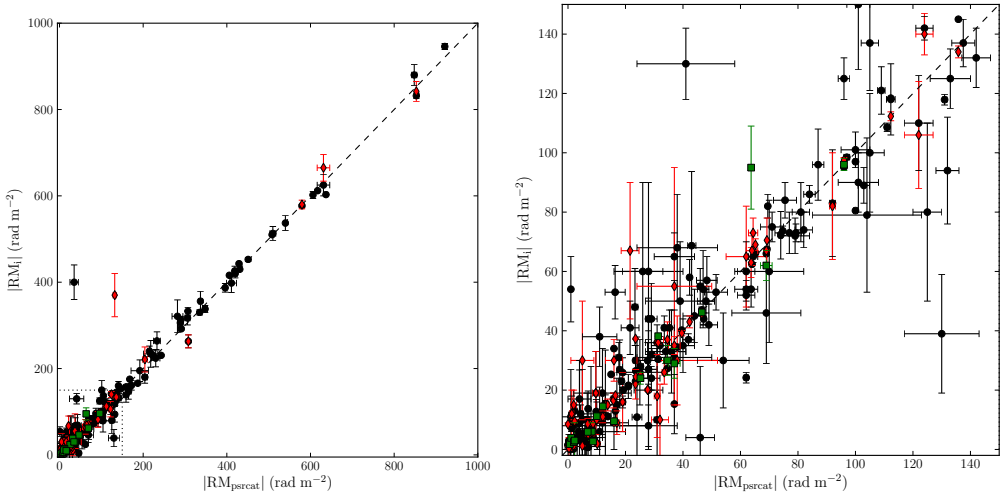

FIGURE 3.8: Comparison of catalogue RMs (x-axis) with independent RMs obtained from the literature (y-axis), see Table A.1 caption for data and references. There are 680 pulsars with an RM published in the catalogue; 215 for which one further published RM was found (black circles), 62 for which a second further published RM was found (blue diamonds) and 18 for which a third published RM was found (red squares). The absolute RM values are shown and the expected $|\mathrm{RM_{psrcat}}|=|\mathrm{RM_i}|$ line is also shown for ease of comparison. *Left:* All pulsars with two or more published RMs in the literature, *right:* 78% of these pulsars for which the absolute RM values are below 150 rad m^{-2}.

profile consists of a single component, these facts may have introduced further uncertainty in aligning the profiles between 1.4 GHz and 3.1 GHz based on peak intensity in Johnston and Weisberg (2006). However, it is most likely that scatter broadening at 1.4 GHz affects the polarisation angle in a frequency dependent way, also affecting the RM measured at this frequency (Noutsos et al., 2009).

PSRs J1412–6145 and J1413–6222 are located at an angular separation of 0.14 and 0.68 degrees from J1413–6141, respectively, with DMs of 514.70 and 808.10 pc cm^{-3}, respectively. J1412–6145 has two measured RMs which are –39(20) rad m^{-2} (Han et al., 2006) and $-130(13)$ rad m^{-2} (Johnston and Weisberg, 2006) and the RM measured towards J1413–6222 is –490(8) rad m^{-2} (Han et al., 2006). If no field reversals are present within the LOS to this small angular region, the DMs and absolute RMs of pulsars located further from the Sun are expected to increase. Since both the DM and absolute RM of J1413–6222 are larger than that for J1413–6141, this provides a good check to the higher RM from (Johnston and Weisberg, 2006) towards J1413–6141. The DM of J1412–6145 is smaller, and may also provide an insight to the lower limit placed on the RM of J1413–6141 from the (Han et al., 2006) measurement. However, this pulsar also has two RMs which differ by 3σ, represented by the black point in the lower right of Fig. 3.8, *right.*

The lower absolute measured RM is larger than the (Han et al., 2006) value for J1413–6141, and increases the difficulty in drawing a conclusion. The RMs for this pulsar may also differ like those for J1413–6141 because the pulse profile of J1412–6145 observed at 1.4 GHz (Manchester et al., 2001) also shows some scatter broadening. Therefore, re-observing both J1413–6141 and J1412–6145 to obtain further RMs for comparison would be interesting. However, these sources are not visible from the telescopes in the northern hemisphere used in this work and hence the mean of the RM measurements will be used in the further analysis, along with the larger measurement uncertainty; –218(40) rad m^{-2} for J1413–6141 and –85(20) rad m^{-2} for J1412–6145.

Another particularly obvious outlier in the left plot of Figure 3.8 is the blue point which represents PSR B1110–65 (J1112–6613). This pulsar has three independent RM measurements, two of which agree within 2σ: –132(4) and –94(18) rad m^{-2} from Noutsos et al. (2008), Han et al. (2006), respectively, using similar observational frequencies but observing epochs five years apart. The third measured RM, –370(50) rad m^{-2} (Costa et al., 1991), is greater than 4σ from the two more recent observations. The change in polarisation angle across the observing band for the (Costa et al., 1991) observations at 600 MHz and 30 MHz bandwidth, 0.025×RM radians, is larger than for the Noutsos et al. (2008) observations at 1.4 GHz with 256 MHz bandwidth, 0.017×RM radians, and therefore should provide more accurate RMs. However, the fractional linear polarisation of 11% was the third lowest in the (Costa et al., 1991) sample and the polarisation error quoted was the largest. The closest pulsar to PSR B1110–65 in terms of angular distance is PSR J1112–6103, 5.2 degrees away, and has a DM which is 2.4-times that of B1110–65 and also an RM which is the opposite sign, providing little insight. Hence, the most precise RM from Noutsos et al. (2008) will be used in further analysis.

The most extreme outlier in the upper left in Fig. 3.8 *right*, is PSR J1809–1917. This pulsar has a DM = 197.1(4) pc cm^{-3} and two published RMs which differ by 3σ: 41(17) rad m^{-2} (Weltevrede and Johnston, 2008), and 130(12) rad m^{-2} (Han et al., 2006). PSR J1809–1943 is the closest pulsar in terms of angular distance, within 0.44 degrees, with DM and RM values of 178(5) pc cm^{-3} and 76(4) rad m^{-2}, respectively, (Camilo et al., 2007). Given the DMs of PSRs J1809–1917 and J1809–1943, the distance to these pulsars is approximately 3.71 kpc and 3.60 kpc, respectively. Hence, if the large-scale magnetic field is approximately the same in the direction to both pulsars, we expect the RM of PSR J1809–1917 to be larger than that for PSR J1809–1943. Consequently, for

PSR J1809–1917 the average of the two RM values and the largest error, $86(17)\,\mathrm{rad\,m^{-2}}$, will be used for the further analysis.

For pulsars with more than one published RM, there are 23 for which the direction of the magnetic field, i.e., the sign of the RM, are in disagreement between one or more independent measurements. These pulsars most commonly have relatively small absolute RM values: the mean and median maximum catalogue RMs for these 23 pulsars is $18\,\mathrm{rad\,m^{-2}}$ and $7\,\mathrm{rad\,m^{-2}}$, respectively. For half of these pulsars, the sign discrepancy can be accounted for by the combined errors in the RM measurements. Further discrepancies could also be attributed to failing to correct for ionospheric Faraday rotation, or to combine the error in the ionospheric model with the measurement uncertainty. The maximum absolute RM for which there is a sign discrepancy is $165.0\,\mathrm{rad\,m^{-2}}$ – which cannot be explained by measurement error, or lack of ionospheric calibration, but may be due to use of the wrong sign convention for one of the measurements.

There is some evidence that the RM of some pulsars may not remain constant over time (e.g. Han et al., 1999), either due to the transverse velocity of the pulsar with respect to the Earth resulting in a slight change in the LOS electron density and/or magnetic field, or due to fundamental changes in linear polarisation emission from the pulsar itself (Weisberg et al., 2004). The RMs for four pulsars with the largest number of catalogued RMs presented in Table A.1 are shown in Fig. 3.9 against time. Indeed, it appears that for all of the pulsars there is some variance in the RM determined from independent observations separated by several years.

The RM data towards PSR B0329+54 (J0332+5434) over five observing epochs from 1968 to 1987 are shown in the top left panel of Fig. 3.9. The measurement from the first epoch was regarded as an outlier. Applying a weighted least squares linear fit to the data result in a gradient of $0.4(20)\,\mathrm{rad\,m^{-2}\ year^{-1}}$, which is consistent with no change in the RM over time. Unfortunately, no measurements after 1987 were identified from the literature, which could have provided a larger time range with which to investigate this. Since this is a very bright pulsar, the RM towards PSR B0329+54 was measured from observations in this work and is further discussed in Section 5.5.2. PSR B0329+54 is also identified to be a mode-changing pulsar (e.g. Chen et al., 2011), where the fractional polarisation and polarisation angles are dependent on the intensity of pulse profile

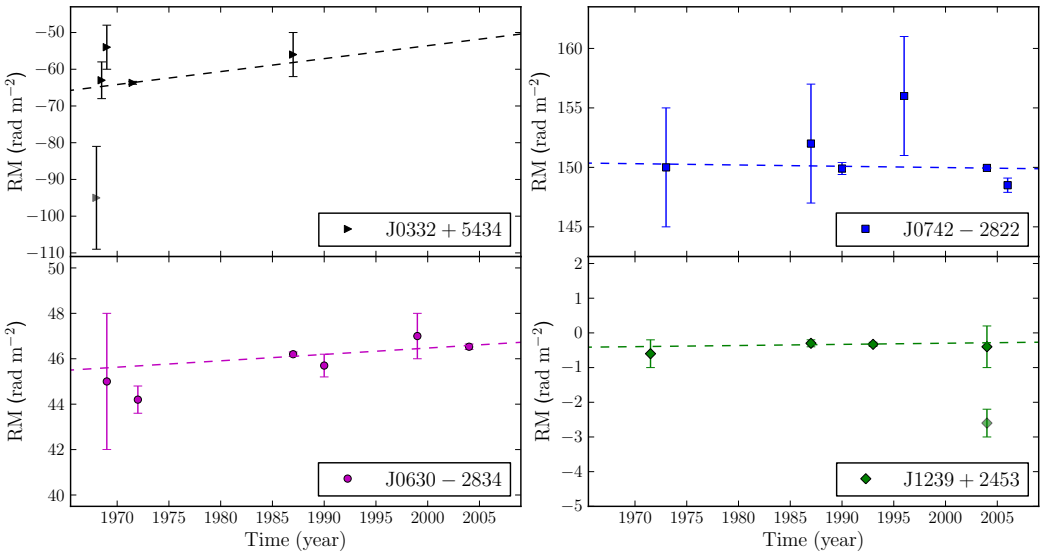

FIGURE 3.9: The RMs collected from Table A.1 are shown against observation epoch (in years) for four selected pulsars with at least five measurements collected from the literature. Where the observation date(s) were not specified, the date of the paper publication was used. Where multiple observation epochs were stated, the average date was used for the plot. The data are shown as points and the weighted least squares fits are shown as dashed lines. Outlying data points for PSRs J0332+5434 and J1239+2453 are shown as a lighter colour and are not included in the weighted least squares linear fit.

components (Mitra et al., 2007). The presence of emission modes may cause the polarisation properties to change over time, or different proportions of modes may affect the resulting RM measurement over time, and is an interesting area of investigation in future.

The RMs towards PSR B0628–28 (J0630–2834) measured between 1969 and 2004 are shown in the lower left of Fig. 3.9. Interestingly, for this particular pulsar, the weighted least-squares linear fit yields an increase in RM at a rate of of 0.0281(4) rad m^{-2} year^{-1}. PSR B0628–28 is a relatively slow pulsar with $P = 1.2444$ s, DM = 34.468(17) pc cm^{-3}, and below-average transverse velocity of 77.29 km s^{-1}, based on the distance of 0.32 kpc from the Sun. No change in DM with time was detected from monthly timing data taken at 1.4 GHz using the Parkes radio telescope, although an upper limit of 0.1 pc cm^{-3} year^{-1} was determined (Petroff et al., 2013). This small (linear) increase in RM may be tracing small changes in the LOS magnetic field as there are no catalogued structures near the pulsar, such as nearby Galactic supernova remnants[2] (Green, 2009). Therefore,

[2] A catalogue of Galactic supernova remnants available at http://www.mrao.cam.ac.uk/surveys/snrs/

this source seems interesting for RM and DM monitoring using lower-frequency observations in future work, as the declination of –28°34´42˝.7 is very close to the limiting declination of the radio telescopes used in this work.

The RMs towards PSR B0740−28 (J0742−2822) measured on six epochs between 1973 and 2006 are shown in the upper right of Fig. 3.9. The RMs measured toward this pulsar have a significant range of 7.5 rad m^{-2}, although this is only 5% of the average RM value (151.06 rad m^{-2}). The weighted least squares linear fit does not indicate a significant long-term change in RM over time, -0.01(5) rad m^{-2} year^{-1}. No change in DM with time was detected from monthly timing data taken at 1.4 GHz using the Parkes radio telescope, and a more stringent upper limit than for PSR B0628–28 was determined, 0.02 pc cm^{-3} year^{-1} (Petroff et al., 2013).

The RMs measured towards PSR B1237+25 (J1239+2453) using observations taken between 1971 and 2004 are shown in the lower right of Fig. 3.9. Four of the data points have a small range, 0.3 rad m^{-2}, although this is 90% of the catalogue value, −0.33(6) rad m^{-2}. There appears to be one outlier at –2.6(4) rad m^{-2} (Johnston et al., 2005), which was taken using Parkes radio telescope in the Southern Hemisphere. The most plausible explanation for this discrepancy is that the ionospheric Faraday rotation was not fully corrected. However, like PSR B0329+54, PSR B1237+25 is also identified to show three modes with differing polarisation characteristics (e.g. Smith et al., 2013). Neglecting this outlier, the weighted least squares fit shows no significant change in RM over time, 0.003(3) rad m^{-2} year^{-1}.

3.5 Catalogue of rotation measures towards extragalactic sources

Table 3.2 shows a summary of the published data for 39631 extragalactic (EG) point sources. These references are also summarised in Oppermann et al. (2012), who collected 41330 data points for EG point source RMs, although some of the data are not yet published, and also includes a number of smaller surveys (N<20), most commonly observed in the Northern sky and are not included in this work. The RMs towards EG sources are highly complementary to the pulsar RMs as they provide information about the magnetic field parallel to the entire LOS through the Galaxy.

The radio telescopes which were used for observing the EG sources in the RM catalogue listed in Table 3.2, and were not included in the previous list for the pulsar observations, are listed in alphabetical order:

- DRAO: DRAO Synthesis Telescope, seven (2×9.14-m and 5×8.53-m diameter) equatorially-mounted antennas on an east-west baseline, located at Dominion Radio Astrophysical Observatory, near Okanagan Falls, Canada.
- WSRT: Westerbork Synthesis Radio Telescope, 14 equatorially mounted 25-m antennas in an East–West linear configuration spanning 2.7 km near Westerbork, The Netherlands.

TABLE 3.2: Summary of RM measurements for EG sources and references. Column 1 gives the reference ID in alphabetical order. Columns 2–6 indicate the telescope, survey name (if applicable), year(s), centre frequency(ies) and bandwidth(s) of the observations. Columns 7–10 show the RM measurement method, whether the ionospheric RM was subtracted, the number of data points and the references for the data and the survey (if applicable). Any information which was not stated is indicated by 'NS'. Notes: $^{(a)}$ compilation of EG sources from ten previously published catalogues, hence various (v) telescopes, frequencies and bandwidths were used, the frequency range given states the lowest and highest observing frequencies in the catalogue. $^{(b)}$ although not corrected, $1\,\mathrm{rad\,m^{-2}}$ added in quadrature to the measurement uncertainty. $^{(c)}$ data were acquired from text files compiled by Jo-Anne Brown and retrieved from http://www.ras.ucalgary.ca/ jocat/RMData.

ID	Telescope	Survey	Year (YY)	ν (MHz)	$\Delta\nu$ (MHz)	Method	Ion	N	ref.
b88$^{(a)(c)}$	v	v	75–88	936–15000	v	PA	N	674	(Broten et al., 1988)
bhg+07$^{(c)}$	ATCA	SGPS	98–01	1336–1432	12×8	PA	N	148	(Brown et al., 2007) (Haverkorn et al., 2006)
btj03$^{(c)}$	DRAO	CGPS	NS	1420	35	PA	N	380	(Brown et al., 2003) (Taylor et al., 2003)
c92$^{(c)}$	VLA		86	1385.1–1664.9	6×12.5	PA	N	56	(Clegg et al., 1992)
gdm01$^{(c)}$	ATCA	SGPS test	97,98	1384	96	PA	N	21	(Gaensler et al., 2001) (McClure-Griffiths et al., 2001)
hbe09	WSRT	WSRT-SINGS	03	1366,1697	132	RM-syn	Y	57	(Heald et al., 2009a) (Braun et al., 2007)
mgh+10	ATCA	South Galactic pole	06,08	1384,2368	128	RM-syn	N$^{(b)}$	341	(Mao et al., 2010)
mgs+08	ATCA	SMC	04	1384	128	PA	N	70	(Mao et al., 2008)
ms96$^{(c)}$	VLA		93	1360,1427.5,1507.5,1638	25	PA	Y	38	(Minter and Spangler, 1996)
ow95$^{(c)}$	VLA		90,92,93	1385–1665,4835,4885	4×50/25,25,25	PA	Y	61	(Oren and Wolfe, 1995)
tss09	VLA	NVSS	93–96	1364.9,1435.1	42	PA	N	37543	(Taylor et al., 2009) (Condon et al., 1998)
vbs+11$^{(c)}$	VLA		08	1365,1485	25	PA,RM-syn	N	194	(Van Eck et al., 2011)

Table 3.2 shows that the published sources of EG RMs are highly dominated by those obtained from the NVSS survey observed with the VLA at L-band Taylor et al. (2009). The summary also shows the difference between the epoch of the observations and publication date ranges between 2 and 13 years. Similarly for the pulsar data, the method most commonly used for measuring RMs has been to fit a gradient to the

polarisation angle as a function of wavelength squared, although RM-synthesis is more increasingly used in recent observations. For example Mao et al. (2010) note that the FWHM of their 'dirty beam' in RM-synthesis is 99 rad m^{-2}. The EG RMs were most commonly not corrected for ionospheric Faraday rotation, the main reason for which was that measurement uncertainties were comparable or larger and in some cases the measurement uncertainty was increased accordingly. In Minter and Spangler (1996) it is noted that calibration for ionospheric Faraday rotation led to a factor of two decrease in both the rms variations in polarisation angle and the noise level of Stokes Q and U images.

The positions and values of the EG RMs collected are shown in Fig. 3.10: yellow through orange to red colours indicate increasingly positive RMs, and green through cyan to royal blue indicate increasingly negative RMs.

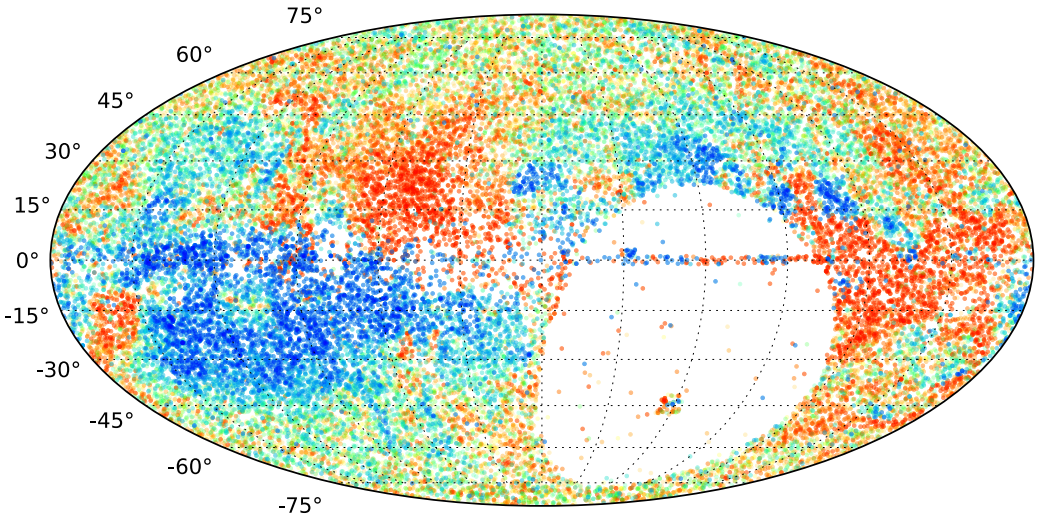

FIGURE 3.10: The locations of extragalactic source RMs collected for this work on the sky. Yellow through orange to red colours represent increasingly positive RMs whilst green through cyan to blue colours represent increasingly negative RMs. The references of the data are summarised in Table 3.2. Galactic coordinates are shown using the Mollweide projection, centred on the direction towards the Galactic Centre, i.e., ℓ=0°.

Figure 3.10 visualises much information about the entire LOS through the Galaxy provided by EG RMs. There are 20372 positive and 18953 negative RM values shown, with median values 19.8 rad m^{-2} and –23.3 rad m^{-2}, respectively. The absolute RM values are high towards the Galactic plane (b<45°) and decrease toward the Galactic poles (b>45°). Despite poorer sampling of EG RMs in part of the Southern sky, there

are notably large regions of positive RMs ($0° < \ell < 90°$,$0° < b < 45°$, $210° < \ell < 240°$,-$30° < b < 15°$) and large regions of negative RMs ($0° < \ell < 150°$,$0° < b <$-$30°$ and $240° < \ell < 360°$,$15° < b < 45°$), (see Oppermann et al., 2012, for further discussion).

The positions and values of the collected RMs towards pulsars and EGs are shown in Fig. 3.10: yellow through orange to red colours indicate increasingly positive RMs, and green through cyan to royal blue indicate increasingly negative RMs. This shows that the RMs from both sources are very complimentary. The pulsars provide three-dimensional probes of the GMF, mostly in the Galactic disk, whilst EGs provide information about the entire LOS through the Galaxy's halo.

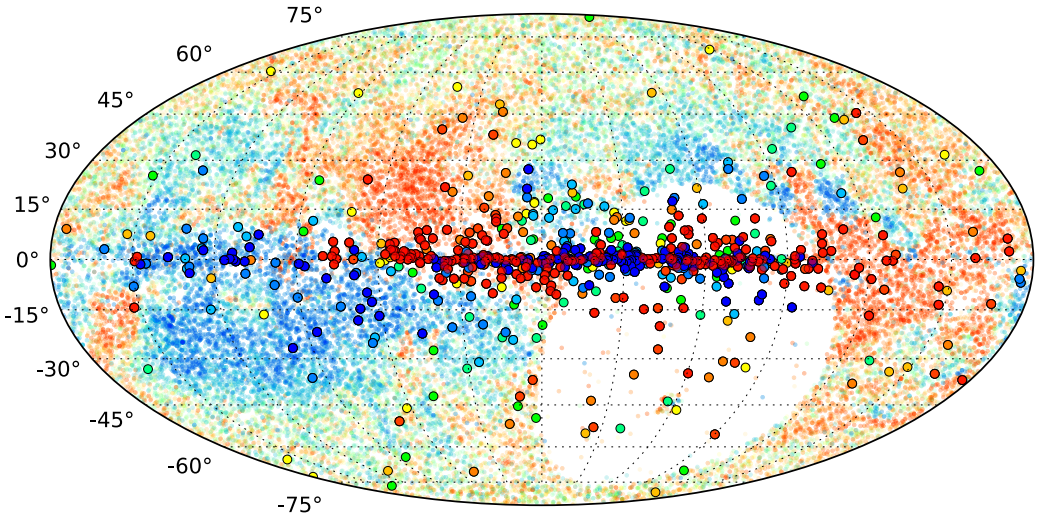

FIGURE 3.11: The distribution of extragalactic sources (points) and pulsars (circles) for which there are published RMs on the sky. Yellow through orange to red colours represent increasingly positive RMs whilst green through cyan to blue colours represent increasingly negative RMs. Both pulsar and extragalactic points are plot using the same colour scale, the references for which are included in Tables 3.1 and 3.2. Galactic coordinates are shown using the Mollweide projection, centred on the direction towards the Galactic Centre, i.e., ℓ=0°.

3.6 Conclusions

EG and pulsar RMs provide very complimentary information. EG RMs are more numerous (39631) than pulsar RMs (680), especially towards the halo of the Galaxy and provide a LOS through the entire extent of the Galaxy and also IGM (although this contribution is a small fraction of the observed RM). Pulsars are more numerous in the Galactic disk and are also distributed at various distances from the Sun, providing

three-dimensional information, mainly in the Galactic disk at intermediate distances. It is desirable to increase the number of known pulsars with RM data – currently 30% of all known pulsars have published RMs – in order to improve the knowledge of the Galactic magnetic field towards these LOSs, especially in sparsely sampled areas of the Galaxy.

RM-synthesis is the preferable method to use to determine RMs from observational data because the polarisation information across the entire observing bandwidth is used, the $n\pi$ ambiguity is minimised, and it relaxes the assumption that there is a single RM towards the LOS.

It is essential to correct RM data for ionospheric Faraday rotation, especially to realise the accuracy in measurements that can be achieved using low-frequency data. This is explored further in Chapter 4.

An interesting area of work in future will be to monitor the ionosphere-corrected RMs towards high transverse-velocity pulsars over monthly to yearly timescales using low-frequency observations to investigate whether there are variations in RMs, and to investigate whether these are correlated with changes in DM.

Chapter 4

Correcting for ionospheric Faraday rotation

4.1 Abstract

Faraday rotation measurements using the current and next generation low-frequency radio telescopes will provide a powerful probe of astronomical magnetic fields. However, achieving the full potential of these measurements requires accurate removal of the time-variable Faraday rotation contribution due to the ionosphere – also a magnetised plasma. We present a code that calculates the amount of ionospheric Faraday rotation for a specific epoch, geographic location, and line-of-sight, using publicly available, GPS-derived total electron content maps and the most recent release of the International Geomagnetic Reference Field. We describe applications of this code for the calibration of radio polarimetric observations, and demonstrate the high accuracy of the modelled ionospheric Faraday rotations using LOFAR pulsar observations. These show that we can accurately determine some of the highest-precision pulsar rotation measures ever achieved. Precision rotation measures can be used to monitor rotation measure variations – either intrinsic or due to the changing line-of-sight through the interstellar medium. This calibration is particularly important for nearby sources, where the ionosphere can contribute a significant fraction of the observed rotation measure. We also discuss the importance of ionospheric Faraday rotation calibration for the emerging generation of low-frequency radio telescopes, such as the SKA and its pathfinders.

Much of the contents of this chapter were published in Sotomayor-Beltran, C., Sobey, C., et al., "Calibrating high-precision Faraday rotation measurements for LOFAR and the next generation of low-frequency radio telescopes", Astronomy & Astrophysics, Volume 552, id.A58, 13 pp. (2013). The code for calculating ionospheric Faraday rotation was written by Carlos Sotomayor-Beltran. The results from LOFAR observations of pulsars, and comparisons with the results output from the ionospheric Faraday rotation code to test its accuracy and reliability for the purpose of correcting Faraday rotation measurements, were performed by the author of this thesis.

4.2 Introduction

The ionosphere is the photoionised layer in the upper atmosphere of the Earth. The Sun is the main source of extreme ultra-violet and X-ray radiation that causes electrons to be ejected from gaseous atmospheric atoms. To a lesser extent, ionisation is also produced by energetic particles in the solar wind and cosmic rays. The ionisation degree in the ionosphere is therefore highly dependent on Solar activity (e.g. Wells, 1943). Thus, there are position- and time-dependent variations on diurnal, seasonal and solar-cycle time-scales. The extent of the ionosphere is between approximately 50 km and 1000 km above the surface of the Earth, within which there are several layers. Radio-wave propagation is most affected by the F-layer, between approximately 200 km and 500 km above the surface of the Earth, see Fig. 4.1. This layer is persistent and is the location of maximum electron content in the ionosphere during the day. There are also several well-known ionospheric anomalies, including the persistent winter anomaly (daytime plasma density in the F-layer is greater in winter than in summer, Lee et al., 2011) and equatorial anomaly (an excess of electrons approximately 20 degrees above and below the magnetic equator due to the equatorial fountain effect, Appleton, 1946).

The ionosphere interacts with radio frequency radiation via its free electrons in several ways, including reflection, absorption, refraction, and Faraday rotation. The ionospheric electron density, $n_{\rm e}$, affects the refractive index, n, dominating electromagnetic wave propagation,

$$n = \sqrt{1 - \frac{\nu_{\rm p}}{\nu}}, \tag{4.1}$$

where the plasma frequency, $\nu_{\rm p}$, is:

$$\nu_{\rm p} = \sqrt{\frac{e^2 n_{\rm e}}{\pi m_0 \varepsilon_0}} = 0.00898\sqrt{n_{\rm e}}\ {\rm Hz}, \tag{4.2}$$

and electron density is measured in m^{-3}. Equation 4.1 dictates the approximate lowest frequency observable from the ground because waves with frequency, ν, less than the plasma frequency, $\nu_{\rm p}$, result in an imaginary refractive index and wave propagation is inhibited. The electron density in the ionosphere is variable depending on solar activity. Therefore, at times of lower solar activity and thus ionospheric electron density (night, autumn, solar minimum), $n_{\rm e}$ $\approx 1\times10^{17}$ electrons/m^{-3} and $\nu_{\rm p}$ $\approx$3 MHz. In contrast, at times where solar activity and thus ionospheric electron density is higher (day, spring, solar maximum), $n_{\rm e}$ $\approx 80\times10^{17}$ electrons/m^{-3} and $\nu_{\rm p}$ $\approx$25 MHz. Consequently, this disadvantage for detecting astronomical signals at low frequency becomes an advantage for communications, where the ionosphere is used to reflect low-frequency radio waves over large distances beyond the radio horizon of the transmission sites.

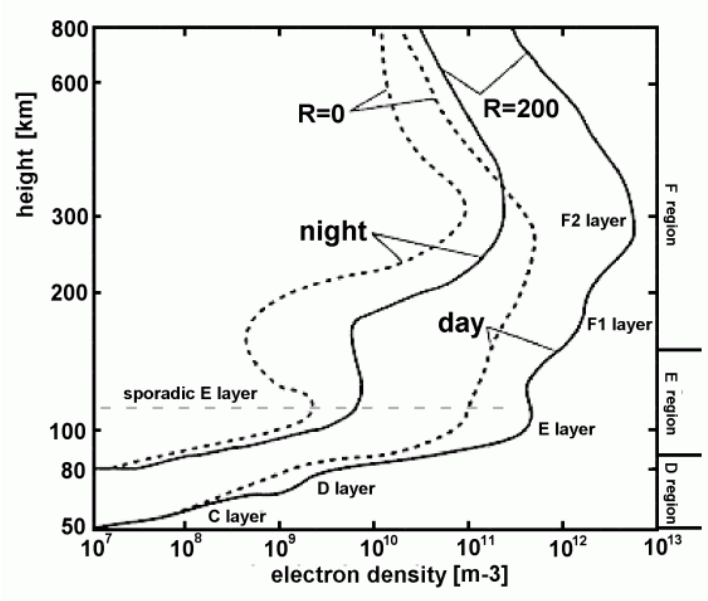

FIGURE 4.1: Typical day and night altitude profiles of the electron density in the ionosphere, where 'R' represents the monthly median solar index. Image courtesy of the Roma2 department of Instituto Nazionale di Geofisica e Volcanologia (http://roma2.rm.ingv.it/en/research_areas/4/ionosphere).

The D-layer in the ionosphere, at a height of approximately 60 km to 90 km above the surface of the Earth, becomes ionised during the day, mostly due to Lyman series-alpha hydrogen radiation (121.5 nm wavelength) ionising nitric oxide (NO). This layer

is responsible for absorption of radio waves within the High Frequency (HF) band (3−30 MHz) and the low-end of the Very High Frequency (VHF) band (30−300 MHz). The LOFAR Low Band Antennas (LBAs), although optimised for receiving 30 MHz to 80 MHz signals, are able to observe the sky from 10 MHz. Therefore, these lowest frequencies can be severely affected by both the minimum usable frequency of the ionosphere and also absorption.

The focus of this chapter is Faraday rotation caused by the ionosphere, which has a notable affect across the range of LOFAR's observing frequencies. Assuming typical values for the ionospheric electron density, $\sim 1.5 \times 10^{17}$ electrons/m^{-3}, and geomagnetic field (parallel to the line of sight), $\sim$0.25 G, the resulting Faraday depth of the ionosphere is 1 rad m^{-2}, shown by Eq. 1.12. Taking the centre of the LOFAR High Band Antenna (HBA) frequency range, 150 MHz ($\sim$2 m wavelength), the additional rotation of the polarisation angle imparted by the ionosphere will be 228.9°. At the centre of the LOFAR optimised LBA frequency range, 55 MHz ($\sim$5.5 m wavelength), the additional rotation of the polarisation angle is even greater, 1702.3°. Although the rotation of the polarisation angle is less pronounced across the recorded bandwidth at higher frequencies, the Faraday depths towards sources are systematically affected by the ionosphere. The direction of the geomagnetic field is such that ionospheric Faraday rotation has a positive contribution to the total Faraday depth of a source observed from the northern hemisphere, and a negative contribution when observed from the southern hemisphere.

The ionosphere has been observed to change on timescales that are often shorter than the length of an astronomical observation. For example, Brentjens (2008) and Pizzo et al. (2011) report Faraday depth variations towards polarised point sources of a few rad m^{-2} over 12 hours. Therefore, the ionospheric contribution to the observed Faraday depth should be corrected for in order to derive reliable Faraday depths due to the ISM alone and is also crucial for comparing Faraday depths of the same source at multiple epochs. This is particularly important for sources, e.g., pulsars, that are relatively nearby and/or located towards the Galactic Halo because the ionospheric Faraday depth may be greater than the Faraday depth of the ISM towards the source. Using the statistics collected in Chapter 3, the line-of-sights (LOSs) towards the 143 known pulsars located at least 300 pc from the galactic plane (those likely to have smaller absolute RM values on average) have a median absolute RM of 30 rad m^{-2}, and tens of these LOS have values less than

$1\,\mathrm{rad\,m^{-2}}$. Furthermore, the 58 pulsars located less than 1 kpc from Earth have a median absolute RM of $10.9\,\mathrm{rad\,m^{-2}}$.

Furthermore, the time-dependent ionospheric Faraday rotation can lead to a decrease in linear polarisation when averaging over multi-hour time intervals at longer wavelengths. Minter and Spangler (1996) also found that application of an ionospheric Faraday rotation calibration led to a factor of two decrease in both the rms variations in polarisation angle and the noise level of Stokes Q and U images.

In addition, knowledge of the Faraday depth of the ionosphere may be used advantageously. Observing sources that have small absolute Faraday depths ($|\mathrm{RM}| \leq \Delta\phi$, see Eq. 3.8) at epochs where the ionospheric Faraday depth is comparatively high ($|\mathrm{RM_{ion}}| > 2\Delta\phi$) can prove useful for distinguishing between the instrumental response ($\phi \approx 0\,\mathrm{rad\,m^{-2}}$) and the source response in the Faraday spectrum.

There have been several ionospheric Faraday rotation models previously presented. Erickson et al. (2001) constructed a simple model based on Global Positioning System (GPS) data. However, this model requires local GPS data, i.e., dual frequency GPS receivers installed at the telescope site(s). Afraimovich et al. (2008) used a well-established empirical ionospheric model, the International Reference Ionosphere (IRI). The IRI provides ionospheric parameters derived mostly from ground-based instruments (e.g., ionosondes) and some space-based instruments (Bilitza and Reinisch, 2008). The model was compared solely with GPS data and no comparison with radio astronomical data was presented. The `ionFR` software presented here is somewhat similar to the `TECOR` task from the Astronomical Imaging Processing System (AIPS Greisen, 2003). However, while `TECOR` requires exporting interferometric data into AIPS, `ionFR` is a standalone package. Pulsar observations that have been corrected for this found typical values for ionospheric Faraday rotation that ranged from –5 to $-1\,\mathrm{rad\,m^{-2}}$ above the Parkes Observatory in the southern hemisphere (Han et al., 2006) and from 0.5 to $4\,\mathrm{rad\,m^{-2}}$ above the Arecibo Observatory in the northern hemisphere (Weisberg et al., 2004).

This chapter presents a summary, test, and application of the code written by Carlos Sotomayor-Beltran that models the ionospheric Faraday depth using publicly available global TEC maps and the latest geomagnetic field model. Subsequently, the robustness of this code is shown by comparing the modelled ionospheric Faraday depths with the

measured Faraday depths towards pulsars from five different LOFAR observing campaigns.

4.3 Ionospheric Faraday rotation model

The `ionFR` code that models the ionospheric Faraday depth, using publicly available global TEC maps and the latest geomagnetic field model, was written by Carlos Sotomayor-Beltran. Therefore, a brief description is given below. Further details about the construction and output of the code are provided in Sotomayor-Beltran et al. (2013).

The Earth's magnetic field is calculated using the eleventh generation of the International Geomagnetic Reference Field (IGRF11; Finlay et al., 2010) released in December 2009. The IGRF is derived by the International Association of Geomagnetism and Aeronomy (IAGA) every five years and is available to download[1]. The IGRF11 is described as the negative gradient of a scalar potential, $\mathrm{B} = -\nabla V$, which is a finite series of spherical harmonics. `ionFR` calls the IGRF11 to deliver the vector components of the geomagnetic field at the ionospheric piercing point (IPP) and uses these to calculate the total geomagnetic field along the LOS, $\mathrm{B_{LOS}}$. The changing angle towards the IPP is the only cause of variation in the geomagnetic field parallel to the LOS. As previously stated, the net direction of the geomagnetic field results in positive ionospheric RMs north of the magnetic equator and negative ionospheric RMs south of the magnetic equator, see Fig. 4.2 *left* which shows the absolute magnitude of the IGRF.

Measurements of the ionospheric free electron content come from several sources. Those used in this work are vertical total electron content (TEC) value maps derived from $\sim$ 200 GPS sites of the International Global Navigation Satellite System Service (IGS) and other institutions (e.g. Schaer, 1999). Vertical TEC is defined as the integral of free electrons in the ionosphere along the zenith direction. For example, the Centre for Orbit Determination in Europe (CODE) offers global ionosphere maps (GIMs) in IONosphere map EXchange format (IONEX), publicly available via anonymous `ftp`[2]. The IONEX files provide vertical TEC values in a geographic grid ($\Delta_{\mathrm{lon.}}$=5°, $\Delta_{\mathrm{lat.}}$=2.5°) with 2-hour time resolution, see Fig. 4.2 *right* for an example GIM. To increase the time resolution, `ionFR` creates new GIMs for every hour by using an interpolation scheme

[1] `http://www.ngdc.noaa.gov/IAGA/vmod/igrf.html`
[2] `ftp://ftp.unibe.ch/aiub/CODE/`

that takes the rotation of the Earth into consideration (Schaer et al., 1998, Eq. 3). The software interpolates the positional measurement grid to estimate the vertical TEC values at a given IPP for each hourly GIM. The interpolation uses a 4-point formula as in Fig. 1 of Schaer et al. (1998). For European telescopes, `ionFR` can also use TEC maps from the Royal Observatory of Belgium (ROB[3]), which are derived from GPS data from a permanent European network. These TEC maps are more finely gridded than those from CODE ($\Delta_{\text{lon.}}$=0.5°, $\Delta_{\text{lat.}}$=0.5°) and have 15-minute time resolution. Comparisons of `ionFR`-modelled Faraday depth based on the CODE/ROB maps are discussed below. The final step in calculating the line-of-sight TEC, TEC_{LOS}, involves dividing the vertical TEC by the cosine of the zenith angle at the IPP. The uncertainties are also calculated in this way using the root-mean-square (RMS) vertical TEC maps that are also provided and are geographically gridded in the same way as the vertical TEC maps. 1σ uncertainties in the vertical TEC maps from CODE are typically between 2 – 5 TECU[4]. The contribution of the ionospheric TEC to the dispersion measure (DM) of the pulsar (of order $10^{-6}\,\text{pc}\,\text{cm}^{-3}$) is much smaller than typical uncertainties in the DM measurements from observations (the median value from the pulsar catalogue is $0.3\,\text{pc}\,\text{cm}^{-3}$). Therefore, correction for dispersion in the ionosphere is not necessary for current observations, although very precise low-frequency long-term pulsar timing projects may begin to require this in the future.

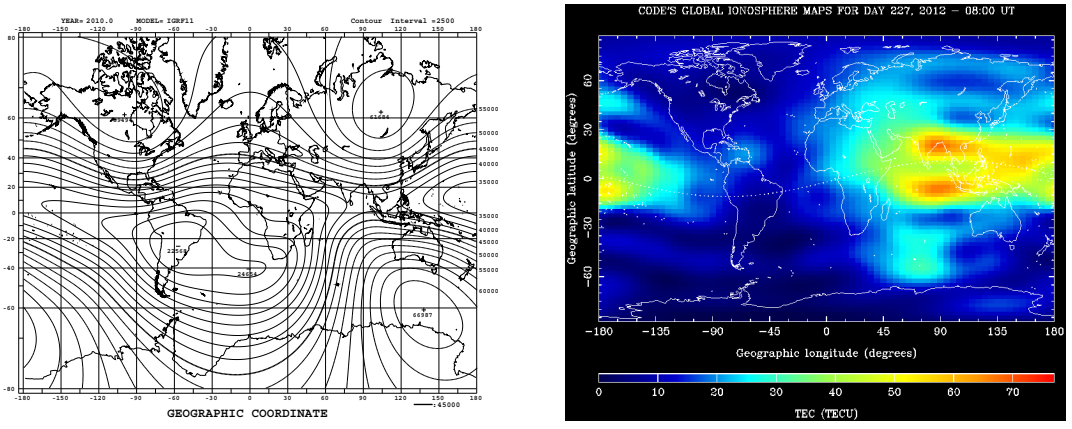

FIGURE 4.2: *Left:* The absolute magnitude of the geomagnetic field (in nanoTesla) output by IGRF11, image courtesy of the World Data Centre for Geomagnetism, Kyoto (http://wdc.kugi.kyoto-u.ac.jp/igrf). *Right:* An example ionospheric global vertical TEC map at 08:00 UT on 14 August 2012 produced by CODE, see text.

[3] `http://gnss.be/Atmospheric_Maps/ionospheric_maps.php`

[4] TEC units (TECU) describe the electron columnar density along a tube of one meter squared cross section. $1\text{TECU} = 1\times10^{16}\,\text{electrons}\,\text{m}^{-2}$

To calculate the ionospheric Faraday depth along the LOS, the ionospheric Faraday depth is calculated at the IPP, assuming that the ionosphere is a thin spherical shell surrounding the Earth, defined as:

$$\phi_{\rm ion} = 2.6 \times 10^{17} {\rm TEC}_{\rm LOS} {\rm B}_{\rm LOS} \tag{4.3}$$

Typical values obtained from testing the code for the LOS towards Cassiopeia A from the centre of the LOFAR core stations in the Netherlands showed that the ionospheric Faraday rotation values were approximately 0.5–9 $\mathrm{rad\,m^{-2}}$ during the last Solar maximum (during 2001) and 0–1 $\mathrm{rad\,m^{-2}}$ during the last Solar minimum (during 2008), although for other lines of sight these values were much higher (Sotomayor-Beltran et al., 2013). This is larger than the typical uncertainties in RM measurements towards pulsars (the median value from the pulsar catalogue is 3 $\mathrm{rad\,m^{-2}}$), especially at low-frequencies (of order 0.15 $\mathrm{rad\,m^{-2}}$ using LOFAR observations in this work, see Chapter 5), and in many cases the RM measurement itself (as explored in Chapter 3). The fractional uncertainties in $\mathrm{B_{LOS}}$ are much smaller than the fractional uncertainties in the $\mathrm{TEC_{LOS}}$. Consequently, to determine the uncertainties in the ionospheric Faraday rotation calculated from `ionFR` only the $\mathrm{TEC_{LOS}}$ values are used. This results in uncertainties of 0.1–0.3 $\mathrm{rad\,m^{-2}}$ in $\phi_{\rm ion}$ using the CODE global TEC maps. Assuming an RMS values of 0.5 TECU for the ROB European TEC maps, this results in smaller uncertainties of 0.03–0.06 $\mathrm{rad\,m^{-2}}$.

4.4 LOFAR pulsar observations and data reduction

The results obtained from the LOFAR observations and comparisons to the results from the ionospheric Faraday rotation code, described below, were my contribution to the project.

To measure Faraday depth variations in the ionosphere and to compare them with those modelled by `ionFR`, four bright polarised pulsars were observed using LOFAR (see Stappers et al., 2011, for a description of LOFAR's pulsar observing modes). One or more pulsars were observed on five separate epochs, at times when the ionosphere was expected to be particularly dynamic (sunrise or sunset). See Table 4.1 for a summary of these five observing campaigns.

For the first campaign we used the coherently combined LOFAR 'Superterp'[5] to observe PSR B0834+06 7 times, using 10-min integrations spaced every 50 min. These started 1.8 hours before sunset (18:25 UT) and continued until more than 2 hours after astronomical twilight (20:40 UT).

In the second Superterp campaign we observed PSR B0834+06 20 times using 3-min integrations spaced every 7 min. These started after astronomical twilight (04:11 UT) and continued until 1.5 hours after sunrise (06:08 UT).

In the third Superterp campaign we observed PSRs B1642−03, B1919+21 and B2217+47 by cycling consecutively through the three pulsars so that each was observed for 12×3-min, spaced every 20 min. This enabled the measurement of ionospheric Faraday depth variations towards three widely separated LOSs quasi-simultaneously, starting before nautical twilight (04:16 UT) and ending two hours after sunrise (05:29 UT).

In the fourth campaign we observed PSR B0834+06 using the LOFAR Superterp stations and two international stations located near Nançay, France and near Onsala, Sweden. The pulsar was quasi-simultaneously observed by each station in 11×3-min integrations spaced by 17 min. These were done during midday when the absolute TEC was expected to be relatively high. This enabled measurements of Faraday depth variations from three locations separated by a longest baseline of 1270 km.

The fifth campaign observed PSR B2217+47 using the HBA international station near Effelsberg (DE601). The pulsar was observed 28 times, each observation lasting 15 minutes with 27-minute gaps, from rise to set. The observations started just before sunset on 1 July 2013, and spanned 19 hours, which also included sunrise on 2 July 2013. Therefore a large range in ionospheric Faraday rotation was explored.

In all cases, data were written as Nyquist sampled complex values for the two orthogonal linear polarisations. The data were recorded using the 200 MHz clock mode, which provides multiple 195.3125 kHz subbands that are further channelised by an online polyphase filter to 12.2 kHz channels with a time resolution of 81.92 μs. Due to limitations on the data rate, $6-11$ MHz of bandwidth were recorded for these observations. In comparison, 80 MHz of bandwidth can now be recorded by LOFAR in this mode. Nonetheless, given the low central observing frequencies (~ 125 MHz) the recorded bandwidths were

[5]The 330-meter-wide inner core of the array, which hosts 6 stations.

TABLE 4.1: Summary of the five LOFAR pulsar observing campaigns. Columns 1–10 show the number of the observing campaign, pulsar B1950 names, date, duration, LOFAR station(s) used (CS00[2-7] indicate the LOFAR 'Superterp' core stations combined in tied-array mode, HBA and LBA indicate High-Band Antenna stations and Low-Band Antenna stations, respectively), individual observation integration times, total number of observations, frequency (ν) range, range in elevation of the source, and LOFAR observation identification numbers (obs. IDs).

No.	PSR (B-name)	Date (dd.mm.yy)	Time range (hh:mm UT)	LOFAR stations (hh:mm UT)	T_{int} (min)	N_{obs}	$\nu_{min} - \nu_{max}$ (MHz)	Elevation (deg)	OBSIDs
1	B0834+06	11.04.11	16:40–22:50	CS00[2-7]HBA	10	7	120–126	20–45	L25152–L25158
2	B0834+06	20.10.11	04:20–07:33	CS00[2-7]HBA	3	20	129–140	37–44	L32350–L32369
3	B1642−03	23.03.12	04:08–07:40	CS00[2-7]HBA	3	12	119–125	16–34	L53966–L53977
	B1919+21	23.03.12	04:04–07:36	CS00[2-7]LBA	3	12	58–64	45–59	L53942–L53953
	B2217+47	23.03.12	04:12–07:44	CS00[2-7]HBA	3	12	119–125	37–72	L53990–L54001
4	B0834+06	10.07.12	11:20–14:43	CS00[2,3,5-7]HBA	3	11	119–129	38–44	L61473–L61483
	B0834+06	10.07.12	11:25–14:48	FR606HBA	3	11	119–129	42–49	L61532–L61542
	B0834+06	10.07.12	11:30–14:53	SE607HBA	3	11	119–129	32–39	L61520–L61530
5	B2217+47	01–02.07.2013	20:30–15:30	DE601	15	28	126–163	08–87	N/A (single station)

still more than adequate to achieve precise RM measurements. The Nyquist sampled complex values were converted from 32-bit to 8-bit samples offline and then coherently dedispersed and folded using the `dspsr` program (van Straten and Bailes, 2011). Radio frequency interference (RFI) was removed using the `pazi` program from the PSRCHIVE[6] library library (Hotan et al., 2004).

The reduced data were analysed using an RM-synthesis program in order to determine a precise Faraday depth for each individual observation. For each data set, the Stokes parameters (I, Q, U, V) and associated uncertainties for each frequency channel were output for the pulsed section of the pulsar profile using the PSRCHIVE program `rmfit`. The frequency, Q and U information were used as the input to the RM-synthesis program, which calculated the Faraday dispersion function (FDF) as a discrete sum for Faraday depths $-50 \leq \phi \leq 50\,\mathrm{rad\,m^{-2}}$ in steps of $0.001\,\mathrm{rad\,m^{-2}}$ using Eq. 3.5, see Fig. 4.3 for two examples. The peak associated with the instrumental DC signal at $\sim 0\,\mathrm{rad\,m^{-2}}$ Faraday depth (Geil et al., 2011, see, e.g.,) was subtracted from the FDF before determining the peak associated with the Faraday depth towards each pulsar LOS. This had no effect on the Faraday peaks of the pulsars since the known RM values (ATNF pulsar catalogue, Manchester et al., 2005a) are $> 2\times$FWHM of the RMSF, see Eq. 3.8. The Faraday depth at which the peak in the FDF occurred was assumed to be the measured Faraday depth of the ISM and ionosphere towards the pulsar, $\phi_{\mathrm{ISM}} + \phi_{\mathrm{ion}}$[7]. For each observing

[6] see http://psrchive.sourceforge.net for more information.

[7] This assumes no Faraday rotation in the pulsar magnetosphere itself (see Wang et al., 2011, Noutsos et al., 2009, for a discussion on possible Faraday rotation within pulsar magnetospheres).

campaign, we estimated the systematic instrumental error by measuring the Faraday depth of the instrumental polarisation peak around $0\,\mathrm{rad\,m^{-2}}$ in the FDF of each observation, weighted by the S/N, and taking the $0\,\mathrm{rad\,m^{-2}}$ $\pm 1\sigma$ limits (Table 4.2). This demonstrated that larger bandwidth observations with higher S/Ns also tended to reduce the scatter in instrumental Faraday depth around $0\,\mathrm{rad\,m^{-2}}$. The total error on the Faraday depth was taken to be the formal error from Eq. 3.10 added in quadrature with the instrumental error. The linear polarisation had S/N > 30 for all observations; this is well above the threshold necessary for reliable Faraday depth measurements (see Macquart et al., 2012, and references therein). While we have shown that LOFAR provides reliable Faraday depths, we note that proper polarisation calibration (e.g. to determine absolute polarisation angles) has not yet been applied to the data.

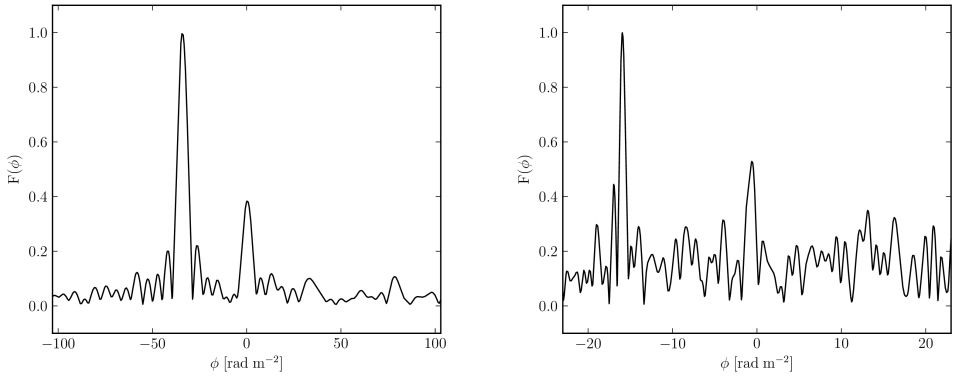

FIGURE 4.3: Examples of the absolute value of the normalised Faraday Dispersion Function (FDF), obtained from two LOFAR observations. The peaks at zero Faraday depth, $\mathrm{F}(\phi \approx 0\,\mathrm{rad\,m^{-2}})$, indicate the instrumental response. *Left:* FDF obtained from a single 3-min HBA observation (119–125 MHz) of PSR B2217+47. The peak centred at $\phi = -34.08\,\mathrm{rad\,m^{-2}}$ is the response due to the polarised flux of the pulsar. The FWHM of the RMSF is $6.6\,\mathrm{rad\,m^{-2}}$. *Right:* FDF obtained from a single 3-min LBA observation (58–64 MHz) of PSR B1919+21. The polarised flux of the pulsar is responsible for the peak at $\phi = -15.94\,\mathrm{rad\,m^{-2}}$. The FWHM of the RMSF is $0.84\,\mathrm{rad\,m^{-2}}$

4.5 Results: comparison between model and observational LOFAR data

The observed and `ionFR`-modelled Faraday depths as a function of time for the five LOFAR observing campaigns are plotted in Figs. 4.4, 4.5, 4.6, and 4.7. In general, the modelled and observed Faraday depth variations agree very well. There are a few instances though where the observed and modelled values differ by more than 1σ. The

measured RMs could still be affected by interference and it is also quite possible that there are unmodelled ionospheric variations on short timescales (see Section 4.6). TEC data from CODE was used for the PSR B0834+06 sunset and sunrise campaigns. CODE and ROB TEC data were both available for the observations that took place in 2012 and are compared in Figs. 4.5 and 4.6. In each case, there is a clear trend in the Faraday depth as a function of time. At sunrise and sunset there is a particularly distinct variation in Faraday depth of approximately $2\,\mathrm{rad\,m^{-2}}$. Even during midday, Fig. 4.6, when the absolute TEC is expected to be high but relatively constant (e.g. Kassim et al., 2007, Fig. 14), smaller variations in Faraday depth are still evident and well modelled in general.

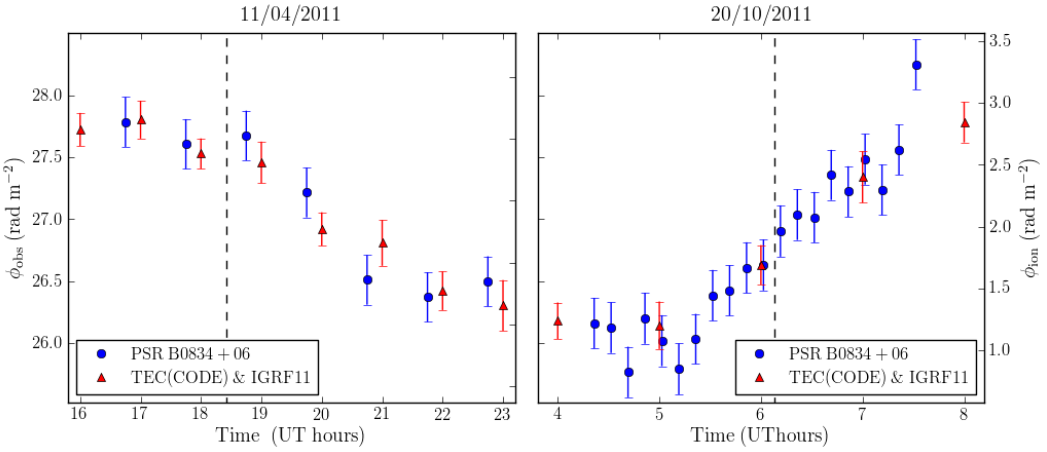

FIGURE 4.4: Observed RMs (ϕ_{obs}, blue circles, left axis labels) and `ionFR`-modelled ionospheric RMs using CODE TEC data (ϕ_{ion}, red triangles, right axis labels) towards PSR B0834+06 as a function of time. *Left:* seven LOFAR Superterp HBA observations during sunset. *Right:* twenty LOFAR Superterp HBA observations during sunrise. The vertical dashed lines indicate the time of sunset and sunrise, respectively. The offsets between ϕ_{obs} and ϕ_{ion} were calculated and are summarised in Table 4.2.

Figs. 4.5 and 4.6 compare the modelled Faraday depths using CODE and ROB TEC data. In both cases, the observations and model show good agreement, although it is evident that there are variations on timescales less than one hour that are not resolved in the model using CODE data. The model using ROB TEC data more accurately fits the observations. The finer gridding and smaller RMS available with the ROB TEC data also allows smaller fluctuations in Faraday depth to be resolved. For the observations of PSR B0834+06 using the Superterp and international stations over midday, Fig. 4.6, this is especially significant, where the variations in the data appear on shorter timescales and in Faraday depths within the error bars of the model using CODE data. Given that

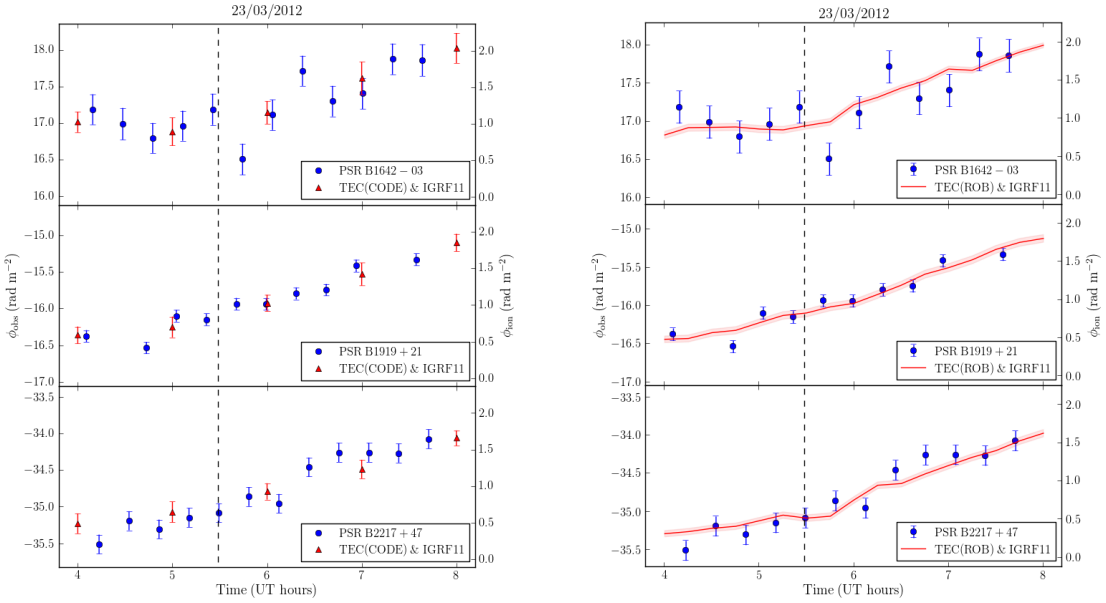

FIGURE 4.5: Observed Faraday depths, $\phi_{\rm observed}$, and `ionFR`-modelled ionospheric Faraday depths, $\phi_{\rm ion}$, towards three pulsars as a function of time during sunrise (observations: blue circles, left axis labels; model: red triangles, right axis labels). *Upper panels:* twelve LOFAR Superterp HBA observations of PSR B1642−03. *Middle panels:* twelve LOFAR Superterp LBA observations of PSR B1919+21. *Lower panels:* twelve LOFAR Superterp HBA observations of PSR B2217+47. The vertical dashed lines indicate the time of sunrise. (a) shows the `ionFR` model using CODE TEC data and IGRF11. (b) shows the `ionFR` model using ROB TEC data and IGRF11.

the model output of `ionFR` shows good agreement with the measured Faraday depths for all of the LOFAR observing campaigns depicted in Figs. 4.4, 4.5, 4.6, and 4.7 we use this model to subtract the contribution of the ionospheric Faraday depth from the measurements in order to determine the Faraday depth of the ISM, $\phi_{\rm ISM}$, in the direction of these pulsars.

To determine $\phi_{\rm ISM}$ for each pulsar, the constant offset that yielded the minimum weighted chi-squared value between the pulsar Faraday depth measurements and the ionospheric modelled Faraday depths from `ionFR` was used (see Table 4.2). Using the CODE data, the reduced chi-squared values range from 0.4 – 1.2, whereas with the ROB data the reduced chi-squared values range from 0.9 – 1.3. The residual differences between the observations and model may be due to small scale variations in the ionosphere that affect the observations but that are not resolved due to the time resolution of the TEC data. The standard deviations of $\phi_{\rm observed} - \phi_{\rm ion}$ divided by the square root of the number of measurements in each observational campaign range from 0.03 – 0.09 rad m^{-2} for the CODE output and from 0.02 – 0.07 rad m^{-2} for the ROB output. This indicates

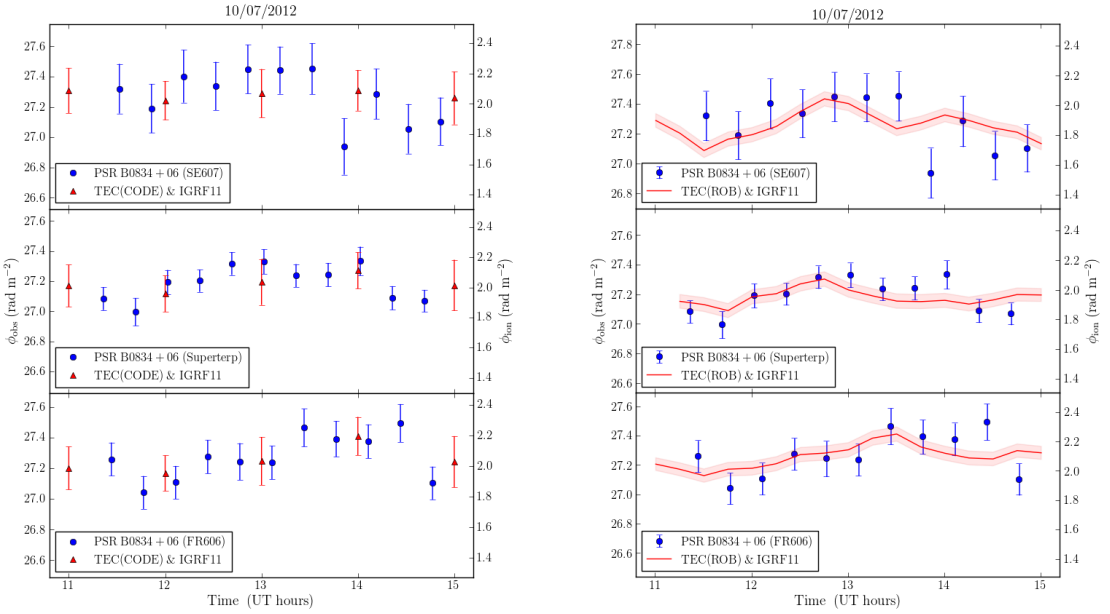

FIGURE 4.6: Observed Faraday depths, $\phi_{\rm observed}$, and `ionFR`-modelled ionospheric Faraday depths, $\phi_{\rm ion}$, towards PSR B0834+06 as a function of time during midday (observations: blue circles, left axis labels; model: red triangles, right axis labels). *Upper panels:* eleven LOFAR HBA observations using the international station near Onsala, Sweden. *Middle panels:* eleven LOFAR Superterp HBA observations. *Lower panels:* eleven LOFAR HBA observations using the international station near Nançay, France. (a) shows the `ionFR` model using CODE TEC data and IGRF11. (b) shows the `ionFR` model using ROB TEC data and IGRF11.

that both fit the measurements well, although the ROB data gives reduced chi-squared values closer to 1 and smaller errors due to the smaller uncertainties compared with the CODE maps. Also, both sources of TEC maps give consistent results, where all $\phi_{\rm ISM}$ values obtained using CODE and ROB data agree within 1-σ for the same observing campaign and LOS. The Faraday depth values for PSR B0834+06 obtained from the three observational campaigns over six months apart also agree at or below the 2-σ level for both CODE and ROB data. The weighted mean for all CODE and ROB data available for PSR B0834+06 gives $\phi_{\rm ISM} = 25.12 \pm 0.07\,{\rm rad\,m^{-2}}$ (5 LOSs) and $\phi_{\rm ISM} = 25.26 \pm 0.05\,{\rm rad\,m^{-2}}$ (3 LOSs), respectively. Although there are two more data sets with CODE data available, the errors assumed for the ROB data are smaller, see below for further discussion. It is worth noting that these are among the most precise pulsar-derived $\phi_{\rm ISM}$ measurements ever obtained (Manchester et al., 2005b, see ATNF catalogue), and improve significantly on the precision of previous RM measurements for these pulsars.

In order to determine the Faraday depth of PSR B0834+06 using an independent instrument, on April 22nd, 2012 at 16:50 UT we performed a 20-minute observation of PSR B0834+06 using the WSRT with the PuMaII pulsar backend (Karuppusamy et al., 2008) from 310 to 390 MHz. We recorded baseband (Nyquist sampled) data, which were folded, dedispersed and subsequently analysed using the same RM-synthesis method described above, yielding $\phi_{\rm observed} = 28.2 \pm 1.8\,{\rm rad\,m^{-2}}$. The `ionFR` code provides a $\phi_{\rm ion} = 2.75 \pm 0.15\,{\rm rad\,m^{-2}}$, using CODE maps, for the given time and LOS of this observation, resulting in a corrected value of $\phi_{\rm ISM}^{\rm WSRT} = 25.4 \pm 1.8\,{\rm rad\,m^{-2}}$. Using ROB maps we calculated a corrected value of $\phi_{\rm ISM}^{\rm WSRT} = 25.1 \pm 1.5\,{\rm rad\,m^{-2}}$. These values are in excellent agreement with the more precise value derived from the LOFAR observations. The precision of the WSRT measurement is lower in part because of the higher observing frequency, see Eqs. 3.8 and 3.10. This demonstrates the power of low-frequency observations for the purpose of determining accurate $\phi_{\rm ISM}$.

Our measured Faraday depths are consistent with previously published measurements for these pulsars, but are significantly more precise. The values of $\phi_{\rm ISM}$ obtained from the LOFAR observations of PSR B0834+06 agree to within 2.5 σ of the catalogue value for this pulsar, ${\rm RM_{psrcat}} = 23.6 \pm 0.7$ rad m^{-2}. It is unclear, but likely, that the catalogue value was calibrated for ionospheric Faraday rotation (see Hamilton and Lyne, 1987§2). That paper also states that the ionosphere contributes $1-8\,{\rm rad\,m^{-2}}$ to other observations, using either a geostationary satellite or an ionosonde, and that the subtraction of this introduces uncertainties of approximately $1-2\,{\rm rad\,m^{-2}}$. The 2.5-σ difference between the $\phi_{\rm ISM}$ obtained using LOFAR and the ATNF catalogue value determined in 1987, plus the possibility that pulsar RMs may change on multi-year timescales (e.g. Weisberg et al., 2004) due to variations in the polarised pulsar emission and/or electron density changes in the LOS through the ISM, provided the motivation for the recent independent comparison observation of PSR B0834+06 using the WSRT.

The values of $\phi_{\rm ISM}$ obtained for the three pulsars observed quasi-simultaneously are also very precise and are in excellent agreement with those of the ATNF pulsar catalogue. Prior measurements for PSR B1642−03 and B1919+21, also calibrated for ionospheric Faraday rotation using geostationary satellite and ionosonde data, give ${\rm RM_{ISM}} = 15.8 \pm 0.3\,{\rm rad\,m^{-2}}$ and ${\rm RM_{ISM}} = -16.5 \pm 0.5\,{\rm rad\,m^{-2}}$, respectively (Hamilton and Lyne, 1987), and are also in good agreement within 1 σ of the values obtained in this work (ROB-subtracted values $\phi_{\rm ISM} = 16.04 \pm 0.18\,{\rm rad\,m^{-2}}$ and $\phi_{\rm ISM} = -16.92 \pm 0.07\,{\rm rad\,m^{-2}}$). A

prior measurement for PSR B2217+47, $\mathrm{RM_{ISM}} = -35.3 \pm 1.8$ rad m^{-2}, also calibrated for ionospheric Faraday rotation using a geostationary satellite (Manchester, 1972), is also in good agreement within 1 σ of the value derived here (ROB-subtracted value $\phi_{\mathrm{ISM}} = -35.60 \pm 0.11$ rad m^{-2}).

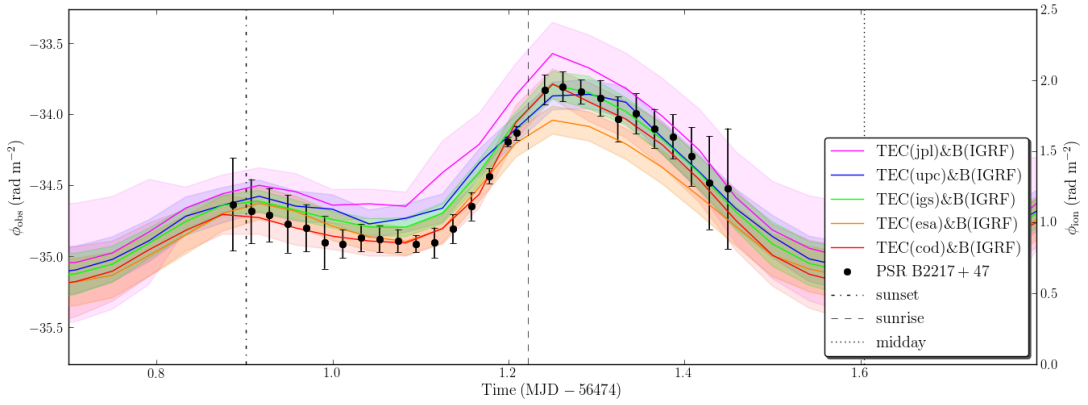

FIGURE 4.7: Observed Faraday depths, ϕ_{observed}, using the international LOFAR station near Effelsberg (DE601) and `ionFR`-modelled ionospheric Faraday depths, ϕ_{ion}, towards PSR B2217+47 as a function of time, from rise until set of the source (observations: blue circles, left axis labels; model: red triangles, right axis labels). The code used to produce the ionospheric Faraday rotation models, very similar to `ionFR`, was provided courtesy of Olaf Wucknitz, private communication.

Figure 4.7 displays the data taken on 1–2 July 2013 using a single LOFAR HBA station situated near Effelsberg. To directly compare different values of the ionospheric RM calculated by using different TEC maps, five sources of TEC maps were used: CODE, European Space Agency (ESA, see http://dgn7.esoc.esa.int/activities/ionosphere/), International GNSS Service (IGS, Hernández-Pajares et al., 2009), Jet Propulsion Laboratory (JPL, see http://iono.jpl.nasa.gov/) and the Technical University of Catalonia (UPC, Garcia-Rigo et al., 2011) – all publicly available via anonymous `ftp`[8]. Figure 4.7 also shows the comparison between the ionospheric RMs derived using these TEC maps and the observational LOFAR data. The different sources of TEC maps show some variation in the RM derived towards PSR B2217+47 over the time period shown. The median errors for entire 48-h period for the CODE, ESA, IGS, JPL, and UPC data are 0.14, 0.12, 0.096, 0.24, and 0.12 rad m^{-2} to 2 s.f., respectively. The minimum error of 0.050 rad m^{-2} was obtained from the IGS data, which uses data combined from the other four TEC map sources. Comparisons between the sources of TEC maps result in the smallest difference of 0.10 rad m^{-2} between minimum (CODE) and maximum (JPL) data is at 11:00 hours UT on 1 Jul 2013. This is comparable, if slightly larger than, the

[8] `ftp://cddis.gsfc.nasa.gov/pub/gps/products/ionex/`

error from measuring RMs using LOFAR. The largest difference of 0.47 rad m^{-2} between minimum (ESA) and maximum (JPL) data is at 06:00 hours UT on 2 Jul 2013. The average RM derived for PSR B2217+47 after the ionosphere was subtracted is –35.83 rad m^{-2}, with standard deviation of 0.10 rad m^{-2} between all five RM_{ISM} calculated. This is just within 1σ errors of the RM previously determined from the observation using the LOFAR superterp. In this case the CODE and IGS data resulted in the smallest chi-squared value after fitting for the RM_{ISM} offset between the ionospheric model and the observational data.

To investigate the spacial dependence of the ionospheric TEC maps and geomagnetic field on correcting the observational data, the ionospheric RM was modelled for a circular area 10 degrees in radius around the position of PSR B1919+21 during the observation on 23 March 2012. The observed RM was corrected for ionospheric Faraday rotation for this area and the chi-squared values for each fit were noted. The smoothed results are shown in Fig. 4.8. This shows that in the directions to the North and South of the position of the pulsar, the RM_{ISM} obtained becomes more positive and negative, respectively, resulting from larger and smaller ionospheric Faraday rotation values calculated using `ionFR`. The centre of the area, which marks the position of the pulsar, resulted in the median RM_{ISM} value, Fig. 4.8 *left*. This also shows that the minimum chi-squared value obtained from the fit is also approximately located at the position of the pulsar, Fig. 4.8 *right*. Although there is a slightly lower minimum chi-squared value (0.04 lower) at ($r \approx 8°$,$\phi \approx 180°$), this may be due to a more southern grid in the TEC map fitting one of the ten data points slightly better by chance. Overall, it is reassuring that the position of the pulsar is the most appropriate to use for the LOS in calculating the ionospheric Faraday rotation from `ionFR`. In this case, the correction of the ionospheric Faraday rotation can be affected by a value greater than the average uncertainties on RMs determined from the observations (0.15 rad m^{-2}) if the LOS position is greater than approximately six degrees from the position of the pulsar.

The results obtained from the LOFAR observations provide a convincing verification of the accuracy of the `ionFR` model. They therefore demonstrate the ability to derive Faraday depths resulting solely due to the ISM by robustly removing the time and direction-dependent Faraday depth introduced by the ionosphere, even during some of the most turbulent periods expected in daily ionospheric variations, see below for further discussion.

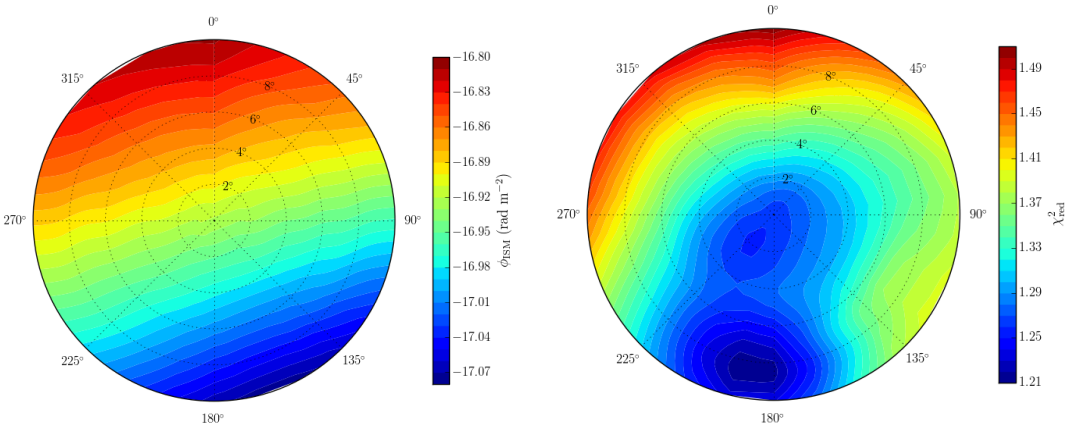

FIGURE 4.8: The $\mathrm{RM_{ISM}}$ (*left*) and resulting chi-squared value (*right*) calculated using the LOFAR LBA observations of PSR B1919+21, shown in Fig. 4.5, after correcting for the ionospheric Faraday rotation calculated for an area 10 degrees in radius around the position of the pulsar. The colour scale range and units are shown to the right of each polar plot.

TABLE 4.2: Summary of results from the five LOFAR pulsar observing campaigns and WSRT observation. Columns 1–11 show the pulsar observed, date (see Table 4.1 for specific times), the telescope, the LOFAR stations (if applicable, see Table 4.1 for specific station names), the FWHM of the RMSF from RM-synthesis, the error introduced by instrumental effects $\sigma_{\rm inst}$, the Faraday depth of the ISM towards the pulsar $\phi_{\rm ISM}$ as determined using the CODE TEC maps, the reduced chi-squared value $\chi^2_{\rm red}$ for comparison between the ionospheric Faraday depths from `ionFR` using CODE TEC data and the observed Faraday depths, the Faraday depth of the ISM towards the pulsar $\phi_{\rm ISM}$ as determined using the ROB TEC maps, the reduced chi-squared value for comparison between the ionospheric Faraday depth produced from `ionFR` using CODE TEC data and the observed Faraday depths. The final column gives the RM value from the pulsar catalogue (Manchester et al., 2005a) for comparison. Note that ROB TEC maps were not available for the observations of PSR B0834+06 taken in 2011. Since a single observation was obtained with WSRT, the reduced chi-squared value is not applicable because the Faraday depth of the ISM was determined by subtracting the Faraday depth of the ionosphere from the observed Faraday depth.

No.	PSR	Date [dd.mm.yy]	Telescope	Station(s)	FWHM$_{RMSF}$ [rad m^{-2}]	$\sigma_{\rm inst}$ [rad m^{-2}]	$\phi^{\rm CODE}_{\rm ISM}$ [rad m^{-2}]	$\chi^2_{\rm red}$ CODE	$\phi^{\rm ROB}_{\rm ISM}$ [rad m^{-2}]	$\chi^2_{\rm red}$ ROB	RM$^{\rm psrcat}_{\rm ISM}$ [rad m^{-2}]
1	B0834+06	11.04.11	LOFAR	Superterp	6.2	0.20	25.15(18)	0.52	–	–	23.6(7)
2	B0834+06	20.10.11	LOFAR	Superterp	9.4	0.20	24.94(24)	0.64	–	–	23.6(7)
3	B1642−03	23.03.12	LOFAR	Superterp	6.6	0.20	15.98(23)	0.8	16.04(18)	1.3	15.8(3)
	B1919+21	23.03.12	LOFAR	Superterp	0.8	0.08	-16.95(12)	0.5	-16.92(07)	1.3	−16.5(5)
	B2217+47	23.03.12	LOFAR	Superterp	6.6	0.13	-35.72(15)	1.0	-35.60(11)	1.1	−35.3(18)
–	B0834+06	22.04.12	WSRT	–	12.0	1.2	25.4(18)	–	25.1(15)	–	23.6(7)
4	B0834+06	10.07.12	LOFAR	Superterp	4.2	0.07	25.16(13)	0.5	25.23(08)	0.9	23.6(7)
	B0834+06	10.07.12	LOFAR	FR606	4.2	0.10	25.21(15)	0.4	25.16(10)	1.2	23.6(7)
	B0834+06	10.07.12	LOFAR	SE607	4.2	0.15	25.22(18)	0.6	25.39(14)	1.0	23.6(7)
5	B2217+47	01–02.07.13	LOFAR	DE601	1.7	0.09	–35.8(1)	0.6	–35.8(1)	0.7	−35.60(11)

4.6 Discussion

The Faraday depths of the ISM towards PSRs B0834+06, B1642−03, B1919+21 and B2217+47 presented here (Table 4.2) are some of the first determined using the RM-synthesis technique and are among the most precise Faraday depth measurements ever made towards a pulsar. In the ATNF catalogue, there are only a dozen measurements with absolute precision $\leq 0.2\,\mathrm{rad\,m^{-2}}$, determined for some of the brightest known pulsars. The fact that the Faraday depths obtained here are also in excellent agreement with the catalogue and/or alternatively determined values also demonstrates the robustness of `ionFR` for subtracting the ϕ_{ion} contribution and hence for allowing us to reap the benefits of low-frequency measurements.

Using multi-beaming capabilities (Stappers et al., 2011), LOFAR will provide high-precision Faraday depth measurements for hundreds of nearby pulsars, which can be used to probe the interstellar magnetic field of the Galaxy (e.g. Sobey et al. 2014, in preparation). Since the observations presented here used just a tenth of the now-available LOFAR bandwidth, the prospects for even higher-precision Faraday depth measurements are excellent, especially using LOFAR LBA observations ($10 - 90\,\mathrm{MHz}$). However, with the TEC data available from ROB these will be limited to precisions of approximately $0.05\,\mathrm{rad\,m^{-2}}$ because of the systematic uncertainty provided by the RMS vertical TEC maps. In other words, more sophisticated calibration techniques will need to be devised in order to reap the *full* benefit of LOFAR's low observing frequencies and large fractional bandwidth. This is especially important for determining possible long-term variations of the Faraday depth of pulsars due to fluctuations in their magnetosphere or the ISM (e.g. Weisberg et al., 2004), particularly as some pulsars have large relative velocities.

Calibrating for ϕ_{ion} is also important for higher-frequency observations. Assuming a bandwidth of 1.25 – 1.45 GHz, such as that of the 7-beam 21-cm receiver used at the Effelsberg 100-m telescope, the theoretical FWHM of the RMSF is $260\,\mathrm{rad\,m^{-2}}$. This yields an uncertainty in Faraday depth of $9.4\,\mathrm{rad\,m^{-2}}$ given a S/N of 20, which is comparable to the ϕ_{ion} reached during solar maximum (see e.g. Sotomayor-Beltran et al., 2013). Given larger bandwidths, such as those planned for the SKA and its pathfinders, this problem becomes worse and is relevant even during night-time and solar minimum. It is also clear that corrections for the ionospheric Faraday depth are important for observations of pulsars and extragalactic sources, particularly towards the

halo of the Galaxy, since the Faraday rotation expected is often much lower than those located towards the plane. For the 650 pulsars with rotation measure data, 284 of these are located over 300 pc above or below the galactic plane and have a median rotation measure of $\sim$39 rad m^{-2}. Ionospheric Faraday depth can thus contribute significantly to the total observed Faraday depth, especially at times near solar maximum or when observing from lower latitude sites.

More finely gridded TEC maps, e.g., from ROB, will help to perform differential Faraday rotation studies between LOFAR core stations and the international stations. It is clear that the international stations are subject to different ionospheric conditions than the core, which results in different amounts of Faraday rotation for the signals arriving at each station. This effect needs to be calibrated for before combining all the LOFAR stations to carry out polarisation studies. Also, to better understand the ionospheric variations only above the LOFAR Dutch stations (max. baseline $\lesssim$ 100 km) more finely gridded TEC maps are needed, or otherwise raw dual-frequency GPS data should be directly analysed. Raw dual-frequency GPS data may also desirable to use when short timescale ionospheric changes (on the order of seconds to a few minutes). For arrays located in Europe (like LOFAR) this is possible due to the considerable number of GPS stations from the permanent European network. However, this is not yet the case for arrays like the GMRT or future SKA. For instance, in India there is only one active station [9] (near Bangalore) that is part of the IGS network. This is also the case for South Africa and Western Australia, where there are a few more stations but they are on average further apart than those in Europe. Regional dedicated networks, like those in Europe, are needed for these arrays in order to gain a more detailed picture of the ionospheric sky over these sites. Also, we note that for a single LBA station operating at the low frequency end of the band, e.g., 20 MHz, the field of view is big enough, $\sim 13^\circ$, that $\sim$ 26 cells from the ROB TEC maps can be fit within it. This shows that within a single LBA station field of view operating at frequencies $\lesssim$ 45 MHz, the ionosphere can change significantly, i.e. by several TECU.

To further improve the accuracy of the `ionFR`-modelled Faraday depths, the Earth will be considered as an ellipsoid and also the various ionospheric layers (D, E, and F) can be treated. A three-dimensional model for the ionosphere should also be possible using ray tracing for three-dimensional tomography of the ionosphere (e.g. Bust and Mitchell,

[9] See `http://igscb.jpl.nasa.gov/network/hourly.html`

2008). An indication that this may be needed for future high-accuracy Faraday depth determinations with LOFAR is the increase in the derived Faraday depth of the ISM towards PSR B0834+06 as a function of latitude in the international station observations, see Fig. 4.9. Since the elevation of the pulsar is lower at higher geographic latitudes in these quasi-simultaneous observations, the LOS towards PSR B0834+06 passes through a larger ionospheric depth as seen from Sweden compared with the Netherlands and France. A correction similar, although not quite as large, as the airmass (the optical path length through Earth's atmosphere) may also be needed (e.g. Wielebinski and Shakeshaft, 1962). Fig. 4.9 shows how the $\phi_{\rm ISM}$ for each station appears to follow the same trend as the airmass. Furthermore, the variation of the geomagnetic field with time is not taken into account in this model because there is not yet scope for this using data currently available. However, this may become possible in the future with more accurate data using newly launched satellites, e.g., ESA's magnetic field mission *Swarm* (e.g. Hamilton, 2013).

4.7 Summary

We have presented `ionFR`, a code that models the ionospheric Faraday rotation using publicly available TEC maps and the IGRF11. We have shown that using comparisons of the `ionFR`-modelled Faraday depths with low-frequency data from LOFAR and the WSRT, the model is robust and accurate for a number of sources over a range of times of day and year. This implies that the model can be used to subtract the ionospheric contribution to Faraday rotation measurements with good confidence. Moreover, the code represents an alternative and cheaper solution when no GPS dual-frequency receivers are co-located with the radio telescope carrying out the observation.

We have shown that calibrating LOFAR data with `ionFR` provides very high-precision pulsar RMs (absolute error $\lesssim 0.1\,\mathrm{rad\,m^{-2}}$). The applicability of precise RMs is broad. These precise RMs can be used, for example, to more accurately map the structure of the Galactic magnetic field. Also, it is now possible to monitor pulsar RMs on multi-year timescales. For example, PSR B0834+06, shows an apparent increase in its RM after $\sim$ 25 years, assuming previous ionospheric calibration was correct.

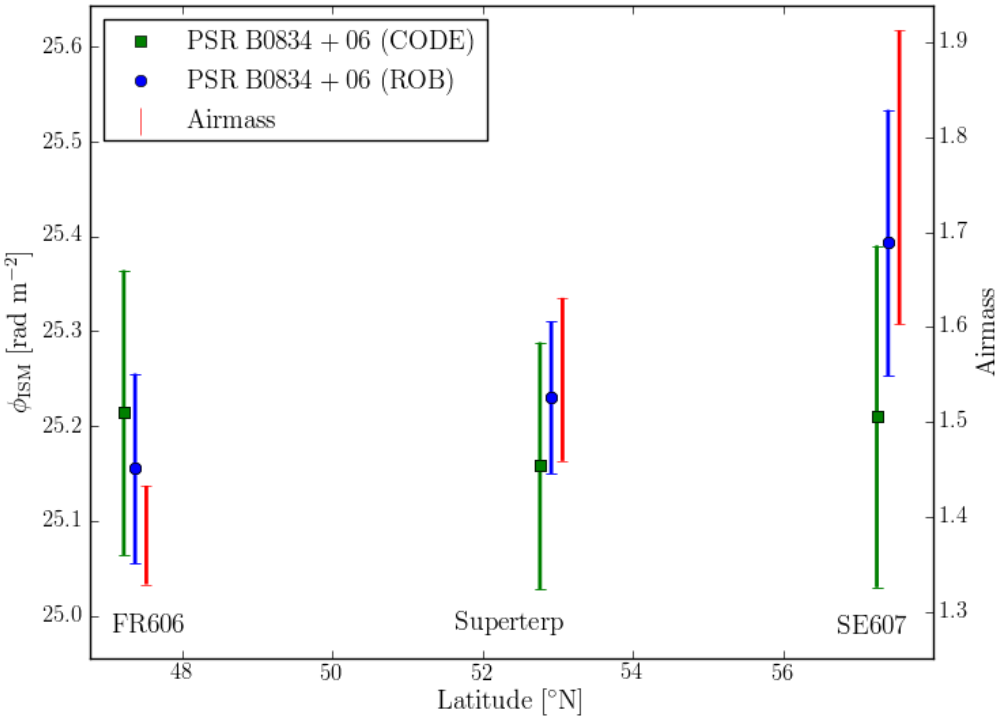

FIGURE 4.9: The measured Faraday depth of the ISM, $\phi_{\rm ISM}$, towards PSR B0834+06, as determined from HBA observations using the LOFAR FR606, Superterp and SE607 stations. These are plotted as a function of the geographic latitudes of the stations. The data points are offset slightly in latitude for ease of comparison. The measurements are also compared with the range in airmass calculated for the station location towards PSR B0834+06 for the duration of the observations (red triangles, *right axis*). The `ionFR` model was run using both TEC data from CODE (green squares) and ROB (blue points).

Lastly, Phase I of the SKA will provide an unprecedented low-frequency radio telescope, capable of making, e.g., a detailed map of the Galactic magnetic field structure through Faraday depth measurements of pulsars. However, given that the ionospheric equatorial anomaly sometimes passes directly over the two sites in South Africa and Western Australia, it will be crucial to have a robust and accurate calibration procedure in place to take full advantage of what the SKA has to offer. This is where the results from this chapter will also be useful.

The code and results from this chapter are utilised in Chapter 5, where more RM measurements taken using LOFAR, WSRT and the Effelsberg 100-m telescope are corrected for ionospheric Faraday rotation in order to obtain an accurate measurement for the RM due to the ISM.

Chapter 5

New pulsar rotation measures towards reconstructing the Galactic magnetic field

5.1 Abstract

A sample of 77 rotation measures (RMs) towards pulsars were measured using the Effelsberg 100-m Telescope, the Westerbork Synthesis Radio Telescope (WSRT), and the Low-Frequency Array (LOFAR) at centre frequencies of 1.3 GHz, 345 MHz, and 150 MHz, respectively. 45 of the RMs in the sample are towards pulsars with no previously published values. The LOFAR data provide the most accurate catalogue of RMs, corrected for ionospheric Faraday rotation using the code presented in Chapter 4, to date. The powerful technique of RM-synthesis was used to measure accurate RMs from the polarisation profiles obtained. These new data are used in combination with previously measured RMs and dispersion measures (DMs) towards pulsars, and RMs towards extragalactic sources presented in Chapter 3, to reconstruct the structure of the Galactic magnetic field using wavelet tomography.

Eighteen of the RMs measured from the observations using LOFAR are to be published in Noutsos, A., Sobey, C., et al., "Pulsar polarisation below 200 MHz: average profiles & propagation effects", Astronomy & Astrophysics, in preparation.

5.2 Introduction

As introduced in Chapter 1, the Galactic magnetic field (GMF) permeates the diffuse ISM and plays an important role in numerous astrophysical processes. The large scale component causes the deflection of high-energy cosmic rays, the small scale components play a role in formation of molecular clouds and star formation. Our Galaxy provides a unique opportunity for higher resolution observations of the Galactic magnetic field (GMF) in comparison to nearby galaxies (Nota and Katgert, 2010). Despite this, the structure of the Milky Way's Galactic magnetic field (GMF) remains largely unexplored (Han, 2004). The GMF is thought of as comprising a large-scale, ordered, regular component, coherent over kilo parsec scales, and a small scale, random, turbulent component. Since the density of RM data decreases dramatically over 1.5 kpc from the Sun, the aim of this chapter is to improve the reconstruction of the large-scale GMF, mainly towards the disk component of the Galaxy.

The RMs towards 77 pulsars were measured, including pulsars with and without catalogue RMs. The goal of the observations were to improve reconstruction of the GMF: by increasing the number of RMs towards known pulsars, and by increasing the accuracy of RMs towards known pulsars. The observations were carried out using three telescopes, with observations centred at three separate radio frequencies. The Effelsberg 100-m radio telescope was used to observe pulsars at 1.3 GHz, and the Westerbork Synthesis Radio Telescope (WSRT) was used to observe pulsars at the lower centre frequency of 350 MHz. Observations at both telescopes included many pulsars without previously published RM data, but also included at least two pulsars for which the RMs were known for comparative purposes. LOFAR observations were also conducted to more accurately determine the RMs towards a sample of pulsars most of which had previously published RMs. RMs were also determined for four pulsars without previously published measurements.

In Section 5.3 we describe the radio observations taken using the 100-m Effelsberg Radio Telescope, the WSRT, and LOFAR. The data were processed, as described in Section 5.4, and were used to provide 77 new and/or improved-accuracy RMs, which are presented in Section 5.5. The current catalogue of RMs introduced in Chapter 3, and the complementary RMs obtained in this work, were used to reconstruct the large-scale

Galactic magnetic field (GMF) using wavelet tomography, Section 5.6. A discussion of the results and the conclusions are presented in Sections 5.7 and 5.8.

5.3 Observations

To obtain polarisation profiles for a sample of 77 pulsars, three telescopes were used to observe at three different radio frequencies: the 100-m Effelsberg Radio Telescope centred at 1347.5 MHz, WSRT centred at 345 MHz, and LOFAR centred at 150 MHz, also used in Chapter 2. The aim of the Effelsberg and WSRT observations were to determine RMs towards pulsars without previously published data, especially towards pulsars located in sparsely sampled areas of the Galaxy, while the aim of the LOFAR observations were to more accurately determine RMs towards pulsars with existing RM data. The set-up at each telescope is further described below, and also summarised in Table 5.1.

Observations using the 100-metre Radio Telescope in Effelsberg, Germany (50.5247°N, 6.8836°E) were conducted using central horn of the 21-cm 7-beam prime focus receiver which is sensitive to 1.26–1.51 GHz frequencies. The central horn has two circular polarisation feeds, a system temperature of 25 K and the main beam FWHM is ∼550 arcseconds. The PSRIX backend (ROACH-board system for online coherent dedispersion) was used to coherently dedisperse and fold the data using the DM and frequency parameters obtained from the pulsar ephemeris file in the pulsar catalogue and the open-source pulsar data processing software package `dspsr` (van Straten and Bailes, 2011). The data were recorded at a centre frequency of 1347.5 MHz with 200 MHz bandwidth and divided into 256 frequency channels, see Table 5.1 for a summary. Dedicated observations were carried out during sessions on 27 February 2011, 31 July 2011, and 12 and 13 February 2012. Data were also obtained from regular MSP timing observations taken from 2011 to 2013 using the same parameters. 32 pulsars were observed once as part of the dedicated program, while the timing observations provided data at least two epochs for a further 12 pulsars. The lower elevation limit of the antenna is 8.1°, therefore sources above declination –31° can be observed. Preceding or following every observation, the telescope was pointed at least 1 arcminute away from the source and the pulsed noise diode was triggered and recorded. This injects a ∼100% linearly polarised square wave with a position angle of 45 degrees with respect to the linear feeds into

the receiver feed horn, and was used in the data analysis for calibrating the polarisation data, see Fig. 5.1.

Theoretical parameters of the Faraday spectrum obtained from RM-synthesis using these observations include: FWHM of the RMSF $\sim 260\,\mathrm{rad\,m^{-2}}$ (Eq. 3.8); maximum absolute Faraday depth accessible $\sim 15000\,\mathrm{rad\,m^{-2}}$ (Eq. 3.7); maximum scale resolvable in the Faraday spectrum $\sim 70\,\mathrm{rad\,m^{-2}}$ (Eq. 3.9).

Observations of 16 pulsars using the WSRT in the Netherlands (52.9147°N, 6.6033°E) were carried out on 14 and 16 December 2012, using the uncooled Multi Frequency Front End receivers in tied-array mode. The signals were recorded and processed using the PuMa-II pulsar backend (Karuppusamy et al., 2008). Eight slightly overlapping 10-MHz wide bands in the 310–380 MHz range were recorded to disk as baseband data, resulting in a total bandwidth of 71 MHz centred at 345.625 MHz, see Table 5.1 for a summary of the observational parameters. The baseband data were coherently dedispersed and folded using the DM and frequency parameters obtained from the pulsar ephemeris file in the pulsar catalogue. The open-source pulsar data processing software package `dspsr` was used to output eight 128-channel filterbank files. Further processing was carried out using the PSRCHIVE software[1] (Hotan et al., 2004) to add all eight frequency bands together and to output a single file with 512 frequency channels, 1024 pulse phase bins, and four polarisation parameters (Stokes I, Q, U, V). After the individual telescopes were phased up, no further polarisation calibration was carried out. This is not expected to affect the RMs obtained, but would be important for determining accurate polarisation pulse profiles.

Theoretical parameters of the Faraday spectrum obtained from RM-synthesis using the WSRT observations include: FWHM of the RMSF $\sim 11\,\mathrm{rad\,m^{-2}}$; maximum absolute Faraday depth accessible $\sim 2500\,\mathrm{rad\,m^{-2}}$; maximum scale resolvable in the Faraday spectrum $\sim 5\,\mathrm{rad\,m^{-2}}$.

LOFAR observations of 26 pulsars were performed between 6 Dec 2011 and 17 Aug 2013 (see van Haarlem et al., 2013, for a description of LOFAR). Several core stations were coherently combined using the LOFAR Blue Gene/P correlator/beam-former to form a tied-array beam (see Stappers et al., 2011, for a description of LOFAR's pulsar observing modes). The majority of the observations used 20 high-band antenna (HBA)

[1] see http://psrchive.sourceforge.net for more information.

core stations with a typical integration time of 10 minutes. Four pulsars were also observed using the six central low-band antennas (LBA) core stations with 27 minutes integration time. The data were written as 32-bit complex values for the two orthogonal linear polarisations. The data from the LOFAR observations were converted to 8-bit samples offline and coherently dedispersed and folded using the appropriate pulsar's rotational ephemeris obtained from the pulsar catalogue, and the `dspsr` program. This resulted in data with a centre frequency of 150 MHz and instantaneous bandwidth of 92 MHz for the HBA observations, and a centre frequency of 56 MHz and bandwidth of 10 MHz for the LBA observations, see see Table 5.1 for a summary of the observational parameters.

The theoretical parameters of the Faraday spectrum obtained from RM-synthesis using the LOFAR HBA observations include: FWHM of the RMSF $\sim 0.7\,\mathrm{rad\,m^{-2}}$; maximum absolute Faraday depth accessible $\sim 200\,\mathrm{rad\,m^{-2}}$; maximum scale resolvable in the Faraday spectrum $\sim 1\,\mathrm{rad\,m^{-2}}$. The theoretical parameters of the Faraday spectrum obtained from RM-synthesis using the LOFAR LBA observations include: FWHM of the RMSF $\sim 0.4\,\mathrm{rad\,m^{-2}}$; maximum absolute Faraday depth accessible $\sim 130\,\mathrm{rad\,m^{-2}}$; maximum scale resolvable in the Faraday spectrum $\sim 0.1\,\mathrm{rad\,m^{-2}}$.

TABLE 5.1: Summary of the parameters used for the polarisation observations for obtaining RMs using the Effelsberg 100-m, WSRT and LOFAR radio telescopes. Columns 1–7 indicate the observing telescope, range of observation dates, centre frequency, frequency bandwidth, individual channel width, sampling time and the expected FWHM of the RMSF from RM-synthesis. For further details, including the sources, integration times and dates, and results see Tables 5.2 and 5.3 for the Effelsberg observations, Table 5.4 for the WSRT observations and Table 5.5 for the LOFAR observations.

Telescope (Name)	Observation dates	ν (MHz)	$\Delta\nu$ (MHz)	$\delta\nu$ (MHz)	τ_{samp} (ms)	$\Delta\phi$ (rad m^{-2})
Effelsberg 100-m	2011–2013	1347.5	200	0.78	0.053	260
WSRT	14–16.12.2012	345.6	71	0.078	0.078	11
LOFAR HBA	2012–2013	150.9	91.8	0.195	0.08	0.65
LOFAR LBA	06.12.2011	55.6	9.8	0.012	0.08	0.36

5.4 Data reduction

The data were reduced to the standard pulsar software format and processed using the PSRCHIVE software package. The data were inspected, and any radio frequency interference (RFI) was removed using the interactive `pazi` tool. Also, during the inspection

the initial pulse frequency and DM were checked to ensure there was no obvious drift of the pulse in phase with respect to time or frequency. A new folding frequency was installed for pulsars with an initially incorrect pulse frequency by timing the pulsar (introduced in Section 1.2.2). In these cases an analytic pulse profile was constructed using the `paas` tool and convolved with the pulse profile from each sub-integration of the frequency-averaged data to create TOAs using the `pat` tool. These TOAs were subtracted from TOAs produced using the model of the original rotational ephemeris to determine the drift rate, from which an improved pulse frequency was determined and output in a new timing ephemeris using the `tempo2` software (Hobbs et al., 2006). A new DM was also determined and installed for pulsars with an initially incorrect value installed using the `pdmp` tool, which searches through a range of DMs to find the value that results in the largest S/N in the pulse profile.

The Effelsberg observations were polarisation calibrated using the square wave generated by the noise diode previously described, see Fig. 5.1 *left*. The differential gain and phase responses of the instrument were calculated independently for each frequency channel recorded, each of which has approximately 200 free model parameters corresponding to the Stokes parameters of the selected pulse longitudes and 12 instrumental parameters (see van Straten, 2002). The instrumental response parameters, calculated for the total bandwidth using the `pac` tool, is shown in Fig. 5.1 *right*. The differential phase is smoothly varying, except at the edges of the PSRIX system recording bands, the differential gain of the receptors is approximately 14% and the absolute gain decreases by approximately 50% with increasing frequency. To achieve accurate time-independent average polarisation profiles, the inverse matrices of the instrumental response and parallactic angle were calculated and applied to the observational data. For the phased array telescopes used for observations, i.e., WSRT and LOFAR, polarisation calibration is more difficult because of the numerous receiving elements and loss of the ability to inject a square wave noise diode signal. Since the average of multiple receiver elements is obtained after coherent summation, and calibrated pulse profiles were not essential to this work, the polarisation data from these telescopes were not calibrated, because this is not expected to significantly affect the RM obtained.

RMs were obtained from the data using the RM-synthesis method described in Section 3.3.3. Figure 5.2 shows the theoretical noiseless RMSF expected using each of the observational setups for the Effelsberg, WSRT and LOFAR HBA telescopes summarised in

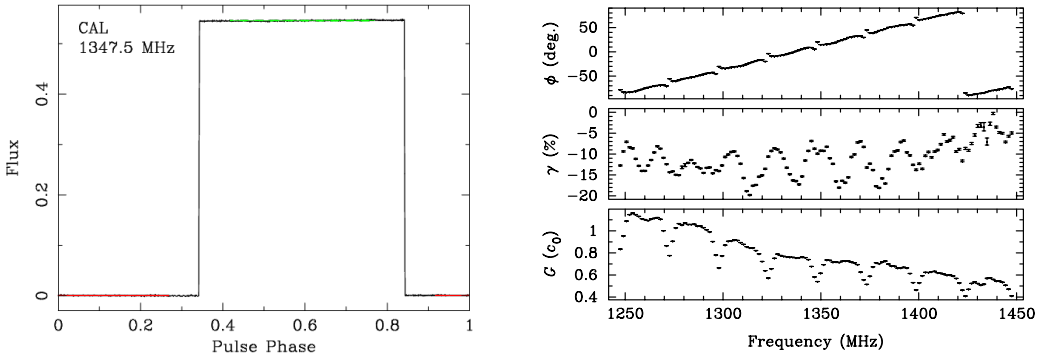

FIGURE 5.1: *Left:* the square wave produced by injection of the noise diode into the receiver. The black line shows the total intensity of the signal. The green line is centred on the mean of the on-pulse signal and the red line centred on the mean off-pulse noise. *Right:* Best-fit model parameters as a function of observing frequency after an observation of PSR J1730–2304 with the Effelsberg telescope centred at 1347.5 MHz with 200 MHz bandwidth on 16 Apr 2012 at 03:05 UT. *Upper to lower panels:* the differential phase, ϕ, the differential gain, γ, and the absolute gain, G, in units of the square root of the reference flux density.

Table 5.1. The RM-synthesis routine was written in `Python`, using the PSRCHIVE interface[2]. The time- and frequency averaged polarisation profiles were read, and dedispersed, and the polarisation profile obtained. RM-synthesis was performed using the Stokes Q and U parameters for pulse phase bins with total linear polarisation greater than the specified S/N threshold (usually S/N>7). Statistics including the linearly polarised S/N, the position in Faraday depth of the instrumental contribution in the Faraday spectra near ≈0 rad m^{-2}, the position and FWHM in Faraday depth of the peak due to the RM towards the pulsar were also collected for determining the uncertainties. The Stokes Q and U values as a function of wavelength squared were fit with a sinusoidal function of the same form as introduced in Section 3.3.1, $Q/U = \mathrm{A}(\lambda^2)\sin(2\,\mathrm{RM}\,\lambda^2+\delta)+\mathrm{C}$, using the initial RM value obtained from RM-synthesis and a non-linear least squares fit with the Levenberg-Marquardt algorithm (Levenberg, 1944). The errors from the covariance matrices from the Stokes Q- and U-frequency fit, and the instrumental error obtained from the position of the instrumental peak in the Faraday spectrum were combined in quadrature to obtain the total measurement uncertainty. The RMs and their uncertainties were recorded and the relevant information was plotted, see Section 5.5.

The ionospheric Faraday rotation was corrected for all of the observational data using the method described in Chapter 4. The ionospheric RM towards the pulsar was calculated for every hour that the source was above the horizon on the day of the observation using

[2]See http://psrchive.sourceforge.net/manuals/python/

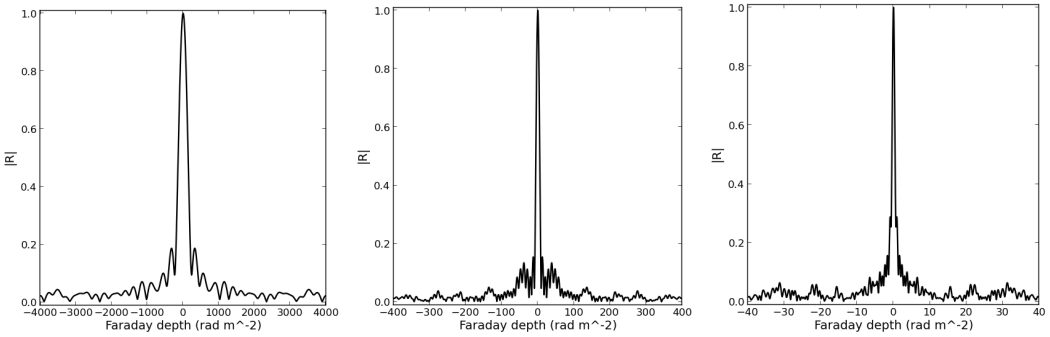

FIGURE 5.2: The normalised absolute value of the RMSF for: Effelsberg 100-m observations centred at 1347.5 MHz with 200 MHz bandwidth (*left*); WSRT observations centred at 345.625 MHz with 80 MHz bandwidth (*centre*); LOFAR observations centred at 150 MHz with 90 MHz bandwidth (*right*). Note the different scales of the x-axes in each case.

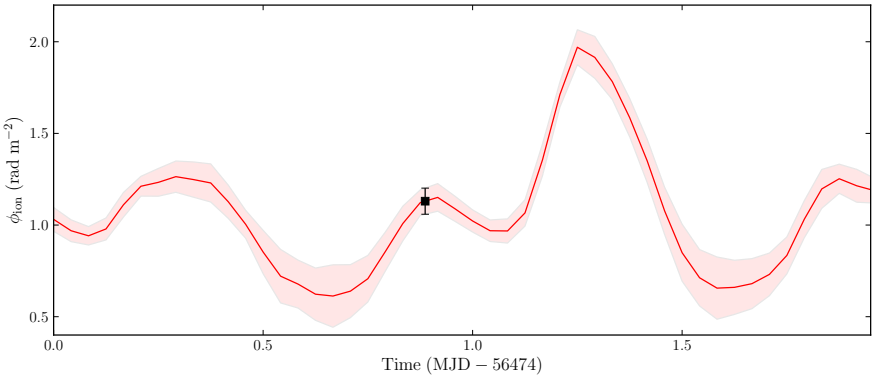

FIGURE 5.3: The modelled RM of the ionosphere (red line), and its uncertainty (shaded red area), towards PSR B2217+47 from the Effelsberg 100-m telescope on 56474 MJD. GNSS TEC maps and IGRF11 were used to determine the electron density and geomagnetic field, respectively, as explained in the text.The black square shows the epoch of the mid-point of the observation (21:17 UT) and the corresponding ionospheric RM and error, which is subtracted from the observed RM.

the TEC maps sourced from GNSS (Hernández-Pajares et al., 2009) and the geomagnetic field model IGRF11 (Finlay et al., 2010). These data were interpolated to calculate the ionospheric RM at the average time of the observation, see Fig. 5.3. Since the majority of the RMs were measured using a single observation, the modelled ionospheric RM was subtracted from the observed RM to obtain the RM due to the ISM alone, and the respective errors were added in quadrature. For the Effelsberg timing observations, where the pulsar RM was measured using at least two epochs, the RM of the ISM was found by calculating the offset between the observed and ionospheric RMs that yielded the minimum chi-squared value, the method also used in Chapter 4.

5.5 Results

Here we present the results of the RMs towards the 77 pulsars observed using the Effelsberg-100m Telescope, WSRT and LOFAR – 45 of which have not been published before. A comparison between the RMs already existing from literature and the RMs measured in this work is shown in Fig. 5.14.

5.5.1 Effelsberg-100m Telescope

Figure 5.4 shows eight examples of the calibrated polarisation pulse profiles for pulsars observed with the Effelsberg-100m Radio Telescope, centred at 1.3 GHz. The linearly polarised pulse profiles were corrected for Faraday rotation using the measured RM values shown in Tables 5.2 or 5.3, which also maximises the fractional linear polarisation. Seven of the pulsars were observed during the dedicated RM observations and one was observed as part of the timing observations. This sample shows some of the wide-ranging pulse profile characteristics exhibited by the pulsars, from which RMs were obtained.

PSRs J0055+5117, J0921+6254, J1811+0702, and J2023+5037 are isolated, non-recycled pulsars, PSRs J0621+1002, J1518+4904, and J1713+0747 are MSPs in binary systems, and PSR J1944+0907 is an isolated MSP. In general, the MSPs often display emission across a larger range in pulse phase than the non-recycled pulsars, i.e., they have larger duty cycles. For example, emission from PSR J0921+6254 is detected over 0.03 in pulse phase, whereas emission from PSR J1944+0907 is detected over 0.8 in pulse phase. This is thought to be due to the smaller size of the light cylinder, and hence the magnetosphere, around MSPs (Lorimer and Kramer, 2012).

The total intensity pulse profiles in Fig. 5.4 show from one (e.g. PSR J1713+0747) to four components (e.g. PSR J1944+0907). The linear and circular polarisation can either look similar (e.g. PSR J0921+6254) or very different (e.g. PSR J0621+1002) to the total intensity profiles. The fractional linear polarisation varies between 5% (PSR J1944+0907) and 50% (J1811+0702). The circular polarisation also shows interesting features, for example, there is a transition in handedness between the pulse components in the double peaked profiles of PSRs J0921+6254, J1713+0747, and the leading component of J1944+0907. A highly-polarised interpulse is present in the profile of PSR J2023+5037, similar to the pulse profile of PSR B0823+26 discussed in

Chapter 2, where both magnetic poles sweep through our LOS. An unpolarised precursor component is also detected before the double-peaked main pulse in the profile of PSR J1811+0702 (centred at 0.705 pulse phase). PSR J1811+0702 also shows a small scattering tail visible as an exponential decay of the pulse towards later pulse phases.

The linear polarisation angles (PAs), shown in the upper panels in Fig. 5.4, also show various interesting characteristics: constant PAs across the pulse phase (PSRs J1518+4904, and J1811+0702); larger swings in the PAs (PSRs J0055+5117, and J1944+0907); or jumps between orthogonal linearly polarised components (PSRs J0921+6254, and J1713+0747). Nevertheless, the Stokes Q and U parameters obtained from each phase bin were successfully used for obtaining RMs.

Figure 5.5 shows the typical output of the RM-synthesis `Python` routine. The data for PSR B1929+10 are shown, including the dedispersed pulse flux density as a function of frequency and pulsar phase (lower left), the RMs and uncertainties as a function of pulse phase (upper left), an example Faraday spectrum determined from the pulse phase with the highest S/N value in linear polarisation (upper right) and the sinusoidal variation of the Stokes Q and U parameter intensities over wavelength squared (lower right). Figure 5.5 shows that as S/N decreases, the RM uncertainties increase, which is expected (Eq. 3.10). This also shows that the RMs may vary across the pulse profile, somewhat like the PAs, which has previously been identified as a result of scattering (Noutsos et al., 2009). In cases such as this, the median RM value is reported in the results tables. The example Faraday spectrum shown in Fig. 5.5 has a FWHM of $300\,\mathrm{rad\,m^{-2}}$. The Stokes Q and U data also show the expected sinusoidal behaviour and appear to be generally well-fit. Some of the Stokes U data towards the shorter wavelengths (higher frequencies) shows deviation from the expected behaviour that is likely due to the resonance in the receiver at approximately 1430 MHz, see the lower left panel in Fig. 5.5. These affected frequencies were later removed using the RFI excision tool `pazi`.

The RMs measured using the single Effelsberg observations during the dedicated sessions are summarised in Table 5.2. The RMs measured using the multi-epoch timing observations are summarised in Table 5.3. Table 5.2 shows 32 pulsars for which an RM was determined. A further 6 pulsars were detected with sufficient S/N in total intensity, however, the linearly polarised intensity was insufficient (less than 3σ) to calculate the RM. Eight of these pulsars have previous RM data, and the values are in good agreement

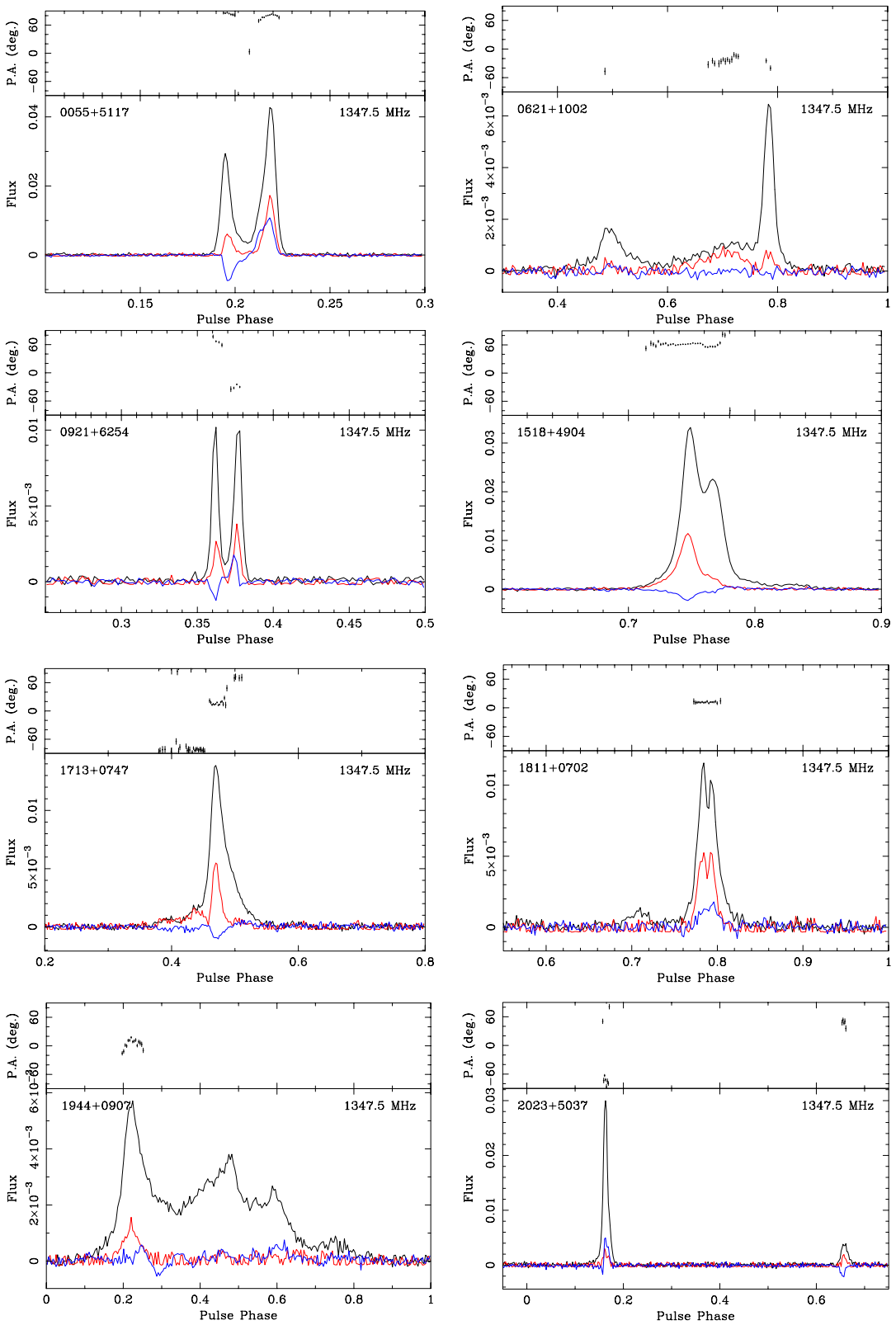

FIGURE 5.4: Example polarisation-calibrated pulse profiles for a sample of eight pulsars observed with the Effelsberg-100m Radio Telescope, centred at 1.3 GHz with 200 MHz bandwidth. In the larger lower panels, the pulsar J2000-name is given in the top left, the frequency is given at the top right, and the pulsar profile is shown in total intensity (black line) and linearly polarised (red line) and circularly polarised intensities (blue line) in arbitrary flux density units, as the profiles are not absolute flux calibrated. In the upper panels, the linear polarisation angle (although not absolutely calibrated) is shown for each pulse phase where the linearly polarised intensity is larger than 3σ.

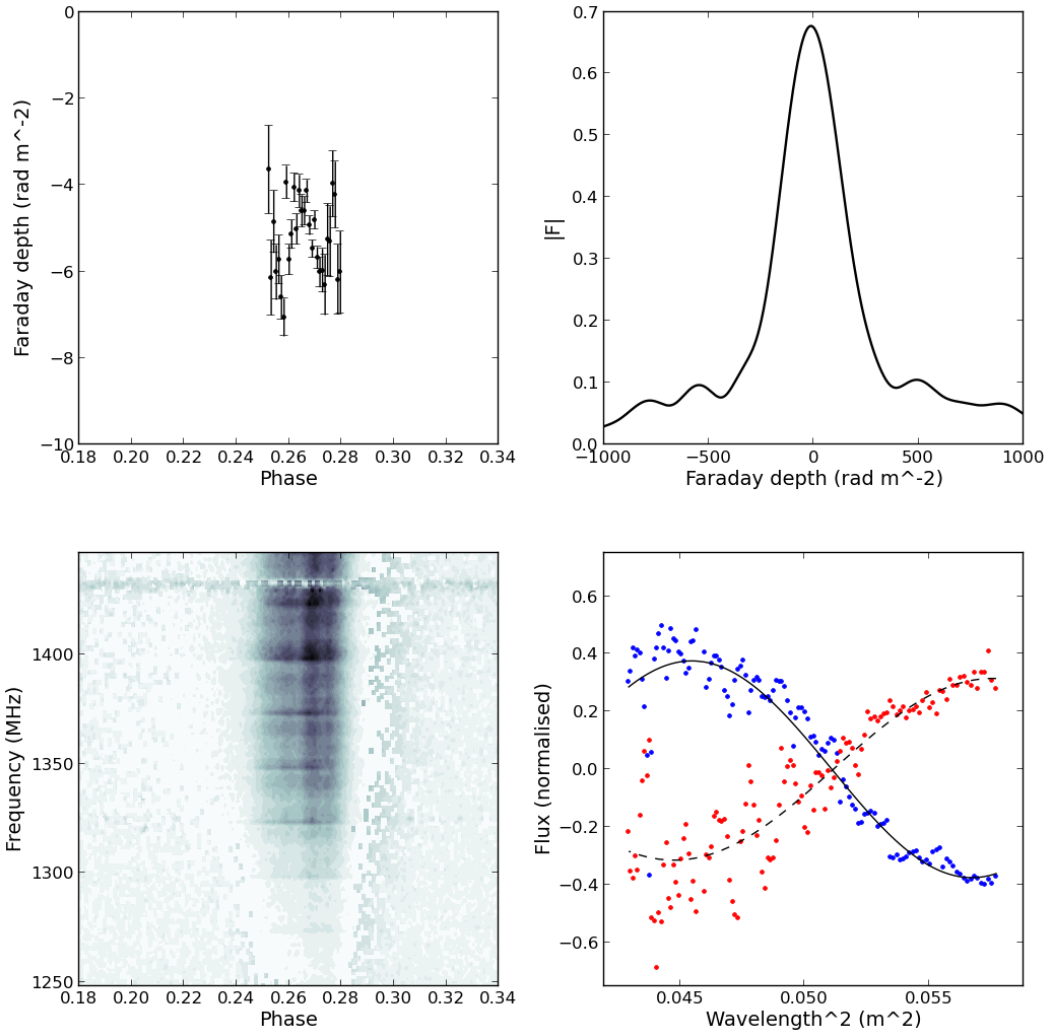

FIGURE 5.5: An overview plot showing the results from RM-synthesis using the polarisation profile of PSR B1929+10 obtained from a 5-minute Effelsberg 100-m Telescope observation centred at 1.3 GHz using 200 MHz bandwidth. *Lower left:* dedispersed pulse flux density as a function of frequency and pulse phase (white through grey to black indicates low to high intensity). *Upper left:* Rotation measures and uncertainties obtained for each pulse phase bin where the linear polarisation was greater than S/N=7. *Upper right:* Example Faraday spectrum obtained from the Stokes Q and U parameters shown in the lower right panel. *Lower right:* Stokes Q and U parameters (blue and red points, respectively) for a single pulse phase bin shown against observing wavelength squared, with the best-fit sinusoids (continuous and dashed lines, respectively).

within errors, see Fig. 5.14. RM values were determined for the 22 other pulsars for the first time from these observations. The 12 RMs summarised in Table 5.3 include eight RMs for which there are no published measurements.

TABLE 5.2: Summary of the results from the single Effelsberg observations. Columns 1–4 show the pulsar name, J2000-name, DM, and RM from version 1.5 of the ATNF pulsar catalogue (psrcat). The pulsars with no catalogue RM are indicated with an asterisk. Columns 5 and 6 show the average MJD of the observation, and integration time. Columns 7–10 show the measured RM, RM calculated for the ionosphere, resulting RM of the ISM, and average magnetic field magnitude and direction of the ISM parallel to the LOS towards the pulsar. All standard 1σ errors are shown in parentheses and are in units of the least significant digit of the quoted value.

PSR name	PSR jname	DM_{psrcat} ($pc\,cm^{-3}$)	RM_{psrcat} ($rad\,m^{-2}$)	Epoch (MJD)	T_{int} (min)	RM_{obs} ($rad\,m^{-2}$)	RM_{ion} ($rad\,m^{-2}$)	RM_{ISM} ($rad\,m^{-2}$)	$\langle B_{\parallel} \rangle$ (μG)
B0011+47	J0014+4746	30.85(7)	*	55969.77798	15	16(10)	1.094(66)	15(10)	0.6(4)
B0052+51	J0055+5117	44.125(15)	*	55969.79313	20	14.6(19)	1.026(59)	14(2)	0.38(5)
B0114+58	J0117+5914	49.423(4)	*	55619.80220	20	–11.5(80)	0.846(74)	–12(8)	-0.3(2)
J0215+6218	J0215+6218	84.00(5)	*	55619.81772	11	391(10)	0.760(79)	390(10)	5.7(1)
J0546+2441	J0546+2441	73.81(3)	*	55619.75646	20	34(6)	1.033(65)	33(6)	0.6(1)
J0621+1002	J0621+1002	36.6010(6)	*	55619.72743	20	73(25)	1.309(65)	71(25)	2.4(8)
J0656-2228	J0656-2228	32.39(17)	38(12)	55969.83973	15	39(19)	1.59(61)	40(20)	1.4(7)
J0726–2612	J0726–2612	69.4(4)	*	55969.86174	30	155(29)	1.675(87)	150(30)	2.7(5)
J0737–2202	J0737–2202	95.7(4)	*	55969.89828	30	–129(21)	1.451(98)	–130(20)	–1.7(3)
J0751+1807	J0751+1807	30.2489(3)	*	55969.91469	20	–43(15)	0.724(36)	–40(20)	–1.8(6)
B0823+26	J0826+2637	19.454(4)	5.9(3)	55969.97430	20	6.5(25)	0.670(63)	6(3)	0.4(2)
B0834+06	J0837+0610	12.889(6)	23.6(7)	55969.95866	15	25.2(38)	0.870(66)	24(4)	2.3(4)
J0838–2621	J0838–2621	116.90(5)	86(13)	55969.94487	35	79.9(97)	1.56(10)	80(10)	0.8(1)
B0917+63	J0921+6254	13.158(18)	*	55970.02435	20	–15.9(58)	0.590(82)	–17(6)	–1.6(5)
J1022+1001	J1022+1001	10.2521(1)	–0.6(5)	55969.99039	20	–2.0(22)	0.866(73)	–3(2)	–0.4(2)
J1024–0719	J1024–0719	6.48520(5)	–8.2(8)	55970.00574	20	–6.5(86)	1.129(81)	–8(8)	–1(1)
J1453+1902	J1453+1902	14.049(4)	*	55970.12268	35	26.5(78)	0.860(80)	25(8)	2.2(7)
J1503+2111	J1503+2111	11.75(6)	*	55970.14430	30	–49(20)	0.815(67)	–50(20)	–5(2)
J1627+1419	J1627+1419	33.8(6)	*	55970.16966	15	31(19)	0.851(55)	30(20)	1.1(7)
J1640+2224	J1640+2224	18.4260(8)	*	55970.20768	30	–41(17)	0.761(72)	–40(20)	–3(1)
J1713+0747	J1713+0747	15.9915(2)	8.4(6)	55970.22199	20	9.9(18)	0.941(78)	9(2)	0.7(1)
J1811+0702	J1811+0702	57.8(1)	*	55970.25740	10	–3.4(81)	1.135(64)	–5(8)	–0.1(2)
J1842+0257	J1842+0257	148.1(11)	*	55969.49311	10	107(32)	2.532(76)	100(30)	0.9(3)
B1918+26	J1920+2650	27.62(9)	*	55969.54719	10	26(29)	1.806(67)	20(30)	1(1)
B1929+10	J1932+1059	3.180(4)	–6.87(2)	55969.43240	5	–5.1(50)	2.307(62)	–7(5)	–3(2)
B1935+25	J1937+2544	53.221(5)	*	55969.56739	10	–27(10)	1.742(61)	–30(10)	–0.69(6)
J1944+0907	J1944+0907	24.34(2)	*	55969.53077	25	35(13)	2.312(72)	30(10)	1.6(7)
B2000+32	J2002+3217	142.21(3)	*	55969.58228	10	82(17)	1.610(59)	80(20)	0.7(2)
J2008+2513	J2008+2513	60.554(9)	*	55969.57548	10	–81(52)	1.760(59)	–80(50)	–2(1)
B2022+50	J2023+5037	33.021(3)	*	55969.60038	10	7(12)	1.751(69)	6(10)	0.2(4)
J2307+2225	J2307+2225	7.08(3)	*	55969.65520	15	–3.1(51)	1.768(50)	–5(5)	–0.9(9)
J2317+1439	J2317+1439	21.907(3)	*	55969.70872	25	–13.4(93)	1.713(47)	–15(9)	–0.9(5)

TABLE 5.3: Summary of the results from selections of Effelsberg multi-epoch observations. Columns 1–4 show the pulsar name, J2000-name, DM, and RM from version 1.5 of the ATNF pulsar catalogue (psrcat), except for PSRs J0426+4933, J2036+2835, J2216+5759 which were obtained from Barr et al. (2013). The pulsars with no catalogue DM or RM are indicated with an asterisk. Columns 5 and 6 show the range in MJD of the observation and the number of 30-minute observations used to measure the RM. Columns 7–12 show the measured DM (if required as an alternative to the catalogue version), weighted average of the measured RM, weighted average of the ionospheric RM, resulting RM of the ISM and chi-squared value, and average magnetic field magnitude and direction of the ISM parallel to the LOS towards the pulsar. All standard 1σ errors are shown in parentheses and are in units of the least significant digit of the quoted value.

PSR name	PSR jname	DM_{psrcat} ($pc\,cm^{-3}$)	RM_{psrcat} ($rad\,m^{-2}$)	Epoch range (MJD)	N_{obs}	DM_{obs} ($pc\,cm^{-3}$)	RM_{obs} ($rad\,m^{-2}$)	RM_{ion} ($rad\,m^{-2}$)	RM_{ISM} ($rad\,m^{-2}$)	χ^2	$\langle B_{\parallel} \rangle$ (μG)
J0348+0432	J0348+0432	40.46313(11)	49.5(13)	56032.74176–56032.74176	1	psrcat	41.9(47)	2.484(61)	39(5)	*	1.2(1)
J0426+4933	J0426+4933	88	*	56225.83400–56277.71077	2	84.4(20)	–79.8(62)	0.797(63)	–81(6)	0.4	–1.2(1)
J0613–0200	J0613–0200	38.77919(6)	9.7(11)	55973.66049–56191.20648	5	psrcat	10.4(39)	2.276(80)	8(4)	2.2	0.3(1)
J1518+4904	J1518+4904	11.61139(8)	*	55997.00763–56207.38604	3	psrcat	–5.9(30)	0.994(69)	–7(3)	0.1	–0.7(3)
J1730–2304	J1730–2304	9.617(2)	-7.2(22)	55997.19189–56298.37754	4	psrcat	–7.5(50)	3.05(11)	–10(5)	1.5	–1.3(7)
J1756–2251	J1756-2251	121.18(2)	*	56298.39895–56298.39895	1	psrcat	15.5(16)	3.614(85)	12(2)	*	0.12(2)
B1913+16	J1915+1606	168.77(1)	430(73)	56115.08298–56135.71263	2	psrcat	356(15)	2.114(76)	350(20)	0.3	2.6(2)
J1918-0642	J1918–0642	26.554(10)	*	56298.51203–56334.44988	2	psrcat	18.4(20)	2.888(93)	16(2)	0.8	0.74(9)
J2010—1323	J2010-1323	22.160(2)	*	56298.60381–56298.60381	1	psrcat	–44.3(61)	2.61(13)	–47(6)	*	–2.6(3)
J2036+2835	J2036+2835	99	*	56277.47479–56310.35963	2	83.3(29)	–99.0(24)	2.024(78)	–101(3)	0.9	–1.49(6)
J2216+5759	J2216+5759	176	*	56256.68061–56277.57413	2	167.47(90)	–13.0(33)	1.418(38)	–14(3)	0.4	–0.11(2)
J2302+4442	J2302+4442	13.762(6)	*	56192.86817–56277.62766	2	psrcat	22.9(46)	1.487(50)	20(5)	1.0	1.8(4)

5.5.2 WSRT

Figure 5.6 shows an example output of the RM-synthesis pipeline from the WSRT observations and Table 5.4 summarises the RM and DM measurements obtained. Figure 5.6 shows the dedispersed pulse flux density as a function of frequency and pulsar phase of PSR J2302+6028 (lower left), the RMs and uncertainties as a function of pulse phase (upper left), an example Faraday spectrum determined from the pulse phase with the highest S/N value in linear polarisation (upper right) and the sinusoidal variation of the Stokes Q and U parameter intensities over wavelength squared (lower right). PSR J2302+6028 is a relatively weak pulsar, with a relatively narrow single component in the pulse profile, and a relatively large absolute RM value for this sample of pulsars. The example Faraday spectrum shown in Fig. 5.6 has a FWHM of $12\,\mathrm{rad\,m^{-2}}$. Therefore, unlike the Faraday spectra obtained from the 1.3 GHz data, the peak caused by the RM value towards the pulsar is far removed from any instrumental contribution near $0\,\mathrm{rad\,m^{-2}}$, which is also the case for the LOFAR data, see below. This figure also shows that the RMs as a function of phase show smaller variations that are within the uncertainties, and that the uncertainty in RM increases as S/N decreases. The Stokes Q and U data also show the expected sinusoidal behaviour and appear to be generally well-fit, despite the much higher frequency of the sinusoidal variation due to the larger RM value and lower observing frequency compared to that in Fig. 5.5.

Table 5.4 shows that RMs towards 14 pulsars without previously published data were obtained. Two bright pulsars with catalogued RMs were observed on both days to check the consistency with the catalogued RMs and also between the different observing epochs. The RMs measured from the two observations of PSR B0329+54 spaced two days apart are in very good agreement with each other. The weighted mean of the observations is –61.84 ± 0.5 rad $\mathrm{m^{-2}}$, which is also in good agreement (2σ) with the catalogue value. An non-significant change in RM towards B0329+54 over time was indicated from published data in Chapter 3. The observations from this work indicate that there may still be a small increase in the RM at a rate of 0.04(1) rad $\mathrm{m^{-2}}$ $\mathrm{year^{-1}}$, although a factor of ten less than the rate of 0.4(20) rad $\mathrm{m^{-2}}$ $\mathrm{year^{-1}}$ previously determined from four epochs published in the literature. However, given the small sample size, it would be interesting to monitor this and other similar sources over time using more precise low-frequency observations to further constrain this. The RMs measured

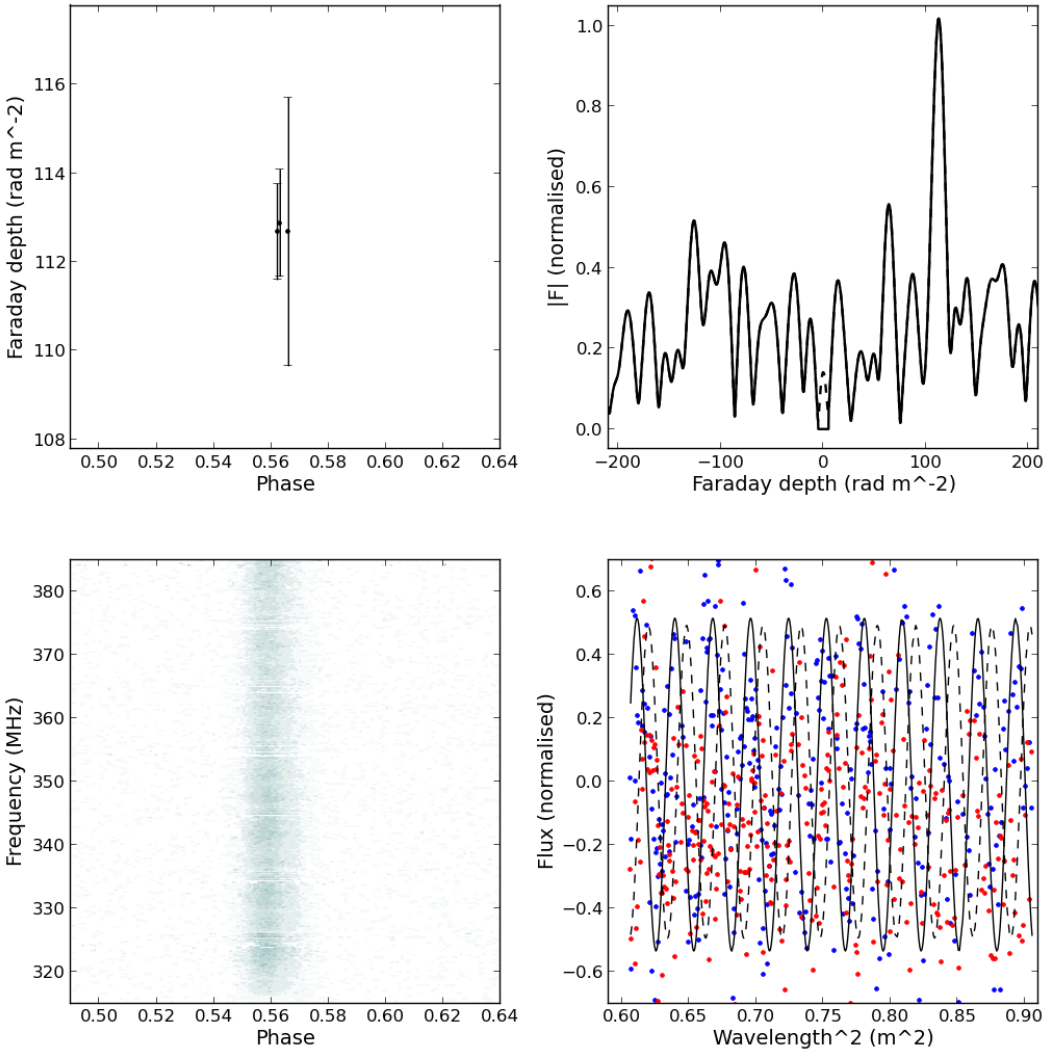

FIGURE 5.6: A 22-minute WSRT observation of PSR J2302+6028 at 350 MHz using 70 MHz bandwidth. *Lower left:* pulse profile in total intensity (black) and linear (red) and circular (blue) polarised intensity; *Lower right:* Stokes Q (blue) and U (red) parameters for a single pulse phase bin against observing wavelength squared, with fitted sinusoids (continuous and dashed lines, respectively); *Upper left:* Faraday depths and errors obtained for each pulse phase bin where the linear polarisation was above the specified S/N; *Upper right:* Example Faraday spectrum obtained from the Stokes Q and U parameters in the lower right panel, the subtracted instrumental signal around 0 rad m^{-2} is shown as a dashed line.

from the two observations of PSR B2016+28 also spaced two days apart are in excellent agreement. The weighted mean of the observations is –35.0(5) rad m^{-2}, which is in excellent agreement with the catalogue value. Also, the 1σ error is less than half of that for the catalogue value.

TABLE 5.4: Summary of the results from the WSRT observations. Columns 1–4 show the pulsar name, J2000-name, DM, and RM from version 1.5 of the ATNF pulsar catalogue (psrcat). The pulsars with no catalogue RM are indicated with an asterisk. Columns 5 and 6 show the average MJD of the observation and integration time. Columns 7–11 show the measured DM (if a DM correction was necessary), measured RM, RM calculated for the ionosphere, resulting RM of the ISM, and average magnetic field magnitude and direction of the ISM parallel to the LOS towards the pulsar. All standard 1σ errors are shown in parentheses and are in units of the least significant digit of the quoted value.

PSR name	PSR jname	DM_{psrcat} ($pc\,cm^{-3}$)	RM_{psrcat} ($rad\,m^{-2}$)	Epoch (MJD)	T_{int} (min)	DM_{obs} ($pc\,cm^{-3}$)	RM_{obs} ($rad\,m^{-2}$)	RM_{ion} ($rad\,m^{-2}$)	RM_{ISM} ($rad\,m^{-2}$)	$\langle B_{\parallel} \rangle$ (μG)
B0329+54	J0332+5434	26.833(10)	–63.7(4)	56275.88715	5	psrcat	–61.38(82)	0.474(62)	–61.9(8)	–2.84(3)
B0329+54	J0332+5434	26.833(10)	–63.7(4)	56277.91932	5	psrcat	–61.33(55)	0.474(41)	–61.8(5)	–2.83(2)
J0546+2441	J0546+2441	73.81(3)	*	56275.90363	20	psrcat	18.6(18)	0.679(52)	18(2)	0.30(3)
J0621+1002	J0621+1002	36.6010(6)	*	56275.95775	40	36.523(3)	–56.7(47)	0.834(52)	–58(5)	–1.9(2)
J0711+0931	J0711+0931	45.0(1)	*	56277.96086	55	46.17(11)	–60.3(27)	0.769(79)	–61(3)	–1.63(7)
J0815+0939	J0815+0939	52.667(9)	*	56277.99419	45	psrcat	–54.0(52)	0.781(56)	–55(5)	–1.3(1)
B1257+12	J1300+1240	10.16550(3)	*	56276.05393	20	10.158(2)	7.7(27)	0.768(43)	7(3)	0.8(3)
J1652+2651	J1652+2651	40.8(2)	*	56275.49066	25	40.72(8)	–30.4(13)	1.62(83)	–32(1)	–0.97(4)
B1726–00	J1728–0007	41.09(3)	*	56277.50812	15	psrcat	38.4(41)	2.542(41)	36(4)	1.1(1)
J1819+1305	J1819+1305	64.9(4)	*	56275.50830	25	64.6(2)	–115.6(29)	1.861(77)	–117(3)	–2.24(6)
B1935+25	J1937+2544	53.221(5)	*	56277.73013	30	psrcat	–32.0(11)	0.844(40)	–33(1)	–0.76(3)
B1953+29	J1955+2908	104.58(5)	*	56275.74663	20	104.511(1)	–16.2(24)	0.648(69)	–17(2)	–0.20(3)
B2000+32	J2002+3217	142.21(3)	*	56277.78802	35	psrcat	87.2(7)	0.529(19)	87(7)	0.75(6)
B2016+28	J2018+2839	14.172(4)	–34.6(14)	56275.79594	10	psrcat	–34.52(38)	0.533(56)	–35.0(4)	–3.05(3)
B2016+28	J2018+2839	14.172(4)	–34.6(14)	56277.79709	10	psrcat	–34.59(60)	0.505(17)	–35.0(6)	–3.05(5)
B2035+36	J2037+3621	93.56(6)	*	56275.81686	24	93.73(9)	–254.9(83)	0.470(71)	–255(8)	–3.6(1)
J2208+5500	J2208+5500	101.03(0)	*	56277.84442	42	104.66(9)	89.4(18)	0.486(28)	89(2)	1.05(2)
J2302+6028	J2302+6028	156.7(1)	*	56275.83628	22	psrcat	113.91(50)	0.470(78)	113.4(5)	0.891(4)

5.5.3 LOFAR

Figure 5.7 shows an example output of the RM-synthesis pipeline from the LOFAR observations and Table 5.5 shows the results of the RM measurements. Figure 5.7 shows the dedispersed pulse flux density as a function of frequency and pulsar phase of PSR B1133+16 (lower left), the RMs and uncertainties as a function of pulse phase (upper left), an example Faraday spectrum determined from the pulse phase with the highest S/N value in linear polarisation (upper right) and the sinusoidal variation of the Stokes Q and U parameter intensities over wavelength squared (lower right). PSR B1133+16 is one of the brightest pulsars in the northern sky, with a relatively narrow double-peaked pulse profile with some emission bridging between the two components. The DM and absolute RM values are relatively small because the pulsar is relatively nearby, 350 pc (Manchester et al., 2005a). Due to the low-frequency and large bandwidth, the example Faraday spectrum shown in Fig. 5.7 has a FWHM of $0.7\,\mathrm{rad\,m^{-2}}$. Therefore, the peak caused by the RM value towards the pulsar is clearly distinguished from any instrumental contribution near $0\,\mathrm{rad\,m^{-2}}$. There also appears to be slight pulse profile evolution towards lower frequencies, where the latter component moves towards slightly later pulse phases. Despite this, Fig. 5.7 also shows that the RMs as a function of phase are constant within errors. The Stokes Q and U data also show good agreement with the expected sinusoidal behaviour and appear to be generally well fit.

The RMs towards 26 pulsars presented in Table 5.5 measured using LOFAR observations are amongst the most accurate measurements of the Faraday rotation caused by the magneto-ionic ISM to date. The largest and smallest errors for the ionospheric Faraday rotation calibrated data are 0.2 and 0.03 rad $\mathrm{m^{-2}}$, respectively. The mean error of the RMs after calibration for the ionosphere is 0.1 rad $\mathrm{m^{-2}}$. There are only eight pulsars catalogued with RM errors less than or equal this value, six of these were calibrated for ionospheric RM (for the two other pulsars this is not clear). The main limitation on the precision of the RM measurement from LOFAR observations becomes the S/N of the linear polarisation and the uncertainties in the ionospheric Faraday rotation calculated using TEC maps. The most common integration time for the observations was just 10-minutes. If a situation arises where even more precise RM data are required, the integration times could be lengthened and observations with the LOFAR LBAs would achieve this.

Two pulsars in Table 5.5 were observed twice, PSRs B0809+74 and J1012+5307. The RMs of the ISM towards the pulsars are expected to remain relatively constant between the observation epochs and this appears to be the case for both. The RM towards PSR B0809+74, measured from two observations separated by 1.3 days, is –13.9 ± 0.1 rad m^{-2} and –13.85 ± 0.07 rad m^{-2}. These measurements agree within the 1σ errors stated and the weighted mean for which can be calculated; –13.87 ± 0.04 rad m^{-2}. The RM towards PSR J1012+5307 measured from two observations almost 9 days apart is 3.0 ± 0.2 rad m^{-2} and 2.92 ± 0.08 rad m^{-2}, which also agree within the 1σ errors. The weighted mean of the two RM measurements is 2.94 ± 0.05 rad m^{-2}. These repeated measurements benefit the measurement of the RM and decrease the overall RM error and also provide a check of the stability of the ionospheric Faraday rotation calibration. Calculating the mean of all of the ionospheric Faraday-corrected RMs is equivalent to calculating the mean of all of the observed RMs and subtracting the mean of all ionospheric RMs.

Table 5.5 also shows that despite the smaller bandwidth used for the LBA observations (10 MHz) compared to the HBA observations (92 MHz), the precision of the measured RM values are approximately equivalent. Since the sensitivity of the LBA array is lower than that of the HBA array, the LBAs are more suitable for monitoring changes in RM towards brighter pulsars, and the HBAs are better suited to measuring RMs towards more known pulsars which do not have previously published RM data.

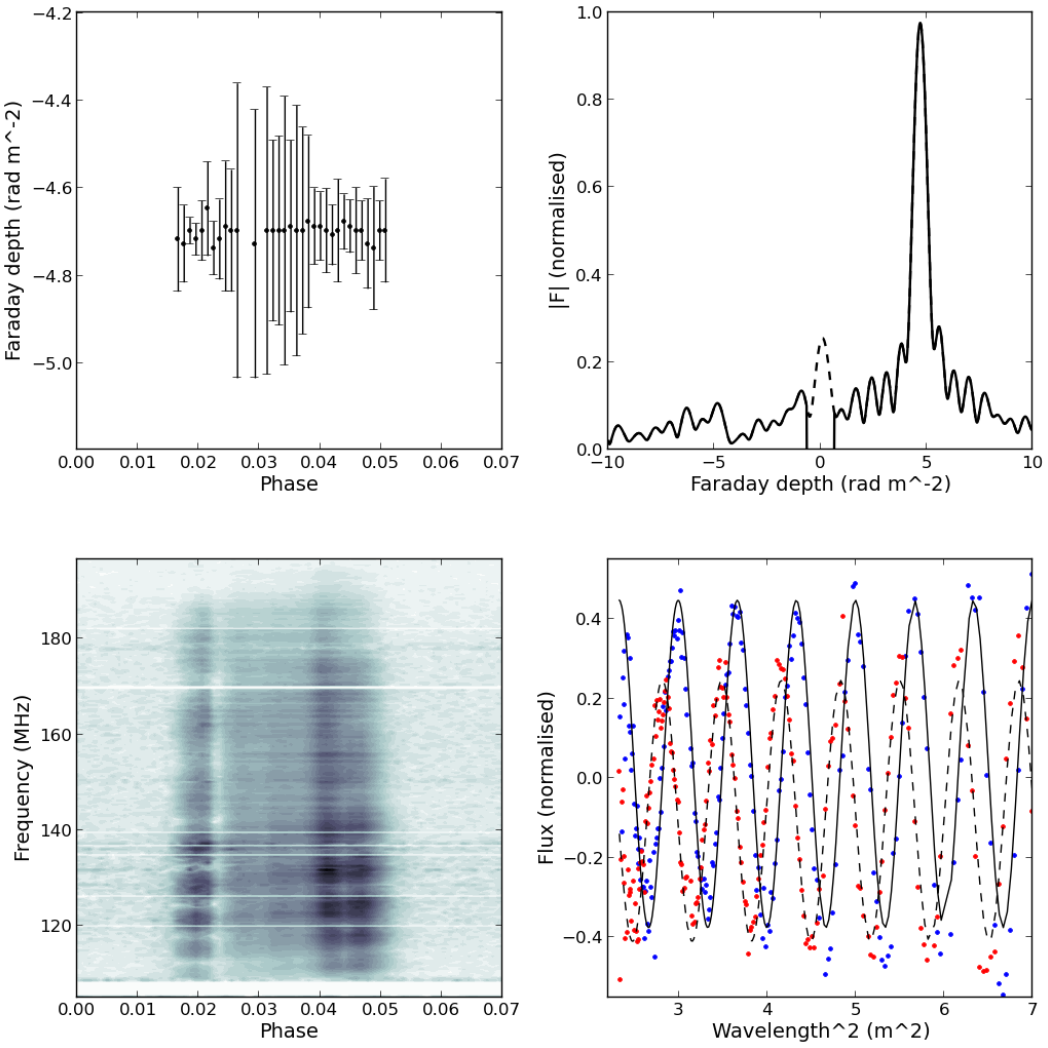

FIGURE 5.7: 10-minute LOFAR observation of PSR B1133+16 at 150.8 MHz using 91 MHz bandwidth and 20 core HBA stations. *Lower left:* linear polarisation of the pulse against frequency, white gaps in frequency indicate where RFI was removed; *Lower right:* Stokes Q (blue) and U (red) parameters for a single pulse phase bin against observing wavelength squared, with fitted sinusoids (continuous and dashed lines, respectively); *Upper left:* Faraday depths and errors obtained for each pulse phase bin where the linear polarisation was above the specified S/N; *Upper right:* Example Faraday spectrum obtained from the Stokes Q and U parameters in the lower right panel, the subtracted instrumental signal around 0 rad m^{-2} is shown as a dashed line.

TABLE 5.5: Summary of the results from the LOFAR HBA and LBA observations, which are shown above and below the dividing line, respectively. Columns 1–4 show the pulsar name, J2000-name, DM and RM from version 1.5 of the ATNF pulsar catalogue (psrcat). The pulsars with no catalogue RM are indicated with an asterisk. Columns 5–7 show the LOFAR observation ID number, average MJD and integration time. Columns 8–12 show the measured DM, measured RM, RM calculated for the ionosphere, resulting RM of the ISM and average magnetic field magnitude and direction of the ISM parallel to the LOS towards the pulsar. All standard 1σ errors are shown in parentheses and are in units of the least significant digit of the quoted value.

PSR name	PSR jname	DM_{psrcat} ($pc\,cm^{-3}$)	RM_{psrcat} ($rad\,m^{-2}$)	obsID	Epoch (MJD)	T_{int} (min)	DM_{obs} ($pc\,cm^{-3}$)	RM_{obs} ($rad\,m^{-2}$)	RM_{ion} ($rad\,m^{-2}$)	RM_{ISM} ($rad\,m^{-2}$)	$\langle B_{\parallel} \rangle$ (μG)
J0030+0451	J0030+0451	4.333(1)	*	L103783	56368.51529	7	4.3328(1)	7.29(20)	6.37(20)	0.9(3)	0.261(9)
B0031–07	J0034–0721	11.38(8)	9.8(2)	L77919	56258.80622	10	10.88(5)	10.941(20)	1.089(70)	9.85(7)	1.12(1)
B0136+57	J0139+5814	73.779(6)	–90(4)	L77917	56258.83687	10	73.816(2)	–93.280(20)	0.444(80)	–93.72(8)	–1.564(1)
B0301+19	J0304+1932	15.737(9)	–8.3(3)	L167146	56513.25014	45	15.670(17)	–6.625(73)	1.87(12)	–8.5(1)	–0.67(1)
B0450+55	J0454+5543	14.495(7)	10(3)	L168085	56521.27063	15	14.589(4)	7.291(56)	1.401(83)	5.9(1)	0.497(8)
B0525+21	J0528+2200	50.937(17)	–39.6(2)	L168084	56521.28421	25	50.831(46)	–37.918(85)	1.818(98)	–39.7(1)	–0.963(3)
B0809+74	J0814+7429	6.116(18)	–11.7(13)	L77929	56258.84491	10	5.717(17)	–13.485(20)	0.43(10)	–13.9(1)	–3.00(2)
B0809+74	J0814+7429	6.116(18)	–11.7(13)	L78237	56260.13398	10	5.746(9)	–13.418(20)	0.428(70)	–13.85(7)	–3.00(2)
B0823+26	J0826+2637	19.454(4)	5.9(3)	L78236	56260.14376	10	19.473(28)	5.894(10)	0.564(60)	5.33(6)	0.337(4)
B0834+06	J0837+0610	12.889(6)	23.6(7)	L78235	56260.15272	10	12.867(67)	25.958(10)	0.768(70)	25.19(7)	2.41(1)
B0950+08	J0953+0755	2.958(3)	–0.66(4)	L78234	56260.20408	10	2.969(2)	2.139(10)	0.666(60)	1.47(6)	0.61(3)
J1012+5307	J1012+5307	9.0233(2)	*	L81047	56280.20689	20	9.0249(2)	3.47(20)	0.469(40)	3.0(2)	0.41(3)
J1012+5307	J1012+5307	9.0233(2)	*	L81268	56289.15626	20	9.0248(1)	3.313(60)	0.397(60)	2.92(8)	0.40(1)
J1022+1001	J1022+1001	10.2521(1)	–0.6(5)	L81050	56280.15930	20	10.254(1)	2.114(80)	0.788(50)	1.33(9)	0.16(1)
B1133+16	J1136+1551	4.864(5)	1.1(2)	L78233	56260.27569	10	4.825(63)	4.703(20)	0.804(70)	3.90(7)	1.00(2)
B1237+25	J1239+2453	9.242(6)	–0.33(6)	L78449	56261.32141	10	9.254(9)	0.862(50)	1.057(60)	–0.19(8)	–0.03(1)
B1257+12	J1300+1240	10.16550(3)	*	L78454	56261.34427	30	10.1555(1)	8.95(20)	1.334(60)	7.6(2)	0.92(3)
B1508+55	J1509+5531	19.613(20)	0.8(7)	L78448	56261.37513	10	19.616(5)	2.629(50)	1.167(60)	1.46(8)	0.092(5)
B1911–04	J1913–0440	89.385(10)	4.4(9)	L77835	56258.62151	10	89.368(5)	6.131(90)	2.255(50)	3.9(1)	0.053(1)
B1919+21	J1921+2153	12.455(6)	–16.5(5)	L77912	56258.73408	10	12.431(71)	–16.070(50)	0.890(50)	–16.96(7)	–1.68(1)
B1929+10	J1932+1059	3.180(4)	–6.87(2)	L77913	56258.72573	10	3.178(1)	–5.814(20)	1.110(40)	–6.92(4)	–2.68(2)
B1937+21	J1939+2134	71.0398(2)	–10(9)	L138647	56434.14446	30	71.021(1)	–9.528(70)	1.721(60)	–11.25(9)	–0.195(2)
B1953+50	J1955+5059	31.974(3)	–22(2)	L77897	56258.71720	10	31.981(3)	–22.956(10)	0.774(50)	–23.73(5)	–0.914(2)
B2021+51	J2022+5154	22.648(6)	–6.5(9)	L77910	56258.76456	10	22.550(4)	–6.231(30)	0.544(60)	–6.78(7)	–0.370(3)
J2043+1711	J2043+1711	20.70987(3)	*	L84518	56311.52926	20	20.7124(2)	–4.19(20)	2.093(70)	–6.3(2)	–0.37(1)
B2111+46	J2113+4644	141.26(9)	–224(2)	L77909	56258.77295	10	141.557(7)	–221.06(20)	0.527(60)	–221.6(2)	–1.929(1)
B2217+47	J2219+4754	43.519(12)	–35.3(18)	L77908	56258.78108	10	43.481(29)	–35.275(1)	0.518(60)	–35.79(6)	–1.014(2)
B2224+65	J2225+6535	36.079(9)	–21(3)	L77907	56258.78946	10	36.403(36)	–22.377(30)	0.504(70)	–22.88(8)	–0.774(3)
B0809+74	J0814+7429	6.116(18)	–11.7(13)	L36789	55901.19792	27	5.764(6)	—13.292(17)	0.579(61)	–13.87(6)	–2.96(1)
B0834+06	J0837+0610	12.889(6)	23.6(7)	L36791	55901.15623	27	12.934(4)	26.204(23)	0.996(68)	25.20(7)	2.401(7)
B0950+08	J0953+0755	2.958(3)	–0.66(4)	L36787	55901.23957	27	2.972(1)	2.381(16)	0.911(46)	1.47(5)	0.61(2)
B1133+16	J1136+1551	4.864(5)	1.1(2)	L36785	55901.28128	27	4.846(4)	5.128(36)	1.070(59)	4.06(7)	1.03(2)

The approximate locations of known pulsars as viewed from above the galactic plane, calculated using the NE2001 model (Cordes and Lazio, 2002), both without and with RM data (from the catalogue and this work) are shown in Fig. 5.8. This shows that we obtained RM data for a good sample of pulsars both close to, and further from, the Sun in the northern sky in Galactic quadrants I to III. The location of all catalogued RMs on the sky towards pulsars (from the catalogue and this work) and extragalactic sources (from the catalogue) are shown in Fig. 5.9. This shows that there are many catalogued RMs towards pulsars in the Galactic plane, and this work obtained a good sample of pulsars both towards the Galactic disk and the halo in the northern sky. These are complemented by the large sample of RMs towards EG sources, also mostly in the northern sky, which provides information about the entire LOS through the Galaxy.

5.6 Wavelet analysis method for reconstructing the Galactic magnetic field

To reduce the effect of small scale fluctuations, due to random small-scale structures, in the reconstruction of the GMF from individual RM data points throughout the galaxy, applying a smoothing technique to the data set allows the large-scale GMF to be more accurately determined. Various filters were tested for this purpose, see Fig. 5.10, to determine which provided a good reconstruction of a test signal while smoothing over small-scale noise fluctuations. The specialised wavelet filter (Fig. 5.10, *right*) is one such method which can be used in conjunction with RM data to determine the large-scale GMF (Stepanov et al., 2002). Benefits of using this method include:

- The noise in RM data caused by small-scale fluctuations of the ISM and unequal spacing of data points can be filtered out.
- The noise amplification is minimised in the analysis of the integral quantities of RM and DM.

The approach we used included decomposing the signal of interest using wavelets, which are a basis of self-similar functions. Often compared to the Fourier transform in which the signals are represented as a sum of sinusoidal functions, wavelets are localised in both physical and Fourier space and are also in discrete form, which makes them they are less

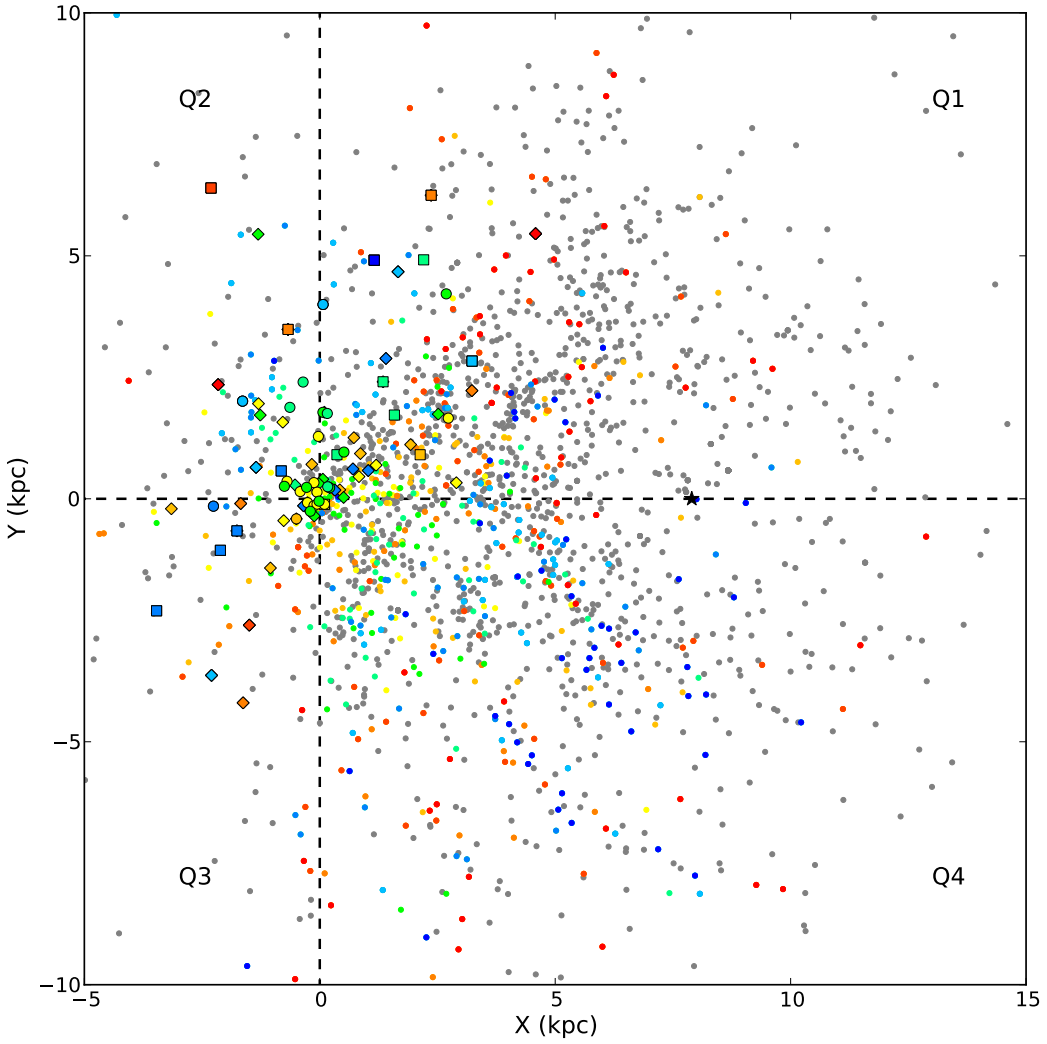

FIGURE 5.8: The approximate location of known pulsars in the Galaxy, using the NE2001 electron density model. Catalogued pulsars without RM data are shown as grey points, catalogued pulsars with RM data are shown as coloured points. The pulsars observed for this work using Effelsberg, WSRT and LOFAR are shown as coloured diamonds, squares and circles, respectively. Points with yellow through orange to red colours represent increasingly positive RMs whilst points with green through cyan to blue colours represent increasingly negative RMs. The position of the Galactic Centre is marked with a black star, and the Galactic quadrants are also labelled.

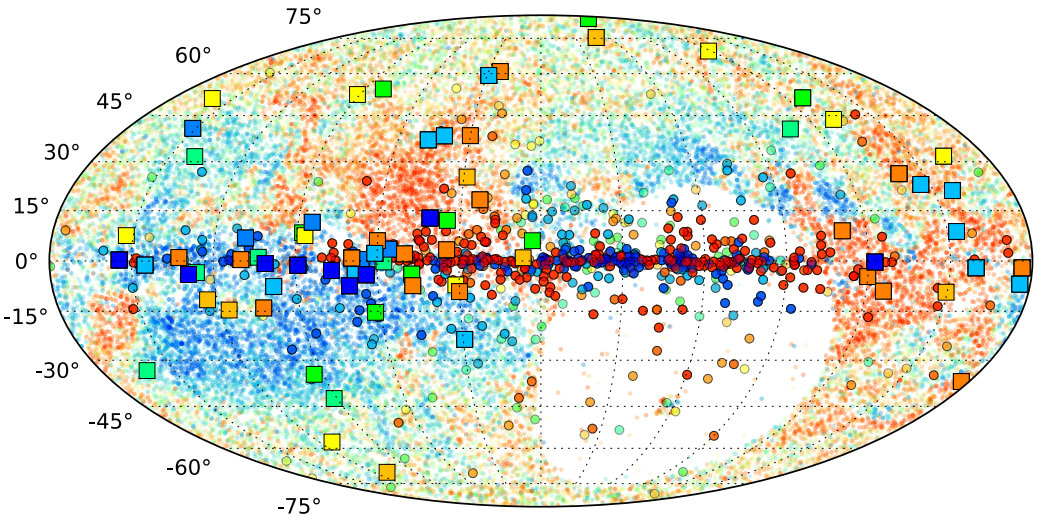

FIGURE 5.9: Location of known pulsars in the Galaxy. The catalogued pulsars with or without RM data are shown as red or black points, respectively. The pulsars which were observed and an RM measured in this work are also shown. The pulsars observed with Effelsberg, WSRT and LOFAR are shown as green squares, blue diamonds and maroon circles, respectively.

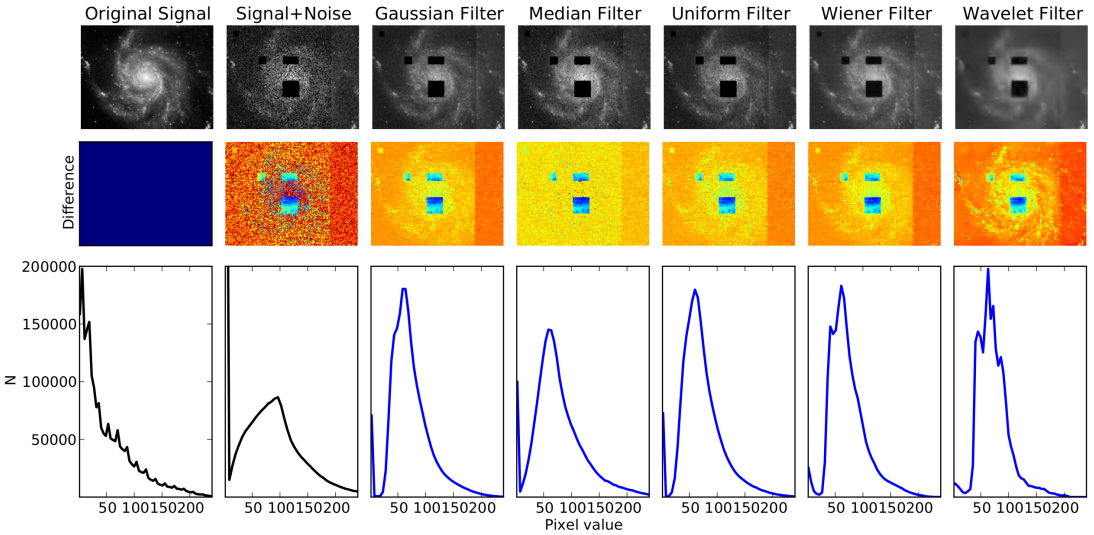

FIGURE 5.10: Various reconstructions of a signal (optical image of galaxy M101 courtesy of ESA/NASA) for testing. *Upper:* The original signal (*left*), added random noise of various scales (*second from left*) and the reconstruction of the signal using various filters, labelled above *third from left to right*. *Middle:* respective differences between original signal and reconstructed signal. *Lower:* respective histograms of pixel values in the images.

computationally complex (O(N) compared to O(N log N) time). There are now many reviews of wavelet analysis (e.g. Starck and Bobin, 2009, and references therein). The wavelet analysis method used in this work and described below was essentially derived from Stepanov et al. (2002).

Given a real signal of interest, represented by the function $F(r, \phi)$ in polar coordinates (r, ϕ), the continuous two-dimensional wavelet transform is given by

$$w(a, r, \phi) = \frac{1}{\sqrt{a}} \int_{\pi}^{\pi} \int_{0}^{\infty} \psi_{a,r,\phi}(r', \phi') F(r', \phi') r' \mathrm{d}r' \phi'. \tag{5.1}$$

$w(a, r, \phi)$ are also known as wavelet coefficients which form a three-parameter family. $\psi_{a,r,\phi}$ are a family of wavelet functions (sometimes known as child wavelets), and a defines the scale in physical space (r, ϕ) where $\psi_{a,r,\phi}(r', \phi') = O(1)$. The family of self-similar child wavelets is generated from the analysing wavelet $\Psi_{a,r,\phi}$ (sometimes known as the mother wavelet) by translation and dilation and are defined as

$$\psi_{a,r,\phi}(r', \phi') = \frac{1}{a} \Phi \left(\frac{s(r, \phi, r', \phi')}{a} \right). \tag{5.2}$$

$s(r, \phi, r', \phi')$ represents the distance between the current and central points of the wavelet (r', ϕ') and (r, ϕ), respectively.

There are many options for the mother wavelet, depending on the required analysis properties. These often have a positive definite function that determines the position of the wavelet, $\Phi(x)$ the envelope, and ...., $h(x)$, such that

$$\Psi(x) = \left(h(x) + C_1 + C_2 x\right) \Phi(x), \tag{5.3}$$

The wavelet used in this work is derived from the non-orthogonal isotropic wavelet function known most commonly as the 'Mexican hat' or Ricker wavelet was used, where $h(x) = 2 - r^2$ and $\Phi = exp(-\frac{r^2}{2})$. This is proportional to the Laplacian of a Gaussian, where x is the distance from the wavelet centre. The constants C_1 and C_2 are determined for each scale a and wavelet position (r, ϕ). Since the observables (RM and DM in this case) are defined as integral LOS quantities with variable limits, instead of differentiating the signals that contain noise, it is preferable to use a differentiated analytical form of the wavelet,

$$\overline{\psi}_{a,r,\phi}(r', \phi') = \frac{\delta \psi_{a,r,\phi}(r', \phi')}{\delta r'} + \frac{\psi_{a,r,\phi}(r', \phi')}{r'}, \tag{5.4}$$

where the envelope, Φ, is as before and $h(x)$ becomes $\frac{1}{r}\left(r^4 - 5r^2 + 2\right)$. This new wavelet $\overline{\psi}$ satisfies the admissibility conditions that the function has a mean and variance of zero, is localised in physical space and takes into account the integral of the function $F(r = 0, \phi) = 0$. Unlike the 'Mexican hat' the new wavelet is not isotropic, and there are two distinct places at which the function has zero value, see Fig. 5.11.

The observables of the GMF signal are discrete point sources spread irregularly throughout the Galaxy with data points becoming less dense with distance from the Sun, see Fig. 5.8. The physical distances between pulsars with RMs are the limitation the minimum useful scale a which can be used in the reconstruction, which beyond 3 kpc can be comparable or greater than the scales of physical interest. It is convenient to use a Monte-Carlo method to calculate the wavelet coefficients,

$$w(a, r, \phi) = -\frac{\Delta S(a, r, \phi)}{\sqrt{a}} \sum_{i=1}^{N} \overline{\psi}_{a,r,\phi}(r'_i, \phi'_i) F(r'_i, \phi'_i)'_i, \tag{5.5}$$

where N is the number of data points i for $F(r, \phi)$, and ΔS is the average area of an individual data point. For a uniform grid of data points, ΔS is constant, however this is not the case for an inhomogeneous distribution. In this case, ΔS is a function of the position and scale of the wavelet and can be chosen to minimise the error arising from the non-uniform distribution,

$$\Delta S(a, r, \phi) = a^2 \left[\sum_{i=1}^{N} \Phi \left(\frac{s(r, \phi, r'_i, \phi'_i)}{a} \right) \right]^{-1} \tag{5.6}$$

where Φ is defined earlier. The approximate number of sample points within the localised wavelet area is given by $a^2/\Delta S$ and should be sufficient to achieve an accurate reconstruction.

Figure 5.12 shows the GMF reconstructed using the method previously described, smoothed to $\sim$ half a kiloparsec scale. The signs of the RMs towards pulsars located at positions Y<0 kpc were changed so that the directions of the magnetic field are consistent across the Galactic plane. The GMF is again shown to have an overall clockwise-directionality, with one field reversal towards the Sagittarius arm, as shown previously (e.g. Van Eck et al., 2011). It is also more difficult to constrain the field in the outer arms because the magnitudes of the RMs are lower because the field direction is more perpendicular to our LOS than for pulsars in the inner Galaxy. Moreover, the number density of known

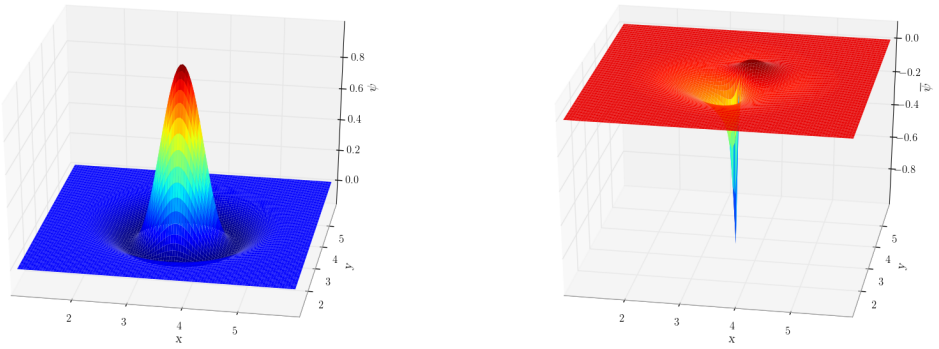

FIGURE 5.11: *Left:* The 'Mexican hat' wavelet. *Right:* The new wavelet family used for reconstructing the GMF, from the derivative of the 'Mexican hat' wavelet function. Both functions shown are centred at $(r = 5, \phi = \pi/4)$ and have scale $a = 0.5$.

pulsar RMs in the outer Galaxy, despite those collected in this work, limits the scale to which the GMF can be reconstructed. It is therefore desirable to continue to measure RMs towards known, as well as newly-discovered, pulsars. In addition, the distances to most pulsars are not independently measured, and so the model is also more dependent on the electron density model used than is desirable. This is further discussed below.

5.7 Discussion

In this section we discuss the results obtained from the polarisation observations and the reconstruction of the magnetic field using the wavelet method. It is essential that the ionospheric RM calculated is accurate, especially for the lower-frequency data, otherwise the RMs calculated due to the ISM alone will be systematically affected. Given the good agreement between the observed RMs and modelled ionospheric RMs for several pulsars and epochs from Chapter 4, we can be confident in the results from the model for these single observations. Figure 5.13 shows the measured RM and associated uncertainty measured at 1.3 GHz, compared with the ionospheric RM and uncertainty, towards PSR J0613–0200, calculated using the `ionFR` code mentioned in Chapter 4, for five timing epochs. Although errors on the observed RMs are larger than that for the modelled ionospheric RM, the data points are in agreement. The variations in the observed RMs show that the larger uncertainties for the higher frequency data are justified, compared to the results from the low-frequency observations in Chapter 4.

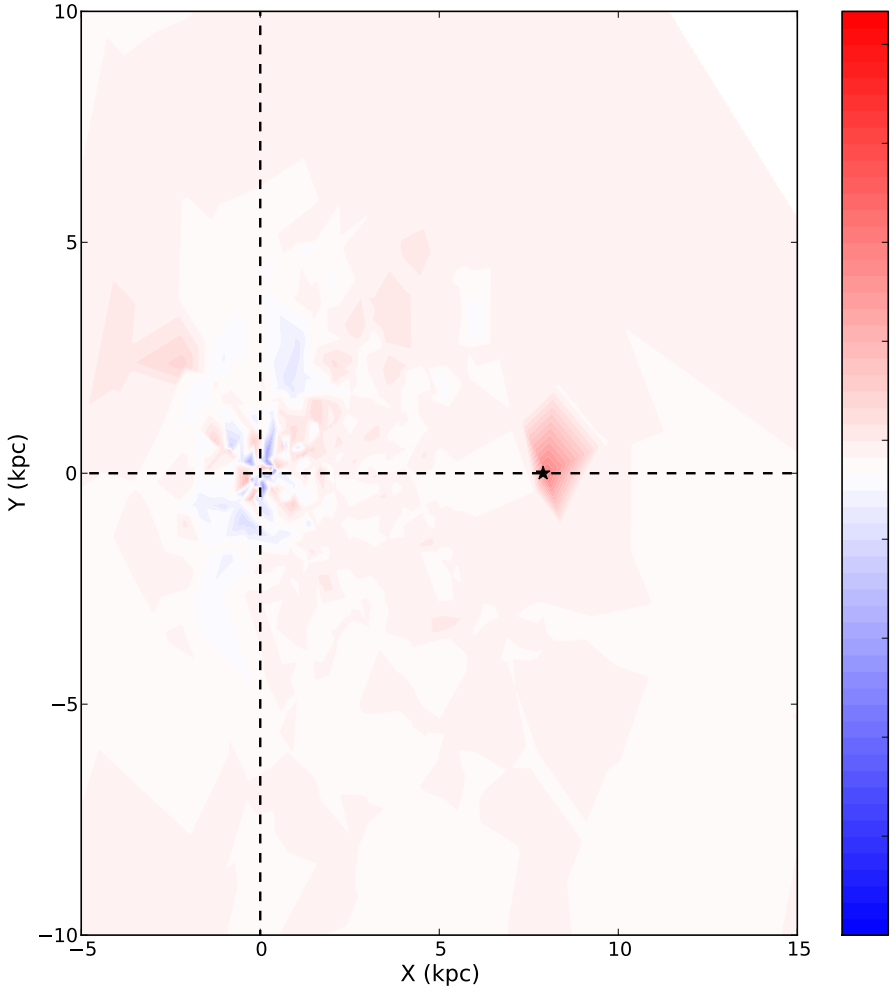

FIGURE 5.12: The reconstruction of the GMF in the plane using the RM and DM data collected in Chapters 3 and 5. Increasingly blue colours show increasingly negative values for counter-clockwise directions and increasingly red values shows increasingly positive values for clockwise directions.

Figure 5.14 shows the comparison between the RMs measured in this work and the RMs from the literature, where previous measurements exist. 24 pulsars are shown with LOFAR data, 12 with Effelsberg data, and two with WSRT data. The figure shows that many of the points are in agreement with the expected trend, that the previously published RMs are in agreement with those measured in this work, within the uncertainties. This infers that the RMs obtained in this work are reliable. It is also evident that the lower-frequency data, i.e., using LOFAR, are more precise than the higher-frequency data (the error bars on the LOFAR data are smaller than the area of the circles in Fig. 5.14). Moreover, the average uncertainty in the average magnetic field parallel to the LOS obtained using LOFAR RM data is decreased by over an order of magnitude as compared to that from the current RM catalogue.

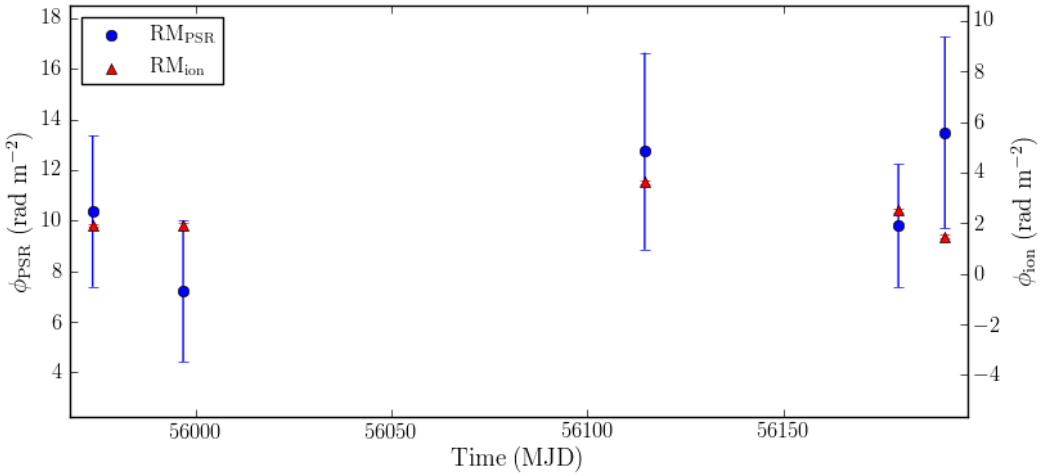

FIGURE 5.13: Comparison of the observed RM (blue circles, left axis labels) and ionospheric RM (red triangles, right axis labels) towards PSR J0613–0200 for five observations spanning over 217 days from 16 February 2012 to 21 September 2012. The ionospheric RM was modelled as explained previously, and in Chapter 4, using IGS TEC maps and IGRF11.

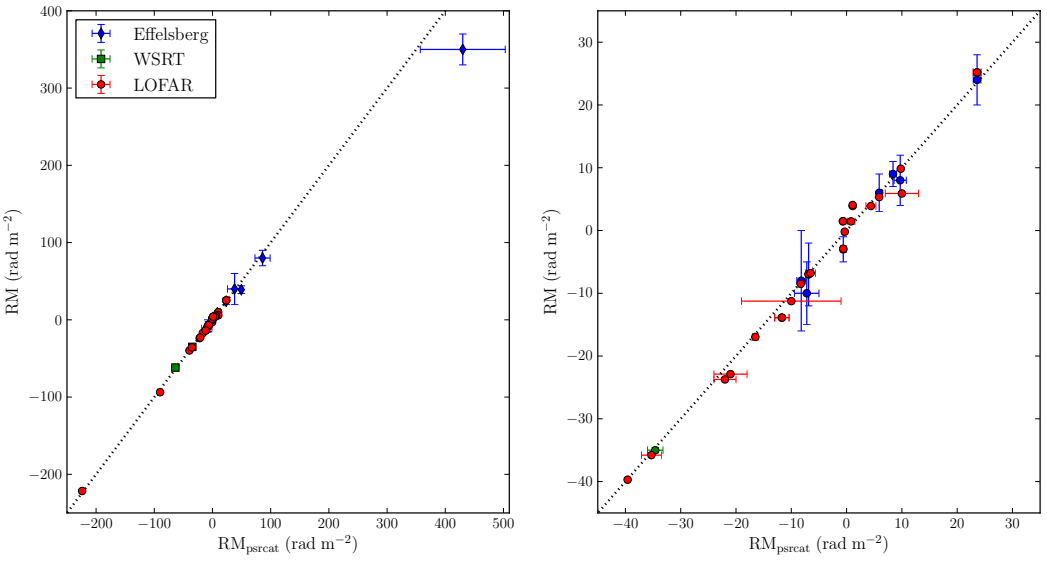

FIGURE 5.14: RMs and uncertainties measured using the Effelsberg (blue diamonds), WSRT (green squares) and LOFAR observations (red circles) from this work are compared to RMs from the literature collected in the ATNF pulsar catalogue. The expected trend (RM = RM$_{psrcat}$) is shown by the black dotted line.

Using `pdmp` to determine the optimal DM may become less accurate than using `tempo2` if there is significant pulse profile evolution across the recorded bandwidth, especially for low-frequency data where pulse profile evolution is often most dramatic due to ISM dispersion, scattering and other effects, e.g., see Fig. 5.7. This is because maximising the S/N may result in several pulse components being incorrectly aligned across the frequency band as there is no template pulse profile for reference. However, the pulsars observed at lower frequencies in this work have relatively simple profiles, most commonly with one or two components. In these cases, the output from `pdmp` gave reasonable and efficient DM solutions. In future, more complex profiles may require two-dimensional modelling to correctly align profiles in order to obtain the Stokes Q and U parameters (Pennucci et al., 2014).

5.7.1 Limitations of the data

H II *regions and small-scale structure:*

Theoretical models of the GMF contain a regular large-scale component coherent over kpc scales and small-scale ($\sim$ 10–100 pc) turbulent fields. Turbulent fields are attributed to localised structures, i.e. H II regions and supernova remnants (SNRs). The 'corruption' of RMs due to enhanced local structures, i.e., H II regions and SNRs, was demonstrated as potentially severe (e.g. Mitra et al., 2003a). Surprisingly, these have only recently been taken into account when determining the large-scale component of the GMF (Nota and Katgert, 2010). Hence, developing an algorithm to give less weight to RMs at positions of abnormally high electron densities and therefore increased Hα intensity is beneficial. H-Alpha intensities from the Wisconsin H-Alpha Mapper (WHAM Haffner et al., 2003) and the Southern H-Alpha Sky Survey Atlas (SHASSA Gaustad et al., 2001) can be used for this purpose. However, this was not applied to this work because it was determined that the number of RMs with which to reconstruct the GMF was already too low to purposefully exclude more data. Instead, the wavelet filter was applied to smooth over any small scale noise caused by small scale structures like H II regions.

Pulsar distances:

Pulsar distances are not well constrained for the majority of the pulsar sample. The distance to most pulsars are determined using an electron density model, which most

commonly is the NE2001 model (Cordes and Lazio, 2002). Since the electron density is not well constrained in some regions of the galaxy, the uncertainty in the distances determined by this method can be on average ∼20% (Cordes and Lazio, 2002).

Of the 2267 known pulsars, just 27 have publicly available independent distance measurements using associations with globular clusters (Harris, 1996) and 64 have publicly available independent parallax measurements using pulsar timing and/or VLBI astrometry[3]. Of these pulsars, eight do not have published RM values and for three of these the DM is currently also unknown. The RMs of three of the pulsars which do not have published RMs were observed for this work, WSRT data was used to determine the RM of PSR B1257+12 and LOFAR data was used to determine the RM of PSRs J0030+0451 and J1012+5307. However, no individual pulsars in globular clusters have measured RMs. It has been noted that when RMs to pulsars in galactic globular clusters are measured, particularly at large distances from the Galactic plane, the vertical component of the GMF should 'immediately become obvious' (Boulares and Cox, 1990). Therefore, the brightest pulsars in globular clusters are obvious targets to further this work. Furthermore, if the RMs of at least two pulsars in the same globular clusters are measured, the intra-cluster magnetic field may also be measured, similar to that for the intra-cluster electron density using DM measurements (Freire et al., 2001).

The distance uncertainties must be considered when determining the three-dimensional galactic magnetic structure, since ideally the pulsars should be 'fixed' reference points in the galaxy to which the magnetic fields are known. There is currently a large and ongoing VLBA survey which aims to determine the parallax of 200 pulsars, improving the current sample by an order of magnitude[4]. For this work, the distance measurements and their uncertainties as they currently stand are taken into account.

It is clear that there is a possibility for obtaining more RM data for the purpose of more accurately reconstructing the GMF. Now that LOFAR is conducting routine observations centred at 150 MHz, with up to 90 MHz bandwidth, a survey of the brightest 200 pulsars in the northern sky promises to deliver a good sample of precise RMs towards pulsars with and without previously published data. This will provide more data points with which to better constrain the GMF towards Galactic quadrants I, II, and III. In future, it will also be possible to undertake a similar strategy using low-frequency pathfinders

[3]A list is available at http://www.astro.cornell.edu/research/parallax/.
[4]see https://safe.nrao.edu/vlba/psrpi/home.html for project status

in the southern hemisphere, such as the MWA, to precisely measure and monitor RMs towards the Galactic centre. Moreover, several searches for undiscovered pulsars are ongoing or are due to commence. The High Time Resolution Universe (HTRU) survey currently under way, using Effelsberg and Parkes Radio Telescopes, and promises to deliver hundreds of new discoveries in the Galactic disk (Barr et al., 2013). Two of the RMs determined using Effelsberg observations, those towards PSRs J0426+4933 and J2036+2835, were discovered in the HTRU survey. The new LOFAR radio telescope is also currently discovering pulsars at lower frequencies, see http://www.astron.nl/lotaas/. Therefore, these discoveries present a prospect for conducting follow-up polarisation observations to obtain RM data towards more LOSs, to allow better construction of the GMF. With new discoveries and ancillary data from increasingly sensitive telescopes planned for the future (i.e. FAST, SKA) the number of pulsars with RM data is destined to improve, paving the way for much exciting science and specifically, greater accuracy in the reconstruction (and monitoring) of the GMF.

5.8 Conclusions

I have presented 77 ionosphere-corrected RMs towards pulsars that were obtained using observations at 1.3 GHz, 350 MHz, and 150 MHz, and the powerful method of RM-synthesis, 45 of which have not previously been measured. The RMs obtained were shown to be reliable by using comparisons between those obtained in this work and those previously measured values presented in Chapter 3. In particular, the RMs obtained using LOFAR improve the accuracy in the magnetic field measurement parallel to the LOS by a factor of at least ten.

The RMs from the catalogue and from this work were used to reconstruct the GMF using wavelet analysis. The new RM data improved the reconstruction in the outer quadrants of the Galaxy, I and II, in the direction of the Galactic anti-centre, where existing data is more sparse compared to towards the Galactic centre. The LOFAR data also improved the accuracy on the reconstruction within a few kpc of the Sun. However, more and more accurate data are required in order to reconstruct a fuller picture of the three-dimensional structure of the GMF.

The importance of increasing the number of known pulsars with RM data, which currently stands at ∼30%, is evident for reconstructing the GMF using wavelets or alternative methods. Follow-up polarisation observations of newly-discovered pulsars from the various ongoing pulsar surveys also present opportunities to increase the sampling of the GMF. Alternative filters for reconstructing the GMF from point source measurements could also be explored, e.g., the extended critical filter, (see Oppermann et al., 2012, and references therein). Next-generation pathfinders to the SKA provide prospects of precise measurements and monitoring of interstellar weather, such as DMs, RMs, and scattering measures; towards better characterisation of the ISM and also towards better correction for these effects in pulsar timing observations towards, e.g., detecting gravitational waves.

Chapter 6

Summary and future outlook

6.1 Summary

This thesis dealt with the study of an ensemble of astrophysical plasmas that share very different parameter space in terms of magnetic field strength and scale. The results drawn show that pulsar observations using next-generation low-frequency radio telescopes, such as LOFAR, can provide valuable insights into pulsar emission characteristics and the ISM. Some final remarks and thoughts on future perspectives are given below.

In **Chapter 2**, *emission characteristics of PSR B0823+26: discovery of a quiet emission mode*, we presented the numerous emission characteristics of a mode-changing pulsar, PSR B0823+26, using LOFAR and multi-frequency observations. We reported on the LOFAR discovery that PSR B0823+26 has a weak and sporadically emitting 'quiet' emission mode that is over 100 times weaker (on average) and a nulling fraction over forty-times greater than that of the more regularly-emitting 'bright' mode. We also found that the transition between emission modes is concurrent across the range of frequencies observed and occurs within one rotational period (0.531 seconds). This provided greater insights into the radio emission behaviour of a normal pulsar with a gargantuan magnetic field ($\sim 10^{12}$ G) – a process which is not yet well understood, but may affect results from using their emission as probes of the ISM and as gravitational wave detectors within a pulsar timing array.

In **Chapter 3**, *published rotation measures and techniques*, the current state of the practical methods and published results of Faraday rotation measures (RMs) towards pulsars, and also extragalactic sources, were collected and reviewed, for the purpose of studying the Galactic magnetic field (GMF, $\sim$ μG). This collection of RMs towards the same pulsars over several epochs from the literature enabled the possible time-dependence of RMs to be investigated, although was inconclusive due to the uncertainties in the measurements.

Chapter 4, *correcting for ionospheric Faraday rotation*, described the effect of the ionosphere on RM measurements towards astronomical sources. Observations of pulsars using the LOFAR demonstrated the high accuracy of a code used to calculate the amount of ionospheric Faraday rotation towards a specific line-of-sight using publicly available, GPS-derived total electron content maps and the geomagnetic reference field ($\sim$ 0.5 G). We showed that we can accurately determine some of the highest-precision RMs towards pulsars ever achieved, towards more accurately measuring and monitoring the GMF.

Chapter 5, *new pulsar rotation measures towards constructing the Galactic magnetic field*, presented the results from polarisation observations centred at frequencies between 150 MHz and 1.3 GHz, used to measure ionosphere-corrected RMs towards 77 pulsars which either did not have published RM data (45) or which increase the accuracy in values in the catalogue RM. The LOFAR observations provided amongst the most accurate RM catalogue of 25 pulsars to date. The RMs towards pulsars and extragalactic collected in Chapters 3 and 5 were used to reconstruct a map of the large-scale GMF using wavelet analysis. We found that the reconstruction is improved by the additional data points in the Galactic plane. However, to more accurately construct the GMF, more RM data and more independent pulsar distance measurements are required, especially towards the Galactic halo, so that a fully three-dimensional reconstruction of the GMF may be possible.

6.2 Future work

The discovery of the quiet emission mode in PSR B0823+26 provides further opportunities to probing different magnetospheric states in a pulsar. Now that polarisation

calibration of LOFAR data is possible (Noutsos et al. in prep, 2014), it will be interesting to investigate the polarisation properties of the B and Q emission states. The mode-separated average polarisation profiles, polarisation position angles, and RMs will provide better characterisation of the emission modes. Lower frequency mode-separated spectra from LOFAR LBA observations and better statistics on the mode changes from more observations will also aid this. This information will provide further insight into the still elusive pulsar radio emission mechanism.

LOFAR is now routinely observing pulsars at 150 MHz with up to 90 MHz bandwidth. Therefore, the RM catalogue collected in Chapter 5 can now be expanded using observations of the brightest 200 pulsars in the Northern sky. This will provisionally provide a significant sample of RMs, some of which have not previously been measured, and which will also increase the accuracy of previously measured RMs. This will provide better constraints on the magnetic field towards the Galactic anti-centre, which currently is sparsely sampled compared to towards the Galactic centre. Following up newly discovered pulsars, using polarisation observations from LOFAR and other telescopes, will also provide new magnetic field data points in sparsely sampled areas of the Galaxy, e.g., towards the halo. Using regular LOFAR pulsar timing observations can also provide more accurate RMs over time, for the purpose of investigating possible DM and RM variations with respect to time (either due to the changing LOS or change in polarised pulsar emission) and whether these quantities are correlated.

The technique of using RM-synthesis on LOFAR observations of polarised pulsars to obtain RMs and subtracting the ionospheric Faraday rotation to infer the intervening magnetic field in the ISM can be applied to other foreground plasmas. For example, excess RM and DM can be used to infer the magnetic field in the Solar wind, which is difficult to measure directly (e.g. You et al., 2012). The difference between the RMs and DMs of pulsars in globular clusters can also infer the magnetic field in the globular cluster, similar to using the DM difference to infer the electron density (Freire et al., 2001).

New generation and future telescopes will improve observational capabilities in terms of sensitivity (instantaneous bandwidth, collecting area) and observing speed. SKA pathfinders including LOFAR, LWA, and MWA are capable of observing the sky at low frequencies to obtain precise RMs towards many pulsars so that these can be measured

and monitored in all quadrants of the Galaxy. An increased number of precise RMs measured towards known and newly-discovered pulsars, especially towards the Galactic halo, will be essential for constructing a three-dimensional model of the Galactic magnetic field. In addition, data collected on other tracers of the magnetic field, such as those previously introduced in Section 1.3.1, e.g., Zeeman splitting, polarisation of diffuse synchrotron radiation, and UHECRs, from these and other telescopes would also be beneficial to our overall three-dimensional picture of the Galactic magnetic field.

Appendix A

Appendix: Pulsar rotation measures from the literature

Table A.1 below lists the catalogue of 680 pulsars with at least one, and up to six, published rotation measures (RMs) in the literature. The most recent RM measurements are usually listed in the most recent version of the ATNF pulsar catalogue version 1.50 (Manchester et al., 2005a). Any other measurements from the literature are also listed with shortened references, which are shown in the caption of Table A.1.

TABLE A.1: RMs from the current pulsar catalogue, including previous measurements. Columns 1–5 show the catalogue values for the pulsar name, jname, DM, RM and RM reference. These are from version 1.50 of the ATNF pulsar catalogue (Manchester et al., 2005a). Columns 7–15 show other RMs and references collected from the literature where possible, in order of decreasing date. The RM references in alphabetical order are: aaa+09d (Abdo et al., 2009), agr+11 (Arzoumanian et al., 2011), ban14 (Bangale, 2011), bbb+13 (Burgay et al., 2013), blr+13 (Boyles et al., 2013), ck03 (Crawford and Keim, 2003), ckr+12 (Camilo et al., 2012b), cmh91 (Costa et al., 1991), cmk01 (Crawford et al., 2001),cng+09 (Camilo et al., 2009a), crc+12 (Camilo et al., 2012a), crj+07 (Camilo et al., 2007), crj+08 (Camilo et al., 2008), crr+09 (Camilo et al., 2009b), ct07 (Crawford and Tiffany, 2007), drb+04 (Demorest et al., 2004), hmm+77 (Hamilton et al., 1977), hbo05 (Hotan et al., 2005), hl87 (Hamilton and Lyne, 1987), hml+06 (Han et al., 2006), hmq99 (Han et al., 1999), hr09 (Hankins and Rankin, 2010), jhv+05 (Johnston et al., 2005), jkk+07 (Johnston et al., 2007), jw06 (Johnston and Weisberg, 2006), kjb+12 (Keith et al., 2012), kjk+08 (Keith et al., 2008), kjr+11 (Keith et al., 2011), klm+00 (Kaspi et al., 2000), lbb+10 (Levin et al., 2010), lbr+13 (Lynch et al., 2013), lfrj12 (Lynch et al., 2012), lsf+06 (Lorimer et al., 2006), mac+02 (McLaughlin et al., 2002), man72 (Manchester, 1972), man74 (Manchester, 1974), mh04 (Manchester and Han, 2004), mh11 (Manchester and Hobbs, 2011), mj95 (Manchester and Johnston, 1995), mwkj03 (Mitra et al., 2003a), nbb+14 (Ng et al., 2014), njkk08 (Noutsos et al., 2008), nms+97 (Navarro et al., 1997) , ojk+08 (O'Brien et al., 2008), qmlg95 (Qiao et al., 1995), rl94 (Rand and Lyne, 1994), rrj01 (Roberts et al., 2001), s68 (Smith, 1968), sj13 (Shannon and Johnston, 2013b), skdl09 (Shitov et al., 2009), sr69 (Staelin and Reifenstein, 1969), tml93 (Taylor et al., 1993), tpc+11 (Theureau et al., 2011b), vdhm97 (van Ommen et al., 1997), vs(a)70 (Vitkevich and Shitov, 1970a), vs(b)70 (Vitkevich and Shitov, 1970b), wck+04 (Weisberg et al., 2004), wj08 (Weltevrede and Johnston, 2008), ymv+11 (Yan et al., 2011).

PSR name	PSR jname	DM (cm^{-3} pc)	RM_{psrcat} ($rad\,m^{-2}$)	$ref_{RM_{psrcat}}$	RM_1 ($rad\,m^{-2}$)	ref_{RM_1}	RM_2 ($rad\,m^{-2}$)	ref_{RM_2}	RM_3 ($rad\,m^{-2}$)	ref_{RM_3}	RM_4 ($rad\,m^{-2}$)	ref_{RM_4}	RM_5 ($rad\,m^{-2}$)	ref_{RM_5}
B0031–07	J0034–0721	11.38(8)	9.8(2)	hl87	12.8(40)	njkk08	10(1)	man74						
B0037+56	J0040+5716	92.595(9)	9(13)	rl94										

Continued on next page

Table A.1 – continued from previous page

PSR name	PSR jname	DM (cm^{-3} pc)	RM_{psrcat} ($rad\,m^{-2}$)	ref_{psrcat}	RM_1 ($rad\,m^{-2}$)	ref_{RM_1}	RM_2 ($rad\,m^{-2}$)	ref_{RM_2}	RM_3 ($rad\,m^{-2}$)	ref_{RM_3}	RM_4 ($rad\,m^{-2}$)	ref_{RM_4}	RM_5 ($rad\,m^{-2}$)	ref_{RM_5}
J0045–7319	J0045–7319	105.4(7)	–14(27)	cmk01										
B0053+47	J0056+4756	18.09(4)	–23(22)	mwkj03										
B0059+65	J0102+6537	65.853(16)	–94(15)	mwkj03										
J0108–1431	J0108–1431	2.38(19)	–0.3(1)	hml+06	3(2)	njkk08	–1(3)	hmq99						
B0105+65	J0108+6608	30.46(5)	–29(3)	man74	–24(4)	hl87								
B0105+68	J0108+6905	61.092(16)	–46(19)	mwkj03										
J0133–6957	J0133–6957	22.948(8)	7(1)	hmq99										
J0134–2937	J0134–2937	21.806(6)	13(2)	hmq99	15.4(30)	njkk08								
B0136+57	J0139+5814	73.779(6)	–90(4)	hl87										
B0138+59	J0141+6009	34.797(11)	–48(3)	hl87	–50(4)	man74								
B0144+59	J0147+5922	40.111(3)	–19(5)	rl94										
B0148–06	J0151–0635	25.66(3)	2(4)	hl87	8.1(70)	njkk08								
B0149–16	J0152–1637	11.922(4)	2(1)	qmlg95	–0.2(30)	njkk08	15(5)	hl87						
B0154+61	J0157+6212	30.21(3)	–29(7)	hl87										
B0203–40	J0206–4028	12.9(12)	–4(5)	qmlg95	8.8(180)	njkk08								
J0211–8159	J0211–8159	24.36(3)	54(9)	hml+06	30(16)	njkk08								
B0226+70	J0231+7026	46.64(3)	–56(21)	mwkj03										
J0248+6021	J0248+6021	370(1)	–158(6)	tpc+11										
B0254–53	J0255–5304	15.9(5)	32(3)	njkk08	–35(3)	hml+06	–10(12)	hmq99						
B0301+19	J0304+1932	15.737(9)	–8.3(3)	man74	–7(1)	njkk08	–5.7(11)	wck+04	–6(3)	hl87				
B0320+39	J0323+3944	26.01(3)	58(3)	hl87										

Continued on next page

Table A.1 – continued from previous page

PSR name	PSR jname	DM (cm^{-3} pc)	RM_{psrcat} ($rad\,m^{-2}$)	ref_{psrcat}	RM_1 ($rad\,m^{-2}$)	ref_{RM_1}	RM_2 ($rad\,m^{-2}$)	ref_{RM_2}	RM_3 ($rad\,m^{-2}$)	ref_{RM_3}	RM_4 ($rad\,m^{-2}$)	ref_{RM_4}	RM_5 ($rad\,m^{-2}$)	ref_{RM_5}
B0329+54	J0332+5434	26.833(10)	–63.7(4)	man72	–54(6)	hl87	(–)58(6)	vs(b)70	–63(5)	sr69	–95(14)	s68		
B0331+45	J0335+4555	47.153(3)	–41(20)	rl94										
J0340+4130	J0340+4130	49.6	56(1)	ban14										
B0339+53	J0343+5312	67.30(6)	–84(20)	mwkj03										
J0348+0432	J0348+0432	40.46313(11)	49.5(13)	lbr+13										
B0353+52	J0357+5236	103.706(4)	261(13)	rl94										
B0355+54	J0358+5413	57.1420(3)	79(4)	hl87										
B0403–76	J0401–7608	21.6(4)	19.0(5)	qmlg95	25.9(50)	njkk08	16(10)	cmh91						
B0402+61	J0406+6138	65.303(7)	9(3)	hl87										
J0421–0345	J0421–0345	44.61(9)	30(14)	hml+06										
J0437–4715	J0437–4715	2.64476(7)	0.0(4)	ymv+11	1.5(2)	nms+97	-8.5(5)	mj95						
J0448–2749	J0448–2749	26.22(4)	24(17)	hml+06	–10.9(270)	njkk08								
B0447–12	J0450–1248	37.041(10)	13(5)	hl87	15.5(180)	njkk08								
B0450–18	J0452–1759	39.903(3)	13.8(7)	hl87	11.1(3)	jkk+07	15(2)	man74						
B0450+55	J0454+5543	14.495(7)	10(3)	hl87										
J0459–0210	J0459–0210	21.02(3)	18(9)	hmq99	26.9(100)	njkk08								
B0458+46	J0502+4654	42.187(8)	–43(6)	hl87										
J0520–2553	J0520–2553	33.77(3)	–12(10)	njkk08	19(15)	hmq99								
B0523+11	J0525+1115	79.345(3)	37(2)	jhv+05	15.3(100)	njkk08	35(3)	wck+04	29(5)	hl87				
B0525+21	J0528+2200	50.937(17)	–39.6(2)	man72	–40.2(3)	jkk+07	–39.2(9)	wck+04	–39(6)	hl87				
B0529–66	J0529–6652	103.2(3)	4(4)	cmh91										

Continued on next page

Table A.1 – continued from previous page

PSR name	PSR jname	DM (cm^{-3} pc)	RM_{psrcat} ($rad\,m^{-2}$)	ref_{psrcat}	RM_1 ($rad\,m^{-2}$)	ref_{RM_1}	RM_2 ($rad\,m^{-2}$)	ref_{RM_2}	RM_3 ($rad\,m^{-2}$)	ref_{RM_3}	RM_4 ($rad\,m^{-2}$)	ref_{RM_4}	RM_5 ($rad\,m^{-2}$)	ref_{RM_5}
B0531+21	J0534+2200	56.791(1)	–42.3(5)	man72	–58(6)	wck+04	–43(2)	hl87						
B0538–75	J0536–7543	17.5(5)	25.2(10)	njkk08	28(2)	hmq99	25.1(5)	vdhm97	24(2)	cmh91				
J0538+2817	J0538+2817	39.570(1)	–7(12)	mwkj03										
J0540–7125	J0540–7125	29.41(7)	43(15)	hmq99	68.7(250)	njkk08								
B0540+23	J0543+2329	77.7115(17)	8.7(7)	hl87	4.4(8)	jkk+07	8.7(7)	wck+04	2.7(6)	man71				
B0559–05	J0601–0527	80.538(5)	64.0(20)	njkk08	62.4(2)	jhv+05	67(5)	hl87						
B0609+37	J0612+3721	27.135(4)	23(9)	wck+04										
J0613–0200	J0613–0200	38.77919(6)	9.7(11)	ymv+11	19(14)	hml+06	19(14)	mh04						
B0611+22	J0614+2229	96.91(7)	69(2)	man74	66.0(3)	jkk+07	67.0(3)	wck+04	62(5)	hl87				
B0621–04	J0624–0424	70.835(11)	49(3)	njkk08	42(7)	hl87								
B0626+24	J0629+2415	84.195(4)	69.5(2)	wck+04	82(4)	hl87								
B0628–28	J0630–2834	34.468(17)	46.53(12)	jhv+05	47(1)	hml+06	45.7(5)	vdhm97	46.2(1)	hl87	44.2(6)	man74	45(3)	vs(a)70
J0631+1036	J0631+1036	125.36(1)	137.5(40)	njkk08	137(8)	hml+06								
B0643+80	J0653+8051	33.332(17)	–32(3)	hl87										
J0656–2228	J0656–2228	32.39(17)	38(12)	njkk08										
B0656+14	J0659+1414	13.977(13)	23.5(4)	wck+04	23.0(3)	jkk+07	22(5)	hl87						
B0655+64	J0700+6418	8.771(5)	–7(6)	hl87										
J0711–6830	J0711–6830	18.4066(6)	21.6(31)	ymv+11	41(9)	hml+06	67(23)	mh04						
J0719–2545	J0719–2545	253.89(6)	164(18)	njkk08										
J0725–1635	J0725–1635	98.98(3)	188(12)	hml+06										
J0729–1448	J0729–1448	92.3(3)	46(1)	jw06	55(6)	hml+06								

Continued on next page

Table A.1 – continued from previous page

PSR name	PSR jname	DM (cm^{-3} pc)	RM_{psrcat} ($rad\,m^{-2}$)	ref_{psrcat}	RM_1 ($rad\,m^{-2}$)	ref_{RM_1}	RM_2 ($rad\,m^{-2}$)	ref_{RM_2}	RM_3 ($rad\,m^{-2}$)	ref_{RM_3}	RM_4 ($rad\,m^{-2}$)	ref_{RM_4}	RM_5 ($rad\,m^{-2}$)	ref_{RM_5}
B0727–18	J0729–1836	61.293(10)	51.5(40)	njkk08	53(6)	hl87								
J0737–3039A	J0737–3039A	48.920(5)	118.4(3)	hbo05	112.3(15)	drb+04								
J0737–3039B	J0737–3039B	48.920(5)	118(12)	drb+04										
B0736–40	J0738–4042	160.8(7)	12.1(6)	njkk08	12.5(6)	jkk+07	11(2)	hml+06	14.5(7)	vdhm97				
B0740–28	J0742–2822	73.782(2)	149.95(5)	jhv+05	148.5(6)	njkk08	156(5)	hmq99	149.9(5)	vdhm97	152(5)	hl87	150(5)	man74
B0743–53	J0745–5353	122.3(19)	–71(4)	njkk08	–75(5)	cmh91								
J0749–4247	J0749–4247	104.595(9)	125(5)	njkk08	80(30)	hml+06								
B0751+32	J0754+3231	39.949(8)	–7(5)	hl87	4(6)	wck+04								
B0756–15	J0758–1528	63.327(3)	55(7)	hl87										
B0808–47	J0809–4753	228.3(12)	105(5)	hml+06	100(20)	cmh91								
B0809+74	J0814+7429	6.116(18)	–11.7(13)	man72										
B0818–13	J0820–1350	40.938(3)	–1.2(4)	hl87	–7.2(12)	jhv+05	–2.8(17)	man72						
B0818–41	J0820–4114	113.4(2)	57.7(5)	qmlg95										
B0820+02	J0823+0159	23.727(6)	13(7)	hl87										
B0823+26	J0826+2637	19.454(4)	5.9(3)	man74	2(6)	hl87								
B0826–34	J0828–3417	52.2(6)	59(3)	hl87										
J0831–4406	J0831–4406	254.0(5)	509(20)	hml+06										
J0834–4159	J0834–4159	240.5(15)	–377(31)	hml+06										
J0835–3707	J0835–3707	112.3(3)	68(47)	hml+06										
B0833–45	J0835–4510	67.99(1)	31.38(1)	jhv+05	30.4(6)	njkk08	36.0(5)	vdhm97	38.17(6)	hmm+77	36.6(1)	man74		
B0834+06	J0837+0610	12.889(6)	23.6(7)	hl87	26.5(6)	jkk+07	24.5(25)	man72						

Continued on next page

Table A.1 – continued from previous page

PSR name	PSR jname	DM (cm^{-3} pc)	RM_{psrcat} ($rad\,m^{-2}$)	ref_{psrcat}	RM_1 ($rad\,m^{-2}$)	ref_{RM_1}	RM_2 ($rad\,m^{-2}$)	ref_{RM_2}	RM_3 ($rad\,m^{-2}$)	ref_{RM_3}	RM_4 ($rad\,m^{-2}$)	ref_{RM_4}	RM_5 ($rad\,m^{-2}$)	ref_{RM_5}
B0835–41	J0837–4135	147.29(7)	135.8(3)	tml93	145.0(1)	jkk+07	134(2)	vdhm97						
J0838–2621	J0838–2621	116.90(5)	86(13)	njkk08										
B0839–53	J0840–5332	156.5(10)	81(3)	qmlg95	80(10)	cmh91								
J0843–5022	J0843–5022	178.47(9)	155(23)	njkk08										
B0844–35	J0846–3533	94.16(11)	144(8)	hl87										
J0849–6322	J0849–6322	91.29(9)	–125(15)	njkk08										
B0853–33	J0855–3331	86.635(16)	165(10)	hl87										
J0855–4644	J0855–4644	238.2(16)	249(22)	hml+06										
J0855–4658	J0855–4658	472.7(12)	350(50)	hml+06										
B0855–61	J0856–6137	95(3)	–70(18)	hmq99										
J0857–4424	J0857–4424	184.429(4)	–75(20)	hmq99										
J0901–4624	J0901–4624	198.8(3)	289(22)	hml+06										
B0903–42	J0904–4246	145.8(5)	284(15)	qmlg95										
B0904–74	J0904–7459	51.1(16)	14(3)	qmlg95										
J0905–4536	J0905–4536	179.7	153(22)	hml+06										
J0905–5127	J0905–5127	196.43	291.0(20)	njkk08	292(3)	hml+06								
B0905–51	J0907–5157	103.72	–23.3(10)	njkk08	–48(13)	vdhm97								
B0906–17	J0908–1739	15.888(3)	–31(4)	jhv+05	–36(6)	hl87								
B0906–49	J0908–4913	180.37(4)	10.0(16)	qmlg95										
B0909–71	J0909–7212	54.3(16)	–18(4)	qmlg95										
B0919+06	J0922+0638	27.271(6)	29.2(3)	jhv+05	32(2)	hl87								

Continued on next page

Table A.1 – continued from previous page

PSR name	PSR jname	DM (cm^{-3} pc)	RM_{psrcat} ($rad\,m^{-2}$)	ref_{psrcat}	RM_1 ($rad\,m^{-2}$)	ref_{RM_1}	RM_2 ($rad\,m^{-2}$)	ref_{RM_2}	RM_3 ($rad\,m^{-2}$)	ref_{RM_3}	RM_4 ($rad\,m^{-2}$)	ref_{RM_4}	RM_5 ($rad\,m^{-2}$)	ref_{RM_5}
J0922–4949	J0922–4949	237.1(3)	–15(5)	hml+06										
B0922–52	J0924–5302	152.9(5)	150(20)	hmq99										
B0923–58	J0924–5814	57.4(3)	–45(1)	hml+06										
B0932–52	J0934–5249	100(2)	18(6)	hmq99										
J0940–5428	J0940–5428	134.5(9)	–31(1)	jw06	–10(24)	ct07	–18(14)	hml+06						
J0941–5244	J0941–5244	157.94(1)	–243(4)	hml+06	–230.5(21)	njkk08								
B0940–55	J0942–5552	180.2(5)	–61.9(2)	tml93										
B0941–56	J0942–5657	159.74(12)	135(4)	hmq99										
B0940+16	J0943+1631	20.32(5)	53(12)	hl87										
B0942–13	J0944–1354	12.497(3)	–7(3)	hl87										
B0943+10	J0946+0951	15.4(5)	13.3(5)	tml93										
B0950+08	J0953+0755	2.958(3)	–0.66(4)	jhv+05	2(2)	hl87	1.8(5)	man72	1.8(5)	man74				
J0954–5430	J0954–5430	200.3(4)	65(10)	hml+06										
B0953–52	J0955–5304	156.9(2)	–97(13)	hmq99										
B0957–47	J0959–4809	92.7(12)	50(6)	hml+06										
J1000–5149	J1000–5149	72.8(3)	46(9)	hml+06										
B0959–54	J1001–5507	130.32(17)	297(18)	hml+06										
J1001–5559	J1001–5559	159.3(9)	112(11)	hml+06										
B1001–47	J1003–4747	98.1(12)	18(4)	hml+06										
B1010–23	J1012–2337	22.51(9)	52(9)	hl87										
B1011–58	J1012–5857	383.9(1)	74(6)	hml+06	72.2(80)	njkk08								

Continued on next page

Table A.1 – continued from previous page

PSR name	PSR jname	DM (cm^{-3} pc)	RM_{psrcat} ($rad\,m^{-2}$)	ref_{psrcat}	RM_1 ($rad\,m^{-2}$)	ref_{RM_1}	RM_2 ($rad\,m^{-2}$)	ref_{RM_2}	RM_3 ($rad\,m^{-2}$)	ref_{RM_3}	RM_4 ($rad\,m^{-2}$)	ref_{RM_4}	RM_5 ($rad\,m^{-2}$)	ref_{RM_5}
J1013–5934	J1013–5934	379.78(17)	–97(7)	hml+06										
J1015–5719	J1015–5719	278.7(6)	96(2)	jw06	125(7)	hml+06								
B1014–53	J1016–5345	66.8(18)	–21(4)	hml+06										
J1016–5857	J1016–5857	394.2(2)	–540(3)	jw06	–537(17)	hml+06								
B1015–56	J1017–5621	439.1	365(7)	njkk08										
J1017–7156	J1017–7156	94.2256	–78(3)	kjb+12										
J1019–5749	J1019–5749	1039.4(11)	–366(10)	hml+06										
J1020–5921	J1020–5921	80(3)	–60(14)	hml+06										
J1022+1001	J1022+1001	10.2521(1)	–0.6(5)	ymv+11										
J1024–0719	J1024–0719	6.48520(8)	–8.2(8)	ymv+11										
J1028–5819	J1028–5819	96.525(2)	–5(4)	kjk+08										
J1034–3224	J1034–3224	50.75(8)	–8(1)	hmq99										
J1036–4926	J1036–4926	136.529(10)	–11(6)	hmq99	–38(10)	njkk08								
B1036–58	J1038–5831	72.74	–15(10)	njkk08										
B1039–19	J1041–1942	33.777(10)	–16(5)	hl87										
B1039–55	J1042–5521	306.5(4)	155(5)	hmq99										
J1043–6116	J1043–6116	449.2(4)	257(23)	hml+06										
J1045–4509	J1045–4509	58.1662(4)	92.0(10)	ymv+11	83(18)	hml+06	82(18)	mh04						
B1044–57	J1046–5813	240.2(5)	133(7)	njkk08	125(10)	hml+06								
J1047–3032	J1047–3032	52.54(7)	–36(23)	njkk08										
J1047–6709	J1047–6709	116.156(2)	–79.3(20)	njkk08	–73(3)	hml+06								

Continued on next page

Table A.1 – continued from previous page

PSR name	PSR jname	DM (cm^{-3} pc)	RM_{psrcat} ($rad\,m^{-2}$)	ref_{psrcat}	RM_1 ($rad\,m^{-2}$)	ref_{RM_1}	RM_2 ($rad\,m^{-2}$)	ref_{RM_2}	RM_3 ($rad\,m^{-2}$)	ref_{RM_3}	RM_4 ($rad\,m^{-2}$)	ref_{RM_4}	RM_5 ($rad\,m^{-2}$)	ref_{RM_5}
B1046–58	J1048–5832	129.1(2)	–155(5)	qmlg95										
J1049–5833	J1049–5833	446.8(15)	359(11)	hml+06										
J1052–5954	J1052–5954	491(3)	–280(24)	wj08										
J1054–5943	J1054–5943	330.7(6)	46(34)	hml+06										
B1054–62	J1056–6258	320.3(6)	4(2)	cmh91										
J1056–7117	J1056–7117	93.04(4)	–22(8)	nbb+14										
B1055–52	J1057–5226	30.1(5)	47.2(8)	tml93	44(2)	njkk08								
B1056–57	J1059–5742	108.7(3)	–75(10)	cmh91										
J1103–5403	J1103–5403	103.915(3)	–103(21)	kjr+11										
J1103–6025	J1103–6025	275.9(3)	569(7)	hml+06										
J1105–6107	J1105–6107	271.01(2)	187(1)	jw06	166(3)	cmk01								
B1107–56	J1110–5637	262.56(6)	419(3)	njkk08	426(11)	hml+06								
J1112–6103	J1112–6103	599.1(7)	242(15)	hml+06										
B1110–65	J1112–6613	249.3(10)	–132(4)	njkk08	–94(18)	hml+06	–370(50)	cmh91						
B1112+50	J1115+5030	9.195(8)	3.2(5)	man74	–4(6)	hl87								
J1115–6052	J1115–6052	228.2(4)	257(18)	wj08										
B1114–41	J1116–4122	40.53(3)	–37(13)	hml+06	31(16)	hmq99	55(40)	vdhm97						
J1117–6154	J1117–6154	493.6(9)	–622(10)	hml+06										
J1119–6127	J1119–6127	707.4(13)	853(2)	jw06	832(6)	hml+06	842(23)	ck03						
B1119–54	J1121–5444	204.7(6)	42(9)	hml+06										
J1123–4844	J1123–4844	92.915(3)	–7(5)	hmq99	–13.7(60)	njkk08								

Continued on next page

Table A.1 – continued from previous page

PSR name	PSR jname	DM (cm^{-3} pc)	RM_{psrcat} ($rad\,m^{-2}$)	ref_{psrcat}	RM_1 ($rad\,m^{-2}$)	ref_{RM_1}	RM_2 ($rad\,m^{-2}$)	ref_{RM_2}	RM_3 ($rad\,m^{-2}$)	ref_{RM_3}	RM_4 ($rad\,m^{-2}$)	ref_{RM_4}	RM_5 ($rad\,m^{-2}$)	ref_{RM_5}
J1123–6102	J1123–6102	439.4(4)	244(8)	hml+06										
J1123–6259	J1123–6259	223.26(3)	54(10)	hml+06										
J1124–6421	J1124–6421	298(3)	–1102(98)	hml+06										
J1125–5825	J1125–5825	124.81(5)	–7(3)	kjb+12										
B1124–60	J1126–6054	280.27(3)	–41(16)	hml+06										
J1126–6942	J1126–6942	55.33(2)	–31(4)	hmq99										
B1131–62	J1133–6250	567.8(5)	848(6)	njkk08	880(24)	hml+06								
B1133+16	J1136+1551	4.864(5)	1.1(2)	jhv+05	8.9(8)	wck+04	3(2)	hl87	3.9(2)	man72				
B1133–55	J1136–5525	85.5(7)	28(5)	qmlg95	–20(20)	cmh91								
J1137–6700	J1137–6700	228.041(9)	–1(13)	hml+06	–11(16)	njkk08								
J1138–6207	J1138–6207	519.8(8)	594(18)	hml+06										
J1141–3107	J1141–3107	30.77(3)	–26(7)	njkk08	–60(30)	hml+06								
J1141–3322	J1141–3322	46.448(17)	–36(5)	njkk08	–33(14)	hml+06								
J1141–6545	J1141–6545	116.080(1)	–84(2)	hml+06	–86(3)	klm+00								
B1143–60	J1146–6030	111.68(7)	–5(4)	njkk08	10(17)	hml+06	30(20)	cmh91						
J1156–5707	J1156–5707	243.5(6)	238(19)	wj08										
B1154–62	J1157–6224	325.2(5)	508.2(5)	tml93	510(2)	hml+06								
J1159–6409	J1159–6409	178(5)	259(13)	hml+06										
J1159–7910	J1159–7910	59.24(2)	–11(9)	hml+06	–6(15)	njkk08								
B1159–58	J1202–5820	145.41(19)	139(3)	hmq99										
J1210–5559	J1210–5559	174.347(3)	58(1)	hmq99										

Continued on next page

Table A.1 – continued from previous page

PSR name	PSR jname	DM (cm^{-3} pc)	RM_{psrcat} ($rad\,m^{-2}$)	ref_{psrcat}	RM_1 ($rad\,m^{-2}$)	ref_{RM_1}	RM_2 ($rad\,m^{-2}$)	ref_{RM_2}	RM_3 ($rad\,m^{-2}$)	ref_{RM_3}	RM_4 ($rad\,m^{-2}$)	ref_{RM_4}	RM_5 ($rad\,m^{-2}$)	ref_{RM_5}
J1211–6324	J1211–6324	333.8(11)	–120(9)	hml+06										
J1224–6208	J1224–6208	454.2(7)	80(7)	hml+06										
B1221–63	J1224–6407	97.47(12)	–3.6(5)	tml93	6(3)	hml+06								
B1222–63	J1225–6408	415.1(5)	337(4)	njkk08	356(23)	hml+06								
J1231–4609	J1231–4609	76(7)	–20(6)	njkk08										
J1231–6303	J1231–6303	301(10)	390(18)	hml+06										
J1236–5033	J1236–5033	105.02(11)	49(13)	njkk08										
B1237+25	J1239+2453	9.242(6)	–0.33(6)	tml93	–2.6(4)	jhv+05	–0.4(6)	wck+04	–0.3(1)	hl87	–0.6(4)	man72		
B1236–68	J1239–6832	94.3(3)	–49(10)	hml+06										
B1237–41	J1240–4124	44.1(12)	15(13)	njkk08										
B1240–64	J1243–6423	297.25(8)	157.8(4)	tml93	157(1)	vdhm97								
J1252–6314	J1252–6314	278.4(13)	330(19)	hml+06										
J1253–5820	J1253–5820	100.584(4)	17.7(10)	njkk08	31(5)	hmq99								
B1254–10	J1257–1027	29.634(9)	8(12)	rl94										
J1301–6305	J1301–6305	374(3)	–631(15)	ct07	–625(25)	jw06	–665(31)	hml+06						
B1259–63	J1302–6350	146.72(3)	21.1(5)	mj95										
J1305–6203	J1305–6203	470.0(15)	–436(15)	hml+06										
B1302–64	J1305–6455	505.0(3)	–420(5)	njkk08	–420(10)	cmh91								
B1303–66	J1306–6617	436.9(2)	396(4)	njkk08	387(10)	hml+06								
J1307–6318	J1307–6318	374(8)	136(23)	hml+06										
B1309–53	J1312–5402	133(2)	143(20)	hml+06										

Continued on next page

Table A.1 – continued from previous page

PSR name	PSR jname	DM (cm^{-3} pc)	RM_{psrcat} ($rad\,m^{-2}$)	ref_{psrcat}	RM_1 ($rad\,m^{-2}$)	ref_{RM_1}	RM_2 ($rad\,m^{-2}$)	ref_{RM_2}	RM_3 ($rad\,m^{-2}$)	ref_{RM_3}	RM_4 ($rad\,m^{-2}$)	ref_{RM_4}	RM_5 ($rad\,m^{-2}$)	ref_{RM_5}
B1309–55	J1312–5516	134.1(16)	141(3)	qmlg95										
J1312–6400	J1312–6400	93.0(12)	40(30)	hml+06										
J1317–6302	J1317–6302	678.1(12)	–504(8)	hml+06										
B1316–60	J1319–6056	400.94(4)	–280.6(20)	njkk08										
J1320–3512	J1320–3512	16.42(10)	–7.8(20)	njkk08										
B1317–53	J1320–5359	97.6(6)	141(4)	njkk08	160(10)	cmh91								
J1322–6241	J1322–6241	618.8(19)	83(14)	hml+06										
J1324–6146	J1324–6146	828(9)	–1546(29)	hml+06										
B1323–58	J1326–5859	287.30(15)	–579.6(9)	njkk08	–577(3)	vdhm97	–580(10)	cmh91						
B1322–66	J1326–6700	209.6(3)	–47(1)	hml+06										
B1323–62	J1327–6222	318.80(6)	–306(8)	hml+06										
B1323–627	J1327–6301	294.91(3)	87.0(20)	njkk08	96(12)	hml+06								
J1327–6400	J1327–6400	680.9(14)	–141(58)	hml+06										
B1325–43	J1328–4357	42.0(10)	–41(3)	hmq99										
B1325–49	J1328–4921	118(2)	170(20)	hmq99										
J1333–4449	J1333–4449	44.3(17)	–71(17)	njkk08										
J1334–5839	J1334–5839	119.2978(9)	54(7)	hml+06										
J1337–6423	J1337–6423	260.32	–135(17)	kjb+12										
B1334–61	J1338–6204	640.3(7)	–459(4)	njkk08										
J1339–4712	J1339–4712	39.9(6)	17(11)	njkk08										
B1336–64	J1340–6456	76.99(13)	–37(23)	njkk08										

Continued on next page

Table A.1 – continued from previous page

PSR name	PSR jname	DM (cm^{-3} pc)	RM_{psrcat} ($rad\,m^{-2}$)	ref_{psrcat}	RM_1 ($rad\,m^{-2}$)	ref_{RM_1}	RM_2 ($rad\,m^{-2}$)	ref_{RM_2}	RM_3 ($rad\,m^{-2}$)	ref_{RM_3}	RM_4 ($rad\,m^{-2}$)	ref_{RM_4}	RM_5 ($rad\,m^{-2}$)	ref_{RM_5}
J1341–6023	J1341–6023	364.6(9)	–688(23)	hml+06										
B1338–62	J1341–6220	717.3(6)	–921(3)	jw06	–946(7)	cmk01								
J1345–6115	J1345–6115	278.1(20)	–61(2)	hml+06										
J1347–5947	J1347–5947	293.4(5)	–548(6)	hml+06										
J1349–6130	J1349–6130	284.6(4)	–380(13)	hml+06										
J1350–5115	J1350–5115	90.388(8)	–2(22)	hml+06										
J1352–6803	J1352–6803	214.6(2)	30(7)	njkk08										
B1352–51	J1355–5153	112.1(4)	55(6)	hml+06										
J1355–6206	J1355–6206	547(3)	–474(6)	hml+06										
J1356–5521	J1356–5521	174.172(6)	101(4)	njkk08	150(22)	hml+06								
B1353–62	J1357–62	416.8(4)	–586(5)	hml+06										
J1357–6429	J1357–6429	128.5(7)	–47(2)	jw06	–54(13)	hml+06								
B1356–60	J1359–6038	293.71(14)	33(5)	hmq99										
B1358–63	J1401–6357	98.0(5)	62(4)	qmlg95	54(1)	vdhm97								
J1403–6310	J1403–6310	305(3)	–709(21)	hml+06										
J1403–7646	J1403–7646	100.6(1)	94(16)	njkk08										
J1406–5806	J1406–5806	229(3)	153(4)	hml+06										
J1406–6121	J1406–6121	542.3(18)	880(60)	hml+06										
J1410–6132	J1410–6132	960(10)	2400(30)	ojk+08										
J1410–7404	J1410–7404	54.24(6)	–4(4)	njkk08										
J1412–6145	J1412–6145	514.7(11)	–130(13)	jw06	–39(20)	hml+06								

Continued on next page

Table A.1 – continued from previous page

PSR name	PSR jname	DM (cm^{-3} pc)	RM_{psrcat} ($rad\,m^{-2}$)	ref_{psrcat}	RM_1 ($rad\,m^{-2}$)	ref_{RM_1}	RM_2 ($rad\,m^{-2}$)	ref_{RM_2}	RM_3 ($rad\,m^{-2}$)	ref_{RM_3}	RM_4 ($rad\,m^{-2}$)	ref_{RM_4}	RM_5 ($rad\,m^{-2}$)	ref_{RM_5}
J1413–6141	J1413–6141	677(8)	–35(10)	hml+06	–400(40)	jw06								
J1413–6222	J1413–6222	808.1(12)	–490(8)	hml+06										
B1409–62	J1413–6307	121.98(6)	44(4)	njkk08	45(9)	hml+06								
J1416–6037	J1416–6037	289.2(10)	336(7)	hml+06										
J1418–3921	J1418–3921	60.49(1)	–15(8)	hmq99										
B1417–54	J1420–5416	129.6(12)	–1(9)	hml+06										
J1420–6048	J1420–6048	358.8(2)	–122(5)	jw06	–110(16)	hml+06	–106(18)	rrj01						
J1424–5822	J1424–5822	323.9(6)	–625(19)	hml+06										
B1424–55	J1428–5530	82.4(6)	4(3)	qmlg95										
B1426–66	J1430–6623	65.3(1)	–19.2(3)	jhv+05	–20(1)	vdhm97								
J1431–5740	J1431–5740	131.46(3)	–50(15)	bbb+13										
J1437–5959	J1437–5959	549.6(11)	–700(25)	cng+09										
B1436–63	J1440–6344	124.2(5)	29(4)	hmq99										
J1446–4701	J1446–4701	55.8340(11)	–14(3)	kjb+12										
J1452–5851	J1452–5851	262.4(15)	47(7)	hml+06										
J1452–6036	J1452–6036	349.7(3)	10(5)	hml+06										
B1449–64	J1453–6413	71.07(2)	–18.6(2)	jhv+05	–23(1)	vdhm97								
B1451–68	J1456–6843	8.6(2)	–4.0(3)	jhv+05	–3(1)	vdhm97								
J1502–5828	J1502–5828	584(4)	362(7)	hml+06										
J1502–6752	J1502–6752	151.75	–225(2)	kjb+12										
B1504–43	J1507–4352	48.7(5)	–34(7)	njkk08	–33(4)	hml+06								

Continued on next page

Table A.1 – continued from previous page

PSR name	PSR jname	DM (cm^{-3} pc)	RM_{psrcat} ($rad\,m^{-2}$)	ref_{psrcat}	RM_1 ($rad\,m^{-2}$)	ref_{RM_1}	RM_2 ($rad\,m^{-2}$)	ref_{RM_2}	RM_3 ($rad\,m^{-2}$)	ref_{RM_3}	RM_4 ($rad\,m^{-2}$)	ref_{RM_4}	RM_5 ($rad\,m^{-2}$)	ref_{RM_5}
B1508+55	J1509+5531	19.613(20)	0.8(7)	man72	0(4)	hl87								
B1507–44	J1510–4422	84(7)	8(8)	hml+06										
B1508–57	J1512–5759	628.7(2)	510(7)	njkk08	513(16)	hml+06								
J1513–5739	J1513–5739	469.7(10)	261(13)	hml+06										
B1509–58	J1513–5908	252.5(3)	216(1)	jw06										
B1510–48	J1514–4834	51.5(8)	18(14)	njkk08										
J1517–4356	J1517–4356	87.78(12)	1(19)	njkk08										
B1518–58	J1522–5829	199.9(2)	–24.2(20)	njkk08										
J1524–5625	J1524–5625	152.7(10)	180(20)	wj08										
J1524–5706	J1524–5706	833(3)	–470(20)	wj08										
J1525–5545	J1525–5545	126.934(7)	–19(9)	nbb+14										
B1524–39	J1527–3931	49(3)	4(1)	hmq99										
B1523–55	J1527–5552	362.7(8)	34(4)	hmq99										
J1528–4109	J1528–4109	89.50(10)	25(8)	njkk08										
J1529–3828	J1529-3828	73.62(2)	–29(9)	nbb+14										
J1530–5327	J1530–5327	49.6(10)	–19(21)	hml+06										
J1531–5610	J1531–5610	110.9(4)	–50(20)	hml+06										
B1530+27	J1532+2745	14.698(18)	1.0(3)	wck+04	54(11)	hl87								
B1530–53	J1534–5334	24.82(1)	–46(17)	hml+06										
B1530–539	J1534–5405	190.82(2)	–69(12)	njkk08	–46(17)	hml+06								
J1535–4114	J1535–4114	66.28(14)	17.7(20)	njkk08										

Continued on next page

Table A.1 – continued from previous page

PSR name	PSR jname	DM (cm^{-3} pc)	RM_{psrcat} ($rad\,m^{-2}$)	ref_{psrcat}	RM_1 ($rad\,m^{-2}$)	ref_{RM_1}	RM_2 ($rad\,m^{-2}$)	ref_{RM_2}	RM_3 ($rad\,m^{-2}$)	ref_{RM_3}	RM_4 ($rad\,m^{-2}$)	ref_{RM_4}	RM_5 ($rad\,m^{-2}$)	ref_{RM_5}
J1536–3602	J1536–3602	96(6)	–24(9)	njkk08										
J1536–5433	J1536–5433	147.5(19)	–155(13)	hml+06										
B1534+12	J1537+1155	11.61436(3)	10.6(2)	wck+04										
B1535–56	J1539–5626	175.88(6)	–18.0(20)	njkk08										
J1540–5736	J1540–5736	304.5(13)	–414(15)	hml+06										
J1541–5535	J1541–5535	428(5)	–256(13)	hml+06										
J1542–5034	J1542–5034	91.0(6)	–70(8)	hmq99										
B1540–06	J1543–0620	18.403(4)	4(4)	hl87										
B1541+09	J1543+0929	35.24(3)	21(2)	hl87	21.6(6)	wck+04								
J1543–5149	J1543–5149	50.92	0(25)	kjb+12										
J1543–5459	J1543–5459	345.7(10)	28(23)	hml+06										
B1541–52	J1544–5308	35.16(7)	–29(7)	hmq99										
J1545–4550	J1545–4550	68.390(8)	–0.6(13)	bbb+13										
J1546–5302	J1546–5302	287(3)	–1135(90)	hml+06										
J1548–5607	J1548–5607	315.5(4)	37(10)	hml+06										
J1549–4848	J1549–4848	55.983(8)	–15(8)	hmq99										
J1550–5242	J1550–5242	337.7(18)	–440(25)	hml+06										
J1550–5418	J1550–5418	830(50)	–1860(20)	crj+08										
J1555–0515	J1555–0515	23.46(3)	1.3(30)	blr+13										
B1552–23	J1555–2341	51.901(15)	–22(8)	hl87										
B1552–31	J1555–3134	73.045(7)	–49(6)	hl87										

Continued on next page

Table A.1 – continued from previous page

PSR name	PSR jname	DM (cm^{-3} pc)	RM_{psrcat} ($rad\,m^{-2}$)	ref_{psrcat}	RM_1 ($rad\,m^{-2}$)	ref_{RM_1}	RM_2 ($rad\,m^{-2}$)	ref_{RM_2}	RM_3 ($rad\,m^{-2}$)	ref_{RM_3}	RM_4 ($rad\,m^{-2}$)	ref_{RM_4}	RM_5 ($rad\,m^{-2}$)	ref_{RM_5}
J1556–5358	J1556–5358	436(3)	–153(16)	hml+06										
J1557–4258	J1557–4258	144.497(2)	–41.9(20)	njkk08	–37(2)	hmq99								
B1556–44	J1559–4438	56.1(4)	–7(1)	hmq99	–5.0(6)	jkk+07	–5.1(5)	vdhm97						
B1555–55	J1559–5545	212.9(3)	–150(20)	hmq99										
J1600–3053	J1600–3053	52.3262(10)	–15.5(10)	ymv+11										
B1557–50	J1600–5044	260.56(9)	119(10)	tml93										
B1556–57	J1600–5751	176.55(8)	–131(8)	hml+06	–117.9(18)	njkk08								
J1601–5335	J1601–5335	194.6(7)	–157(35)	hml+06										
B1558–50	J1602–5100	170.93(7)	71.5(11)	tml93										
J1603–2531	J1603–2531	53.763(4)	15(4)	hml+06										
B1600–27	J1603–2712	46.201(16)	–5(3)	hl87										
J1603–5657	J1603–5657	264.07(2)	28(3)	njkk08	27(5)	hmq99								
J1603–7202	J1603–7202	38.0471(1)	27.7(8)	ymv+11	30(6)	hml+06	20.1(5)	mh04						
B1600–49	J1604–4909	140.8(5)	–16(6)	hmq99	34.0(1)	jkk+07								
J1604–7203	J1604–7203	54.370(5)	22(11)	hmq99										
B1601–52	J1605–5257	35.1(3)	1.0(20)	njkk08										
B1604–00	J1607–0032	10.682(5)	6.5(10)	man74	–6(4)	hl87								
J1610–5006	J1610–5006	416(3)	–756(23)	hml+06										
J1610–5303	J1610–5303	380.1(8)	–335(30)	hml+06										
J1611–4949	J1611–4949	556.8(18)	–405(22)	hml+06										
B1607–52	J1611–5209	127.57(5)	–79(5)	njkk08	–72(6)	hml+06								

Continued on next page

Table A.1 – continued from previous page

PSR name	PSR jname	DM (cm^{-3} pc)	RM_{psrcat} ($rad\,m^{-2}$)	ref_{psrcat}	RM_1 ($rad\,m^{-2}$)	ref_{RM_1}	RM_2 ($rad\,m^{-2}$)	ref_{RM_2}	RM_3 ($rad\,m^{-2}$)	ref_{RM_3}	RM_4 ($rad\,m^{-2}$)	ref_{RM_4}	RM_5 ($rad\,m^{-2}$)	ref_{RM_5}
J1612+2008	J1612+2008	19.544(10)	22(3)	blr+13										
B1609–47	J1613–4714	161.2(3)	–138(7)	hml+06										
B1612+07	J1614+0737	21.39(3)	40(4)	hl87	35(9)	wck+04								
J1614–3937	J1614–3937	152.44(2)	133(16)	njkk08										
B1610–50	J1614–5048	582.8(3)	–451(2)	hml+06	–452.7(50)	njkk08								
B1612–29	J1615–2940	44.79(14)	–30(13)	hl87										
J1615–5444	J1615–5444	312.6(5)	–232(28)	hml+06										
B1611–55	J1615–5537	124.48(8)	–54(16)	njkk08										
J1618–4723	J1618–4723	134.7(3)	39(4)	hml+06										
J1622–4332	J1622–4332	230.68(2)	140(20)	hmq99										
J1622–4950	J1622–4950	820(30)	–1484(1)	lbb+10										
B1620–09	J1623–0908	68.183(10)	–85(20)	hl87										
B1620–26	J1623–2631	62.8633(5)	–8(20)	mh04	–8(20)	hml+06								
B1620–42	J1623–4256	295(5)	–15(8)	hml+06										
J1623–4949	J1623–4949	183.3(10)	–42(7)	hml+06										
J1625–4048	J1625–4048	145(6)	–7(15)	hml+06										
J1628–4804	J1628–4804	952(3)	–431(43)	hml+06										
J1630–4719	J1630–4719	489.6(16)	–339(10)	hml+06										
B1626–47	J1630–4733	498(5)	–348(6)	njkk08	–338(8)	hml+06								
J1632–4818	J1632–4818	758(5)	–515(39)	hml+06										
J1633–2009	J1633–2009	48.19(6)	–0.1(12)	blr+13										

Continued on next page

Table A.1 – continued from previous page

PSR name	PSR jname	DM (cm^{-3} pc)	RM_{psrcat} ($rad\,m^{-2}$)	ref_{psrcat}	RM_1 ($rad\,m^{-2}$)	ref_{RM_1}	RM_2 ($rad\,m^{-2}$)	ref_{RM_2}	RM_3 ($rad\,m^{-2}$)	ref_{RM_3}	RM_4 ($rad\,m^{-2}$)	ref_{RM_4}	RM_5 ($rad\,m^{-2}$)	ref_{RM_5}
B1630–44	J1633–4453	474.1(3)	159(6)	njkk08	139(17)	hml+06								
B1629–50	J1633–5015	398.41(8)	406.1(20)	njkk08										
B1633+24	J1635+2418	24.32(4)	31(4)	wck+04										
J1635–4944	J1635–4944	474(6)	–23(15)	hml+06										
B1634–45	J1637–4553	193.23(7)	10(5)	njkk08	12(4)	hml+06								
J1637–4642	J1637–4642	417.0(12)	13(18)	hml+06										
J1638–4417	J1638–4417	436.0(7)	160(25)	wj08										
J1638–4608	J1638–4608	424.3(8)	335(12)	hml+06										
J1639–4359	J1639–4359	258.9(16)	129(18)	hml+06										
B1635–45	J1639–4604	258.91(4)	–28(12)	njkk08	–60(30)	hml+06								
B1636–47	J1640–4715	591.7(8)	–411(12)	njkk08	–398(22)	hml+06								
J1641–2347	J1641–2347	27.7(3)	–22(4)	njkk08										
J1643–1224	J1643–1224	62.4121(2)	–308.1(10)	ymv+11	–263(15)	hml+06	–263(15)	mh04						
B1641–45	J1644–4559	478.8(8)	–617(1)	hml+06	–612(2)	vdhm97								
B1642–03	J1645–0317	35.727(3)	15.8(3)	hl87	17(2)	jhv+05	16.5(25)	man72						
B1643–43	J1646–4346	490.4(3)	–62(7)	hml+06	–24.2(18)	njkk08	–65(17)	cmk01						
B1641–68	J1646–6831	43(2)	105(3)	qmlg95	137(16)	vdhm97								
J1648–3256	J1648–3256	128.278(6)	–60(15)	hmq99										
J1648–4611	J1648–4611	392.9(17)	–682(26)	hml+06										
J1649–4349	J1649–4349	398.6(12)	759(17)	hml+06										
J1650–1654	J1650–1654	43.25(15)	7(14)	njkk08										

Continued on next page

Table A.1 – continued from previous page

PSR name	PSR jname	DM (cm^{-3} pc)	RM_{psrcat} ($rad\,m^{-2}$)	ref_{psrcat}	RM_1 ($rad\,m^{-2}$)	ref_{RM_1}	RM_2 ($rad\,m^{-2}$)	ref_{RM_2}	RM_3 ($rad\,m^{-2}$)	ref_{RM_3}	RM_4 ($rad\,m^{-2}$)	ref_{RM_4}	RM_5 ($rad\,m^{-2}$)	ref_{RM_5}
J1650–4502	J1650–4502	319.7(8)	130(10)	hml+06										
B1648–17	J1651–1709	33.46(6)	4(8)	hl87										
B1648–42	J1651–4246	482(3)	–154(5)	hml+06										
B1647–52	J1651–5222	179.1(6)	–38(5)	hmq99										
J1651–7642	J1651–7642	80(10)	54(6)	njkk08										
J1652–1400	J1652–1400	49.5(13)	–49(10)	njkk08										
B1649–23	J1652–2404	68.41(3)	–24(8)	hl87										
B1650–38	J1653–3838	207.2(2)	–82(3)	njkk08	–74(6)	hml+06								
J1653–4249	J1653–4249	416.1(11)	25(17)	hml+06										
J1655–3048	J1655–3048	154.3(3)	–63(10)	njkk08										
J1700–3312	J1700–3312	166.97(9)	–15(3)	hmq99	–25.3(4)	njkk08								
B1658–37	J1701–3726	303.4(5)	–605.9(20)	njkk08	–602(8)	hml+06								
B1657–45	J1701–4533	526.0(6)	4(4)	njkk08	17(13)	hml+06								
J1702–4128	J1702–4128	367.1(7)	–160(20)	wj08										
J1702–4310	J1702–4310	377(3)	–35(12)	jw06										
B1700–18	J1703–1846	49.551(15)	–29(3)	hl87										
B1700–32	J1703–3241	110.306(14)	–21.7(5)	hl87										
J1703–4851	J1703–4851	150.29(3)	–46(5)	njkk08	–4(24)	hml+06								
B1659–60	J1704–6016	54(5)	50(10)	qmlg95										
B1702–19	J1705–1906	22.907(3)	–19.2(10)	njkk08										
J1705–3423	J1705–3423	146.36(10)	–44(8)	hml+06										

Continued on next page

Table A.1 – continued from previous page

PSR name	PSR jname	DM (cm^{-3} pc)	RM_{psrcat} ($rad\,m^{-2}$)	ref_{psrcat}	RM_1 ($rad\,m^{-2}$)	ref_{RM_1}	RM_2 ($rad\,m^{-2}$)	ref_{RM_2}	RM_3 ($rad\,m^{-2}$)	ref_{RM_3}	RM_4 ($rad\,m^{-2}$)	ref_{RM_4}	RM_5 ($rad\,m^{-2}$)	ref_{RM_5}
J1705–3950	J1705–3950	207.1(13)	–106(14)	wj08										
J1705–4108	J1705–4108	1077(6)	916(15)	hml+06										
B1703–40	J1707–4053	360.0(2)	168(4)	njkk08										
J1708–3426	J1708–3426	190.7(3)	–176(15)	hml+06										
J1708–3506	J1708–3506	146.8(2)	–15(5)	kjb+12										
B1706–16	J1709–1640	24.873(5)	–2(5)	jhv+05	–2.5(10)	vdhm97	–1.3(3)	hl87	–2.5(10)	man74				
B1706–44	J1709–4429	75.69(5)	–7(4)	qmlg95	0.70(7)	jhv+05								
J1713+0747	J1713+0747	15.9915(2)	8.4(6)	ymv+11										
J1715–3903	J1715–3903	313.1(17)	250(15)	hml+06										
B1714–34	J1717–3425	587.7(7)	–191(14)	hml+06										
J1717–4043	J1717–4043	452.6(12)	–993(17)	hml+06										
J1717–5800	J1717–5800	125.22(14)	39(20)	njkk08										
J1718–3718	J1718–3718	371.1(17)	–160(22)	mh11										
J1718–3825	J1718–3825	247.4(3)	113(10)	hml+06										
J1719–1438	J1719–1438	36.766(2)	16(4)	kjb+12										
B1715–40	J1719–4006	386.6(2)	–218(17)	njkk08	–234(31)	hml+06								
B1718–02	J1720–0212	66.98(4)	17(3)	hl87										
B1717–16	J1720–1633	44.83(3)	–12(13)	hml+06										
B1717–29	J1720–2933	42.64(3)	21(5)	hl87										
J1720–3659	J1720–3659	381.6(5)	–99(7)	hml+06										
B1718–35	J1721–3532	496.0(4)	159(4)	njkk08										

Continued on next page

Table A.1 – continued from previous page

PSR name	PSR jname	DM (cm^{-3} pc)	RM_{psrcat} ($rad\,m^{-2}$)	ref_{psrcat}	RM_1 ($rad\,m^{-2}$)	ref_{RM_1}	RM_2 ($rad\,m^{-2}$)	ref_{RM_2}	RM_3 ($rad\,m^{-2}$)	ref_{RM_3}	RM_4 ($rad\,m^{-2}$)	ref_{RM_4}	RM_5 ($rad\,m^{-2}$)	ref_{RM_5}
B1718–32	J1722–3207	126.064(8)	90(7)	hl87										
B1718–36	J1722–3632	416.2(2)	–307(8)	hml+06	–332.8(90)	njkk08								
B1719–37	J1722–3712	99.50(4)	104(3)	hmq99										
J1723–3659	J1723–3659	254.2(3)	–219(11)	hml+06										
J1730–2304	J1730–2304	9.617(2)	–7.2(22)	ymv+11										
B1727–33	J1730–3350	259(5)	–142(5)	cmk01	–132(10)	hml+06								
J1731–1847	J1731–1847	106.56(6)	19(1)	kjb+12										
B1727–47	J1731–4744	123.33(2)	–429.1(5)	tml93	–443(2)	vdhm97								
J1732–5049	J1732–5049	56.822(6)	–8.5(67)	ymv+11										
B1730–22	J1733–2228	41.14(3)	–12(3)	njkk08	–9(4)	hl87								
B1730–37	J1733–3716	153.5(3)	–335.0(20)	njkk08	–330(6)	hml+06								
J1735–0243	J1735–0243	55.4(5)	28.3(19)	blr+13										
B1732–07	J1735–0724	73.512(4)	38(3)	hl87	34.5(3)	jkk+07								
J1737–0811	J1737–0811	55.311(3)	71.4(14)	blr+13										
J1737–3137	J1737–3137	488.2(10)	448(17)	wj08										
B1734–35	J1737–3555	89.41(4)	50(4)	njkk08										
J1738–2955	J1738–2955	223.4(6)	–200(20)	wj08										
B1735–32	J1738–3211	49.59(4)	7(9)	hml+06										
J1739–1313	J1739–1313	58.2(5)	34.1(20)	njkk08										
B1736–29	J1739–2903	138.56(3)	–236(18)	hml+06										
J1739–3023	J1739–3023	170.0(3)	–74(18)	hml+06										

Continued on next page

Table A.1 – continued from previous page

PSR name	PSR jname	DM (cm^{-3} pc)	RM_{psrcat} ($rad\,m^{-2}$)	ref_{psrcat}	RM_1 ($rad\,m^{-2}$)	ref_{RM_1}	RM_2 ($rad\,m^{-2}$)	ref_{RM_2}	RM_3 ($rad\,m^{-2}$)	ref_{RM_3}	RM_4 ($rad\,m^{-2}$)	ref_{RM_4}	RM_5 ($rad\,m^{-2}$)	ref_{RM_5}
B1736–31	J1739–3131	600.1(12)	32(8)	rl94										
J1740+1000	J1740+1000	23.85(5)	23.8(28)	mac+02										
B1737+13	J1740+1311	48.673(4)	64.4(16)	wck+04	65(2)	jhv+05	73(5)	hl87						
B1737–30	J1740–3015	152.15(2)	–168.0(7)	njkk08	–157(2)	rl94								
B1738–08	J1741–0840	74.90(5)	124(6)	hl87										
B1737–39	J1741–3927	158.5(6)	204(6)	hml+06	180(14)	hmq99	221(29)	vdhm97						
J1742–4616	J1742–4616	115.96(14)	–38(6)	njkk08										
B1740–31	J1743–3150	193.05(7)	–215(4)	njkk08	–240(12)	hml+06								
J1743–4212	J1743–4212	131.94(5)	–20(6)	njkk08										
J1744–1134	J1744–1134	3.13908(4)	–1.6(7)	ymv+11										
J1745–2900	J1745–2900	1778(3)	–67000(500)	sj13	–66960(50)	efk+13								
B1742–30	J1745–3040	88.373(4)	101(7)	hl87	90(10)	hl87								
B1745–12	J1748–1300	99.364(6)	67(7)	hl87										
B1746–30	J1749–3002	509.4(3)	–290(3)	njkk08	–313(7)	qmlg95								
B1747–31	J1750–3157	206.34(4)	111(8)	hml+06	108.6(14)	njkk08								
J1750–3503	J1750–3503	189.35(2)	173(11)	hmq99										
B1747–46	J1751–4657	20.4(4)	19(1)	hmq99	16(2)	vdhm97								
B1749–28	J1752–2806	50.372(8)	96.0(2)	hl87	95.1(3)	jkk+07	97.5(9)	vdhm97	95(2)	man74				
B1750–24	J1753–2501	672(3)	21(17)	rl94										
J1755–3716	J1755–3716	167.603(19)	54(3)	nbb+14										
B1753–24	J1756–2435	367.1(4)	–130(7)	rl94										

Continued on next page

Table A.1 – continued from previous page

PSR name	PSR jname	DM (cm^{-3} pc)	RM_{psrcat} ($rad\,m^{-2}$)	ref_{psrcat}	RM_1 ($rad\,m^{-2}$)	ref_{RM_1}	RM_2 ($rad\,m^{-2}$)	ref_{RM_2}	RM_3 ($rad\,m^{-2}$)	ref_{RM_3}	RM_4 ($rad\,m^{-2}$)	ref_{RM_4}	RM_5 ($rad\,m^{-2}$)	ref_{RM_5}
B1754–24	J1757–2421	179.454(11)	16(5)	njkk08	–9(9)	hml+06								
B1756–22	J1759–2205	177.157(5)	6(7)	hl87	1(10)	hml+06								
B1758–03	J1801–0357	120.37(3)	32(11)	hmq99										
J1801–2154	J1801–2154	387.9(14)	160(40)	wj08										
B1758–23	J1801–2304	1073.9(6)	–1156(19)	cmk01										
B1757–24	J1801–2451	289.0(10)	637(12)	hml+06	603.0(5)	jkk+07								
B1758–29	J1801–2920	125.613(14)	–62(3)	njkk08	–60(10)	qmlg95								
J1801–3210	J1801–3210	176.7(4)	226(4)	kjb+12										
B1800–21	J1803–2137	233.99(5)	–27(3)	rl94										
B1800–27	J1803–2712	165.5(3)	–165(6)	njkk08	147(18)	qmlg95								
J1805–0619	J1805–0619	146.22(9)	82(14)	njkk08										
B1804–08	J1807–0847	112.3802(11)	166(9)	hl87										
J1807–2459A	J1807–2459A	134.00401(58)	160.4(6)	lfrj12										
J1807–2459B	J1807–2459B	137.1535(20)	157(1)	lfrj12										
B1804–27	J1807–2715	312.98(3)	–47(14)	hl87										
J1808–0813	J1808–0813	151.27(6)	77(5)	njkk08	73(7)	hmq99								
B1805–20	J1808–2057	606.8(9)	93(11)	hml+06										
J1808–3249	J1808–3249	147.37(19)	289(6)	njkk08										
J1809–1917	J1809–1917	197.1(4)	41(17)	wj08	130(12)	hml+06								
J1809–1943	J1809–1943	178(5)	76(4)	crj+07										
B1806–21	J1809–2109	381.91(5)	256(24)	hml+06										

Continued on next page

Table A.1 – continued from previous page

PSR name	PSR jname	DM (cm^{-3} pc)	RM_{psrcat} ($rad\,m^{-2}$)	ref_{psrcat}	RM_1 ($rad\,m^{-2}$)	ref_{RM_1}	RM_2 ($rad\,m^{-2}$)	ref_{RM_2}	RM_3 ($rad\,m^{-2}$)	ref_{RM_3}	RM_4 ($rad\,m^{-2}$)	ref_{RM_4}	RM_5 ($rad\,m^{-2}$)	ref_{RM_5}
J1809–3547	J1809–3547	193.84(7)	379(18)	hml+06										
B1806–53	J1810–5338	45(2)	58(3)	qmlg95										
J1811–0154	J1811–0154	148.1(3)	46(11)	njkk08										
J1811–2405	J1811–2405	60.64(6)	23(3)	kjb+12										
B1811+40	J1813+4013	41.487(18)	47(6)	hl87										
J1815–1738	J1815–1738	728(3)	175(20)	wj08										
B1813–26	J1816–2650	128.12(3)	90(5)	hl87										
B1813–36	J1817–3618	94.3(5)	66(4)	qmlg95										
J1817–3837	J1817–3837	102.847(6)	102.9(20)	njkk08	89(6)	hml+06								
B1815–14	J1818–1422	622.0(4)	1168(13)	hml+06										
J1818–1519	J1818–1519	845(6)	1157(23)	hml+06										
B1818–04	J1820–0427	84.435(17)	69.2(2)	hl87	67.5(6)	jkk+07	70.5(75)	man72						
B1817–13	J1820–1346	776.7(17)	893(12)	hml+06										
B1817–18	J1820–1818	436.0(12)	–70(12)	njkk08	–60(24)	hml+06								
B1819–22	J1822–2256	121.20(4)	124(3)	njkk08	142(4)	qmlg95	140(7)	hl87						
J1822–4209	J1822–4209	72.514(5)	–13(9)	hml+06										
J1823–0154	J1823–0154	135.87(5)	153(24)	hml+06										
B1821+05	J1823+0550	66.775(3)	145(10)	hl87										
B1820–11	J1823–1115	428.59(9)	–354(10)	hml+06										
B1820–31	J1823–3106	50.245(4)	95(5)	hl87										
B1821–11	J1824–1118	603(2)	213(17)	hml+06										

Continued on next page

Table A.1 – continued from previous page

PSR name	PSR jname	DM (cm^{-3} pc)	RM_{psrcat} ($rad\,m^{-2}$)	ref_{psrcat}	RM_1 ($rad\,m^{-2}$)	ref_{RM_1}	RM_2 ($rad\,m^{-2}$)	ref_{RM_2}	RM_3 ($rad\,m^{-2}$)	ref_{RM_3}	RM_4 ($rad\,m^{-2}$)	ref_{RM_4}	RM_5 ($rad\,m^{-2}$)	ref_{RM_5}
J1824–1159	J1824–1159	463.4(24)	407(15)	hml+06										
B1821–19	J1824–1945	224.648(5)	–303(15)	hl87										
B1821–24A	J1824–2452A	120.502(2)	77.8(6)	ymv+11										
B1822+00	J1825+0004	56.618(9)	21(13)	wck+04										
B1822–09	J1825–0935	19.38(4)	65.2(2)	hl87	66.2(3)	jkk+07	69(2)	man74						
B1822–14	J1825–1446	357(5)	–899(10)	rl94										
B1823–11	J1826–1131	320.58(6)	229(23)	rl94										
B1823–13	J1826–1334	231.0(10)	10(5)	rl94										
J1827–0934	J1827–0934	259.2(5)	–386(24)	hml+06										
J1828–1101	J1828–1101	607.4(5)	45(20)	wj08										
B1826–17	J1829–1751	217.108(9)	306(6)	hmq99	317(16)	hl87								
B1828–11	J1830–1059	161.50(20)	47(5)	rl94										
B1829–08	J1832–0827	300.869(10)	39(7)	rl94										
J1832–0836	J1832–0836	28.18(9)	25(17)	bbb+13										
B1831–03	J1833–0338	234.538(13)	–41(4)	hl87										
B1830–08	J1833–0827	411(2)	–470(7)	rl94										
B1831–04	J1834–0426	79.308(8)	100(5)	hl87										
B1832–06	J1835–0643	472.9(10)	62(38)	hml+06										
J1835–1106	J1835–1106	132.679(3)	42(3)	njkk08										
B1834–10	J1836–1008	316.98(3)	–1000(99)	hl87										
J1837–0045	J1837–0045	86.98(9)	130(17)	njkk08										

Continued on next page

Table A.1 – continued from previous page

PSR name	PSR jname	DM (cm^{-3} pc)	RM_{psrcat} ($rad\,m^{-2}$)	ref_{psrcat}	RM_1 ($rad\,m^{-2}$)	ref_{RM_1}	RM_2 ($rad\,m^{-2}$)	ref_{RM_2}	RM_3 ($rad\,m^{-2}$)	ref_{RM_3}	RM_4 ($rad\,m^{-2}$)	ref_{RM_4}	RM_5 ($rad\,m^{-2}$)	ref_{RM_5}
J1837–0604	J1837–0604	462(1)	450(25)	wj08										
J1837+1221	J1837+1221	100.6(4)	173(24)	njkk08										
J1837–1837	J1837–1837	100.74(13)	138(8)	njkk08										
B1839+56	J1840+5640	26.698(11)	–3(3)	hl87										
J1841–0345	J1841–0345	194.32(6)	447(15)	wj08										
B1838–04	J1841–0425	325.487(15)	406(4)	rl94	416.0(8)	jkk+07								
J1841–0500	J1841–0500	532(1)	–2993(50)	crc+12										
B1839+09	J1841+0912	49.107(8)	53(5)	hl87										
B1839–04	J1842–0359	195.98(8)	326(9)	rl94										
B1841–04	J1844–0433	123.158(20)	7(13)	rl94										
B1841–05	J1844–0538	412.8(3)	16(16)	rl94										
B1842+14	J1844+1454	41.510(4)	109.0(13)	jhv+05	121(8)	hl87								
B1842–04	J1845–0434	230.8(17)	–248(10)	hml+06										
J1845–0743	J1845–0743	281.0(3)	440(12)	wj08										
B1844–04	J1847–0402	141.979(5)	117(8)	hl87										
B1845–01	J1848–0123	159.531(8)	580(30)	tml93										
B1845–19	J1848–1952	18.23(7)	7(3)	hl87										
B1846–06	J1849–0636	148.168(12)	–35(21)	hmq99										
B1848+13	J1850+1335	60.147(8)	146(8)	rl94	152.7(6)	jkk+07								
B1848+12	J1851+1259	70.615(16)	158(16)	rl94										
J1852–2610	J1852–2610	56.814(19)	–21(1)	hmq99	–21.2(40)	njkk08								

Continued on next page

Table A.1 – continued from previous page

PSR name	PSR jname	DM (cm^{-3} pc)	RM_{psrcat} ($rad\,m^{-2}$)	ref_{psrcat}	RM_1 ($rad\,m^{-2}$)	ref_{RM_1}	RM_2 ($rad\,m^{-2}$)	ref_{RM_2}	RM_3 ($rad\,m^{-2}$)	ref_{RM_3}	RM_4 ($rad\,m^{-2}$)	ref_{RM_4}	RM_5 ($rad\,m^{-2}$)	ref_{RM_5}
J1853–0004	J1853–0004	438.2(8)	647(16)	wj08										
J1853–0649	J1853–0649	44.541(36)	34.7(32)	lbr+13										
B1852+10	J1854+1050	207.2(3)	502(25)	wck+04										
B1851–14	J1854–1421	130.40(3)	103(9)	hl87										
B1853+01	J1856+0113	96.74(12)	–140(30)	hml+06										
B1854+00	J1857+0057	82.39(11)	104(19)	wck+04	79(26)	hml+06								
B1855+02	J1857+0212	506.77(18)	423(21)	hml+06										
B1855+09	J1857+0943	13.300(4)	16.4(35)	ymv+11	53(9)	hml+06								
B1857–26	J1900–2600	37.994(5)	–2.3(8)	jhv+05	–13(2)	hmq99	–9.5(5)	vdhm97	–3(6)	hl87	–7.3(8)	hl87		
B1851–79	J1900–7951	39(5)	43(12)	qmlg95										
B1859+01	J1901+0156	105.394(7)	–122(9)	hml+06										
B1859+03	J1901+0331	402.080(12)	–237.4(15)	hl87										
B1859+07	J1901+0716	252.81(7)	282(13)	rl94	321(38)	wck+04								
J1901–0906	J1901–0906	72.677(18)	29.0(20)	njkk08	44(12)	hmq99								
J1901–1740	J1901–1740	24.4(6)	63(33)	njkk08										
B1900+05	J1902+0556	177.486(13)	–113(11)	hl87										
B1900+01	J1903+0135	245.167(6)	72.3(10)	hl87										
B1900–06	J1903–0632	195.611(10)	203(10)	hl87										
J1903–0848	J1903–0848	66.99(4)	4.4(9)	blr+13										
J1904+0004	J1904+0004	233.61(4)	289(6)	njkk08	306(9)	hml+06								
J1906+0746	J1906+0746	217.780(2)	150(10)	lsf+06										

Continued on next page

Table A.1 – continued from previous page

PSR name	PSR jname	DM (cm^{-3} pc)	RM_{psrcat} ($rad\,m^{-2}$)	ref_{psrcat}	RM_1 ($rad\,m^{-2}$)	ref_{RM_1}	RM_2 ($rad\,m^{-2}$)	ref_{RM_2}	RM_3 ($rad\,m^{-2}$)	ref_{RM_3}	RM_4 ($rad\,m^{-2}$)	ref_{RM_4}	RM_5 ($rad\,m^{-2}$)	ref_{RM_5}
B1905+39	J1907+4002	30.96(3)	7(3)	hl87										
B1907+00	J1909+0007	112.787(6)	–40(15)	hl87										
B1907+10	J1909+1102	149.982(4)	540(20)	hl87										
J1909–3744	J1909–3744	10.3934(2)	–6.6(8)	ymv+11										
B1907–03	J1910–0309	205.53(3)	152(7)	hl87										
B1907+03	J1910+0358	82.93(10)	–127(7)	hl87										
B1907+12	J1910+1231	258.64(12)	978(15)	wck+04										
B1910+20	J1912+2104	88.34(3)	148(10)	hl87										
B1911–04	J1913–0440	89.385(10)	4.4(9)	jhv+05	12(3)	hl87								
B1911+13	J1913+1400	145.052(5)	435(30)	hl87										
B1913+10	J1915+1009	241.693(10)	431(22)	hl87	430.0(6)	jkk+07								
B1913+16	J1915+1606	168.77(1)	430(73)	hml+06										
B1913+167	J1915+1647	62.57(7)	172(3)	wck+04	161(11)	hl87								
B1914+09	J1916+0951	60.953(6)	100(6)	hl87	97.0(1)	jkk+07								
B1914+13	J1916+1312	237.009(11)	280(15)	hl87										
B1915+13	J1917+1353	94.538(4)	233(8)	hl87	264(21)	man71								
B1915+22	J1917+2224	134.93(12)	192(49)	wck+04										
J1918–1052	J1918–1052	62.73(80)	–47.6(60)	lbr+13										
B1917+00	J1919+0021	90.315(16)	120(7)	hl87										
J1919+0134	J1919+0134	191.9(4)	47(4)	njkk08										
B1919+14	J1921+1419	91.64(4)	275(60)	hr09										

Continued on next page

Table A.1 – continued from previous page

PSR name	PSR jname	DM (cm^{-3} pc)	RM_{psrcat} ($rad\,m^{-2}$)	ref_{psrcat}	RM_1 ($rad\,m^{-2}$)	ref_{RM_1}	RM_2 ($rad\,m^{-2}$)	ref_{RM_2}	RM_3 ($rad\,m^{-2}$)	ref_{RM_3}	RM_4 ($rad\,m^{-2}$)	ref_{RM_4}	RM_5 ($rad\,m^{-2}$)	ref_{RM_5}
B1918+19	J1921+1948	153.85(5)	160(20)	hl87										
B1919+21	J1921+2153	12.455(6)	–16.5(5)	hl87	–13(3)	jhv+05	–18.2(6)	man74						
B1920+20	J1922+2018	203.31(10)	301(7)	wck+04										
B1920+21	J1922+2110	217.086(18)	282(14)	hl87										
B1921+17	J1923+1706	142.5(6)	380(220)	wck+04										
J1923+2515	J1923+2515	18.85766(19)	10.8(38)	lbr+13										
B1923+04	J1926+0431	102.243(19)	0(11)	hl87										
B1924+16	J1926+1648	176.885(11)	320(14)	hl87										
B1925+18	J1927+1852	254(1)	417(70)	wck+04										
B1929+10	J1932+1059	3.180(4)	–6.87(2)	jhv+05	–6.1(10)	hl87	–8.6(18)	man72	–5.9(6)	wck+04				
B1929+20	J1932+2020	211.151(11)	10(6)	hl87										
B1930+22	J1932+2220	219.2(5)	173(11)	hl87										
J1932–3655	J1932–3655	59.88(1)	–8(3)	njkk08	6(3)	hmq99								
B1933+16	J1935+1616	158.521(3)	–10.2(3)	jhv+05	–2(2)	hl87	–1.9(4)	man72						
B1937+21	J1939+2134	71.0398(2)	6.7(6)	ymv+11	–10(9)	rl94								
J1941+0121	J1941+0121	52.7(7)	–92.0(3)	blr+13										
B1937–26	J1941–2602	50.036(3)	–33.5(8)	jhv+05	–41(4)	qmlg95	–26(4)	hl87						
J1943+0609	J1943+0609	70.76(6)	–11(15)	njkk08										
B1940–12	J1943–1237	28.918(15)	–10(8)	hl87										
B1941–17	J1944–1750	56.32(6)	–40(12)	hl87										
B1942–00	J1945–0040	59.71(6)	–45(7)	hl87										

Continued on next page

Table A.1 – continued from previous page

PSR name	PSR jname	DM (cm^{-3} pc)	RM_{psrcat} ($rad\,m^{-2}$)	ref_{psrcat}	RM_1 ($rad\,m^{-2}$)	ref_{RM_1}	RM_2 ($rad\,m^{-2}$)	ref_{RM_2}	RM_3 ($rad\,m^{-2}$)	ref_{RM_3}	RM_4 ($rad\,m^{-2}$)	ref_{RM_4}	RM_5 ($rad\,m^{-2}$)	ref_{RM_5}
B1944+17	J1946+1805	16.220(16)	–28.0(4)	hl87	–44(7)	hl87								
B1944+22	J1946+2244	140(20)	2(20)	wck+04										
B1943–29	J1946–2913	44.309(15)	–28(10)	hml+06	8(7)	hmq99								
B1946+35	J1948+3540	129.075(3)	116(6)	hl87										
B1946–25	J1949–2524	23.07(3)	–13(8)	hmq99										
B1951+32	J1952+3252	45.006(19)	–182(8)	wck+04										
B1952+29	J1954+2923	7.932(7)	–18(3)	hl87										
B1953+50	J1955+5059	31.974(3)	–22(2)	hl87										
B2000+40	J2002+4050	131.334(12)	145(7)	rl94										
B2002+31	J2004+3137	234.820(8)	30(6)	hl87										
B2003–08	J2006–0807	32.39(3)	–62(3)	njkk08	–52(5)	hl87								
B2011+38	J2013+3845	238.217(8)	78(4)	rl94										
B2016+28	J2018+2839	14.172(4)	–34.6(14)	man72	–27.3(21)	wck+04	–37(6)	hl87	–30(5)	s68				
J2021+3651	J2021+3651	367.5(10)	524(4)	aaa+09d										
B2020+28	J2022+2854	24.640(3)	–74.7(3)	man74	-73.7(16)	wck+04	–78(4)	hl87						
J2022+3842	J2022+3842	429.1(5)	270	agr+11										
B2021+51	J2022+5154	22.648(6)	–6.5(9)	man72	–2(6)	hl87								
B2028+22	J2030+2228	71.83(3)	–192(21)	wck+04	–195(25)	hr09								
J2030+3641	J2030+3641	246.0(7)	514(1)	ckr+12										
J2032+4127	J2032+4127	114.8(1)	215(1)	crr+09										
J2033+0042	J2033+0042	37.84(13)	–71.2(22)	lbr+13										

Continued on next page

Table A.1 – continued from previous page

PSR name	PSR jname	DM (cm^{-3} pc)	RM_{psrcat} ($rad\,m^{-2}$)	ref_{psrcat}	RM_1 ($rad\,m^{-2}$)	ref_{RM_1}	RM_2 ($rad\,m^{-2}$)	ref_{RM_2}	RM_3 ($rad\,m^{-2}$)	ref_{RM_3}	RM_4 ($rad\,m^{-2}$)	ref_{RM_4}	RM_5 ($rad\,m^{-2}$)	ref_{RM_5}
J2033–1938	J2033–1938	23.47(9)	–17.7(5)	blr+13										
B2034+19	J2037+1942	36(3)	–97(10)	wck+04	–98.5(8)	hr09								
J2038–3816	J2038–3816	33.96(6)	38(14)	njkk08	68(18)	hml+06	30(15)	hmq99						
B2043–04	J2046–0421	35.799(10)	–1(3)	hl87										
B2044+15	J2046+1540	39.844(11)	–100(5)	wck+04	–101(6)	hl87								
B2045–16	J2048–1616	11.456(5)	–10.0(1)	hl87	–10.2(8)	njkk08	–10.0(3)	jkk+07	–11.2(6)	vdhm97	–10.8(4)	man72		
B2048–72	J2053–7200	17.3(4)	17.0(10)	qmlg95	15(9)	hml+06	9(4)	hmq99						
B2053+21	J2055+2209	36.361(13)	–100(7)	hr09	–80.5(3)	wck+04								
B2053+36	J2055+3630	97.3140(19)	–68(4)	hl87										
J2108–3429	J2108–3429	30.22(1)	39(12)	njkk08	50(20)	hmq99								
B2106+44	J2108+4441	139.827(11)	–146(9)	hl87										
J2111+2106	J2111+2106	59.74(14)	–75.3(8)	blr+13										
B2110+27	J2113+2754	25.113(4)	–37(7)	wck+04	–65(8)	hl87								
B2111+46	J2113+4644	141.26(9)	–224(2)	man72	–230(11)	hl87								
B2113+14	J2116+1414	56.149(7)	–25(8)	hl87	–26(11)	wck+04								
B2122+13	J2124+1407	30.12(10)	–48.3(36)	hr09	–57(8)	wck+04								
J2124–3358	J2124–3358	4.601(3)	–5.0(9)	ymv+11	5(2)	hml+06	1.2(1)	mh04						
J2129–5721	J2129–5721	31.853(4)	23.5(8)	ymv+11	30(5)	hml+06	37.3(2)	mh04						
J2144–3933	J2144–3933	3.35(1)	–2(10)	hmq99										
J2145–0750	J2145–0750	8.9977(14)	–1.3(7)	ymv+11	12(6)	hml+06	12(8)	mh04						
B2148+63	J2149+6329	128(1)	–160(7)	hl87										

Continued on next page

Table A.1 – continued from previous page

PSR name	PSR jname	DM (cm^{-3} pc)	RM_{psrcat} ($rad\,m^{-2}$)	ref_{psrcat}	RM_1 ($rad\,m^{-2}$)	ref_{RM_1}	RM_2 ($rad\,m^{-2}$)	ref_{RM_2}	RM_3 ($rad\,m^{-2}$)	ref_{RM_3}	RM_4 ($rad\,m^{-2}$)	ref_{RM_4}	RM_5 ($rad\,m^{-2}$)	ref_{RM_5}
B2148+52	J2150+5247	148.930(4)	–44(11)	mwkj03										
B2152–31	J2155–3118	14.85(5)	21(3)	hl87										
B2154+40	J2157+4017	70.857(11)	–44(2)	man74										
B2210+29	J2212+2933	74.50(3)	–168(5)	wck+04	–175.3(15)	hr09								
B2217+47	J2219+4754	43.519(12)	–35.3(18)	man72	–41(6)	hl87								
J2222–0137	J2222–0137	3.27511(10)	1.8(6)	blr+13										
J2225+35	J2225+35	51.8	49.8	skdl09										
B2224+65	J2225+6535	36.079(9)	–21(3)	hl87										
B2227+61	J2229+6205	124.614(17)	–125(22)	mwkj03										
J2236–5527	J2236–5527	20.0(5)	27.8(14)	bbb+13										
J2240+5832	J2240+5832	263.50(5)	24(4)	tpc+11										
J2241–5236	J2241–5236	11.41085(3)	14(6)	kjr+11										
B2241+69	J2242+6950	40.74(18)	–30(30)	mwkj03										
J2248–0101	J2248–0101	29.05(3)	33(12)	hml+06										
B2255+58	J2257+5909	151.082(6)	–322(11)	hl87										
B2303+30	J2305+3100	49.544(16)	–75.5(40)	wck+04	–84(6)	hl87								
B2306+55	J2308+5547	46.538(8)	–34(3)	hl87										
B2310+42	J2313+4253	17.2758(13)	7(2)	hl87										
B2315+21	J2317+2149	20.906(7)	–37(3)	hl87										
B2319+60	J2321+6024	94.591(18)	–230(10)	hl87	–224(20)	man74								
B2321–61	J2324–6054	14.0(6)	–11(8)	hml+06										

Continued on next page

Table A.1 – continued from previous page

PSR name	PSR jname	DM (cm^{-3} pc)	RM_{psrcat} ($rad\,m^{-2}$)	ref_{psrcat}	RM_1 ($rad\,m^{-2}$)	ref_{RM_1}	RM_2 ($rad\,m^{-2}$)	ref_{RM_2}	RM_3 ($rad\,m^{-2}$)	ref_{RM_3}	RM_4 ($rad\,m^{-2}$)	ref_{RM_4}	RM_5 ($rad\,m^{-2}$)	ref_{RM_5}
B2323+63	J2325+6316	197.37(5)	–102(14)	hl87										
B2324+60	J2326+6113	122.613(5)	–221(10)	hl87										
B2327–20	J2330–2005	8.458(13)	16(3)	hl87	9.5(6)	jkk+07	30(7)	hml+06	9.5(2)	hl87				
B2334+61	J2337+6151	58.410(15)	–100(18)	mwkj03										
J2346–0609	J2346–0609	22.504(19)	–5(1)	hmq99	–4.1(60)	njkk08								
B2351+61	J2354+6155	94.662(6)	–77(6)	hl87										

Bibliography

L. Feretti, G. Giovannini, F. Govoni, and M. Murgia. Clusters of galaxies: observational properties of the diffuse radio emission. *A&AR*, 20:54, May 2012. doi: 10.1007/s00159-012-0054-z.

K. E. Kunze. Cosmological magnetic fields. *Plasma Physics and Controlled Fusion*, 55 (12):124026, December 2013. doi: 10.1088/0741-3335/55/12/124026.

R. Beck and R. Wielebinski. *Magnetic Fields in Galaxies*, page 641. Springer Science+Business Media Dordrecht, 2013. doi: 10.1007/978-94-007-5612-0_13.

C. Kouveliotou, S. Dieters, T. Strohmayer, J. van Paradijs, G. J. Fishman, et al. An X-ray pulsar with a superstrong magnetic field in the soft γ-ray repeater SGR1806 - 20. *Nature*, 393:235–237, May 1998. doi: 10.1038/30410.

V. Angelopoulos, J. P. McFadden, D. Larson, C. W. Carlson, S. B. Mende, et al. Tail Reconnection Triggering Substorm Onset. *Science*, 321:931–, August 2008. doi: 10.1126/science.1160495.

G. A. Medina Tanco, E. M. de Gouveia dal Pino, and J. E. Horvath. Deflection of Ultra–High-Energy Cosmic Rays by the Galactic Magnetic Field: From the Sources to the Detector. *ApJ*, 492:200, January 1998. doi: 10.1086/305044.

S. V. Troitsky. Magnetic deflections and possible sources of clustered ultra-high-energy cosmic rays. *Astroparticle Physics*, 26:325–331, November 2006. doi: 10.1016/j.astropartphys.2006.07.006.

T. Peters, R. Banerjee, R. S. Klessen, and M.-M. Mac Low. The Interplay of Magnetic Fields, Fragmentation, and Ionization Feedback in High-mass Star Formation. *ApJ*, 729:72, March 2011. doi: 10.1088/0004-637X/729/1/72.

R. M. Crutcher. Magnetic Fields in Molecular Clouds. *ARA&A*, 50:29–63, September 2012. doi: 10.1146/annurev-astro-081811-125514.

A. Boulares and D. P. Cox. Galactic hydrostatic equilibrium with magnetic tension and cosmic-ray diffusion. *ApJ*, 365:544–558, December 1990. doi: 10.1086/169509.

A. A. Schekochihin and S. C. Cowley. *Turbulence and Magnetic Fields in Astrophysical Plasmas*, page 85. Springer, 2007.

G. E. Hale. On the Probable Existence of a Magnetic Field in Sun-Spots. *ApJ*, 28:315, November 1908. doi: 10.1086/141602.

X. H. Sun, W. Reich, A. Waelkens, and T. A. Enßlin. Radio observational constraints on Galactic 3D-emission models. *A&A*, 477:573–592, January 2008. doi: 10.1051/0004-6361:20078671.

R. D. Davies. Structure of the Galactic Magnetic Field. *Nature*, 218:435–437, May 1968. doi: 10.1038/218435a0.

C. L. Van Eck, J. C. Brown, J. M. Stil, K. Rae, S. A. Mao, et al. Modeling the Magnetic Field in the Galactic Disk Using New Rotation Measure Observations from the Very Large Array. *ApJ*, 728:97, February 2011. doi: 10.1088/0004-637X/728/2/97.

M. Kramer, I. H. Stairs, R. N. Manchester, M. A. McLaughlin, A. G. Lyne, et al. Tests of General Relativity from Timing the Double Pulsar. *Science*, 314:97–102, October 2006a. doi: 10.1126/science.1132305.

P. B. Demorest, T. Pennucci, S. M. Ransom, M. S. E. Roberts, and J. W. T. Hessels. A two-solar-mass neutron star measured using Shapiro delay. *Nature*, 467:1081–1083, October 2010. doi: 10.1038/nature09466.

D. R. Lorimer and M. Kramer. *Handbook of Pulsar Astronomy*, pages 32,54–62,70,71,85–103,165–169,200–207. Cambridge University Press, Cambridge, UK, October 2012.

S. D. Bates, D. R. Lorimer, and J. P. W. Verbiest. The pulsar spectral index distribution. *MNRAS*, 431:1352–1358, May 2013. doi: 10.1093/mnras/stt257.

A. Hewish, S. J. Bell, J. D. H. Pilkington, P. F. Scott, and R. A. Collins. Observation of a Rapidly Pulsating Radio Source. *Nature*, 217:709–713, February 1968. doi: 10.1038/217709a0.

G. Swarup. Giant metrewave radio telescope (GMRT). In T. J. Cornwell and R. A. Perley, editors, *IAU Colloq. 131: Radio Interferometry. Theory, Techniques, and Applications*, volume 19 of *Astronomical Society of the Pacific Conference Series*, pages 376–380, 1991.

B. W. Stappers, J. W. T. Hessels, A. Alexov, K. Anderson, T. Coenen, et al. Observing pulsars and fast transients with LOFAR. *A&A*, 530:A80, June 2011. doi: 10.1051/0004-6361/201116681.

M. P. van Haarlem, M. W. Wise, A. W. Gunst, G. Heald, J. P. McKean, et al. LOFAR: The LOw-Frequency ARray. *A&A*, 556:A2, August 2013. doi: 10.1051/0004-6361/201220873.

N. Kassim, S. White, P. Rodriquez, J. Hartman, B. Hicks, et al. The Long Wavelength Array (LWA): A Large HF/VHF Array for Solar Physics, Ionospheric Science, and Solar Radar. In *Advanced Maui Optical and Space Surveillance Technologies Conference*, September 2010.

D. Mitchell, L. J. Greenhill, M. Clark, F. Briggs, J. Bowman, et al. The Murchison Widefield Array. In *RFI Mitigation Workshop*, 2010.

M. A. Garrett, J. M. Cordes, D. R. Deboer, J. L. Jonas, S. Rawlings, et al. The Square Kilometre Array (SKA) - Phase 1 Design Concept. In *ISKAF2010 Science Meeting*, 2010.

W. Baade and F. Zwicky. Cosmic Rays from Super-novae. *Proceedings of the National Academy of Science*, 20:259–263, May 1934. doi: 10.1073/pnas.20.5.259.

J. D. H. Pilkington, A. Hewish, S. J. Bell, and T. W. Cole. Observations of some further Pulsed Radio Sources. *Nature*, 218:126–129, April 1968. doi: 10.1038/218126a0.

J. Chadwick. Possible Existence of a Neutron. *Nature*, 129:312–312, February 1932. doi: 10.1038/129312a0.

S. Chandrasekhar. The Maximum Mass of Ideal White Dwarfs. *ApJ*, 74:81, July 1931. doi: 10.1086/143324.

R. N. Manchester, G. B. Hobbs, A. Teoh, and M. Hobbs. The Australia Telescope National Facility Pulsar Catalogue. *AJ*, 129:1993–2006, April 2005a. doi: 10.1086/428488.

J. W. T. Hessels, S. M. Ransom, I. H. Stairs, P. C. C. Freire, V. M. Kaspi, et al. A Radio Pulsar Spinning at 716 Hz. *Science*, 311:1901–1904, March 2006. doi: 10.1126/science.1123430.

A. Wolszczan and D. A. Frail. A planetary system around the millisecond pulsar PSR1257 + 12. *Nature*, 355:145–147, January 1992. doi: 10.1038/355145a0.

J. Antoniadis, P. C. C. Freire, N. Wex, T. M. Tauris, R. S. Lynch, et al. A Massive Pulsar in a Compact Relativistic Binary. *Science*, 340:448, April 2013. doi: 10.1126/science.1233232.

M. Burgay, N. D'Amico, A. Possenti, R. N. Manchester, A. G. Lyne, et al. An increased estimate of the merger rate of double neutron stars from observations of a highly relativistic system. *Nature*, 426:531–533, December 2003. doi: 10.1038/nature02124.

D. C. Backer, S. R. Kulkarni, C. Heiles, M. M. Davis, and W. M. Goss. A millisecond pulsar. *Nature*, 300:615–618, December 1982. doi: 10.1038/300615a0.

T. M. Tauris and E. P. J. van den Heuvel. Formation of the Galactic Millisecond Pulsar Triple System PSR J0337+1715–A Neutron Star with Two Orbiting White Dwarfs. *ApJL*, 781:L13, January 2014. doi: 10.1088/2041-8205/781/1/L13.

P. Goldreich and W. H. Julian. Pulsar Electrodynamics. *ApJ*, 157:869, August 1969. doi: 10.1086/150119.

R. A. Hulse and J. H. Taylor. Discovery of a pulsar in a binary system. *ApJL*, 195: L51–L53, January 1975. doi: 10.1086/181708.

J. H. Taylor and J. M. Weisberg. A new test of general relativity - Gravitational radiation and the binary pulsar PSR 1913+16. *ApJ*, 253:908–920, February 1982. doi: 10.1086/159690.

A. G. Lyne, M. Burgay, M. Kramer, A. Possenti, R. N. Manchester, et al. A Double-Pulsar System: A Rare Laboratory for Relativistic Gravity and Plasma Physics. *Science*, 303:1153–1157, February 2004. doi: 10.1126/science.1094645.

J. M. Cordes and T. J. W. Lazio. NE2001.I. A New Model for the Galactic Distribution of Free Electrons and its Fluctuations. *ArXiv Astrophysics e-prints*, July 2002.

A. Noutsos, S. Johnston, M. Kramer, and A. Karastergiou. New pulsar rotation measures and the Galactic magnetic field. *MNRAS*, 386:1881–1896, June 2008. doi: 10.1111/j.1365-2966.2008.13188.x.

R. Dib and V. M. Kaspi. 16 yr of RXTE Monitoring of Five Anomalous X-Ray Pulsars. *ApJ*, 784:37, March 2014. doi: 10.1088/0004-637X/784/1/37.

E. Amato. The Theory of Pulsar Wind Nebulae. *International Journal of Modern Physics Conference Series*, 28:1460160, March 2014. doi: 10.1142/S2010194514601604.

G. F. Bignami, P. A. Caraveo, A. De Luca, and S. Mereghetti. The magnetic field of an isolated neutron star from X-ray cyclotron absorption lines. *Nature*, 423:725–727, June 2003.

K. Liu, E. F. Keane, K. J. Lee, M. Kramer, J. M. Cordes, et al. Profile-shape stability and phase-jitter analyses of millisecond pulsars. *MNRAS*, 420:361–368, February 2012. doi: 10.1111/j.1365-2966.2011.20041.x.

G. Hobbs, A. Archibald, Z. Arzoumanian, D. Backer, M. Bailes, et al. The International Pulsar Timing Array project: using pulsars as a gravitational wave detector. *Classical and Quantum Gravity*, 27(8):084013, April 2010. doi: 10.1088/0264-9381/27/8/084013.

A. G. Lyne and F. G. Smith. Linear Polarization in Pulsating Radio Sources. *Nature*, 218:124–126, April 1968. doi: 10.1038/218124a0.

H. D. Craft, J. M. Comella, and F. D. Drake. Submillisecond Radio Intensity Variations in Pulsars. *Nature*, 218:1122–1124, June 1968a. doi: 10.1038/2181122a0.

R. R. Clark and F. G. Smith. Polarization of Radio Pulses from Pulsar CP 0328. *Nature*, 221:724–726, February 1969. doi: 10.1038/221724a0.

V. Radhakrishnan, D. J. Cooke, M. M. Komesaroff, and D. Morris. Evidence in Support of a Rotational Model for the Pulsar PSR 0833-45. *Nature*, 221:443–446, February 1969. doi: 10.1038/221443a0.

M. M. Komesaroff, D. Morris, and D. J. Cooke. Linear Polarization and Pulse Shape Measurements on Nine Pulsars. *Aplett*, 5:37, 1970.

R. N. Manchester. Observations of Pulsar Polarization at 410 and 1665 MHz. *ApJS*, 23: 283, September 1971. doi: 10.1086/190240.

M. M. McKinnon and D. R. Stinebring. A Statistical Model for the Orthogonal Modes of Polarization in Pulsar Radio Emission. *ApJ*, 502:883–897, August 1998. doi: 10.1086/305924.

A. G. Lyne and R. N. Manchester. The shape of pulsar radio beams. *MNRAS*, 234: 477–508, October 1988.

V. Radhakrishnan and D. J. Cooke. Magnetic Poles and the Polarization Structure of Pulsar Radiation. *Aplett*, 3:225, 1969.

J. E. Everett and J. M. Weisberg. Emission Beam Geometry of Selected Pulsars Derived from Average Pulse Polarization Data. *ApJ*, 553:341–357, May 2001. doi: 10.1086/320652.

R. T. Gangadhara. Circular polarization in pulsars due to curvature radiation. *The Astrophysical Journal*, 710(1):29, 2010. URL `http://stacks.iop.org/0004-637X/710/i=1/a=29`.

D. B. Melrose and Q. Luo. Circular polarization in pulsar radio emission due to intrinsically relativistic effects. *MNRAS*, 352:915–923, August 2004. doi: 10.1111/j.1365-2966.2004.07986.x.

A. F. Cheng and M. A. Ruderman. A theory of subpulse polarization patterns from radio pulsars. *ApJ*, 229:348–360, April 1979. doi: 10.1086/156959.

E. F. Keane. Radio pulsar variability. In *IAU Symposium*, volume 291 of *IAU Symposium*, pages 295–300, March 2013. doi: 10.1017/S1743921312023927.

T. H. Hankins, J. S. Kern, J. C. Weatherall, and J. A. Eilek. Nanosecond radio bursts from strong plasma turbulence in the Crab pulsar. *Nature*, 422:141–143, March 2003.

A. Lyne, F. Graham-Smith, P. Weltevrede, C. Jordan, B. Stappers, et al. Evolution of the Magnetic Field Structure of the Crab Pulsar. *Science*, 342:598–601, November 2013. doi: 10.1126/science.1243254.

A. Lyne, G. Hobbs, M. Kramer, I. Stairs, and B. Stappers. Switched Magnetospheric Regulation of Pulsar Spin-Down. *Science*, 329:408–, July 2010. doi: 10.1126/science.1186683.

J. van Leeuwen and A. N. Timokhin. On Plasma Rotation and Drifting Subpulses in Pulsars: Using Aligned Pulsar B0826-34 as a Voltmeter. *ApJ*, 752:155, June 2012. doi: 10.1088/0004-637X/752/2/155.

J. Li, A. Spitkovsky, and A. Tchekhovskoy. Resistive Solutions for Pulsar Magnetospheres. *ApJ*, 746:60, February 2012a. doi: 10.1088/0004-637X/746/1/60.

F. D. Drake and H. D. Craft. Second Periodic Pulsation in Pulsars. *Nature*, 220:231–235, October 1968. doi: 10.1038/220231a0.

J. M. Rankin. Toward an empirical theory of pulsar emission. III - Mode changing, drifting subpulses, and pulse nulling. *ApJ*, 301:901–922, February 1986. doi: 10.1086/163955.

J. A. Gil and M. Sendyk. Drifting Subpulses in PSR B0943+10. *ApJ*, 585:453–463, March 2003. doi: 10.1086/346079.

P. A. Sturrock. A Model of Pulsars. *ApJ*, 164:529, March 1971. doi: 10.1086/150865.

M. A. Ruderman and P. G. Sutherland. Theory of pulsars - Polar caps, sparks, and coherent microwave radiation. *ApJ*, 196:51–72, February 1975. doi: 10.1086/153393.

A. F. Cheng and M. A. Ruderman. Particle acceleration and radio emission above pulsar polar caps. *ApJ*, 235:576–586, January 1980. doi: 10.1086/157661.

M. Ruderman. Evolution and radiation in pulsar polar CAP models. In W. Sieber and R. Wielebinski, editors, *Pulsars: 13 Years of Research on Neutron Stars*, volume 95 of *IAU Symposium*, pages 87–97, 1981.

A. V. Filippenko and V. Radhakrishnan. Pulsar nulling and drifting subpulse phase memory. *ApJ*, 263:828–834, December 1982. doi: 10.1086/160553.

R. T. Edwards, B. W. Stappers, and A. G. J. van Leeuwen. Unusual subpulse modulation in PSR B0320+39. *A&A*, 402:321–329, April 2003. doi: 10.1051/0004-6361:20030255.

J. G. Davies, A. G. Lyne, F. G. Smith, V. A. Izvekova, A. D. Kuzmin, et al. The magnetic field structure of PSR 0809 + 74. *MNRAS*, 211:57–68, November 1984.

M. A. Ruderman. Crystallization and Torsional Oscillations of Superdense Stars. *Nature*, 218:1128–1129, June 1968. doi: 10.1038/2181128a0.

J. C. Clemens and R. Rosen. Observations of Nonradial Pulsations in Radio Pulsars. *ApJ*, 609:340–353, July 2004. doi: 10.1086/421013.

T. E. Hassall, B. W. Stappers, P. Weltevrede, J. W. T. Hessels, A. Alexov, et al. Differential frequency-dependent delay from the pulsar magnetosphere. *A&A*, 552:A61, April 2013. doi: 10.1051/0004-6361/201220764.

P. Weltevrede, R. T. Edwards, and B. W. Stappers. The subpulse modulation properties of pulsars at 21 cm. *A&A*, 445:243–272, January 2006a. doi: 10.1051/0004-6361:20053088.

D. C. Backer. Pulsar Nulling Phenomena. *Nature*, 228:42–43, October 1970a. doi: 10.1038/228042a0.

N. Wang, R. N. Manchester, and S. Johnston. Pulsar nulling and mode changing. *MNRAS*, 377:1383–1392, May 2007. doi: 10.1111/j.1365-2966.2007.11703.x.

A. G. Lyne and M. Ashworth. The effect of nulls upon subpulse drift in PSRs 0809+74 and 0818-13. *MNRAS*, 204:519–536, August 1983.

A. G. J. van Leeuwen, B. W. Stappers, R. Ramachandran, and J. M. Rankin. Probing drifting and nulling mechanisms through their interaction in PSR B0809+74. *A&A*, 399:223–229, February 2003. doi: 10.1051/0004-6361:20021630.

J. D. Biggs. An analysis of radio pulsar nulling statistics. *ApJ*, 394:574–580, August 1992. doi: 10.1086/171608.

V. Gajjar, B. C. Joshi, and M. Kramer. A survey of nulling pulsars using the Giant Meterwave Radio Telescope. *MNRAS*, 424:1197–1205, August 2012. doi: 10.1111/j.1365-2966.2012.21296.x.

A. Esamdin, A. G. Lyne, F. Graham-Smith, M. Kramer, R. N. Manchester, et al. Mode switching and subpulse drifting in PSR B0826-34. *MNRAS*, 356:59–65, January 2005. doi: 10.1111/j.1365-2966.2004.08444.x.

S. Burke-Spolaor, S. Johnston, M. Bailes, S. D. Bates, N. D. R. Bhat, et al. The High Time Resolution Universe Pulsar Survey - V. Single-pulse energetics and modulation properties of 315 pulsars. *MNRAS*, 423:1351–1367, June 2012. doi: 10.1111/j.1365-2966.2012.20998.x.

M. Kramer, A. G. Lyne, J. T. O'Brien, C. A. Jordan, and D. R. Lorimer. A Periodically Active Pulsar Giving Insight into Magnetospheric Physics. *Science*, 312:549–551, April 2006b. doi: 10.1126/science.1124060.

M. Kramer. Recent discoveries in the dynamic radio sky. In D. Phelan, O. Ryan, and A. Shearer, editors, *High Time Resolution Astrophysics: The Universe at Sub-Second Timescales*, volume 984 of *American Institute of Physics Conference Series*, pages 63–72, February 2008. doi: 10.1063/1.2896947.

F. Camilo, S. M. Ransom, S. Chatterjee, S. Johnston, and P. Demorest. PSR J1841-0500: A Radio Pulsar That Mostly is Not There. *ApJ*, 746:63, February 2012a. doi: 10.1088/0004-637X/746/1/63.

J. T. O'Brien, M. Kramer, A. G. Lyne, D. R. Lorimer, and C. A. Jordan. Sometimes a Pulsar! *Chinese Journal of Astronomy and Astrophysics Supplement*, 6(2):020000–7, December 2006.

D. R. Lorimer, A. G. Lyne, M. A. McLaughlin, M. Kramer, G. G. Pavlov, et al. Radio and X-Ray Observations of the Intermittent Pulsar J1832+0029. *ApJ*, 758:141, October 2012. doi: 10.1088/0004-637X/758/2/141.

M. P. Surnis, B. C. Joshi, M. A. McLaughlin, and V. Gajjar. Discovery of an Intermittent Pulsar: PSR J1839+15. *ArXiv e-prints*, October 2012.

R. P. Eatough, M. Kramer, A. G. Lyne, and M. J. Keith. A coherent acceleration search of the Parkes multibeam pulsar survey - techniques and the discovery and timing of 16 pulsars. *MNRAS*, 431:292–307, May 2013a. doi: 10.1093/mnras/stt161.

A. N. Timokhin. A model for nulling and mode changing in pulsars. *MNRAS*, 408: L41–L45, October 2010. doi: 10.1111/j.1745-3933.2010.00924.x.

D. C. Backer. Peculiar Pulse Burst in PSR 1237 + 25. *Nature*, 228:1297–1298, December 1970b. doi: 10.1038/2281297a0.

A. G. Lyne. Mode changing in pulsar radiation. *MNRAS*, 153:27P, 1971.

J. M. Rankin, A. Wolszczan, and D. R. Stinebring. Mode changing and quasi-periodic modulation in pulsar 1737+13, a bright, five-componented pulsar. *ApJ*, 324:1048–1055, January 1988. doi: 10.1086/165961.

D. C. Backer, J. M. Rankin, and D. B. Campbell. Orthogonal mode emission in geometric models of pulsar polarisation. *Nature*, 263:202–207, September 1976. doi: 10.1038/263202a0.

D. Morris, W. Sieber, D. C. Ferguson, and N. Bartel. Changes in the average pulse shape of PSR 0355 + 54 at 11 CM wavelength. *A&A*, 84:260–262, April 1980.

J. M. Cordes, J. Rankin, and D. C. Backer. Orthogonal modes of polarization from pulsar PSR 2020+28. *ApJ*, 223:961–972, August 1978. doi: 10.1086/156328.

G. R. Huguenin, J. H. Taylor, and T. H. Troland. The Radio Emission from Pulsar MP 0031-07. *ApJ*, 162:727, December 1970. doi: 10.1086/150704.

T. H. Hankins and A. Wolszczan. The drifting subpulse phenomenon observed in three pulsars with triple profiles. *ApJ*, 318:410–420, July 1987. doi: 10.1086/165377.

W. T. S. Deich, J. M. Cordes, T. H. Hankins, and J. M. Rankin. Null transition times, quantized drift modes, and no memory across nulls for PSR 1944 + 17. *ApJ*, 300:540–550, January 1986. doi: 10.1086/163831.

G. A. E. Wright and L. A. Fowler. Mode-changing and quantized subpulse drift-rates in pulsar PSR 2319+60. *A&A*, 101:356–361, September 1981.

W. Hermsen, J. W. T. Hessels, L. Kuiper, J. van Leeuwen, D. Mitra, et al. Synchronous X-ray and Radio Mode Switches: A Rapid Global Transformation of the Pulsar Magnetosphere. *Science*, 339:436–, January 2013. doi: 10.1126/science.1230960.

L. A. Nowakowski. PSR 0540 + 23 revisited - Three components, drifting subpulses, and mode switching. *ApJ*, 377:581–587, August 1991. doi: 10.1086/170386.

H.-G. Wang, J.-L. Chen, Z.-G. Wen, and F.-P. Pi. On the mode switching timescales of pulsar PSR B0329+54. In *IAU Symposium*, volume 291 of *IAU Symposium*, pages 549–551, March 2013. doi: 10.1017/S1743921312024830.

A. A. Abdo, M. Ajello, A. Allafort, L. Baldini, J. Ballet, et al. The Second Fermi Large Area Telescope Catalog of Gamma-Ray Pulsars. *ApJS*, 208:17, October 2013. doi: 10.1088/0067-0049/208/2/17.

D. R. Lorimer, M. Bailes, M. A. McLaughlin, D. J. Narkevic, and F. Crawford. A Bright Millisecond Radio Burst of Extragalactic Origin. *Science*, 318:777–, November 2007. doi: 10.1126/science.1147532.

R. N. Manchester, G. B. Hobbs, A. Teoh, and M. Hobbs. ATNF Pulsar Catalog (Manchester+, 2005). *VizieR Online Data Catalog*, 7245:0, August 2005b.

B. S. Tanenbaum, G. A. Zeissig, and F. D. Drake. Parameters of the Plasma Affecting the Radiation of Pulsar 1. *Science*, 160:760, May 1968. doi: 10.1126/science.160.3829.760.

T. E. Hassall, B. W. Stappers, J. W. T. Hessels, M. Kramer, A. Alexov, et al. Wide-band simultaneous observations of pulsars: disentangling dispersion measure and profile variations. *A&A*, 543:A66, July 2012. doi: 10.1051/0004-6361/201218970.

J. G. Ables and R. N. Manchester. Hydrogen-line absorption observations of distant pulsars. *A&A*, 50:177–184, July 1976.

J. P. W. Verbiest, M. Bailes, W. van Straten, G. B. Hobbs, R. T. Edwards, et al. Precision Timing of PSR J0437-4715: An Accurate Pulsar Distance, a High Pulsar Mass, and a Limit on the Variation of Newton's Gravitational Constant. *ApJ*, 679: 675–680, May 2008. doi: 10.1086/529576.

A. T. Deller, S. J. Tingay, M. Bailes, and J. E. Reynolds. Precision Southern Hemisphere VLBI Pulsar Astrometry. II. Measurement of Seven Parallaxes. *ApJ*, 701:1243–1257, August 2009. doi: 10.1088/0004-637X/701/2/1243.

W. E. Harris. A Catalog of Parameters for Globular Clusters in the Milky Way. *AJ*, 112:1487, October 1996. doi: 10.1086/118116.

R. Ramachandran, D. Mitra, A. A. Deshpande, D. M. McConnell, and J. G. Ables. Measurement of scatter broadening for 27 pulsars at 327 MHz. *MNRAS*, 290:260–264, September 1997.

D. A. Moffett and T. H. Hankins. Multifrequency Radio Observations of the Crab Pulsar. *ApJ*, 468:779, September 1996. doi: 10.1086/177734.

D. M. Gould and A. G. Lyne. Multifrequency polarimetry of 300 radio pulsars. *MNRAS*, 301:235–260, November 1998. doi: 10.1046/j.1365-8711.1998.02018.x.

D. A. Moffett and T. H. Hankins. Polarimetric Properties of the Crab Pulsar between 1.4 and 8.4 GHZ. *ApJ*, 522:1046–1052, September 1999. doi: 10.1086/307654.

J. W. Armstrong, B. J. Rickett, and S. R. Spangler. Electron density power spectrum in the local interstellar medium. *ApJ*, 443:209–221, April 1995. doi: 10.1086/175515.

M. M. Komesaroff, J. G. Ables, and P. A. Hamilton. Linear Polarization Measurements of PSR 0833-45 and their Relevance to Pulsar Models. *Aplett*, 9:101, August 1971.

R. Narayan. The Physics of Pulsar Scintillation. *Royal Society of London Philosophical Transactions Series A*, 341:151–165, October 1992. doi: 10.1098/rsta.1992.0090.

P. Weltevrede and S. Johnston. Profile and polarization characteristics of energetic pulsars. *MNRAS*, 391:1210–1226, December 2008. doi: 10.1111/j.1365-2966.2008.13950.x.

R. Beck, A. Shukurov, D. Sokoloff, and R. Wielebinski. Systematic bias in interstellar magnetic field estimates. *A&A*, 411:99–107, November 2003. doi: 10.1051/0004-6361:20031101.

J. S. Hall. Observations of the Polarized Light from Stars. *Science*, 109:166–167, February 1949. doi: 10.1126/science.109.2825.166.

W. A. Hiltner. Polarization of Light from Distant Stars by Interstellar Medium. *Science*, 109:165, February 1949. doi: 10.1126/science.109.2825.165.

G. R. Farrar. The Galactic magnetic field and ultrahigh-energy cosmic ray deflections. *Comptes Rendus Physique*, 15:339–348, April 2014. doi: 10.1016/j.crhy.2014.04.002.

P. Hennebelle and O. Iffrig. Simulations of magnetized multiphase galactic disk regulated by supernovae explosions. *ArXiv e-prints*, May 2014.

T. Nota and P. Katgert. The large-scale magnetic field in the fourth Galactic quadrant. *A&A*, 513:A65, April 2010. doi: 10.1051/0004-6361/200911803.

J. L. Han. The Large-Scale Magnetic Field Structure of Our Galaxy: Efficiently Deduced from Pulsar Rotation Measures. In B. Uyaniker, W. Reich, and R. Wielebinski, editors, *The Magnetized Interstellar Medium*, pages 3–12, February 2004.

R. M. Crutcher, B. Wandelt, C. Heiles, E. Falgarone, and T. H. Troland. Magnetic Fields in Interstellar Clouds from Zeeman Observations: Inference of Total Field Strengths by Bayesian Analysis. *ApJ*, 725:466–479, December 2010. doi: 10.1088/0004-637X/725/1/466.

P. Fosalba, A. Lazarian, S. Prunet, and J. A. Tauber. Statistical Properties of Galactic Starlight Polarization. *ApJ*, 564:762–772, January 2002. doi: 10.1086/324297.

D. T. Chuss, J. A. Davidson, J. L. Dotson, C. D. Dowell, R. H. Hildebrand, et al. Magnetic Fields in Cool Clouds within the Central 50 Parsecs of the Galaxy. *ApJ*, 599:1116–1128, December 2003. doi: 10.1086/379538.

X. H. Sun, J. L. Han, W. Reich, P. Reich, W. B. Shi, et al. A Sino-German λ6 cm polarization survey of the Galactic plane. I. Survey strategy and results for the first survey region. *A&A*, 463:993–1007, March 2007. doi: 10.1051/0004-6361:20066001.

J. L. Han, R. N. Manchester, A. G. Lyne, G. J. Qiao, and W. van Straten. Pulsar Rotation Measures and the Large-Scale Structure of the Galactic Magnetic Field. *ApJ*, 642:868–881, May 2006. doi: 10.1086/501444.

J. C. Brown, M. Haverkorn, B. M. Gaensler, A. R. Taylor, N. S. Bizunok, et al. Rotation Measures of Extragalactic Sources behind the Southern Galactic Plane: New Insights into the Large-Scale Magnetic Field of the Inner Milky Way. *ApJ*, 663:258–266, July 2007. doi: 10.1086/518499.

N. Oppermann, H. Junklewitz, G. Robbers, M. R. Bell, T. A. Enßlin, et al. An improved map of the Galactic Faraday sky. *A&A*, 542:A93, June 2012. doi: 10.1051/0004-6361/201118526.

G. R. Farrar, R. Jansson, I. J. Feain, and B. M. Gaensler. Galactic magnetic deflections and Centaurus A as a UHECR source. *JCAP*, 1:023, January 2013. doi: 10.1088/1475-7516/2013/01/023.

C. Wang, J. L. Han, and D. Lai. The Faraday rotation in the pulsar magnetosphere. *MNRAS*, 417:1183–1191, October 2011. doi: 10.1111/j.1365-2966.2011.19333.x.

R. J. Rand and A. G. Lyne. New Rotation Measures of Distant Pulsars in the Inner Galaxy and Magnetic Field Reversals. *MNRAS*, 268:497, May 1994.

R. Stepanov, T. G. Arshakian, R. Beck, P. Frick, and M. Krause. Magnetic field structures of galaxies derived from analysis of Faraday rotation measures, and perspectives for the SKA. *A&A*, 480:45–59, March 2008. doi: 10.1051/0004-6361:20078678.

R. N. Manchester. Pulsar Rotation and Dispersion Measures and the Galactic Magnetic Field. *ApJ*, 172:43, February 1972. doi: 10.1086/151326.

D. Mitra, R. Wielebinski, M. Kramer, and A. Jessner. The effect of HII regions on rotation measure of pulsars. *A&A*, 398:993–1005, February 2003a. doi: 10.1051/0004-6361:20021702.

J. C. Brown, A. R. Taylor, and B. J. Jackel. Rotation Measures of Compact Sources in the Canadian Galactic Plane Survey. *ApJS*, 145:213–223, April 2003. doi: 10.1086/346082.

J. L. Han, R. N. Manchester, E. M. Berkhuijsen, and R. Beck. Antisymmetric rotation measures in our Galaxy: evidence for an A0 dynamo. *A&A*, 322:98–102, June 1997.

S. A. Mao, B. M. Gaensler, M. Haverkorn, E. G. Zweibel, G. J. Madsen, et al. A Survey of Extragalactic Faraday Rotation at High Galactic Latitude: The Vertical Magnetic Field of the Milky Way Toward the Galactic Poles. *ApJ*, 714:1170–1186, May 2010. doi: 10.1088/0004-637X/714/2/1170.

M. Haverkorn, J. C. Brown, B. M. Gaensler, and N. M. McClure-Griffiths. The Outer Scale of Turbulence in the Magnetoionized Galactic Interstellar Medium. *ApJ*, 680:362–370, June 2008. doi: 10.1086/587165.

R. N. Manchester. Structure of the Local Galactic Magnetic Field. *ApJ*, 188:637–644, March 1974. doi: 10.1086/152757.

R. Beck. Galactic and extragalactic magnetic fields - a concise review. *Astrophysics and Space Sciences Transactions*, 5:43–47, October 2009. doi: 10.5194/astra-5-43-2009.

V. I. Pariev, S. A. Colgate, and J. M. Finn. A Magnetic α-ω Dynamo in AGN Disks. II. Magnetic Field Generation, Theories, and Simulations. *ApJ*, 658:129–160, March 2007. doi: 10.1086/510735.

L. M. Widrow. Origin of galactic and extragalactic magnetic fields. *Reviews of Modern Physics*, 74:775–823, 2002. doi: 10.1103/RevModPhys.74.775.

P. Weltevrede, B. W. Stappers, and R. T. Edwards. The subpulse modulation properties of pulsars at 92 cm and the frequency dependence of subpulse modulation. *A&A*, 469:607–631, July 2007. doi: 10.1051/0004-6361:20066855.

J. L. Herfindal and J. M. Rankin. Deep analyses of nulling in Arecibo pulsars reveal further periodic behaviour. *MNRAS*, 393:1391–1402, March 2009. doi: 10.1111/j.1365-2966.2008.14119.x.

S. L. Redman and J. M. Rankin. On the randomness of pulsar nulls. *MNRAS*, 395: 1529–1532, May 2009. doi: 10.1111/j.1365-2966.2009.14632.x.

N. J. Young, B. W. Stappers, P. Weltevrede, A. G. Lyne, and M. Kramer. On the pulse intensity modulation of PSR B0823+26. *MNRAS*, 427:114–126, November 2012. doi: 10.1111/j.1365-2966.2012.21934.x.

G. Hobbs, A. G. Lyne, M. Kramer, C. E. Martin, and C. Jordan. Long-term timing observations of 374 pulsars. *MNRAS*, 353:1311–1344, October 2004. doi: 10.1111/j.1365-2966.2004.08157.x.

T. V. Shabanova, V. D. Pugachev, and K. A. Lapaev. Timing Observations of 27 Pulsars at the Pushchino Observatory from 1978 to 2012. *ApJ*, 775:2, September 2013. doi: 10.1088/0004-637X/775/1/2.

H. D. Craft, R. V. E. Lovelace, and J. M. Sutton. New pulsar. *IAUcirc*, 2100:1, 1968b.

D. R. Lorimer, J. A. Yates, A. G. Lyne, and D. M. Gould. Multifrequency flux density measurements of 280 pulsars. *MNRAS*, 273:411–421, March 1995.

J. P. W. Verbiest, J. M. Weisberg, A. A. Chael, K. J. Lee, and D. R. Lorimer. On Pulsar Distance Measurements and Their Uncertainties. *ApJ*, 755:39, August 2012. doi: 10.1088/0004-637X/755/1/39.

A. D. Kuz'min, B. Y. Losovskii, and K. A. Lapaev. Measurements of the scattering of pulsar radio emission. *Astronomy Reports*, 51:615–623, August 2007. doi: 10.1134/S1063772907080021.

O. Löhmer, A. Jessner, M. Kramer, R. Wielebinski, and O. Maron. Observations of pulsars at 9 millimetres. *A&A*, 480:623–628, March 2008. doi: 10.1051/0004-6361:20066806.

N. Bartel, W. Sieber, and R. Wielebinski. Observations of pulsars at 14.8 and 22.7 GHz. *A&A*, 68:361–365, August 1978.

W. Becker, M. C. Weisskopf, A. F. Tennant, A. Jessner, J. Dyks, et al. Revealing the X-Ray Emission Processes of Old Rotation-powered Pulsars: XMM-Newton Observations of PSR B0950+08, PSR B0823+26, and PSR J2043+2740. *ApJ*, 615:908–920, November 2004. doi: 10.1086/424498.

N. E. Kassim and T. J. W. Lazio. Upper Limits on the Continuum Emission from Geminga at 74 and 326 MHZ. *ApJL*, 527:L101–L104, December 1999. doi: 10.1086/312406.

A. von Hoensbroech and K. M. Xilouris. Effelsberg multifrequency pulsar polarimetry. *A&AS*, 126:121–149, November 1997.

J. H. Seiradakis, J. A. Gil, D. A. Graham, A. Jessner, M. Kramer, et al. Pulsar profiles at high frequencies. I. The data. *A&AS*, 111:205, June 1995.

M. Daszuta, W. Lewandowski, and J. Kijak. Scintillation observations of PSR B0823+26. *MNRAS*, 436:2492–2499, December 2013. doi: 10.1093/mnras/stt1750.

R. Karuppusamy, B. Stappers, and W. van Straten. PuMa-II: A Wide Band Pulsar Machine for the Westerbork Synthesis Radio Telescope. *PASP*, 120:191–202, February 2008. doi: 10.1086/528699.

W. van Straten and M. Bailes. DSPSR: Digital Signal Processing Software for Pulsar Astronomy. *PASA*, 28:1–14, January 2011. doi: 10.1071/AS10021.

A. W. Hotan, W. van Straten, and R. N. Manchester. PSRCHIVE and PSRFITS: An Open Approach to Radio Pulsar Data Storage and Analysis. *PASA*, 21:302–309, 2004. doi: 10.1071/AS04022.

M. Kramer, A. Karastergiou, Y. Gupta, S. Johnston, N. D. R. Bhat, et al. Simultaneous single-pulse observations of radio pulsars. IV. Flux density spectra of individual pulses. *A&A*, 407:655–668, August 2003. doi: 10.1051/0004-6361:20030842.

M. A. Brentjens and A. G. de Bruyn. Faraday rotation measure synthesis. *A&A*, 441: 1217–1228, October 2005. doi: 10.1051/0004-6361:20052990.

C. Sotomayor-Beltran, C. Sobey, J. W. T. Hessels, G. de Bruyn, A. Noutsos, et al. Calibrating high-precision Faraday rotation measurements for LOFAR and the next generation of low-frequency radio telescopes. *A&A*, 552:A58, April 2013. doi: 10.1051/0004-6361/201220728.

D. C. Backer, V. Boriakoff, and R. N. Manchester. Wide Integrated Pulse Profiles of Pulsars. *Nature Physical Science*, 243:77–78, June 1973. doi: 10.1038/physci243077a0.

Kenneth Levenberg. A method for the solution of certain non-linear problems in least squares. *The Quarterly of Applied Mathematics*, 2:164–168, 1944.

M. Kramer. Geometrical analysis of average pulsar profiles using multi-component Gaussian FITS at several frequencies. II. Individual results. *A&AS*, 107:527–539, November 1994.

J. Gil, Y. Gupta, P. B. Gothoskar, and J. Kijak. Frequency Dependence of Pulsar Radiation Patterns. *ApJ*, 565:500–510, January 2002. doi: 10.1086/324497.

T. H. Hankins and L. A. Fowler. Frequency dependence of the main pulse to interpulse separation for seven pulsars. *ApJ*, 304:256–264, May 1986. doi: 10.1086/164159.

P. Weltevrede, G. A. E. Wright, B. W. Stappers, and J. M. Rankin. The bright spiky emission of pulsar B0656+14. *A&A*, 458:269–283, October 2006b. doi: 10.1051/0004-6361:20065572.

M. A. McLaughlin, A. G. Lyne, D. R. Lorimer, M. Kramer, A. J. Faulkner, et al. Transient radio bursts from rotating neutron stars. *Nature*, 439:817–820, February 2006. doi: 10.1038/nature04440.

D. C. Backer. Correlation of Subpulse Structure in a Sequence of Pulses from Pulsar PSR 1919+21. *Nature*, 227:692–695, August 1970c. doi: 10.1038/227692a0.

R. T. Edwards and B. W. Stappers. Drifting sub-pulse analysis using the two-dimensional Fourier transform. *A&A*, 393:733–748, October 2002. doi: 10.1051/0004-6361:20021067.

R. T. Edwards and B. W. Stappers. The frequency-dependence of drifting subpulse patterns. *A&A*, 410:961–966, November 2003. doi: 10.1051/0004-6361:20031326.

I. Backus, D. Mitra, and J. M. Rankin. The topology and polarization of subbeams associated with the 'drifting' subpulse emission of pulsar B0943+10 - VI. Analysis of an 8-h Giant Metrewave Radio Telescope observation. *MNRAS*, 418:1736–1745, December 2011. doi: 10.1111/j.1365-2966.2011.19595.x.

K. Liu, J. P. W. Verbiest, M. Kramer, B. W. Stappers, W. van Straten, et al. Prospects for high-precision pulsar timing. *MNRAS*, 417:2916–2926, November 2011. doi: 10.1111/j.1365-2966.2011.19452.x.

P. B. Jones. An incomplete model of RRATs and of nulls mode changes and subpulses. *MNRAS*, 431:2756–2765, May 2013. doi: 10.1093/mnras/stt372.

S. Burke-Spolaor and M. Bailes. The millisecond radio sky: transients from a blind single-pulse search. *MNRAS*, 402:855–866, February 2010. doi: 10.1111/j.1365-2966.2009.15965.x.

E. F. Keane, M. Kramer, A. G. Lyne, B. W. Stappers, and M. A. McLaughlin. Rotating Radio Transients: new discoveries, timing solutions and musings. *MNRAS*, 415:3065–3080, August 2011. doi: 10.1111/j.1365-2966.2011.18917.x.

N. J. Young, P. Weltevrede, B. W. Stappers, A. G. Lyne, and M. Kramer. On the apparent nulls and extreme variability of PSR J1107-5907. *MNRAS*, 442:2519–2533, August 2014. doi: 10.1093/mnras/stu1036.

N. Bartel, W. Sieber, R. Wielebinski, N. S. Kardashev, N. I. Nikolaev, et al. Simultaneous two-station single pulse observations of radio pulsars over a broad frequency range. I - With particular reference to PSR 0809+74. *A&A*, 93:85–92, January 1981.

I. Contopoulos. The coughing pulsar magnetosphere. *A&A*, 442:579–586, November 2005. doi: 10.1051/0004-6361:20053143.

I. Contopoulos and A. Spitkovsky. Revised Pulsar Spin-down. *ApJ*, 643:1139–1145, June 2006. doi: 10.1086/501161.

A. A. Deshpande and J. M. Rankin. The topology and polarization of sub-beams associated with the 'drifting' sub-pulse emission of pulsar B0943+10 - I. Analysis of Arecibo 430- and 111-MHz observations. *MNRAS*, 322:438–460, April 2001. doi: 10.1046/j.1365-8711.2001.04079.x.

J. Li, A. Spitkovsky, and A. Tchekhovskoy. On the Spin-down of Intermittent Pulsars. *ApJL*, 746:L24, February 2012b. doi: 10.1088/2041-8205/746/2/L24.

M. Kramer, S. Johnston, and W. van Straten. High-resolution single-pulse studies of the Vela pulsar. *MNRAS*, 334:523–532, August 2002. doi: 10.1046/j.1365-8711.2002.05478.x.

J. M. Weisberg, J. M. Cordes, S. C. Lundgren, B. R. Dawson, J. T. Despotes, et al. Arecibo 1418 MHZ Polarimetry of 98 Pulsars: Full Stokes Profiles and Morphological Classifications. *ApJS*, 121:171–217, March 1999. doi: 10.1086/313189.

S. A. Petrova. On the nature of precursors in the radio pulsar profiles. *MNRAS*, 384: L1–L5, February 2008. doi: 10.1111/j.1745-3933.2007.00401.x.

D. Mitra and J. M. Rankin. Toward an Empirical Theory of Pulsar Emission. VII. On the Spectral Behavior of Conal Beam Radii and Emission Heights. *ApJ*, 577:322–336, September 2002. doi: 10.1086/342136.

M. M. McKinnon. Birefringence as a Mechanism for the Broadening and Depolarization of Pulsar Average Profiles. *ApJ*, 475:763–769, February 1997.

A. Noutsos, A. Karastergiou, M. Kramer, S. Johnston, and B. W. Stappers. Phase-resolved Faraday rotation in pulsars. *MNRAS*, 396:1559–1572, July 2009. doi: 10.1111/j.1365-2966.2009.14806.x.

D. H. Staelin and E. C. Reifenstein, III. Faraday Rotation in Pulsars. *ApJL*, 156:L121, June 1969. doi: 10.1086/180362.

V. V. Vitkevich and Y. P. Shitov. Linear Polarization of MP 0628 and its Emission at Metre Wavelengths. *Nature*, 226:1235–1236, June 1970a. doi: 10.1038/2261235a0.

S. P. O'Sullivan, S. Brown, T. Robishaw, D. H. F. M. Schnitzeler, N. M. McClure-Griffiths, et al. Complex Faraday depth structure of active galactic nuclei as revealed by broad-band radio polarimetry. *MNRAS*, 421:3300–3315, April 2012. doi: 10.1111/j.1365-2966.2012.20554.x.

B. F. C. Cooper and R. M. Price. Faraday Rotation Effects associated with the Radio Source Centaurus A. *Nature*, 195:1084–1085, September 1962. doi: 10.1038/1951084a0.

M. Burgay, M. Bailes, S. D. Bates, N. D. R. Bhat, S. Burke-Spolaor, et al. The High Time Resolution Universe Pulsar Survey - VII. Discovery of five millisecond pulsars and the different luminosity properties of binary and isolated recycled pulsars. *MNRAS*, 433: 259–269, July 2013. doi: 10.1093/mnras/stt721.

G. Heald, R. Braun, and R. Edmonds. The Westerbork SINGS survey. II Polarization, Faraday rotation, and magnetic fields. *A&A*, 503:409–435, August 2009a. doi: 10.1051/0004-6361/200912240.

B. J. Burn. On the depolarization of discrete radio sources by Faraday dispersion. *MNRAS*, 133:67, 1966.

G. Heald, R. Braun, and R. Edmonds. The Westerbork SINGS survey. II Polarization, Faraday rotation, and magnetic fields. *A&A*, 503:409–435, August 2009b. doi: 10.1051/0004-6361/200912240.

R. F. Pizzo, A. G. de Bruyn, G. Bernardi, and M. A. Brentjens. Deep multi-frequency rotation measure tomography of the galaxy cluster A2255. *A&A*, 525:A104, January 2011. doi: 10.1051/0004-6361/201014158.

J. M. Weisberg, J. M. Cordes, B. Kuan, K. E. Devine, J. T. Green, et al. Arecibo 430 MHz Pulsar Polarimetry: Faraday Rotation Measures and Morphological Classifications. *ApJS*, 150:317–341, January 2004. doi: 10.1086/379802.

D. H. F. M. Schnitzeler, P. Katgert, and A. G. de Bruyn. WSRT Faraday tomography of the Galactic ISM at λ ˜ 0.86 m. I. The GEMINI data set at (l, b) = (181deg, 20deg). *A&A*, 494:611–622, February 2009. doi: 10.1051/0004-6361:20078912.

M. R. Bell and T. A. Enßlin. Faraday synthesis. The synergy of aperture and rotation measure synthesis. *A&A*, 540:A80, April 2012. doi: 10.1051/0004-6361/201118672.

E. B. Fomalont. Image Analysis. In G. B. Taylor, C. L. Carilli, & R. A. Perley, editor, *Synthesis Imaging in Radio Astronomy II*, volume 180 of *Astronomical Society of the Pacific Conference Series*, page 301, 1999.

A. A. Abdo, M. Ackermann, M. Ajello, W. B. Atwood, L. Baldini, et al. Pulsed Gamma-rays from PSR J2021+3651 with the Fermi Large Area Telescope. *ApJ*, 700:1059–1066, August 2009. doi: 10.1088/0004-637X/700/2/1059.

Z. Arzoumanian, E. V. Gotthelf, S. M. Ransom, S. Safi-Harb, R. Kothes, et al. Discovery of an Energetic Pulsar Associated with SNR G76.9+1.0. *ApJ*, 739:39, September 2011. doi: 10.1088/0004-637X/739/1/39.

P. Bangale. Discovery of New Radio and Gamma-Ray Pulsars Associated with Unidentified Fermi Sources. Master's thesis, Chalmers University of Technology, Sweden, 2011.

J. Boyles, R. S. Lynch, S. M. Ransom, I. H. Stairs, D. R. Lorimer, et al. The Green Bank Telescope 350 MHz Drift-scan survey. I. Survey Observations and the Discovery of 13 Pulsars. *ApJ*, 763:80, February 2013. doi: 10.1088/0004-637X/763/2/80.

F. Crawford and N. C. Keim. Radio Polarization of the Young High-Magnetic-Field Pulsar PSR J1119-6127. *ApJ*, 590:1020–1025, June 2003. doi: 10.1086/375131.

F. Camilo, M. Kerr, P. S. Ray, S. M. Ransom, S. Johnston, et al. PSR J2030+3641: Radio Discovery and Gamma-Ray Study of a Middle-aged Pulsar in the Now Identified Fermi-LAT Source 1FGL J2030.0+3641. *ApJ*, 746:39, February 2012b. doi: 10.1088/0004-637X/746/1/39.

M. E. Costa, P. M. McCulloch, and P. A. Hamilton. Polarization observations of 17 southern pulsars at 600 MHz. *MNRAS*, 252:13–18, September 1991.

F. Crawford, R. N. Manchester, and V. M. Kaspi. Polarization Properties of Nine Southern Radio Pulsars. *AJ*, 122:2001–2007, October 2001. doi: 10.1086/323107.

F. Camilo, C.-Y. Ng, B. M. Gaensler, S. M. Ransom, S. Chatterjee, et al. Out of the Frying Pan: A Young Pulsar with a Long Radio Trail Emerging from SNR G315.9-0.0. *ApJL*, 703:L55–L58, September 2009a. doi: 10.1088/0004-637X/703/1/L55.

F. Camilo, J. Reynolds, S. Johnston, J. P. Halpern, S. M. Ransom, et al. Polarized Radio Emission from the Magnetar XTE J1810-197. *ApJL*, 659:L37–L40, April 2007. doi: 10.1086/516630.

F. Camilo, J. Reynolds, S. Johnston, J. P. Halpern, and S. M. Ransom. The Magnetar 1E 1547.0-5408: Radio Spectrum, Polarimetry, and Timing. *ApJ*, 679:681–686, May 2008. doi: 10.1086/587054.

F. Camilo, P. S. Ray, S. M. Ransom, M. Burgay, T. J. Johnson, et al. Radio Detection of LAT PSRs J1741-2054 and J2032+4127: No Longer Just Gamma-ray Pulsars. *ApJ*, 705:1–13, November 2009b. doi: 10.1088/0004-637X/705/1/1.

F. Crawford and C. L. Tiffany. Flux Densities and Radio Polarization Characteristics of Two Vela-like Pulsars. *AJ*, 134:1231–1236, September 2007. doi: 10.1086/521020.

P. Demorest, R. Ramachandran, D. C. Backer, S. M. Ransom, V. Kaspi, et al. Orientations of Spin and Magnetic Dipole Axes of Pulsars in the J0737-3039 Binary Based on Polarimetry Observations at the Green Bank Telescope. *ApJL*, 615:L137–L140, November 2004. doi: 10.1086/426429.

R. P. Eatough, H. Falcke, R. Karuppusamy, K. J. Lee, D. J. Champion, et al. A strong magnetic field around the supermassive black hole at the centre of the Galaxy. *Nature*, 501:391–394, September 2013b. doi: 10.1038/nature12499.

P. A. Hamilton, P. M. McCulloch, R. N. Manchester, J. G. Ables, and M. M. Komesaroff. Detection of change in rotation measure of the VELA pulsar. *Nature*, 265:224, January 1977. doi: 10.1038/265224a0.

A. W. Hotan, M. Bailes, and S. M. Ord. PSR J0737-3039A: baseband timing and polarimetry. *MNRAS*, 362:1267–1272, October 2005. doi: 10.1111/j.1365-2966.2005.09389.x.

P. A. Hamilton and A. G. Lyne. Faraday rotation measurements on 163 pulsars. *MNRAS*, 224:1073–1081, February 1987.

J. L. Han, R. N. Manchester, and G. J. Qiao. Pulsar rotation measures and the magnetic structure of our Galaxy. *MNRAS*, 306:371–380, June 1999. doi: 10.1046/j.1365-8711.1999.02544.x.

T. H. Hankins and J. M. Rankin. Arecibo Multi-Frequency Time-Aligned Pulsar Average-Profile and Polarization Database. *AJ*, 139:168–175, January 2010. doi: 10.1088/0004-6256/139/1/168.

S. Johnston, G. Hobbs, S. Vigeland, M. Kramer, J. M. Weisberg, et al. Evidence for alignment of the rotation and velocity vectors in pulsars. *MNRAS*, 364:1397–1412, December 2005. doi: 10.1111/j.1365-2966.2005.09669.x.

S. Johnston, M. Kramer, A. Karastergiou, G. Hobbs, S. Ord, et al. Evidence for alignment of the rotation and velocity vectors in pulsars - II. Further data and emission heights. *MNRAS*, 381:1625–1637, November 2007. doi: 10.1111/j.1365-2966.2007.12352.x.

S. Johnston and J. M. Weisberg. Profile morphology and polarization of young pulsars. *MNRAS*, 368:1856–1870, June 2006. doi: 10.1111/j.1365-2966.2006.10263.x.

M. J. Keith, S. Johnston, M. Bailes, S. D. Bates, N. D. R. Bhat, et al. The High Time Resolution Universe Pulsar Survey - IV. Discovery and polarimetry of millisecond pulsars. *MNRAS*, 419:1752–1765, January 2012. doi: 10.1111/j.1365-2966.2011.19842.x.

M. J. Keith, S. Johnston, M. Kramer, P. Weltevrede, K. P. Watters, et al. A high-frequency search for radio pulsars in three EGRET error boxes. *MNRAS*, 389:1881–1884, October 2008. doi: 10.1111/j.1365-2966.2008.13711.x.

M. J. Keith, S. Johnston, P. S. Ray, E. C. Ferrara, P. M. Saz Parkinson, et al. Discovery of millisecond pulsars in radio searches of southern Fermi Large Area Telescope sources. *MNRAS*, 414:1292–1300, June 2011. doi: 10.1111/j.1365-2966.2011.18464.x.

V. M. Kaspi, A. G. Lyne, R. N. Manchester, F. Crawford, F. Camilo, et al. Discovery of a Young Radio Pulsar in a Relativistic Binary Orbit. *ApJ*, 543:321–327, November 2000. doi: 10.1086/317103.

L. Levin, M. Bailes, S. Bates, N. D. R. Bhat, M. Burgay, et al. A Radio-loud Magnetar in X-ray Quiescence. *ApJL*, 721:L33–L37, September 2010. doi: 10.1088/2041-8205/721/1/L33.

R. S. Lynch, J. Boyles, S. M. Ransom, I. H. Stairs, D. R. Lorimer, et al. The Green Bank Telescope 350 MHz Drift-scan Survey II: Data Analysis and the Timing of 10 New Pulsars, Including a Relativistic Binary. *ApJ*, 763:81, February 2013. doi: 10.1088/0004-637X/763/2/81.

R. S. Lynch, P. C. C. Freire, S. M. Ransom, and B. A. Jacoby. The Timing of Nine Globular Cluster Pulsars. *ApJ*, 745:109, February 2012. doi: 10.1088/0004-637X/745/2/109.

D. R. Lorimer, I. H. Stairs, P. C. Freire, J. M. Cordes, F. Camilo, et al. Arecibo Pulsar Survey Using ALFA. II. The Young, Highly Relativistic Binary Pulsar J1906+0746. *ApJ*, 640:428–434, March 2006. doi: 10.1086/499918.

M. A. McLaughlin, Z. Arzoumanian, J. M. Cordes, D. C. Backer, A. N. Lommen, et al. PSR J1740+1000: A Young Pulsar Well Out of the Galactic Plane. *ApJ*, 564:333–342, January 2002. doi: 10.1086/324151.

R. N. Manchester and J. L. Han. Polarization Observations of Nine Southern Millisecond Pulsars. *ApJ*, 609:354–362, July 2004. doi: 10.1086/420918.

R. N. Manchester and G. Hobbs. A Giant Glitch in PSR J1718-3718. *ApJL*, 736:L31, August 2011. doi: 10.1088/2041-8205/736/2/L31.

R. N. Manchester and S. Johnston. Polarization properties of two pulsars. *ApJL*, 441: L65–L68, March 1995. doi: 10.1086/187791.

D. Mitra, R. Wielebinski, M. Kramer, and A. Jessner. The effect of HII regions on rotation measure of pulsars. *A&A*, 398:993–1005, February 2003b. doi: 10.1051/0004-6361:20021702.

C. Ng, M. Bailes, S. D. Bates, N. D. R. Bhat, M. Burgay, et al. The High Time Resolution Universe pulsar survey - X. Discovery of four millisecond pulsars and updated timing solutions of a further 12. *MNRAS*, 439:1865–1883, April 2014. doi: 10.1093/mnras/stu067.

J. Navarro, R. N. Manchester, J. S. Sandhu, S. R. Kulkarni, and M. Bailes. Mean Pulse Shape and Polarization of PSR J0437-4715. *ApJ*, 486:1019–1025, September 1997.

J. T. O'Brien, S. Johnston, M. Kramer, A. G. Lyne, M. Bailes, et al. PSR J1410-6132: a young, energetic pulsar associated with the EGRET source 3EG J1410-6147. *MNRAS*, 388:L1–L5, July 2008. doi: 10.1111/j.1745-3933.2008.00481.x.

G. Qiao, R. N. Manchester, A. G. Lyne, and D. M. Gould. Polarization and Faraday rotation measurements of southern pulsars. *MNRAS*, 274:572–588, May 1995.

M. S. E. Roberts, R. W. Romani, and S. Johnston. Multiwavelength Studies of PSR J1420-6048, a Young Pulsar in the Kookaburra. *ApJL*, 561:L187–L190, November 2001. doi: 10.1086/324752.

F. G. Smith. Faraday Rotation of Radio Waves from the Pulsars. *Nature*, 220:891–892, November 1968. doi: 10.1038/220891a0.

R. M. Shannon and S. Johnston. Radio properties of the magnetar near Sagittarius A* from observations with the Australia Telescope Compact Array. *MNRAS*, 435: L29–L32, August 2013a. doi: 10.1093/mnrasl/slt088.

Y. P. Shitov, A. D. Kuzmin, D. V. Dumskii, and B. Y. Losovsky. Detection of the new rotating radio transient pulsar PSR J2225+35. *Astronomy Reports*, 53:561–563, June 2009. doi: 10.1134/S1063772909060080.

J. H. Taylor, R. N. Manchester, and A. G. Lyne. Catalog of 558 pulsars. *ApJS*, 88: 529–568, October 1993. doi: 10.1086/191832.

G. Theureau, D. Parent, I. Cognard, G. Desvignes, D. A. Smith, et al. PSRs J0248+6021 and J2240+5832: young pulsars in the northern Galactic plane. Discovery, timing, and gamma-ray observations. *A&A*, 525:A94, January 2011a. doi: 10.1051/0004-6361/201015317.

T. D. van Ommen, F. D'Alessandro, P. A. Hamilton, and P. M. McCulloch. Polarimetric observations of southern pulsars at 800 and 950 MHz. *MNRAS*, 287:307–327, May 1997.

V. V. Vitkevich and Y. P. Shitov. New results in investigating interstellar plasma by means of its "transillumination" ("radio-raying") using pulsars. *Radiophysics and Quantum Electronics*, 13:1457–1465, December 1970b. doi: 10.1007/BF01033000.

W. M. Yan, R. N. Manchester, W. van Straten, J. E. Reynolds, G. Hobbs, et al. Polarization observations of 20 millisecond pulsars. *MNRAS*, 414:2087–2100, July 2011. doi: 10.1111/j.1365-2966.2011.18522.x.

G. C. Bower, M. C. H. Wright, H. Falcke, and D. C. Backer. Interferometric Detection of Linear Polarization from Sagittarius A* at 230 GHz. *ApJ*, 588:331–337, May 2003. doi: 10.1086/373989.

R. N. Manchester, A. G. Lyne, F. Camilo, J. F. Bell, V. M. Kaspi, et al. The Parkes multi-beam pulsar survey - I. Observing and data analysis systems, discovery and timing of 100 pulsars. *MNRAS*, 328:17–35, November 2001. doi: 10.1046/j.1365-8711.2001.04751.x.

J. L. Chen, H. G. Wang, N. Wang, A. Lyne, Z. Y. Liu, et al. Long-term Monitoring of Mode Switching for PSR B0329+54. *ApJ*, 741:48, November 2011. doi: 10.1088/0004-637X/741/1/48.

D. Mitra, J. M. Rankin, and Y. Gupta. Absolute broad-band polarization behaviour of PSR B0329+54: a glimpse of the core emission process. *MNRAS*, 379:932–944, August 2007. doi: 10.1111/j.1365-2966.2007.11988.x.

E. Petroff, M. J. Keith, S. Johnston, W. van Straten, and R. M. Shannon. Dispersion measure variations in a sample of 168 pulsars. *MNRAS*, 435:1610–1617, October 2013. doi: 10.1093/mnras/stt1401.

D. A. Green. A revised Galactic supernova remnant catalogue. *Bulletin of the Astronomical Society of India*, 37:45–61, March 2009.

E. Smith, J. Rankin, and D. Mitra. Core and conal component analysis of pulsar B1237+25 - II. Investigation of the segregated modes. *MNRAS*, 435:1984–2002, November 2013. doi: 10.1093/mnras/stt1404.

N. W. Broten, J. M. MacLeod, and J. P. Vallee. Catalogue of unambiguous (Faraday-thin, one-component, spectrum-selected) rotation measures for galaxies and quasars. *ApSS*, 141:303–331, February 1988. doi: 10.1007/BF00639497.

M. Haverkorn, B. M. Gaensler, N. M. McClure-Griffiths, J. M. Dickey, and A. J. Green. The Southern Galactic Plane Survey: Polarized Radio Continuum Observations and Analysis. *ApJS*, 167:230–238, December 2006. doi: 10.1086/508467.

A. R. Taylor, S. J. Gibson, M. Peracaula, P. G. Martin, T. L. Landecker, et al. The Canadian Galactic Plane Survey. *AJ*, 125:3145–3164, June 2003. doi: 10.1086/375301.

A. W. Clegg, J. M. Cordes, J. M. Simonetti, and S. R. Kulkarni. Rotation measures of low-latitude extragalactic sources and the magnetoionic structure of the Galaxy. *ApJ*, 386:143–157, February 1992. doi: 10.1086/171000.

B. M. Gaensler, J. M. Dickey, N. M. McClure-Griffiths, A. J. Green, M. H. Wieringa, et al. Radio Polarization from the Inner Galaxy at Arcminute Resolution. *ApJ*, 549: 959–978, March 2001. doi: 10.1086/319468.

N. M. McClure-Griffiths, A. J. Green, J. M. Dickey, B. M. Gaensler, R. F. Haynes, et al. The Southern Galactic Plane Survey: The Test Region. *ApJ*, 551:394–412, April 2001. doi: 10.1086/320095.

R. Braun, T. A. Oosterloo, R. Morganti, U. Klein, and R. Beck. The Westerbork SINGS survey. I. Overview and image atlas. *A&A*, 461:455–470, January 2007. doi: 10.1051/0004-6361:20066092.

S. A. Mao, B. M. Gaensler, S. Stanimirović, M. Haverkorn, N. M. McClure-Griffiths, et al. A Radio and Optical Polarization Study of the Magnetic Field in the Small Magellanic Cloud. *ApJ*, 688:1029–1049, December 2008. doi: 10.1086/590546.

A. H. Minter and S. R. Spangler. Observation of Turbulent Fluctuations in the Interstellar Plasma Density and Magnetic Field on Spatial Scales of 0.01 to 100 Parsecs. *ApJ*, 458:194, February 1996. doi: 10.1086/176803.

A. L. Oren and A. M. Wolfe. A Faraday rotation search for magnetic fields in quasar damped LY alpha absorption systems. *ApJ*, 445:624–641, June 1995. doi: 10.1086/175726.

A. R. Taylor, J. M. Stil, and C. Sunstrum. A Rotation Measure Image of the Sky. *ApJ*, 702:1230–1236, September 2009. doi: 10.1088/0004-637X/702/2/1230.

J. J. Condon, W. D. Cotton, E. W. Greisen, Q. F. Yin, R. A. Perley, et al. The NRAO VLA Sky Survey. *AJ*, 115:1693–1716, May 1998. doi: 10.1086/300337.

H. W. Wells. Effects of solar activity on the ionosphere and radio communications. *Proceedings of the IRE*, 31(4):147–157, April 1943. ISSN 0096-8390. doi: 10.1109/JRPROC.1943.229732.

W. K. Lee, H. Kil, Y.-S. Kwak, Q. Wu, S. Cho, et al. The winter anomaly in the middle-latitude f region during the solar minimum period observed by the constellation observing system for meteorology, ionosphere, and climate. *Journal of Geophysical Research: Space Physics*, 116(A2):n/a–n/a, 2011. ISSN 2156-2202. doi: 10.1029/2010JA015815. URL `http://dx.doi.org/10.1029/2010JA015815`.

E. V. Appleton. Two anomalies in the ionosphere. *Nature*, 157:691, May 1946.

M. A. Brentjens. Deep Westerbork observations of Abell 2256 at 350 MHz. *A&A*, 489:69–83, October 2008. doi: 10.1051/0004-6361:20077174.

W. C. Erickson, R. A. Perley, C. Flatters, and N. E. Kassim. Ionospheric corrections for VLA observations using Local GPS data. *A&A*, 366:1071–1080, February 2001. doi: 10.1051/0004-6361:20000359.

E. L. Afraimovich, G. Y. Smolkov, P. V. Tatarinov, and Y. V. Yasukevich. Influence of the ionosphere on radio astronomical signals according to GPS sounding and ionospheric modeling. In *Society of Photo-Optical Instrumentation Engineers (SPIE) Conference Series*, volume 6936 of *Society of Photo-Optical Instrumentation Engineers (SPIE) Conference Series*, May 2008. doi: 10.1117/12.783664.

D. Bilitza and B. W. Reinisch. International Reference Ionosphere 2007: Improvements and new parameters. *Advances in Space Research*, 42:599–609, August 2008. doi: 10.1016/j.asr.2007.07.048.

E. W. Greisen. AIPS, the VLA, and the VLBA. *Information Handling in Astronomy - Historical Vistas*, 285:109, March 2003. doi: 10.1007/0-306-48080-8_7.

C. C. Finlay, S. Maus, C. D. Beggan, T. N. Bondar, A. Chambodut, et al. International Geomagnetic Reference Field: the eleventh generation. *Geophysical Journal International*, 183:1216–1230, December 2010. doi: 10.1111/j.1365-246X.2010.04804.x.

S. Schaer. Mapping and predicting the earth's ionosphere using the global positioning system. *Geod.-Geophys. Arb. Schweiz, Vol. 59,*, 59, 1999.

S. W. Schaer, W. Gurtner, and J. Feltens. IONEX: The IONosphere Map EXchange Format Version 1. In *Proceedings of the 1998 IGS Analysis Centres Workshop*, pages 233–247, ESOC, Darmstadt, Germany, February 1998.

P. M. Geil, B. M. Gaensler, and J. S. B. Wyithe. Polarized foreground removal at low radio frequencies using rotation measure synthesis: uncovering the signature of hydrogen reionization. *MNRAS*, 418:516–535, November 2011. doi: 10.1111/j.1365-2966.2011.19509.x.

J.-P. Macquart, R. D. Ekers, I. Feain, and M. Johnston-Hollitt. On the reliability of polarization estimation using Rotation Measure Synthesis. *ArXiv e-prints*, March 2012.

N. E. Kassim, T. J. W. Lazio, W. C. Erickson, R. A. Perley, W. D. Cotton, et al. The 74 MHz System on the Very Large Array. *ApJS*, 172:686–719, October 2007. doi: 10.1086/519022.

M. Hernández-Pajares, J.M. Juan, J. Sanz, R. Orus, A. Garcia-Rigo, et al. The igs vtec maps: a reliable source of ionospheric information since 1998. *Journal of Geodesy*, 83 (3-4):263–275, 2009. ISSN 0949-7714. doi: 10.1007/s00190-008-0266-1. URL `http://dx.doi.org/10.1007/s00190-008-0266-1`.

A. Garcia-Rigo, E. Monte, M. Hernández-Pajares, J. M. Juan, J. Sanz, et al. Global prediction of the vertical total electron content of the ionosphere based on gps data.

Radio Science, 46(6):n/a–n/a, 2011. ISSN 1944-799X. doi: 10.1029/2010RS004643. URL `http://dx.doi.org/10.1029/2010RS004643`.

G. S. Bust and C. N. Mitchell. History, current state, and future directions of ionospheric imaging. *Reviews of Geophysics*, 46(1), 2008. doi: 10.1029/2006rg000212. URL `http://opus.bath.ac.uk/5671/`.

R. Wielebinski and J. R. Shakeshaft. Faraday Rotation of Polarized Galactic Radio Emission. *Nature*, 195:982–983, September 1962. doi: 10.1038/195982a0.

B. Hamilton. Rapid modelling of the large-scale magnetospheric field from Swarm satellite data. *Earth, Planets, and Space*, 65:1295–1308, November 2013. doi: 10.5047/eps.2013.09.003.

G. B. Hobbs, R. T. Edwards, and R. N. Manchester. TEMPO2, a new pulsar-timing package - I. An overview. *MNRAS*, 369:655–672, June 2006. doi: 10.1111/j.1365-2966.2006.10302.x.

W. van Straten. Radio Astronomical Polarimetry and Phase-coherent Matrix Convolution. *ApJ*, 568:436–442, March 2002. doi: 10.1086/338810.

E. D. Barr, D. J. Champion, M. Kramer, R. P. Eatough, P. C. C. Freire, et al. The Northern High Time Resolution Universe pulsar survey - I. Setup and initial discoveries. *MNRAS*, 435:2234–2245, November 2013. doi: 10.1093/mnras/stt1440.

R. Stepanov, P. Frick, A. Shukurov, and D. Sokoloff. Wavelet tomography of the Galactic magnetic field. I. The method. *A&A*, 391:361–368, August 2002. doi: 10.1051/0004-6361:20020552.

J.-L. Starck and J. Bobin. Astronomical Data Analysis and Sparsity: from Wavelets to Compressed Sensing. *ArXiv e-prints*, March 2009.

T. T. Pennucci, P. B. Demorest, and S. M. Ransom. Elementary Wideband Timing of Radio Pulsars. *ApJ*, 790:93, August 2014. doi: 10.1088/0004-637X/790/2/93.

L. M. Haffner, R. J. Reynolds, S. L. Tufte, G. J. Madsen, K. P. Jaehnig, et al. The Wisconsin Hα Mapper Northern Sky Survey. *ApJS*, 149:405–422, December 2003. doi: 10.1086/378850.

J. E. Gaustad, P. R. McCullough, W. Rosing, and D. Van Buren. A Robotic Wide-Angle Hα Survey of the Southern Sky. *PASP*, 113:1326–1348, November 2001. doi: 10.1086/323969.

P. C. Freire, M. Kramer, A. G. Lyne, F. Camilo, R. N. Manchester, et al. Detection of Ionized Gas in the Globular Cluster 47 Tucanae. *ApJL*, 557:L105–L108, August 2001. doi: 10.1086/323248.

X. P. You, W. A. Coles, G. B. Hobbs, and R. N. Manchester. Measurement of the electron density and magnetic field of the solar wind using millisecond pulsars. *MNRAS*, 422: 1160–1165, May 2012. doi: 10.1111/j.1365-2966.2012.20688.x.

R. M. Shannon and S. Johnston. Radio properties of the magnetar near Sagittarius A* from observations with the Australia Telescope Compact Array. *ArXiv e-prints*, May 2013b.

G. Theureau, D. Parent, I. Cognard, G. Desvignes, D. A. Smith, et al. PSRs J0248+6021 and J2240+5832: young pulsars in the northern Galactic plane. Discovery, timing, and gamma-ray observations. *A&A*, 525:A94, January 2011b. doi: 10.1051/0004-6361/201015317.

Erklärung

Ich versichere, dass ich die von mir vorgelegte Dissertation selbständig angefertigt, die benutzten Quellen und Hilfsmittel vollständig angegeben und die Stellen der Arbeit- einschlielich Tabellen, Karten und Abbildungen –, die anderen Werken im Wortlaut oder dem Sinn nach entnommen sind, in jedem Einzelfall als Entlehnung kenntlich gemacht habe; dass diese Dissertation noch keiner anderen Fakultät oder Universität zur Prfung vorgelegen hat; dass sie noch nicht verffentlicht worden ist sowie, da ich eine solche Veröffentlichung vor Abschluss des Promotionsverfahrens nicht vornehmen werde. Die Bestimmungen dieser Promotionsordnung sind mir bekannt. Die von mir vorgelegte Dissertation ist von Prof. Dr. Michael Kramer betreut worden.

Unterschrift: _____

Datum: _____

Publications

Refereed

1. Calibrating high-precision Faraday rotation measurements for LOFAR and the next generation of low-frequency radio telescopes. C. Sotomayor-Beltran, **C. Sobey**, J. W. T. Hessels, G. de Bruyn, A. Noutsos, et al. Astronomy & Astrophysics, Volume 552, id.A58, 13 pp. (2013)

2. LOFAR discovery of a quiet emission mode in PSR B0823+26. **C. Sobey**, N. J. Young, J. W. T. Hessels, P. Weltevrede, A. Noutsos, et al. Monthly Notices of the Royal Astronomical Society, submitted (2014)

Proceedings, Oral & Poster Contributions

1. Pulsar Rotation Measures and the Large-Scale Magnetic Structure of the Milky Way. **C. Sobey**, A. Noutsos, M. Kramer. Poster Contribution. Proceedings of the 25th Texas Symposium on Relativistic Astrophysics. Heidelberg, Germany (2010)

2. Investigating astrophysical plasmas using LOFAR observations of pulsars. **C. Sobey**, LOFAR collaboration. Oral Presentation. American Astronomical Society, AAS Meeting #223, #212.02. National Harbor, USA (2014)

In preparation

1. Pulsar Polarisation Below 200 MHz: Average Profiles & Propagation Effects. A. Noutsos, **C. Sobey**, V. I. Kondratiev, P. Weltevrede, J. P. W. Verbiest, et al. Astronomy & Astrophysics, in preparation (2014).

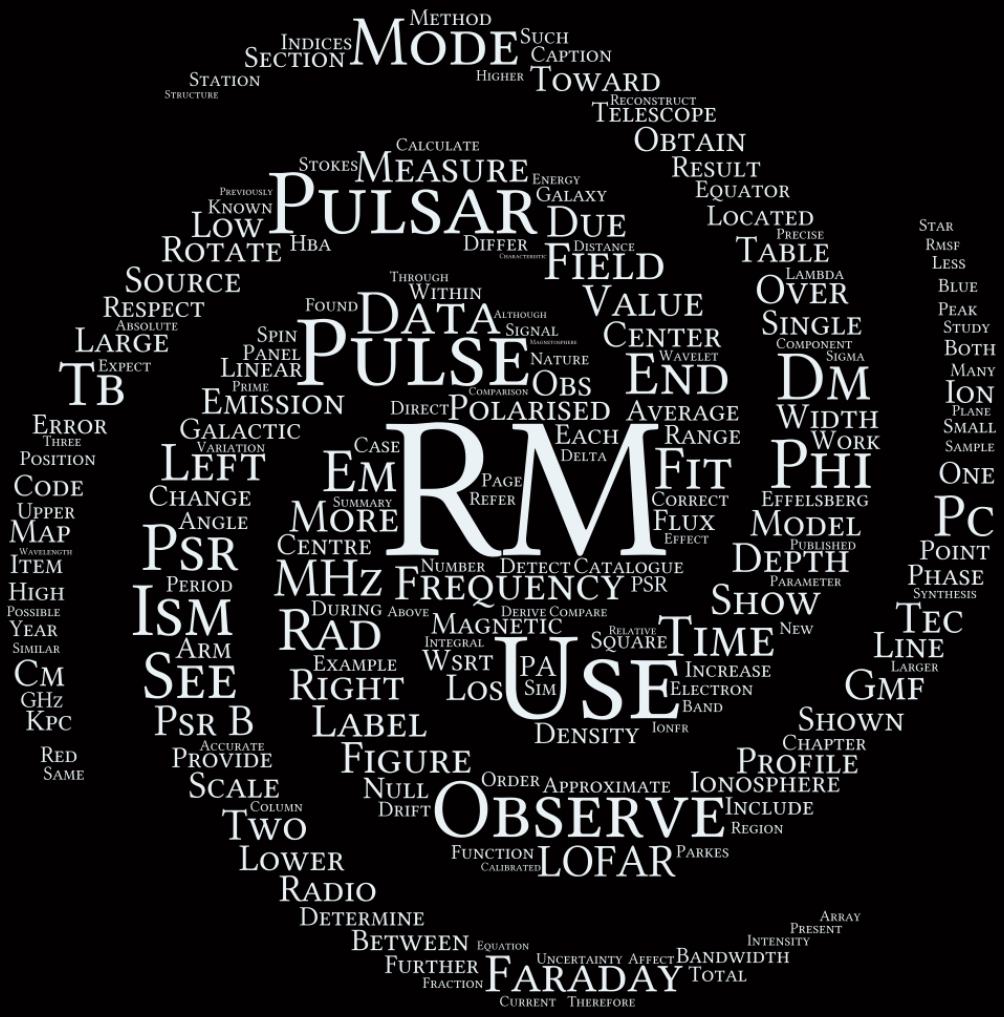
RM
Pulsar
Pulse
Use
Observe
Mode
Data
Measure
Obtain
Result
Equator
Located
Table
Field
Value
Over
Single
Center
End
Dm
Width
Phi
Fit
Em
Left
Psr
Mhz
Frequency
Rad
Time
See
Right
Label
Figure
Scale
Two
Lower
Radio
Determine
Between
Further
Faraday
Lofar
Ism
Tb
Pc
Tec
Gmf
Shown
Profile
Ionosphere
Include
Depth
Model
Show
Line
Phase
Point
Ion
One
Small
Many
Both
Blue
Peak
Study
Less
Star
Rmsf
Sample
Work
Range
Each
Delta
Case
Page
Refer
Correct
Flux
Effect
Effelsberg
Published
Parameter
Synthesis
Plane
Lambda
Component
Sigma
Wavelet
Nature
Obs
Polarised
Average
Direct
Comparison
Emission
Linear
Panel
Spin
Found
Within
Through
Signal
Although
Magnetospheres
Value
Due
Differ
Distance
Characteristic
Rotate
Hba
Low
Known
Previously
Energy
Galaxy
Measure
Stokes
Calculate
Telescope
Reconstruct
Toward
Higher
Caption
Such
Mode
Indices
Section
Station
Structure
Method
Source
Respect
Absolute
Large
Expect
Error
Three
Position
Code
Upper
Map
Wavelength
Item
High
Possible
Year
Similar
Cm
Ghz
Kpc
Red
Same
Psr B
Accurate
Provide
Arm
Change
Angle
Left
Galactic
Variation
Emission
Prime
Tb
Large
Respect
Source
Rotate
Low
Known
Previously
Pulsar
Stokes
Measure
Station
Structure
Indices
Section
Mode
Method
Such
Caption
Higher
Toward
Telescope
Reconstruct
Obtain
Result
Equator
Located
Precise
Table
Lambda
Over
Single
Component
Sigma
Wavelet
Nature
Obs
End
Dm
Width
Work
Range
Each
Delta
Case
Page
Refer
Correct
Flux
Effect
Effelsberg
Phi
Fit
Em
Left
Psr
Mhz
Frequency
Rad
Time
See
Right
Label
Figure
Scale
Two
Lower
Radio
Determine
Between
Further
Faraday
Lofar
Ism
Tb
Pc
Tec
Gmf
Shown
Profile
Ionosphere
Include
Depth
Model
Show
Line
Phase
Point
Ion
One
Small
Many
Both
Blue
Peak
Study
Less
Star
Rmsf
Sample
Plane
Smaller
Parkes
Region
Chapter
Ionfr
Band
Electron
Increase
Sim
Pa
Wsrt
Integral
Square
Relative
New
Derive
Compare
During
Above
Psr
Parameter
Published
Point
Phase
Synthesis
Larger
Line
Tec
Show
Model
Depth